

**SYNTHESES AND APPLICATIONS OF TRIPLY FERROCENE-BRIDGED
BOROXINE CYCLOPHANE, PERFLUORINATED POROUS MATERIALS,
AND METAL-MACROCYCLIC FRAMEWORKS**

A Dissertation Presented to
the Faculty of the Department of Chemistry
University of Houston

In Partial Fulfillment
of the Requirements for the Degree
Doctor of Philosophy

By
Teng-Hao Chen

August 2014

**SYNTHESES AND APPLICATIONS OF TRIPLY FERROCENE-BRIDGED
BOROXINE CYCLOPHANE, PERFLUORINATED POROUS MATERIALS,
AND METAL-MACROCYCLIC FRAMEWORKS**

Teng-Hao Chen

APPROVED:

Prof. Ognjen Š. Miljanić, Chairman

Prof. Allan J. Jacobson

Prof. T. Randall Lee

Prof. Loi H. Do

Prof. Jeffrey Rimer

Dean, College of Natural Sciences and
Mathematics

Dedicated to my grandfather

who looks after me from heaven

ACKNOWLEDGMENTS

Exactly five years have passed since I decided to study Ph.D. in Chemistry at the University of Houston. As people say, choosing an advisor or a research group is like a marriage. Five years is not long for a marriage (maybe too long for somebody), but is enough to influence my whole life. I am very glad to marry this group for the past five years and eventually reach the destination. The most important person during my graduate student life is my advisor Professor Ognjen Miljanić. I still remember the scenario when we had the interview in his empty office which was just moved from Fleming Building to SERC. At that time my shape was still fit. He has always encouraged me since the first day we met and I barely feel pressure under his direction. Instead, he has given me so much freedom on my research that I cannot even count how many projects I failed. His scientific discipline allows me to think openly and critically. My motivation to develop 3D printed crystal structure models was inspired by him as well. Another thing I need to emphasize is that I have learned many unusual English words and phrases from his writing, even though I do not know how to use them. Undoubtedly, I am deeply grateful to have him as a boss but more like a friend; his first experience of riding a scooter was with me.

Among the faculty in our department, I would like to express my great appreciation to Professor Allan J. Jacobson for his kindness and generosity. As the first student working on the porous materials in my lab, I did not have many resources and lab

instruments needed to finish my work. I asked his group for help very often and had fruitful results. Professor Olafs Daugulis allowed his student Ilya Popov to collaborate with us, and their well-established organometallics chemistry has immensely benefited my research. I am indebted to Professor T. Randall Lee and Dr. Oussama Zenasni for teaching me how to use the contact angle instrument. I also wish to express my gratitude to Dr. James Korp, who was always bothered by me with all the problems about crystal structure analysis. Moreover, due to the great management of the adsorption instrument in Professor Jeffrey Rimer's group (Chemical & Biomolecular Engineering), I was able to conduct my experiments efficiently. I thank Professor Mircea Dincă's group at MIT for teaching me how to perform adsorption experiments.

A great lab and a comfortable working environment are essential for productive research and the most important factor is people. Without my group members' accompany and support, it would be extremely lonely for me on the journey of research. Since I joined the lab, Dr. Karolina Osowska and Jaebum Lim taught me everything from fundamental details. After me, Qing Ji, Rio Carlo Lirag, Minyoung Jo, Ha Le, Chia-Wei Hsu, Dr. Musabbir Saeed, Xiao Liang, and Mohamed Hashim joined the group, and everyone works hard to keep this group in a good shape. It is a joyful lab! Friends out of my own lab are equally important because they have made my off-research time colorful. We had really good time on a badminton court, and of course I won a lot. All my Taiwanese friends are wonderful, and speaking Taiwanese to them made me feel homesick. Especially, the Huang-Chi Du couple, we shared so much good time on baseball, my favorite sport, and we often worked out together. Chieng-Hung Li and I

came to study Ph.D. at the same time and we fought together in the Organic Synthesis class.

In my research, nothing can be finished without collaborations. There are three people worthy of another 100 pages for addressing my appreciation. First of all, Watchareeya Kaveevivitchai, my classmate from Professor Jacobson's lab, has helped me and taught me about all the inorganic chemistry experiments I needed. It is super lucky for me to have such a good friend when working in other labs. Second, Ilya Popov, from Professor Daugulis's lab, is an extremely intelligent and skillful organic chemist and he has made a tremendous contribution to my research. He is a wonderful friend to our entire group and is willing to share all his knowledge. Third, Dr. Yu-Chun Chuang, a researcher at National Synchrotron Radiation Research Center in Taiwan, has dealt with all my troublesome crystal structures and helped me collaborate with Dr. Yu-Sheng Chen at Argonne National Laboratory. Our relationship is only that we both are the alumni of the National Taiwan University, but his assistance has been the most important part that enables my research to go any further.

Finally, my deepest gratitude goes to my family. As a professor, my father has given me many precious pieces of advice that keep my path in this journey. My mother has always encouraged me and prayed for me. With my brother coming with me to Texas at the same time and two uncles living in Houston, I have not felt lonely at all and had a lot of good food in these five years. The dissertation is for all of them!

**SYNTHESES AND APPLICATIONS OF TRIPLY FERROCENE-BRIDGED
BOROXINE CYCLOPHANE, PERFLUORINATED POROUS MATERIALS,
AND METAL-MACROCYCLIC FRAMEWORKS**

An Abstract of a Dissertation Presented to
the Faculty of the Department of Chemistry
University of Houston

In Partial Fulfillment
of the Requirements for the Degree
Doctor of Philosophy

By
Teng-Hao Chen

August 2014

ABSTRACT

This dissertation presents the syntheses and characterizations of triply ferrocene-bridged boroxine cyclophane, fluorinated metal-organic frameworks and noncovalent organic framework, metal-macrocyclic frameworks, and the host-guest chemistry of the macrocycle. A procedure for the production of 3D models of crystal structures is reported as well.

Chapter One. This chapter summarizes previous work and applications on porous materials such as metal-organic frameworks, covalent organic frameworks, and crystalline noncovalent organic porous materials.

Chapter Two. The syntheses of ferrocene-based ligands as building blocks for MOF construction and the synthesis of triply ferrocene-bridged boroxine cyclophane are presented.

Chapter Three. This chapter describes the syntheses and characterizations of six perfluorinated metal-organic frameworks as well as their superhydrophobic properties and unique adsorption behaviors.

Chapter Four. The synthesis and characterization of a perfluorinated noncovalent organic framework and its exceptional affinity for fluorocarbons and Freons are discussed.

Chapter Five. The use of shape-persistent dehydrobenzannulene macrocycles for the syntheses of Zn- and Zr-based metal-macrocyclic frameworks is presented. The host-guest chemistry of the macrocycles with fluorinated arenes is also studied.

Chapter Six. Step by step procedures for the production of 3D models of crystal structures and pictorial examples of 3D printed models are displayed.

TABLE OF CONTENTS

Acknowledgments	iv
Abstract	viii
Table of Contents	x
List of Figures	xvii
List of Schemes	xxvii
List of Tables	xxix
List of Abbreviations and Acronyms	xxxix

Chapter One Crystalline Porous Materials Based on Organic Molecules

1.1 Introduction.....	1
1.2 Metal-Organic Frameworks.....	3
1.2.1 Modular Synthesis of MOFs.....	3
1.2.1.1 Conventional Synthesis.....	3
1.2.1.2 Alternative Synthetic Methods.....	4
1.2.1.3 Structure-directing Approaches.....	6
1.2.2 Rise of the Ligands: Applications of Sophisticated Organic Linkers in MOF Chemistry.....	8
1.2.2.1 Postsynthetic Modification.....	10
1.2.2.2 Application-based Linkers.....	12

1.2.3	Applications of MOFs Based on High Porosity, Structures, and Functional Components.....	15
1.2.3.1	Applications Based on High Porosity of MOFs.....	16
1.2.3.2	Applications Based on the Structures of MOFs.....	20
1.2.3.3	Applications Based on Functional Components of MOFs.....	22
1.2.4	Conclusions and Outlook.....	25
1.3	Covalent Organic Frameworks.....	27
1.3.1	Dynamic Covalent Chemistry.....	28
1.3.2	Modular Synthesis of COFs.....	31
1.3.3	Applications of COFs.....	37
1.3.3.1	Gas Adsorption.....	37
1.3.3.2	Catalysis.....	38
1.3.3.3	Semiconduction and Photoconduction.....	39
1.3.4	Conclusions and Outlook.....	41
1.4	Crystalline Noncovalent Porous Organic Materials.....	41
1.4.1	Intrinsically Porous Organic Crystals.....	43
1.4.2	Extrinsically Porous Organic Crystals.....	46
1.4.3	Conclusions and Outlook.....	49
1.5	References.....	50

Chapter Two Synthesis and Characterization of Ferrocene-Based Boroxine Cyclophane

2.1	Introduction.....	62
2.2	Results and Discussion.....	66
2.2.1	Syntheses of Ferrocene-based MOF Precursors.....	66
2.2.2	Synthesis of Triply Ferrocene-bridged Boroxine Cyclophane.....	67
2.2.3	Crystal Structure Analysis of Compound 4	70
2.2.4	Testing of Compound 4 as an Anion Receptor.....	72
2.2.5	Solid-state Cyclic Voltammetry of Compound 4	73
2.3	Conclusions and Outlook.....	75
2.4	Experimental Section.....	76
2.4.1	General Methods.....	76
2.4.2	Syntheses of Compound 1–4	77
2.4.3	¹ H and ¹³ C NMR Spectra of Compound 1–4	81
2.4.4	Fourier-transform Infrared Spectra of Compound 1–4	84
2.4.5	X-ray Crystallographic Analysis of Compound 4	86
2.4.6	Solid-state Cyclic Voltammetry of Compound 4	87
2.5	References.....	88

Chapter Three Syntheses and Properties of Perfluorinated Metal-Organic Frameworks

3.1	Introduction.....	94
3.1.1	Fluorinated Metal-Organic Frameworks.....	94
3.1.2	Copper-catalyzed C–H Bond Functionalization.....	95
3.2	Results and Discussion.....	97
3.2.1	Syntheses and Crystal Structure Analyses of MOFFs.....	97
3.2.2	Thermogravimetric Analyses of MOFFs.....	105
3.2.3	Gas and Vapor Adsorption of MOFFs.....	106
3.2.4	Advancing Contact Angle Measurements of MOFFs.....	109
3.3	Conclusions and Outlook.....	110
3.4	Experimental Section.....	111
3.4.1	General Methods.....	111
3.4.2	Syntheses of MOFFs.....	112
3.4.3	X-ray Crystallographic Analyses of MOFFs.....	115
3.4.4	Fourier-transform Infrared Spectra of MOFFs.....	128
3.4.5	Powder X-ray Diffraction Patterns of MOFFs.....	131
3.4.6	Thermogravimetric Analyses of MOFFs.....	135
3.4.7	Gas and Water Vapor Adsorption Isotherms.....	136
3.4.8	Advancing Contact Angle Measurements.....	139
3.4.9	Supercritical CO ₂ Activation of MOFF-5 and -6.....	140

3.5	References.....	141
-----	-----------------	-----

Chapter Four Synthesis, Characterization, and Applications of a Perfluorinated Noncovalent Organic Framework

4.1	Introduction.....	146
4.2	Results and Discussion.....	149
4.2.1	Synthesis of Compound 1	149
4.2.2	Crystal Structure Analysis of Compound 1	150
4.2.3	Stability of Compound 1	153
4.2.4	Sorption Properties of Compound 1	156
4.3	Conclusions and Outlook.....	160
4.4	Experimental Section.....	161
4.4.1	General Methods.....	161
4.4.2	Synthesis, Sublimation, and Stability Testing of Compound 1	162
4.4.3	¹ H and ¹⁹ F NMR Spectra.....	163
4.4.4	X-ray Crystallographic Analysis of Compound 1	166
4.4.5	Fourier-transform Infrared Spectra.....	169
4.4.6	Differential Scanning Calorimetry Analysis of Compound 1	170
4.4.7	Powder X-ray Diffraction Patterns of Compound 1	170
4.4.8	Gas Sorption Isotherms.....	171
4.4.9	Thermogravimetric Vapor Adsorption.....	172
4.4.10	Advancing Water Contact Angle Measurements.....	177

4.5	References.....	177
-----	-----------------	-----

**Chapter Five Shape-Persistent Dehydrobenzannulene Macrocycles:
Incorporation into Metal-Organic Frameworks and Host-Guest Chemistry with
Fluoroarenes**

5.1	Introduction.....	183
5.2	Results and Discussion.....	186
5.2.1	Syntheses and Crystal Structure Analyses of MCMOFs.....	186
5.2.2	Characterization of MCMOFs.....	191
5.2.3	Host-Guest Chemistry of Macrocycle 2	192
5.3	Conclusions and Outlook.....	195
5.4	Experimental Section.....	197
5.4.1	General Methods.....	197
5.4.2	Syntheses of MCMOFs.....	198
5.4.3	Cocrystallization of Macrocycle 2 and Guest Molecules.....	199
5.4.4	X-ray Crystallographic Analyses.....	200
5.4.5	Fourier-transform Infrared Spectra of MCMOFs.....	216
5.4.6	Powder X-ray Diffraction Patterns of MCMOFs.....	217
5.4.7	Gas Sorption Isotherms.....	218
5.4.8	Supercritical CO ₂ Activation of Zn-MCMOF.....	219
5.5	References.....	220

Chapter Six Procedure for the Production of 3D Models of Crystal Structures

6.1	Introduction.....	224
6.2	Procedure.....	228
6.3	3D Modified Crystal Structures and 3D Printed Models.....	238
6.3.1	Triply Ferrocene-bridged Boroxine Cyclophane.....	238
6.3.2	MOFF-2.....	239
6.3.3	Unit Cell of MOFF-3.....	240
6.3.4	Supercell of MOFF-3.....	241
6.3.5	MOFF-5.....	242
6.3.6	MOFF-6.....	243
6.3.7	nCOF.....	244
6.3.8	$[\pi \cdots \pi]$ Stacking of Macrocycle 1 in Zn-MCMOF.....	245
6.3.9	Zn-MCMOF.....	246
6.3.10	Zr-MCMOF.....	247
6.3.11	1,3,5-Trifluorobenzene@macrocycle 2	248
6.3.12	1,4-Trifluorobenzene@macrocycle 2	249
6.3.13	Unit Cell of $V^{4+}(\text{O})\text{BDC}$	250
6.3.14	Unit Cell of MOF-5.....	251
6.4	Conclusions and Outlook.....	252
6.5	References.....	252

LIST OF FIGURES

Figure 1.1	Coordination of TPE-based ligand to Cd clusters within a MOF immobilizes it, causing fluorescence enhancement.....	13
Figure 1.2	Examples of ligands used by Dincă et al. to construct MOFs with high charge mobilities.....	14
Figure 1.3	Example of an interpenetrated (A, MOF-14) and non-interpenetrated (B, MOF-143) isorecticular MOF $\text{Cu}_3(\text{BTB})_2$	17
Figure 1.4	(A) Chemical structure of the linker used for NU-110 synthesis. (B) Packing of NU-110 in a $2 \times 2 \times 2$ unit cell in X-ray crystal structure looking down <i>a</i> -axis.....	18
Figure 1.5	(A) Schematic representation of the construction of PCN-88 and its 3D framework structure. (B) Simulated locations of CO_2 and N_2 molecules in PCN-88 for CO_2/N_2 (15:85) mixture.....	21
Figure 1.6	Schematic representation of asymmetric alkyl and alkynylzinc additions catalyzed by the MOF-based Ti-BINOLate catalyst within large open channels.....	24
Figure 1.7	The longest ligand ever to be incorporated into a MOF.....	26
Figure 1.8	Schematic representation of COFs based on boroxine (A), boronate ester (B), imine (C), hydrazine (D), and triazine (E)	

	linkages.....	31
Figure 1.9	Some commonly used COF building blocks categorized into different geometries.....	34
Figure 1.10	The syntheses of TpPa-1 and TpPa-2 by the combined reversible and irreversible reaction.....	37
Figure 1.11	Schematic representation of imine-linked COF and its coordination with a Pd ion.....	39
Figure 1.12	(A) Schematic representation of the synthesis of 2D TP-COF. (B) The chemical structure of NiPc-BTDA-COF.....	40
Figure 1.13	(A) Chemical structure of calix[4]arene. (B) Capped-stick representation of its crystal structure viewed along the threefold axis. (C) Space-filling representation of CF ₃ Br@calix[4]arene.....	43
Figure 1.14	Molecular structure, crystal structure of individual molecule, and crystal packing of tetrahedral imine cage.....	45
Figure 1.15	The condensation of triptycene tetraol and triboronic acid forms a cuboctahedral cage. Space-filling and stick representation of molecular packing of the cage.....	46
Figure 1.16	(A) Chemical structure of TPP and its extrinsically porous crystal structure. (B) Chemical structure of 4TMSEBP and its extrinsically porous crystal structure.....	47

Figure 1.17	Molecular structure of organic building block; H-bonding interactions observed in HOF-8; 2D supramolecular layer structure and supramolecular microporous structure of HOF-8.....	48
Figure 1.18	(A) The formation of ribbon-like structures by H-bonding of 4,5-disubstituted benzimidazolones. (C) Crystal structure of porous molecular crystal made from triptycene trisbenzimidazolone.....	48
Figure 2.1	(A) Synthesis and the crystal structure of 1,1'-ferrocenedicarboxylate-zinc cluster. (B) Ring-opening reaction of 1,1'-ferrocene-dimethylsilane with the bridging OH-group between two AlO ₆ octahedra of MIL-53(Al). (C) Incorporation of ferrocene into the channel of MIL-53(Al).....	64
Figure 2.2	Photographs of crystals of compound 4	69
Figure 2.3	Thermogravimetric analysis of compound 4	70
Figure 2.4	Crystal structure of ferrocene–boroxine cyclophane 4	71
Figure 2.5	Asymmetric unit in the crystal structure of 4	72
Figure 2.6	Solid-state cyclic voltammograms of (A) compound 4 and (B) a blank electrode.....	74
Figure 2.7	¹ H NMR spectrum of compound 1	81
Figure 2.8	¹³ C NMR spectrum of compound 1	81
Figure 2.9	¹ H NMR spectrum of compound 2	82

Figure 2.10	^1H NMR spectrum of 1,1'-ferrocenediboronic acid 3	82
Figure 2.11	^{13}C NMR spectrum of 1,1'-ferrocenediboronic acid 3	83
Figure 2.12	^1H NMR spectrum of compound 4	83
Figure 2.13	Fourier-transform infrared spectrum of compound 1	84
Figure 2.14	Fourier-transform infrared spectrum of compound 2	84
Figure 2.15	Fourier-transform infrared spectrum of compound 3	85
Figure 2.16	Fourier-transform infrared spectrum of compound 4	85
Figure 3.1	Examples of fluorinated linkers employed in MOF synthesis.....	95
Figure 3.2	Examples of extensively fluorinated linkers.....	98
Figure 3.3	X-ray crystal structure of MOFF-1	99
Figure 3.4	X-ray crystal structure of MOFF-2	100
Figure 3.5	X-ray crystal structure of MOFF-3	101
Figure 3.6	X-ray crystal structure of MOFF-4	102
Figure 3.7	Synchrotron X-ray crystal structure of MOFF-5	104
Figure 3.8	Synchrotron X-ray crystal structure of MOFF-6	105
Figure 3.9	Comparison of TGA traces of MOFFs 1–6	106
Figure 3.10	Adsorption isotherms for N_2 (77 K), O_2 (77 K), and CO_2 (293 K) sorption within MOFF-3	108

Figure 3.11	Adsorption of H ₂ O vapor in MOFFs 1–3 at 293 K.....	109
Figure 3.12	Fourier-transform infrared spectrum of MOFF-1	128
Figure 3.13	Fourier-transform infrared spectrum of MOFF-2	129
Figure 3.14	Fourier-transform infrared spectrum of MOFF-3	129
Figure 3.15	Fourier-transform infrared spectrum of MOFF-4	130
Figure 3.16	Fourier-transform infrared spectrum of MOFF-5	130
Figure 3.17	Fourier-transform infrared spectrum of MOFF-6	131
Figure 3.18	Powder X-ray diffraction pattern of MOFF-1	132
Figure 3.19	Powder X-ray diffraction pattern of MOFF-2	132
Figure 3.20	Powder X-ray diffraction pattern of MOFF-3	133
Figure 3.21	Powder X-ray diffraction pattern of MOFF-4	133
Figure 3.22	Powder X-ray diffraction pattern of MOFF-5	134
Figure 3.23	Powder X-Ray diffraction pattern of MOFF-6	134
Figure 3.24	TGA traces of (A) MOFF-1 , (B) MOFF-2 , (C) MOFF-3 , (D) MOFF-4 , (E) MOFF-5 , and (F) MOFF-6	135
Figure 3.25	N ₂ (77 K) adsorption isotherms of (A) MOFF-1 , (B) MOFF-2 , (C) MOFF-3 , (D) MOFF-5 , and (E) MOFF-6	137
Figure 3.26	H ₂ O vapor (293 K) adsorption isotherms of MOFFs 1–3	138
Figure 3.27	Pictures of oven-dried MOFFs 1–4 after a drop of water was	

	placed onto the samples.....	140
Figure 4.1	Crystal structure of compound 1	152
Figure 4.2	PXRD patterns of compound 1 after treatment with various solvents and drying.....	153
Figure 4.3	Thermal stability of compound 1 . (A) TGA in nitrogen and air. (B) Variable temperature PXRD.....	155
Figure 4.4	Gas sorption in crystals of compound 1 . (A) Uptake of N ₂ (77 K), O ₂ (77 K) and CO ₂ (195 K). (B) Uptake of H ₂ O vapor (298 K)....	157
Figure 4.5	Sorption of perfluorohexane (C ₆ F ₁₄) in crystals of 1	159
Figure 4.6	Comparison of PXRD patterns of compound 1 from solvothermal synthesis and sublimed sample.....	163
Figure 4.7	¹ H NMR spectrum of compound 6	164
Figure 4.8	¹⁹ F NMR spectrum of compound 6	165
Figure 4.9	¹ H NMR spectrum of compound 1	165
Figure 4.10	¹⁹ F NMR spectrum of compound 1	166
Figure 4.11	Fourier-transform infrared spectrum of compound 6	169
Figure 4.12	Fourier-transform infrared spectrum of compound 1	169
Figure 4.13	Differential scanning calorimetry analysis of compound 1	170
Figure 4.14	A schematic diagram of the apparatus for the thermogravimetric	

	analysis of adsorption.....	172
Figure 4.15	Thermogravimetric analysis of adsorption of perfluorohexane (C ₆ F ₁₄) in 1	173
Figure 4.16	Thermogravimetric analysis of adsorption of CFC-113 (Cl ₂ FC–CClF ₂) in 1	173
Figure 4.17	Thermogravimetric analysis of adsorption of HCFC-225ca (CF ₃ CHF ₂ CHCl ₂) in 1	174
Figure 4.18	Thermogravimetric analysis of adsorption of toluene in 1	174
Figure 4.19	Thermogravimetric analysis of adsorption of <i>n</i> -hexane in 1	175
Figure 4.20	Thermogravimetric analysis of adsorption of cyclohexane in 1	175
Figure 4.21	Thermogravimetric analysis of adsorption of chloroform in 1	176
Figure 4.22	Thermogravimetric analysis of adsorption of dichloromethane in 1	176
Figure 4.23	Picture of compound 1 after a drop of water was placed onto the sample.....	177
Figure 5.1	Shape-persistent macrocyclic ligand 1 used in the syntheses of MCMOFs, and 2 for the studies of host-guest chemistry.....	185
Figure 5.2	Single crystal synchrotron structure of Zn-MCMOF	187
Figure 5.3	Synthesis and single crystal X-ray structure of Zr-MCMOF	190

Figure 5.4	(A) TGA traces of Zn- and Zr-MCMOF . (B) The PXRD patterns of the reversible crystallinity of Zn-MCMOF	192
Figure 5.5	Single crystal X-ray structures of (A) macrocycle 2 ; (B) hexafluorobenzene@ 2 ; (C) 1,2,4,5-tetrafluorobenzene@ 2 ; (D) 1,3,5-trifluorobenzene@ 2 ; (E) 1,4-difluorobenzene@ 2	194
Figure 5.6	Fourier-transform infrared spectrum of Zn-MCMOF	216
Figure 5.7	Fourier-transform infrared spectrum of Zr-MCMOF	216
Figure 5.8	Powder X-ray diffraction pattern of Zn-MCMOF	217
Figure 5.9	Powder X-ray diffraction pattern of Zr-MCMOF	217
Figure 5.10	N ₂ (77 K) adsorption isotherm of Zn-MCMOF	218
Figure 5.11	N ₂ (77 K) adsorption isotherm of Zr-MCMOF	219
Figure 6.1	Picture of commercial molecular model kits.....	225
Figure 6.2	3D printed models of caffeine molecules and DNA.....	226
Figure 6.3	A model of segment of zeolite's infinite network.....	227
Figure 6.4	Exemplary screenshot during the setup steps in Blender.....	229
Figure 6.5	2D representation of the MOFF-3 structure produced directly from its .cif file using <i>Mercury 3.3</i>	230
Figure 6.6	Exemplary screenshot of ePMV interface.....	231
Figure 6.7	Exemplary screenshot during the processing of procedure 10	232

Figure 6.8	Exemplary screenshot during the processing of procedure 11	233
Figure 6.9	The screenshot of <i>Shapeways</i> webpage after the .wrl file of MOFF-3 was uploaded.....	235
Figure 6.10	3D modified crystal structure of triply ferrocene-bridged boroxine cyclophane.....	238
Figure 6.11	3D printed model of triply ferrocene-bridged boroxine cyclophane.....	238
Figure 6.12	3D modified crystal structure of MOFF-2	239
Figure 6.13	3D printed model of MOFF-2	239
Figure 6.14	3D modified crystal structure of the unit cell of MOFF-3	240
Figure 6.15	3D printed model of the unit cell of MOFF-3	240
Figure 6.16	3D modified crystal structure of the supercell of MOFF-3	241
Figure 6.17	3D printed model of the supercell of MOFF-3	241
Figure 6.18	3D modified crystal structure of MOFF-5	242
Figure 6.19	3D printed model of MOFF-5	242
Figure 6.20	3D modified crystal structure of MOFF-6	243
Figure 6.21	3D printed model of MOFF-5	243
Figure 6.22	3D modified crystal structure of nCOF	244
Figure 6.23	3D printed model of nCOF	244

Figure 6.24	3D modified crystal structure of $[\pi\cdots\pi]$ stacking of macrocycle 1 in Zn-MCMOF	245
Figure 6.25	3D printed model of $[\pi\cdots\pi]$ stacking of macrocycle 1 in Zn-MCMOF	245
Figure 6.26	3D modified crystal structure of Zn-MCMOF	246
Figure 6.27	3D printed model of Zn-MCMOF	246
Figure 6.28	3D modified crystal structure of Zr-MCMOF	247
Figure 6.29	3D printed model of Zr-MCMOF	247
Figure 6.30	3D modified crystal structure of 1,3,5-trifluorobenzene @macrocycle 2	248
Figure 6.31	3D printed model of 1,3,5-trifluorobenzene@macrocycle 2	248
Figure 6.32	3D modified crystal structure of 1,4-trifluorobenzene @macrocycle 2	249
Figure 6.33	3D printed model of 1,4-trifluorobenzene@macrocycle 2	249
Figure 6.34	3D modified crystal structure of the unit cell of $V^{4+}(O)BDC$	250
Figure 6.35	3D printed model of the unit cell of $V^{4+}(O)BDC$	250
Figure 6.36	3D modified crystal structure of the unit cell of MOF-5.....	251
Figure 6.37	3D printed model of the unit cell of MOF-5.....	251

LIST OF SCHEMES

Scheme 1.1	Conceptual Approach of MOF Synthesis.....	4
Scheme 1.2	SBU Precursor Approach for MOF Synthesis.....	8
Scheme 1.3	Postsynthetic Thermolysis of a Zn ₄ O-based MOF.....	10
Scheme 1.4	Aromatizing Ring Metathesis of a Tetravinyl Substituted Ligand within a Zn-based MOF.....	11
Scheme 1.5	Schematic Representation of Dynamic Covalent Reactions Used in the Preparation of COFs.....	29
Scheme 1.6	(A) Exchange between Nitroso Compounds and Their Azodioxide Dimers and (B) Polymerization of Tetrahedrally Substituted Organic Linker.....	33
Scheme 1.7	Combinations of Building Blocks with Different Geometries for Synthesizing 2D COFs.....	35
Scheme 1.8	Schematic Representation of the Surface Engineering of Tetragonal NiPc-COF.....	36
Scheme 2.1	Reduced and Oxidized States of Ferrocene.....	62
Scheme 2.2	One of the Electrochemical Recognition Binding Modes of Ferrocene (Fc).....	63

Scheme 2.3	Syntheses of Compounds 1 and 2	67
Scheme 2.4	Syntheses of 1,1'-Ferrocenediboronic Acid 3 and Triply Ferrocene-bridged Boroxine Cyclophane 4	68
Scheme 3.1	Copper-catalyzed Dehydrogenative Cross-coupling Protocols....	96
Scheme 4.1	Synthesis of Compound 1	150

LIST OF TABLES

Table 2.1	Crystallographic Data of Compound 4	86
Table 3.1	Advancing Contact Angle Measurements of MOFFs	110
Table 3.2	Crystallographic Data of MOFF-1	115
Table 3.3	Crystallographic Data of MOFF-2	119
Table 3.4	Crystallographic Data of MOFF-3	121
Table 3.5	Crystallographic Data of MOFF-4	123
Table 3.6	Crystallographic Data of MOFF-5	125
Table 3.7	Crystallographic Data of MOFF-6	127
Table 4.1	Sorption Capacities and Other Characteristics of Guest Adsorbed within the Pores of Compounds 1	160
Table 4.2	Crystallographic Data of Compound 1	167
Table 5.1	Crystallographic Data of Zn-MCMOF	201
Table 5.2	Crystallographic Data of Zr-MCMOF	203
Table 5.3	Crystallographic Data of Macrocycle 2	206
Table 5.4	Crystallographic Data of Hexafluorobenzene@ 2	207
Table 5.5	Crystallographic Data of Tetrafluorobenzene@ 2	210

Table 5.6	Crystallographic Data of 1,3,5-Trifluorobenzene@ 2	212
Table 5.7	Crystallographic Data of 1,4-Difluorobenzene@ 2	214

ABBREVIATIONS AND ACRONYMS

1D	one-dimensional
2D	two-dimensional
3D	three-dimensional
BET	Brunauer-Emmett-Teller
BOC	<i>tert</i> -butyloxycarbonyl
.cif	crystallographic information files
CFC	chlorofluorocarbon
COF	covalent organic framework
COP	covalent organic polyhedron
Cp	η^5 -cyclopentadienyl
CV	cyclic voltammetry
DABCO	1,4-diazabicyclo[2.2.2]octane
DCC	dynamic covalent chemistry
DCM	dichloromethane
DEF	<i>N,N</i> -diethylformamide
DMA	<i>N,N</i> -dimethylacetamide
DMF	<i>N,N</i> -dimethylformamide
DMSO	dimethyl sulfoxide
DNA	deoxyribonucleic acid
DSC	differential scanning calorimetry

ESI	electrospray ionization
ePMV	embedded Python Molecular Viewer
Et	ethyl
Et ₃ N	triethylamine
Et ₂ O	ether
EtOH	ethanol
Fc	ferrocene
FT-IR	Fourier-transform infrared
Hex	<i>n</i> -hexane
HCFC	hydrochlorofluorocarbon
<i>t</i> -heptyl	(triethyl)methyl
HOF	hydrogen-bonded organic framework
HRMS	high resolution mass spectrometry
Me	methyl
MeOH	methanol
MOF	metal-organic framework
MOFF	perfluorinated metal-organic framework
MOP	metal-organic polyhedron
nCOF	noncovalent organic framework
NMR	nuclear magnetic resonance
Ph	phenyl
(<i>i</i> -Pr) ₂ NH	diisopropylamine
<i>t</i> Bu	<i>tert</i> -butyl

SCD	supercritical carbon dioxide
SBU	secondary building unit
TGA	thermogravimetric analysis
THF	tetrahydrofuran
TMS	trimethylsilyl
UV	ultraviolet
VRML (.wrl)	Virtual Reality Modelling Language
X3D (.x3d)	Extensible 3D

Chapter One

Crystalline Porous Materials Based on Organic Molecules

1.1 Introduction

A solid material can be considered porous when the voids of its structure are large enough to accommodate guest molecules.¹ Crystalline porous materials with porosities in the microporous (< 2 nm), mesoporous (2–50 nm), and macroporous (> 50 nm) ranges are extensively used in industrial applications, in the areas of catalysis, separation, and filtration.² Their appeal in these applications comes from their uniform porosities, high surface areas, high adsorption capacities, catalytic activities, ion-exchange abilities, and size/shape selectivities. Research on crystalline porous materials has been focused on inorganic compounds for a long time. Among them, zeolites (microporous aluminosilicate minerals) are of vital importance to the chemical and petrochemical industries.³ Since the term "zeolite" first shown in the scientific literature in 1756,⁴ the adsorption and ion-exchange properties of natural zeolites were exhaustively studied. Starting in the late 1930s,³ various syntheses and structural characterization studies of artificial zeolites were carried out as well. Worldwide consumption of zeolites (natural and synthetic) is estimated at five million metric tons per year.³ In addition to inorganic components, incorporation of organic molecules into porous materials could allow tuning of solution processibility, hydrophilicity/phobicity, and could allow introduction of specific

catalytic groups.⁵ Therefore, work on new porous materials that include both inorganic and organic elements is one of the most active areas of research in materials chemistry.

In the past two decades, organic functional elements have been playing increasingly prominent roles in the field of porous materials. There are three emerging classes of crystalline porous materials based on organic molecules: metal-organic frameworks (MOFs) as inorganic-organic hybrid materials, covalent organic frameworks (COFs) built using reversible covalent bond formation, and crystalline noncovalent porous organic materials held together by weak interactions between individual molecules; the latter two classes are based entirely on organic building blocks. These porous materials feature high surface areas, low densities, high flexibilities, and highly modular syntheses. Typically, inorganic porous materials possess stronger and more rigid frameworks, with higher thermal (up to 1000 °C) and chemical stability, whereas porous materials based on organic molecules provide richer varieties of topologies, functionalities, and functional groups. A very high degree of predictability of the final structure can be achieved in the synthesis of MOFs and COFs. The modular synthesis of these three materials allows the creation of crystalline functional porous materials with novel architectures geared toward diverse applications, especially in gas storage, catalysis, molecular separation, sensing, semiconductor, and drug delivery. We anticipate that rational design of organic-based porous materials will have new technological applications. This chapter will briefly introduce the three kinds of porous materials mentioned above, setting the ground for subsequent chapters which explore these materials in some of the main research avenues pursued in this dissertation.

1.2 Metal-Organic Frameworks

1.2.1 Modular Synthesis of MOFs

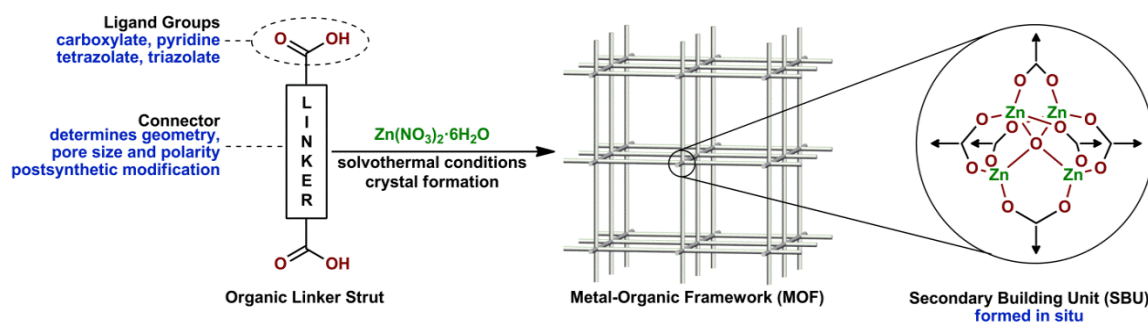
MOFs are crystallographically ordered hybrid materials constructed from inorganic metal cluster nodes and organic linkers that connect those nodes into infinite one-, two-, or three-dimensional frameworks.⁶ Because of their high and permanent porosities, easily modified surface characteristics, and thermal stability, MOFs are promising materials for uses in gas storage and separation, fuel reprocessing, environmental remediation, sensing, and catalysis.⁶ Perhaps the most appealing feature of MOFs is their modular structure which can be altered by changing metal sources, organic linkers, and conditions to produce topologies with desired porosities, chemical and thermal stabilities, and functional groups.

1.2.1.1 Conventional Synthesis

The conventional synthesis of MOFs is relatively straightforward (Scheme 1.1): a solution of an organic linker and a metal salt is heated without stirring in a high-boiling solvent, and the produced precipitates are often of sufficiently high crystallinity to permit direct analysis by X-ray crystallography. The phase uniformity of bulk materials can be investigated by powder X-ray diffraction (PXRD) analysis. Both compositional (molar ratio of starting materials, choice of solvents, pH of solution, etc.) and process parameters (reaction temperature, pressure, reaction time, cooling rate, etc.), determine the phase formation of MOFs and the crystal morphology. However, the conventional synthetic

investigations are time- and material-consuming. High-throughput methods for solvothermal syntheses have been a powerful tool to accelerate the discovery of new materials and to optimize reaction procedures.⁷ One of the most challenging tasks for using MOFs in industrial applications is keeping their superior properties (high porosity, thermal and chemical stability, phase uniformity, crystallinity, etc.) while scaling up the reactions.⁸ Laboratory synthetic methods must be adapted and several issues should be solved: cost of starting materials and solvents, environmental friendly reagents, mild reaction conditions, purification and activation process, and high yields. Thus, alternative synthetic routes are being explored.

Scheme 1.1 Conceptual Approach of MOF Synthesis



1.2.1.2 Alternative Synthetic Methods

The energy needed to carry out a chemical reaction that forms a MOF can be introduced into the solution through other means, e.g., electrical potential, electromagnetic radiation, or mechanic process.⁸ Each method could be used to generate new materials that cannot be obtained otherwise. Microwave reactions have been used in

organic synthetic chemistry for a long time.⁹ By applying the appropriate frequency, collision takes place between the polar molecules in an electromagnetic field. The increase in kinetic energy leads to a very energy-efficient method of heating. The reactions can often be carried out at a temperature 100 °C above the boiling point of the solvent, with reaction times less than one hour. Microwave-assisted MOF synthesis provides the acceleration of crystallization and higher purity of products. For instance, Cohen and co-workers performed the cyanation of the UiO-66-Br (composed of Zr⁴⁺ and Br-BDC) achieved with CuCN and microwave irradiation to produce UiO-66-CN.¹⁰

Mueller and co-workers at BASF performed the first electrochemical synthesis of MOFs in 2005.¹¹ The main advantage of this process was its exclusion of anions like nitrate, perchlorate, acetate, or chloride during the large-scale production process. Without metal salts, continuously introducing metal ions into the reaction solution via anodic dissolution can lead to continuous industrial process with higher solids content compared to conventional synthetic methods.¹²

Mechanochemical reactions carried out by milling or grinding are attractive means to systematically explore various modes of molecular self-assembly.¹³ The milling mechanochemistry is able to avoid bulk solvent that is the greatest contributor to environmental impact of the synthesis. Simultaneously, the limitations of solution-based chemistry, such as solubility, solvent complexation, or solvolysis can be avoided. It has also been demonstrated that the well-established molecular self-assembly phenomena in solution chemistry, such as reversible covalent or noncovalent bonds formation, thermodynamic equilibration, and structure templating, are also accessible in milling

mechanochemistry via recently developed highly efficient methodologies, e.g. ion- or liquid-assisted grinding. Moreover, in some cases metal salts can be replaced by metal oxides as a starting material, which results in the formation of water as the only side product.⁸

Sonochemistry is widely used in the synthesis of nanomaterials by applying high-intensity ultrasound to a reaction mixture.¹⁴ This method will be beneficial for future applications, since its fast synthesis process could allow the scaleup of MOFs. Moreover, nanocrystalline particles, which are often obtained by sonochemical syntheses, are also anticipated to have diverse applications compared to large size materials. However, this method of MOF synthesis is still largely unexplored.¹⁵

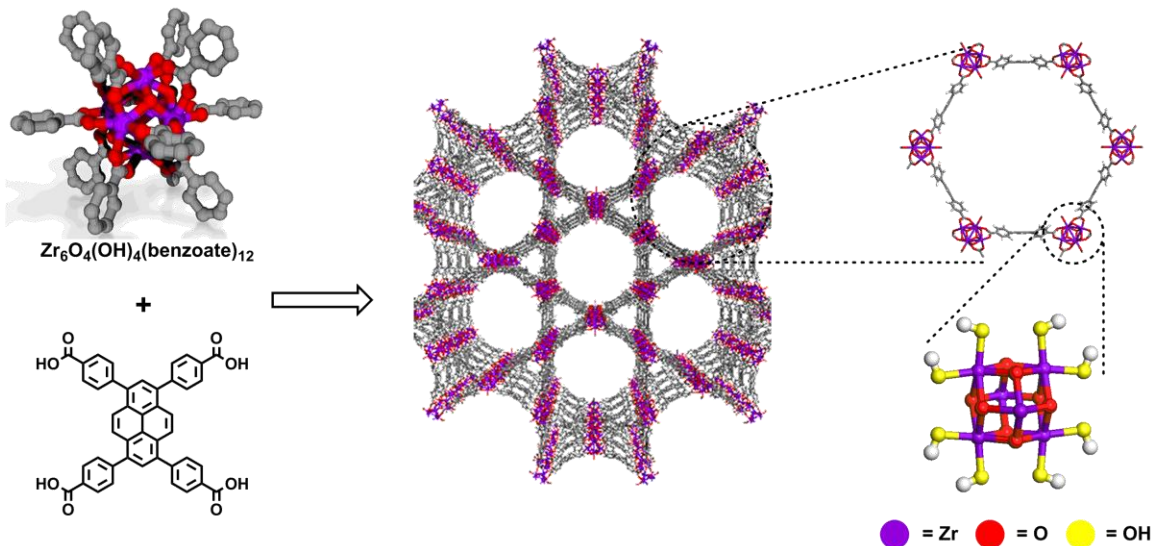
1.2.1.3 Structure-directing Approaches

Since the chemistry of MOFs originated within solid-state inorganic chemistry, many concepts from zeolite chemistry were quickly extended to MOF synthesis. With the same organic linker, the choice of metal source would determine the coordination geometry and the resulting topology and—to a certain extent—physical properties of the framework. In addition, the solvents used in the synthesis of MOFs play a significant role in the deprotonation of ligands, filling the space between ligand molecules, as a terminal group in SBUs, or as a template for structure formation.⁸ Space filling by different guest molecules and the removal of them could largely influence the structure of MOF and has been extensively studied.¹⁶ An ionic liquid can act both as a solvent and a structure-directing agent, which is called ionothermal synthesis.¹⁷ In zeolite chemistry,

mineralizers such as fluorides, which can help in solubilizing the starting materials during the reaction, can be added into the reaction mixture for modifying the crystallization process. This method has been applied in MOF synthesis as well.¹⁸

Typically, the self-assembling process of MOF formation starts from isolated metal ions and organic polydentate ligands. Metal ions with high oxidation state (e.g., V^{4+} , Zr^{4+} , Fe^{3+} , and La^{3+}) can adopt multiple coordination geometries and form complicated SBUs, which hamper the self-assembly and self-correction of frameworks during the crystallization and often lead to formation of polycrystalline or amorphous products. An alternative route is to first prepare inorganic SBU precursors by reacting metal ions with monotopic ligands. Then these intermediates can be subjected to polytopic ligands that can replace the monotopic ones, bridging the SBUs.¹⁹ Recently, this approach was successfully applied to the synthesis of a MOF from Zr^{4+} and tetraacid ligand (Scheme 1.2).²⁰ This combination of SBU and polydentate ligand was initially assumed too complicated to allow the formation of a crystalline product. However, the monotopic benzoate ligands on the $[Zr_6O_4(OH)_4(benzoate)_{12}]$ SBU cluster could be partially replaced by the tetraacid ligands. The robust topology of the material and the available coordination sites for ligand exchange or incorporation provide a broader way to MOF applications.²¹

Scheme 1.2 SBU Precursor Approach for MOF Synthesis²⁰



1.2.2 Rise of the Ligands: Applications of Sophisticated Organic Linkers in MOF Chemistry²²

Recent years have brought out a mini-revolution in the MOF area, with the realization that organic ligands need not be only inert structural elements, but could yield tremendous benefits if their functional and reactive nature were to be exploited. This represented quite a significant cultural departure: MOFs were traditionally developed within the domain of solid state inorganic chemistry, meaning that little initial attention was devoted to the ligands, the “O” of the MOFs. The past decade has witnessed the synthesis of more and more MOFs with elaborately functionalized organic ligand groups.²³

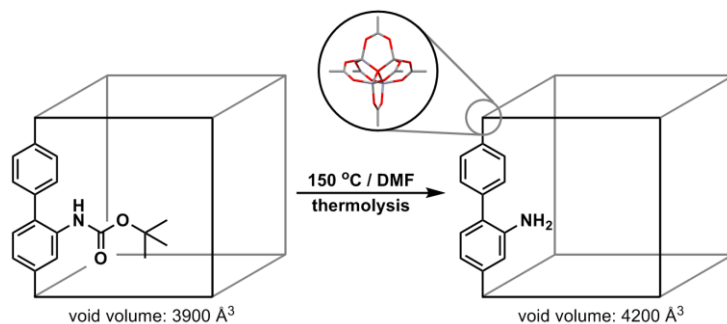
Properties of small functional molecules are easy to study in solution, but organic chemists typically struggle to translate these characteristics onto the more practically relevant solid-state devices. Solid state brings with it the challenges of unpredictable structures of molecular crystals, aggregation, and self-quenching in the case of optically active materials. MOFs offer distinct advantages in that respect. First, as they are covalently connected structures, positions of individual ligands within the extended structures are predictable to a very high degree. Second, MOFs are not close-packed structures: thus, small molecules can be site-isolated, increasing the probability that they will behave as designed in solution—with the relatively manageable caveat that appropriate ligating groups have to be appended onto the functional organic molecule. In fact, this site isolation can contribute to single molecule reactivity (analogous to that observed using matrix isolation methodology), which can occasionally be difficult to observe even in dilute solution because of interference of solvents or other species. This was illustrated in Long's study of Cr-coordinated benzenes in a MOF-5 derivative, wherein the complexes of Cr with H₂ and N₂ were greatly stabilized relative to solution conditions.²⁴

Contributions of organic ligands to the functionality of a MOF can come from their chemical reactivity, their capability to engage in specific (or nonspecific) noncovalent interactions, or simply from their physical properties.

1.2.2.1 Postsynthetic Modification

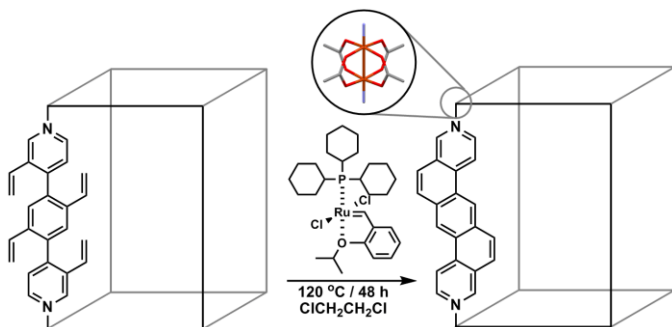
Chemical reactivity of organic ligands within MOFs has been extensively explored under the heading of postsynthetic modification (PSM).²⁵ In this class of protocols, a MOF ligand bears two sets of functional groups: one whose purpose is to bind to a metal and create a MOF, and another which will engage in secondary reactivity once the MOF is already formed. For example, Cohen et al. used the exposed amino groups of a carboxylate-based MOF to create highly hydrophobic MOFs through acylation with long-chain acyl chlorides.²⁶ In a formal reverse of this reaction, Telfer used thermolysis of -NHBoc (Boc = *tert*-butoxycarbonyl) groups within a low-porosity MOF (Scheme 1.3) to remove the Boc functionality, thus liberating empty space within the framework.²⁷ This "spatial protecting group" approach can in principle be used to synthesize non-interpenetrated versions of frameworks for which the direct synthesis yields only interpenetrated nets. In both strategies, digestion of the synthesized MOF allowed nuclear magnetic resonance (NMR) spectroscopic analysis of the created material that in turn confirmed the chemical change that occurred on the ligand.

Scheme 1.3 Postsynthetic Thermolysis of a Zn_4O -based MOF



Postsynthetic modification allows the introduction of new function onto ligands, as well as liberation of strongly ligating groups (such as catechols) which would have interfered with MOF synthesis.²⁸ MOF environment also opens new avenues of reactivity for the ligand itself. For example, subjecting the bipyridine ligand found within MOF (Scheme 1.4) to alkene metathesis catalysts in solution resulted in a sluggish and incomplete ring-closing reaction; once this ligand was immobilized and site-isolated within Zn-based MOF, the same transformation proceeded in high yield, giving framework containing a polycyclic aromatic hydrocarbon (PAH) moiety.²⁹

Scheme 1.4 Aromatizing Ring Metathesis of a Tetravinyl Substituted Ligand within a Zn-based MOF



Covalent reactions are not the only class of postsynthetic modification available to MOFs. Stoddart and Zaworotko created MOFs containing crown ether³⁰ and calixarene³¹ moieties, which can bind electron-poor aromatics and potassium ions, respectively. Using noncovalent recognition, both Stoddart³² and Loeb³³ incorporated mechanically interlocked molecules (catenanes and rotaxanes) within MOFs. Tailored noncovalent interactions can also contribute to the enhancement of selectivity in gas

sorption—which remains among the most actively pursued applications of MOFs. For example, using electrochemically active tetracyanoquinodimethane (TCNQ) ligand as a linker in a Zn-based MOF, Kitagawa et al. have shown enhanced adsorption of O₂ and NO relative to other small gas molecules (e.g., C₂H₂, Ar, CO₂, N₂, and CO).³⁴ This rare selectivity was a combined consequence of charge-transfer interactions between TCNQ and these two gaseous guests, and the gated opening and closing of the pores of the framework. Zhou and co-workers used precisely designed organic ligands to achieve an optimal steric match between the size of pores and the size of a CO₂ molecule, producing a material with high selectivity for this guest.³⁵

1.2.2.2 Application-based Linkers

One of the major impetuses for the development of organic and organometallic chemistry in MOFs is the potential use of these materials as catalysts. The benefits of MOFs as catalysts are obvious: as insoluble crystalline materials, they are similar to heterogeneous catalysts in their easy recovery and high potential throughput. At the same time, their atomically defined structures and isolation of catalytic sites are clearly reminiscent of homogeneous catalysts, which have been the subject of an immense and sustained research effort in the chemistry community.³⁶

Physical properties of ligands can also play a critical role in the applications of MOFs. For example, highly hydrophobic ligands can be used to repel water, while simultaneously maintaining the ability to bind nonpolar guests. This feature was explored by Cohen in MOFs substituted with hydrophobic groups,³⁴ as well as Omary's³⁷ group in

the synthesis and applications of extensively fluorinated MOFs in the binding of hydrocarbons. Other hydrophobic MOFs based on metal pyrazolates were shown to capture volatile organic compounds.³⁸

It is well-known that optical properties of organic molecules change as one moves from dilute solution to the solid state. Typical result of such aggregation is fluorescence quenching, but aggregation-induced emission (AIE) has been recently gaining attention.³⁹ MOFs can also serve as platforms for coordinative immobilization of ligand, changing its emission properties. Dincă's group has recently demonstrated that tetraphenylethylene (TPE) core—which is non-fluorescent in solution—turns its emission ON once incorporated into Zn- and Cd-based MOFs.⁴⁰ This effect was observed despite the fact that rotation of the ligands was not completely suppressed (Figure 1.1).

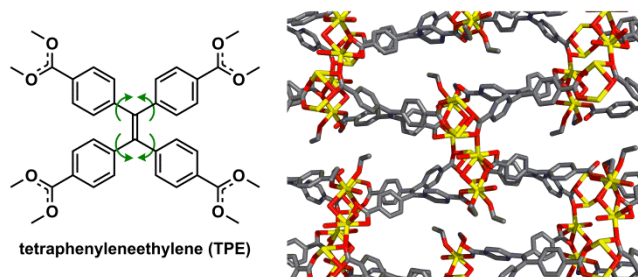


Figure 1.1 Coordination of TPE-based ligand shown on the left to Cd clusters within a MOF (right) immobilizes it, causing fluorescence enhancement.

An exciting and still quite underexplored area of development is the creation of semiconductive and conductive MOFs. As high surface area materials, conductive MOFs could advance the fields of fuel cells, supercapacitor, and battery research, electrochemical sensing, and electrocatalysis.⁴¹ Dincă and co-workers have recently

introduced two classes of MOFs with intriguing conductivity profiles. The first one⁴² was inspired by high conductivity of tetrathiafulvalene (TTF)/TCNQ complex; this Zn-based MOF utilizes tetrathiafulvalene-tetrabenzoic acid (H_4 TTFTB, shown in Figure 1.2, left) as the ligand. In this framework, benzoate groups coordinate to Zn, constructing a helical array of $[\pi \cdots \pi]$ stacked tetrathiafulvalene (TTF) units. Even without any particular treatment, some of the TTF units are partially oxidized, and this doping contributes to high charge mobility of $0.2 \text{ cm}^2 \text{ V}^{-1} \text{ s}^{-1}$ —higher than that of many polythiophene polymers. Very recently, the same group disclosed a Ni-MOF based on 2,3,6,7,10,11-hexaaminotriphenylene (HATP, shown in Figure 1.2, right) as the ligand.⁴³ This crystalline material is composed of infinite 2D hexagonal sheets that form the 3D network through a slipped parallel arrangement of the planes. This material was characterized by remarkably high conductivity for MOFs: 2 S m^{-1} when measured in pellet form, and 40 S m^{-1} in the thin film.

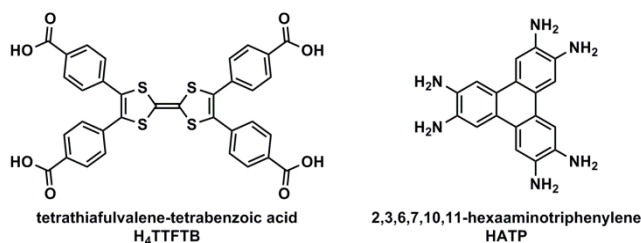


Figure 1.2 Examples of ligands used by Dincă et al. to construct MOFs with high charge mobilities.

In a very recent study,⁴⁴ Allendorf's group has shown that the infusion of electrochemically active TCNQ molecules into the well-known (but non-conductive) HKUST-1⁴⁵ framework led to $\sim 10^6$ -fold increase in conductivity, to approx. 7 S m^{-1} . The

conductivity of TCNQ-infiltrated frameworks could be tuned by varying the TCNQ loading. On a molecular level, TCNQ guests replaced the weakly coordinated solvent molecules found in the axial positions of the Cu(II)-paddlewheel clusters of which HKUST-1 is composed, establishing a charge conjugation pathway.

1.2.3 Applications of MOFs Based on High Porosity, Structures, and Functional Components

The chemical and thermal stability of MOFs is generally lower than that of zeolites and other inorganic porous materials due to the relatively weak metal-ligand bonds. Many are air- or moisture-sensitive so their handling need to be performed under an inert atmosphere. However, the remarkably high surface area, tunable functionality, and modular synthesis of MOFs enable more diverse potential applications than in the case of conventional inorganic porous materials. Numerous applications of MOFs have been comprehensively reviewed.⁶ In the current stage of MOF research, studying and understanding the pros and cons of explored applications is necessary for designing a new MOF with promising properties. In this section, we summarize the applications of MOFs from three vantage points: porosity, structure, and components of MOFs. Various combinations of these three characteristics will determine the potential applications of the MOFs.

1.2.3.1 Applications Based on High Porosity of MOFs

One of the most unique properties of MOFs compared to fully inorganic porous materials is their ultrahigh porosity. The highly porous MOFs are promising candidates for high pressure storage of gases such as hydrogen,⁴⁶ methane,⁴⁷ and carbon dioxide.⁴⁸ The most common strategy to expand the micropores in MOFs to mesopores is to systematically enlarge the linker in the chosen topology. However, interpenetration (also called catenation) often results due to the larger volume of space afforded by the increased linker length, which reduces the porosity and surface area of the resulting MOF.⁴⁹ By controlling the reaction conditions (e.g., temperature, concentration, solvent system, and metal-ligand ratio), it is possible to obtain non-interpenetrated structures (Figure 1.3).⁵⁰ For such structures, the large cavities are filled with disordered solvent molecules that make obtaining strongly diffracting single crystals difficult. The poor data quality makes the determination of the single crystal structure of mesoporous MOFs extremely difficult with the use of conventional X-ray diffractometers. Therefore, for highly porous MOFs, synchrotron radiation is commonly used for the collection of high quality data needed for rigorous structure refinement. Sometimes, an approach combining X-ray crystallography and structural modeling is utilized to construct the structure of highly porous MOF, or to help locate the linker substituents.

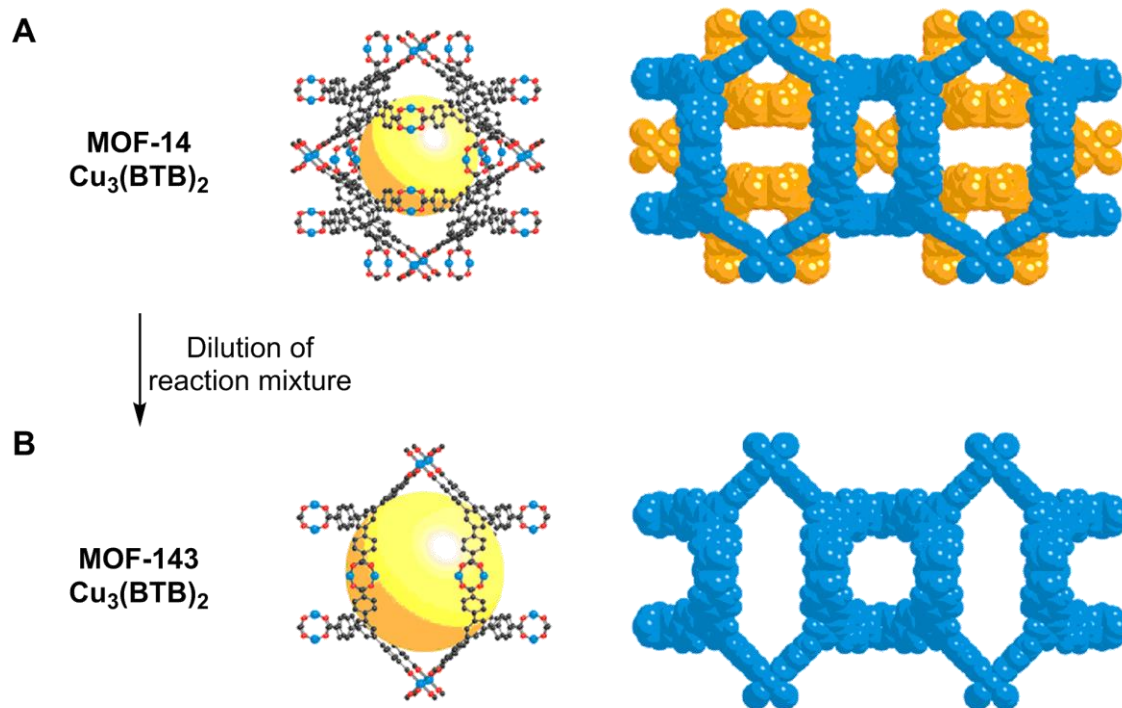


Figure 1.3 Example of an interpenetrated (A, MOF-14)⁵¹ and non-interpenetrated (B, MOF-143)⁵⁰ isorecticular MOF $\text{Cu}_3(\text{BTB})_2$; BTB = 4,4',4''-benzene-1,3,5-triyl-tribenzoate. Left: single crystal structures of $\text{Cu}_3(\text{BTB})_2$ are composed of Cu_2 paddlewheels and triangular organic linkers. The yellow ball is placed in the structure for clarity and to indicate space in the cage. Colors: Cu, blue; C, black; O, red. Hydrogen atoms are omitted for clarity. Right: Space-filling illustration of corresponding MOFs.

However, the synthesis of large pore MOFs is often restricted by the solubility and preparation of the corresponding organic linkers. So far, only certain geometries of organic linkers (e.g. triangular hexacarboxylic acid linker, Figure 1.4A) are suitable for the purpose of high porosity but the synthesis is complex (elaborate organic synthesis is

needed), time consuming (multi-step synthesis necessitates several deprotection, separation, and purification steps), expensive (catalysts with noble metals like palladium are often used), and with low overall reaction yields. Therefore, it is very challenging to scale up these highly porous MOFs. The mesoporous MOF NU-110 is currently record holder in terms of the Brunauer-Emmett-Teller (BET) surface area with values exceeding $7,000 \text{ m}^2 \text{ g}^{-1}$ (Figure 1.4B).⁵²

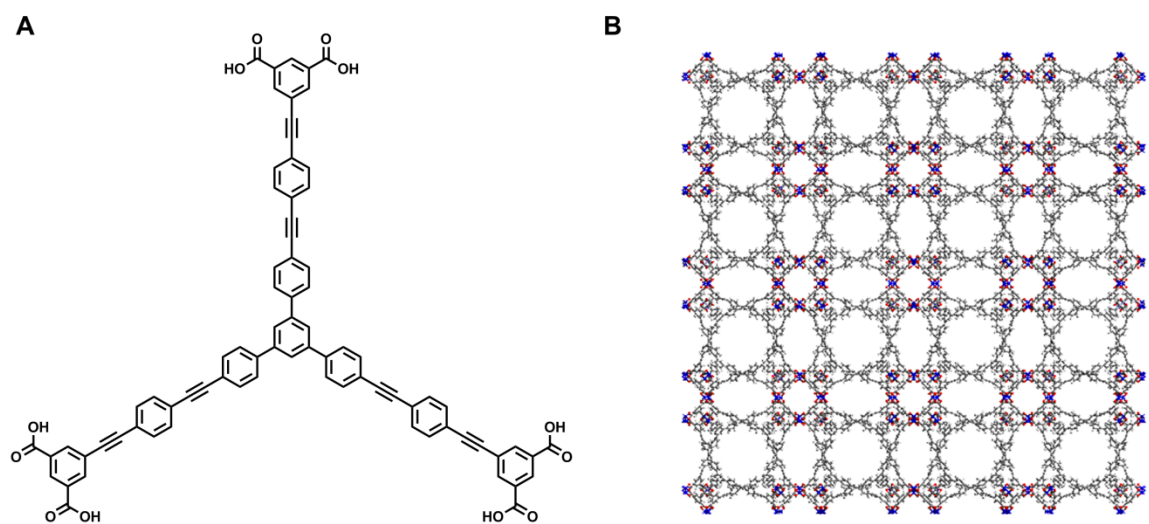


Figure 1.4 (A) Chemical structure of the linker used for NU-110 synthesis. (B) Packing of NU-110 in a $2 \times 2 \times 2$ unit cell in X-ray crystal structure looking down a -axis. Colors: Cu, blue; C, gray; O, red.

One of the most common problems in characterizing mesoporous MOFs is the determination of BET surface areas. Mostly the deviation comes from the different ways in which material is handled and activated. Having consistent and standardized determine method to apparent BET surface areas is important for the comparison of mesoporous

MOFs. A possible problem of mesoporous frameworks is that their labile structure can easily cause distortions in the linker especially when evacuating the solvents from the pores. As a result, the structures collapse and the materials lose their crystallinity and porosity.⁵³ Supercritical carbon dioxide (SCD) drying is the most commonly used method for the activation of mesoporous MOFs but is still costly and time-consuming.⁵⁴

Since the mesoporous MOFs appear to have many problems during the desolvation, using such MOFs as adsorbents in the liquid phase is a very promising direction, since here desolvation is not needed. Mesoporous MOFs provide adequate pore and aperture size for adsorption of large organic molecules. These features make them very promising candidates for separation applications in the liquid phase. Yang et al. have used MIL-101(Cr) as an HPLC stationary phase for separation of C₆₀ and C₇₀.⁵⁵ Xu et al. applied Zn₄O(L)_{1.5} (L = 6,6'-(2,2-bis((6-carboxynaphthalen-2-yl)oxy)methyl)propane-1,3-diyl)bis(oxy)di-2-naphthalenecarboxylate) with hierarchical pore sizes (16.1, 18.6, and 38.3 Å) as a column-chromatographic filler for the separation of large dye molecules. Two dyes—Basic Red 1 and Food Green 3—were successfully separated via size exclusion mechanisms. However, compared to microporous MOFs, investigations performed on separation using mesoporous MOFs are relatively rare. Thus, more studies are needed on adsorption/separation in the liquid phase.

1.2.3.2 Applications Based on the Structures of MOFs

Porous solids are widely used as adsorbents or membrane fillers for separations and purifications of various chemicals. The use of zeolites in many industrial processes has strongly influenced the global economy. The modularity of MOFs provides an ideal platform for designing the structure for desired molecular separation. Crystalline nature of MOFs allows their structures to be easily characterized by single-crystal X-ray diffraction. The corresponding structural study also allows the exploration of the relationship between structure and various interactions, which can guide the design and synthesis of novel, improved MOFs. In fact, a number of adsorption phenomena are directly determined by the regular pore size distribution, flexibility of structures, and functionality in a MOF.⁵⁶

Efficient separations of light gases (H_2 , N_2 , O_2 , CO_2 , and CH_4) have been important issues in industrial, energetic, environmental, and economic fields. One of the most appealing applications of MOFs is selective adsorption and separation of light gases.⁵⁷ Many selective adsorption properties can be modified by tuning the surface functionality, the size of cavity, and polarity of the structure. For CO_2 (kinetic diameter 3.3 Å) capture, Zhou and co-workers synthesized a MOF PCN-88 with a precisely designed cavity, termed a ‘single-molecule trap’, with the desired size and properties suitable for trapping target CO_2 molecules (Figure 1.5).³⁵ In fact, many MOFs have displayed selective adsorption behavior for small gas molecules.⁵⁷ Moreover, separation of mixed gases performed by breakthrough experiments or gas chromatography has been

studied, e.g. CH_4/CO_2 ,⁵⁸ $\text{C}_2\text{H}_2/\text{CO}_2$,⁵⁹ and Xe/Kr .⁶⁰ Nevertheless, it is still a long way to go to make these adsorptive applications practical and cost effective.

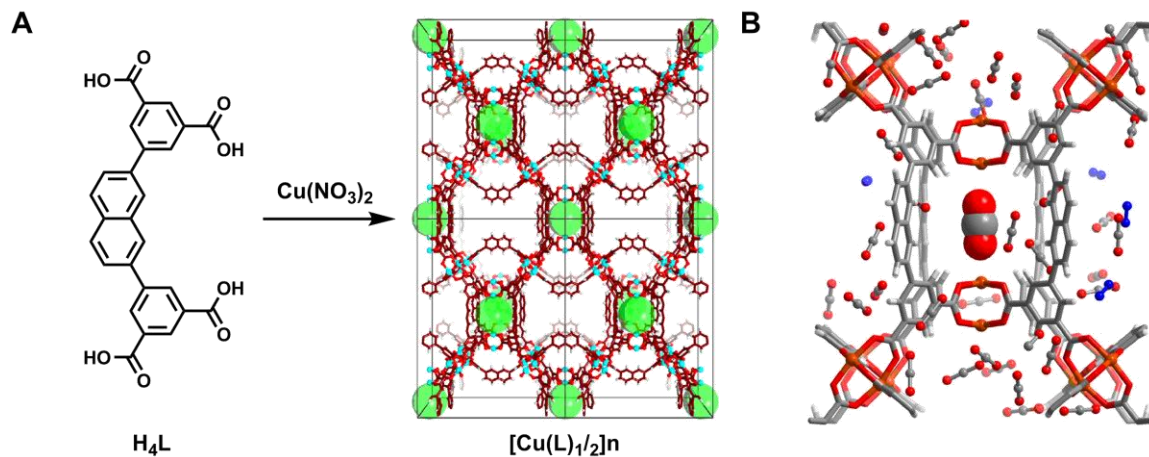


Figure 1.5 (A) Schematic representation of the construction of PCN-88 and its 3D framework structure. Colors: Cu, cyan; O, red; C, brown; and H, light grey. The green sphere represents the free space inside the built-in caves. (B) Simulated locations of CO_2 and N_2 molecules in PCN-88 for CO_2/N_2 (15:85) mixture. Viewed along the crystallographic c direction.

Molecules trapped in a uniform restricted space also afford unique properties that are difficult to investigate in the bulk state. Thus, the uniform space can be utilized as a molecular reactor to conduct reactions or stabilize reaction intermediates.⁶¹ Recently, Fujita and co-workers confined target molecules in a MOF and performed single crystal X-ray analyses that did not require the crystallization of the molecules.⁶² Tiny crystals of MOF $\{[(\text{Co}(\text{NCS})_2)_3(\text{L})_4] \cdot x(\text{solvent})\}_n$ and $\{[(\text{ZnI}_2)_3(\text{L})_2] \cdot x(\text{solvent})\}_n$ (L = tris(4-pyridyl)-1,3,5-triazine) were soaked in a solution of the target, such that the porous structure trapped the target molecules. Crystallographic analysis determined the absorbed

guest structures—which by themselves were difficult to crystallize—along with the host framework. Most importantly, the analysis only required microgram amounts of the sample.

Flexibility or dynamic character in a MOF is very unique structural property compared to zeolites. The structural changes often directly influence the adsorption behavior.¹⁶ The structural flexibility of some MOFs can be exploited to perform highly selective adsorption of structural isomers, which may be a goal difficult to attain with a rigid porous material. Adsorptive separations refer to the process by which a mixture is separated based on differences in adsorption/desorption behavior of distinct components in the mixture. Meanwhile, different diffusion rates in the pores or channels caused by the steric effect or interactions between molecules and framework could induce an efficient separation. A number of gas and liquid phase separations have been conducted by flexible MOFs. The most promising one is the separation of structural isomers of hydrocarbons or aromatics that is still a big issue in petrochemical industry. For instance, a mixture of ethylbenzene, *m*-xylene, and *p*-xylene can be chromatographically separated on a column packed with MIL-47, $[V^{4+}(O)(BDC)]$, in the liquid phase, with hexane as the eluent at 298 K.⁶³

1.2.3.3 Applications Based on Functional Components of MOFs

The variety of metal ions, organic linkers, and structural motifs affords an essentially infinite number of possible combinations. These combinations determine the topology and physical properties of the framework. Each component (organic or

inorganic) of MOFs could have its own application. Furthermore, postsynthetic modification increases the range of the synthetic variability. Although mostly the molecular adsorption and separation of MOFs rely on the porosity and structure as mentioned in the last two sections, both inorganic and organic components of MOFs could have additional influences. For example, metal clusters with open coordination sites can provide a basis for stronger chemisorptive interaction between metals and guests molecules, and thus enhance the affinity of the material toward the guest molecules.⁴⁸ In addition, increasing the polarity of a structure by introducing partially or extensively fluorinated linkers was studied in order to modify the selective adsorption of gas molecules.⁶⁴ Owing to the overwhelming growth in the area of MOF research, I will only briefly introduce some particular applications based on the rational design of components, e.g. asymmetric catalysis, chemical sensing, and electro/photoconduction.

The ability to assemble well-defined organic building blocks into a solid framework with crystallographic order makes MOFs particularly suitable for generating single-site solid catalysts with unprecedented uniformly distributed catalytic sites and open channels for shape-, size-, chemo-, and stereoselective reactions. A series of mesoporous chiral MOFs with the framework formula [(BINOL-TC)-Cu₂(solvent)₂] (where BINOL-TCs were BINOL-based tetracarboxylates coordinated with Ti(O^{*i*}Pr)₄ via postsynthetic modification) were highly active asymmetric catalysts for diethylzinc and alkynylzinc additions, which converted aromatic aldehydes into chiral secondary alcohols (Figure 1.9).⁶⁵

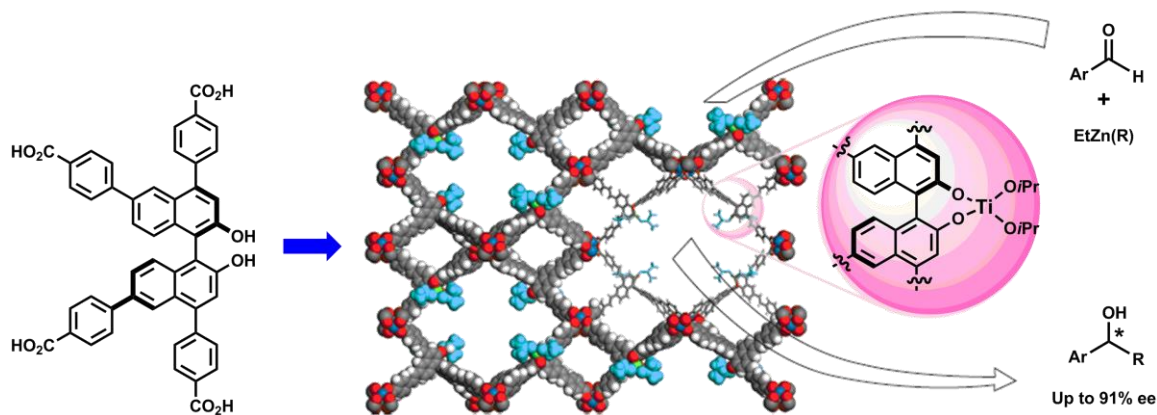


Figure 1.6 Schematic representation of asymmetric alkyl and alkynylzinc additions catalyzed by the MOF-based Ti-BINOLate catalyst within large open channels.

Lin and co-workers performed oxygen sensing with MOFs built from phosphorescent cyclometalated iridium tris(2-phenylpyridine) complexes.⁶⁶ The metal-ligand charge transfer emission of the MOF can be reversibly quenched by oxygen. Moreover, the permanent porosity of MOF allowed for rapid diffusion of oxygen through the open channels, leading to efficient and reversible quenching. The functionalization of the framework via orthogonal incorporation of different sensing motifs can enhance the selectivity of MOF sensors.

Porous and conductive materials are under exploration for energy conversion and storage applications such as electrodes, batteries, capacitors, and fuel cell membranes.⁶⁷ Again, the modularity of MOFs provides a route to porous and conductive materials. For instance, sulfur-based bridging linkers have been widely used in conductive polymers, and have crossed over to MOF area recently (Figure 1.1).⁴² Stacking of redox-active molecules such as TTF-TCNQ (TTF = tetrathiafulvalene, TCNQ = tetracyanoquinodimethane) was exploited to construct porous conductive MOFs. Porous

conductive MOFs with their tunable functionality create promising platforms for applications in energy conversion and storage. However, this field of MOF research is still in its infancy, and more research is needed.

1.2.4 Conclusions and Outlook

In summary, the field of MOF synthesis is blossoming and broadening its scope. While conventional syntheses methods have been widely used, the fields of mechano-, sono-, and electrochemical synthesis as well as microwave-assisted syntheses are emerging. These could be of interest for scale-up of syntheses and the application of MOFs. MOFs offer an even larger platform of structural varieties compared to zeolites. Some other preparative approaches such as the use of structure-directing agents, ionic liquids, and SBUs precursors, have been studied as well.

What outstanding challenges are still left for these ligand-focused MOFs? It would be intriguing to see an organic reaction be involved in the synthesis of MOFs. At present, all MOFs are prepared by controlled coordination of the prepared ligand to the metal; in principle, it should be possible to polymerize a pre-formed metal-cluster through a purely organic reaction (e.g., dimerization of terminal alkynes or thiols), offering a complementary synthetic method. On the other hand, having fragile organic ligands that can collapse upon mild chemical stimuli would allow the preparation of easily degradable MOFs, beckoning applications in delivery of molecular cargos. Incorporation of functional molecular switches into MOFs could yield materials with well-defined and very different states that could be used to bind and subsequently release

a guest, or turn optical properties ON and OFF.⁶⁸ In the long term, incorporation of structurally more ambitious ligands—e.g., short polymers, DNA oligomers, or peptides—into MOFs could yield mesoporous structures with elaborately functionalized pores that could be used in unique inclusion application, including binding of biological targets. While mesoporous MOF typically pose challenges in terms of structural sensitivity toward collapse and lowered crystallinity, the prospect of handling these structures has received a fillip by Stoddart and Yaghi's reticulation of the ligand shown in Figure 1.10, which contained eleven benzene rings in a linear sequence.⁶⁹ The resultant MOFs had pore apertures measuring 98 Å in diameter!

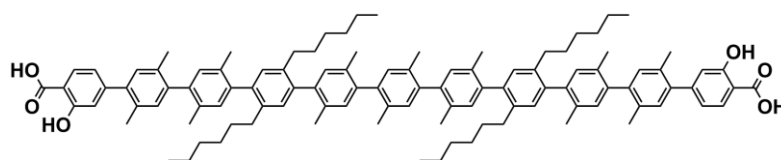


Figure 1.7 The longest ligand ever to be incorporated into a MOF.

Finally, the range of emergent phenomena that could be explored within MOFs would be further enhanced if their structures were not always homogeneous and ordered across the entire crystal. Yaghi's work on the chemically heterogeneous multivariate MOFs (MTV-MOFs)—which are created by coordination of metals to a number of similar but non-identical ligands within the same crystal—shows promising first results in being able to characterize MOFs with limited long-range order.⁷⁰ This move toward increased complexity would sacrifice some of the facility of characterization that is associated with crystallographically ordered structures, but would undoubtedly open up entirely new avenues for fundamental and practical exploration of next-generation MOFs.

The modular nature of MOF synthesis and the tunable functionality have led to numerous novel porous materials for potential applications in many other areas, such as asymmetric catalysis, energy conversion and storage, and chemical sensing. However, due to their high costs and limited thermal and hydrolytic stability, more efforts are needed to make these applications truly practical.

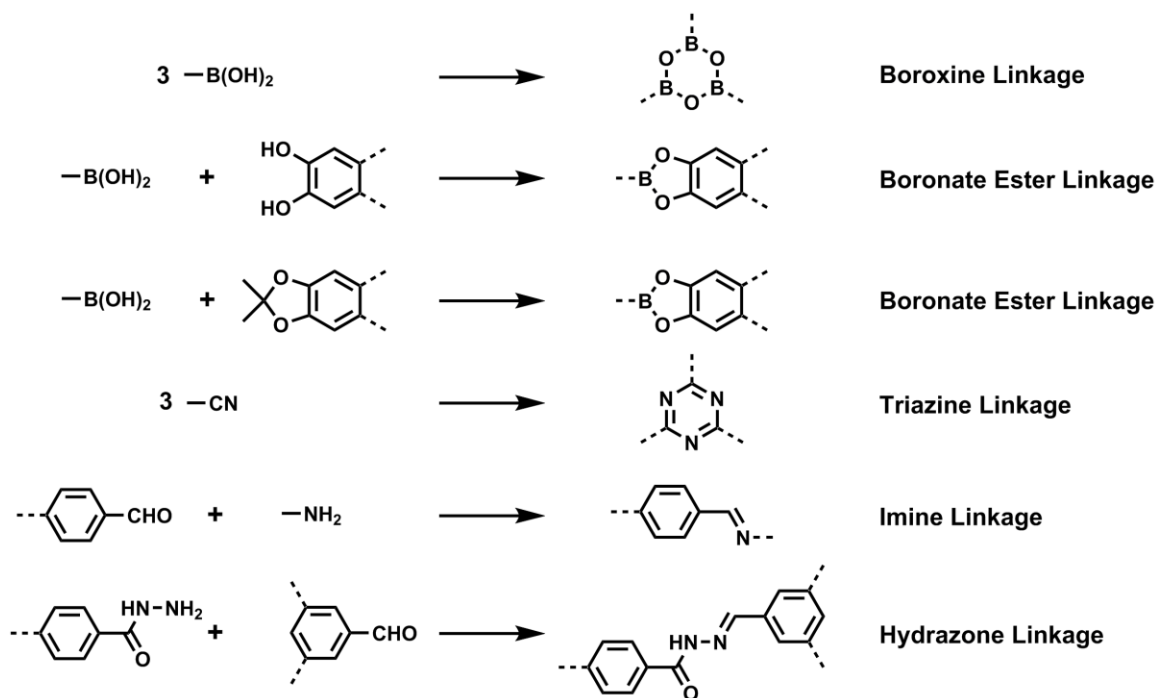
1.3 Covalent Organic Frameworks

Covalent organic frameworks (COFs) are a class of 2D and 3D crystalline porous polymers that are built through reversible covalent bond formation,⁷¹ between organic building blocks with light elements (e.g., C, N, O, B, Si, and H). Their structure and functionality can be designed and achieved by the atomically precise integration of organic units. They have recently emerged as a new molecular platform for gas storage, catalysis, and optoelectronic applications. The syntheses and development of COFs strongly rely on dynamic covalent chemistry. The modular structure and applications of COFs can also be tuned by rational design of organic building blocks. This section will briefly describe the basic design concepts, the modular syntheses, and applications of COFs.

1.3.1 Dynamic Covalent Chemistry

Research on porous organic materials has been focused on organic polymeric materials for a long time.⁷² The synthesis of organic porous polymers has always been carried out by covalent bond formations, generally under kinetically controlled, irreversible conditions. Normally, it is difficult to obtain crystalline material via an irreversible reaction and thus the characterization of structure by single crystal X-ray analysis is impossible. Moreover, without long-range ordered porous structure, the control of uniform pore size and specific surface area of materials becomes an important issue to be solved. In contrast, dynamic covalent chemistry (DCC) relies on reversible covalent chemical reactions that achieve thermodynamic minimum of the system at equilibrium via free exchange of molecular components.⁷³ DCC features the reversible covalent bonds that can be broken and reformed, thus allowing “error-correction” and “proof-reading” characters which can lead to the most thermodynamically stable products. Applying DCC to the synthesis of organic porous polymers (Scheme 1.5), the self-healing process can reduce the incidence of structural defects and assist the formation of an ordered structure.

Scheme 1.5 Schematic Representation of Dynamic Covalent Reactions Used in the Preparation of COFs



COFs are 2D or 3D polymeric materials formed through DCC: reversible reactions between one or more oligofunctional precursors proceed until a thermodynamically stable structure is formed. Due to their modular synthesis, crystallographic order, high thermal stability, and composition of light elements, COFs are promising for applications such as light harvesting, gas storage and separation, catalysis, as well as components of electronic devices. The first examples of COFs, based on dynamic boroxine and catechol/boronate ester linkages, were prepared by Yaghi's group in 2005 (Figure 1.8A).⁷⁴ The slow removal of water was essential for the error-correction process that resulted in well-defined microcrystalline materials. Subsequently, several reversible covalent reactions have been exploited in the synthesis of COFs

(Scheme 1.5). A majority of COFs were synthesized from building blocks with boronic acids, which can either self-condense or react with dialcohols to form six-membered boroxine and five-membered boronate ester linkages (Figure 1.8B), respectively. In addition, Dichtel et al. utilized a $\text{BF}_3 \cdot \text{Et}_2\text{O}$ -catalysed deprotection of catechol acetonides to prepare COFs based on phthalocyanine boronate esters.⁷⁵ This *in situ* deprotection protocol provided an alternative route that avoids the oxidation and solubility issues when using large aromatic dialcohols. While boron-based COFs initially dominated the field, in recent years other dynamic functional motifs based on e.g. imines⁷⁶ (Figure 1.8C) and hydrazones⁷⁷ (Figure 1.8D) have been explored in the COF synthesis. There is another class of COFs prepared via the cyclical trimerization of cyano groups under ionothermal conditions⁷⁸ (Figure 1.8E). This material provides high thermal, chemical, and mechanical stabilities as well as a high degree of conjugation. However, it possesses low crystallinity due to the poor reversibility of the trimerization reaction.

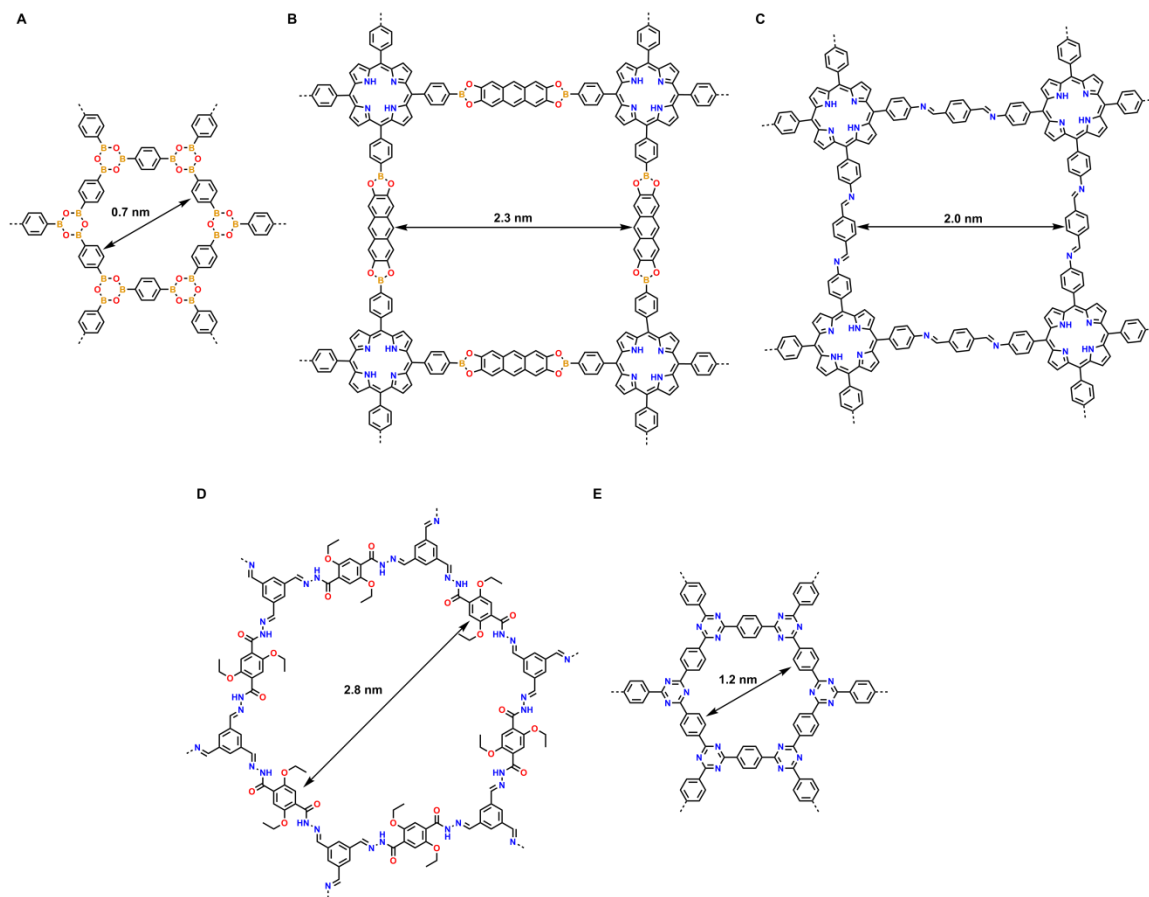


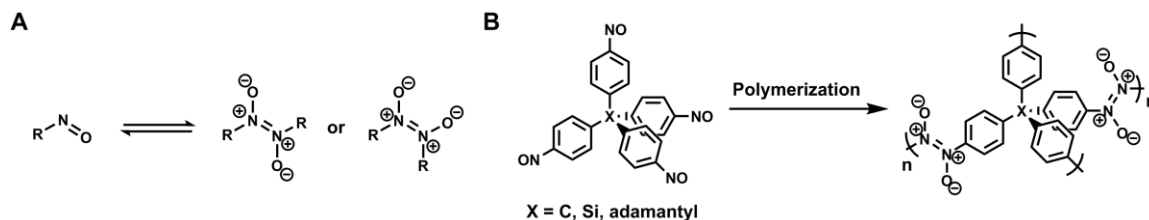
Figure 1.8 Schematic representation of COFs based on boroxine (A), boronate ester (B), imine (C), hydrazone (D), and triazine (E) linkages.

1.3.2 Modular Synthesis of COFs

COFs are mostly produced as microcrystalline powders and analyzed by powder X-ray diffraction (PXRD). Their structures can be assigned by matching computationally predicted structures and the obtained diffraction patterns. The structural simulation of COFs provides an important tool in revealing their stacked structures; this is especially helpful in the case of 2D COFs. So far, obtaining large enough crystal for single crystal X-ray analysis is still a tough task, and this phenomenon indicates a kinetic problem in

COF synthesis. To obtain good quality single crystals, the rate of crystal growth must be slower than the rate of the reversible covalent bond formation. However, the kinetics of most employed dynamic reactions seems too slow to allow efficient error-correction needed for the growth of single crystals. Recently, Wuest et al. have demonstrated that a facile exchange (with low activation barrier 20–30 kcal mol⁻¹) between azodioxides and nitroso compounds (Scheme 1.6A) leads to the growth of large crystals.⁷⁹ They used rigid tetrahedrally substituted precursors (Scheme 1.6B) to form first single-crystalline COFs, which were characterized by single crystal X-ray analysis afterward. About the same time, the crystal structure of a new covalent organic framework, prepared by an imine condensation of tetra-(4-anilyl)methane and 4,4'-biphenyldialdehyde, was determined by single-crystal 3D electron diffraction using the rotation electron diffraction method for data collection.⁸⁰ The successful determination of the structure of a COF directly from microcrystalline compound is a significant landmark in the development of COF chemistry. Crystallographic information is typically supplemented by data from infrared spectroscopy, solid-state NMR spectroscopy, elemental analysis, and X-ray photoelectron spectroscopy, which together establish the chemical linkages, functional groups, and elemental compositions of the COFs.

Scheme 1.6 (A) Exchange between Nitroso Compounds and Their Azodioxide Dimers and (B) Polymerization of Tetrahedrally Substituted Organic Linker



To obtain a crystallographically ordered COF, the geometry of the building blocks should be well-preserved in the COF. The conformationally rigid building blocks should be symmetric and contain reactive functional groups that trigger dynamic covalent bond formation without any irreversible side reactions. Furthermore, the rigid conformation of the building blocks allows the prediction and computational simulation of COFs' topologies. Symmetric building blocks can be classified into linear, triangular, cross-shaped, or tetrahedral geometries, referring to the directional symmetry of the reactive groups (Figure 1.9). As shown in Figure 1.8, the geometry of the building blocks determines the resulting COF structure. Therefore, the combinations of diverse geometries of linkers can lead to the construction of COFs with different pore size and shape. For instance, selected combinations of planar blocks (e.g., linear, triangular, and cross-shape linkers) will afford 2D COFs with 1D channels (Scheme 1.7). Combinations of tetrahedral only or tetrahedral and linear linkers can lead to 3D COFs. The rigid nature and discrete bonding direction of arenes enables suitable building blocks to build COF via aromatic $[\pi \cdots \pi]$ stacking systems. The advances in synthetic organic chemistry and

the diversity of explored aromatic systems should allow numerous building block combinations.

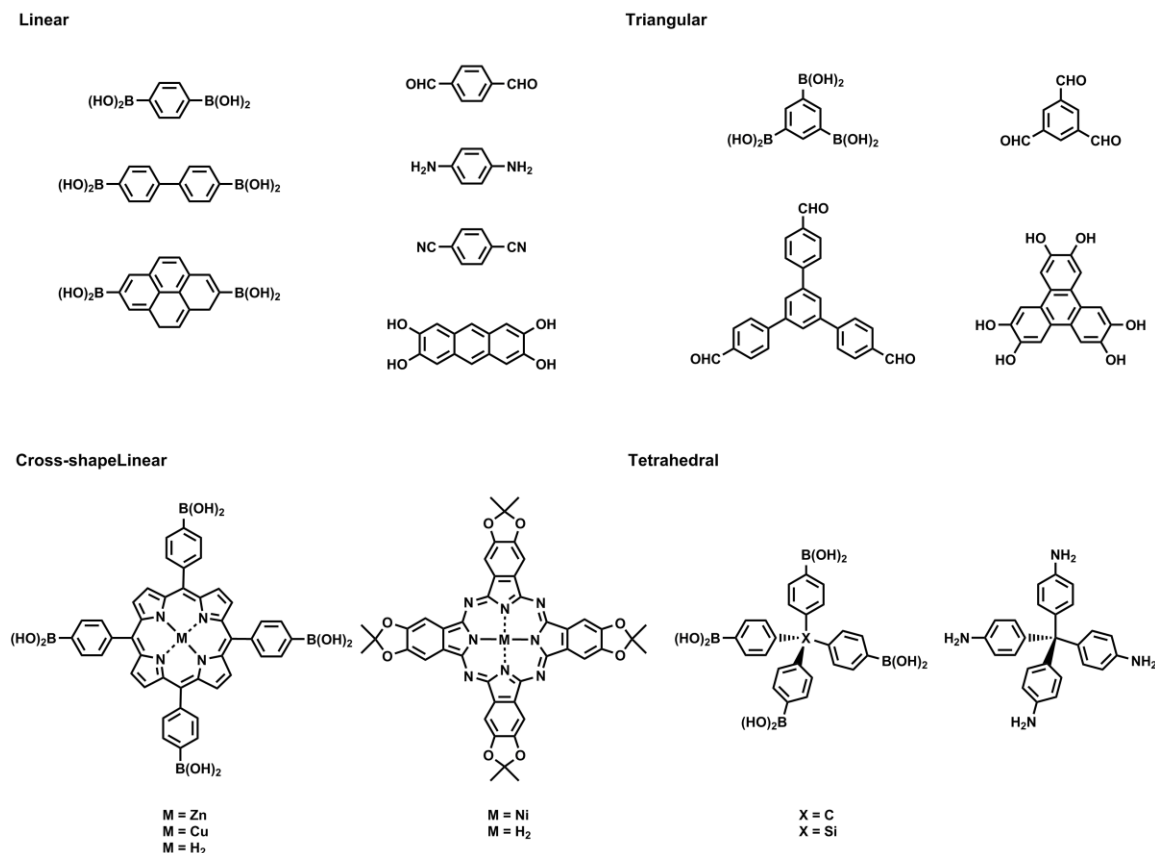
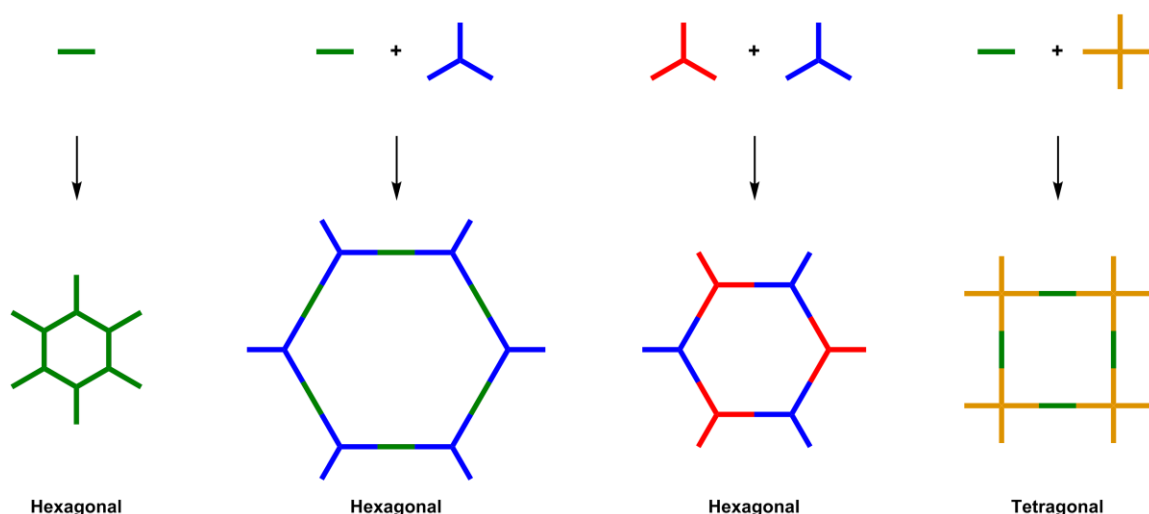


Figure 1.9 Some commonly used COF building blocks categorized into different geometries.

Solvothermal synthesis is a typical method for the preparation of COFs. To obtain crystalline frameworks, the combinations of reaction media (mixed solvent systems) and conditions (temperature, pressure, and concentration) should be experimentally adjusted. Typically, a closed reaction environment is required to allow the presence of water which can trigger the reverse reaction in the system. In addition, molten metal salts have been developed to provide ionothermal conditions for the synthesis of COFs.⁷⁸ Microwave

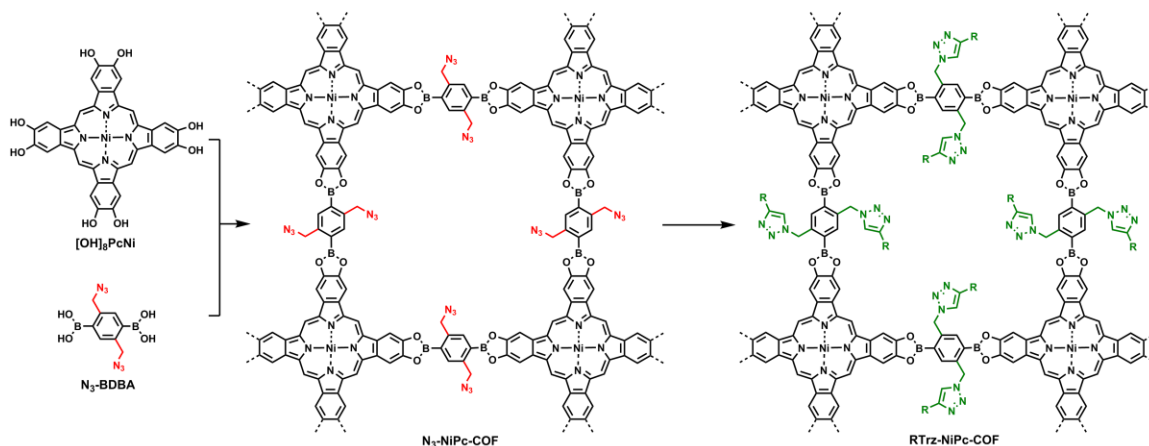
reactions have also been exploited to facilitate solvothermal reactions.⁸¹ In addition to solvothermal synthetic methods aimed at producing crystals of COFs, COF monolayers have been successfully deposited on substrates such as metal surfaces⁸² and graphene sheets.⁸³

Scheme 1.7 Combinations of Building Blocks with Different Geometries for Synthesizing 2D COFs



Jiang et al. have introduced postsynthetic modification into the synthesis of COFs to allow the incorporation of a variety of organic functionalities into the channels (Scheme 1.8).⁸⁴ They used azide-appended building blocks for the synthesis of COFs with azide units anchored on the walls for further chemical reactions. These azide units underwent a quantitative click reaction with alkynes to modify pore surfaces with desired functional groups and properties. Several functional groups such as alkyl chains, acetyl, aromatic units, ester, and chromophoric moieties have been integrated into the walls of COFs.

Scheme 1.8 Schematic Representation of the Surface Engineering of Tetragonal NiPc-COF.



Since reverse disassembly reactions can occur after the synthesis, COFs in general completely decompose even in the presence of ambient humidity, which remains a challenge that prevents their usage in most practical applications. Banerjee et al. reported the two COFs, TpPa-1 and TpPa-2, formed using a combination of reversible and irreversible organic reactions (Figure 1.10).⁸⁵ They were synthesized by the reaction of 1,3,5-triformylphloroglucinol (Tp) with p-phenylenediamine (Pa-1) or 2,5-dimethyl-p-phenylenediamine (Pa-2), respectively. They showed exceptional resistance toward boiling water and acid treatment, and TpPa-2 was also proven stable in a basic medium (9N NaOH). Remarkably, both COFs retained their crystallinity and gas adsorption properties under these conditions.

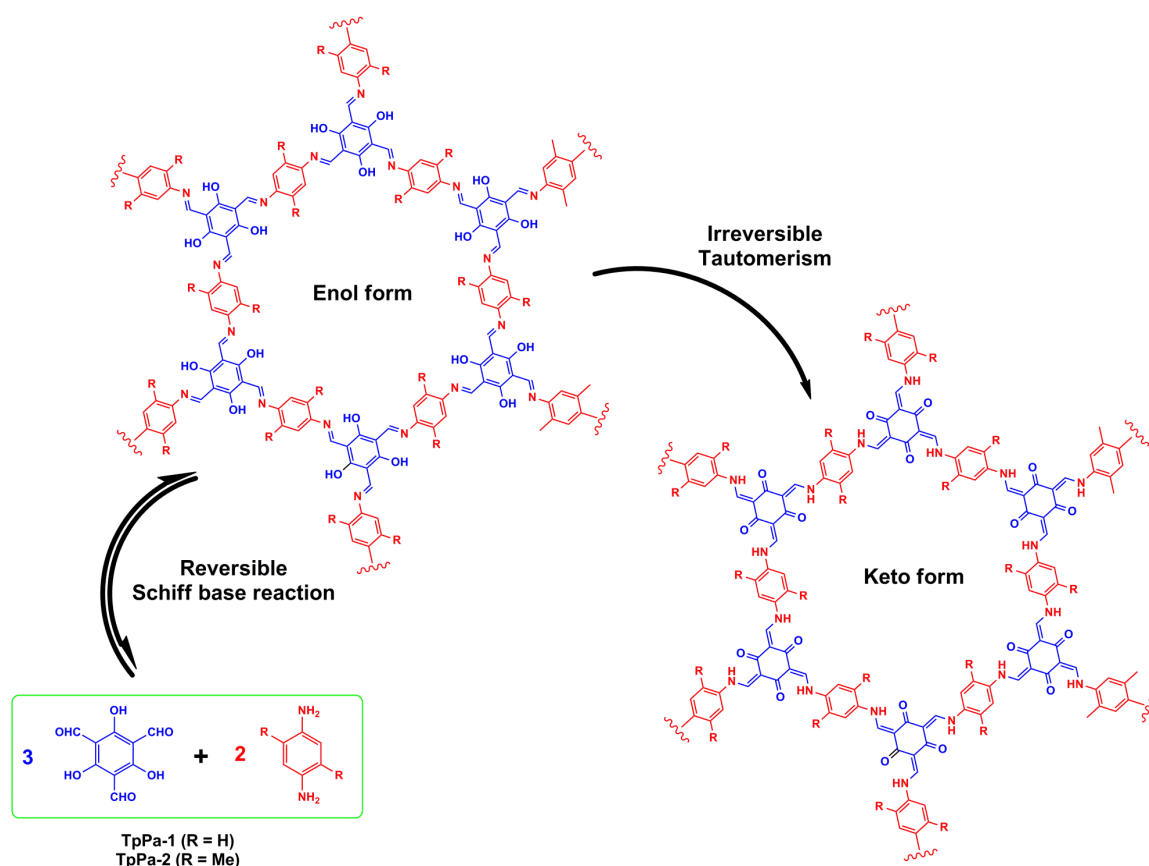


Figure 1.10 The syntheses of TpPa-1 and TpPa-2 by the combined reversible and irreversible reaction. The total reaction proceeds in two steps: (1) reversible Schiff-base reaction and (2) irreversible enol-to-keto tautomerism.

1.3.3 Applications of COFs

1.3.3.1 Gas Adsorption

COFs have been considered promising materials for gas storage applications due to their thermal stability, high surface area, and most importantly, composition of light elements, which conducts to the low density of COFs and high adsorption density. The storage capabilities of COFs for gases, such as hydrogen, methane, and carbon dioxide,

have been widely investigated.⁷¹ Generally speaking, the gas adsorption capacity of a COF primarily relies on the components and structure of its frameworks. So far, the largest number of BET surface area is 4210 m²g⁻¹ from COF-103, which was built from tetra(4-dihydroxyborylphenyl)silane.⁸⁶

1.3.3.2 Catalysis

Heterogeneous catalysis is one of the most practical applications in porous materials. However, due to the absence of exposed metal ions and catalytic active organic functional groups in the frameworks, the exploration on catalysis of COFs is very rare compared to MOFs or zeolites. Imine-based COF-LZU1 can load Pd ions into its pores, where they coordinate to nitrogen atoms in the COFs, to afford Pd/COF-LZU1 (Figure 1.11).⁸⁷ The Pd ions on the COF walls are catalytically active and accessible to reaction substrates, allowing a heterogeneous catalytic reaction to be carried out. Pd/COF-LZU1 can catalyze Suzuki–Miyaura coupling reaction in various reactants and shows excellent yields (96–98%) of the reaction products, and exhibits high stability and recyclability.

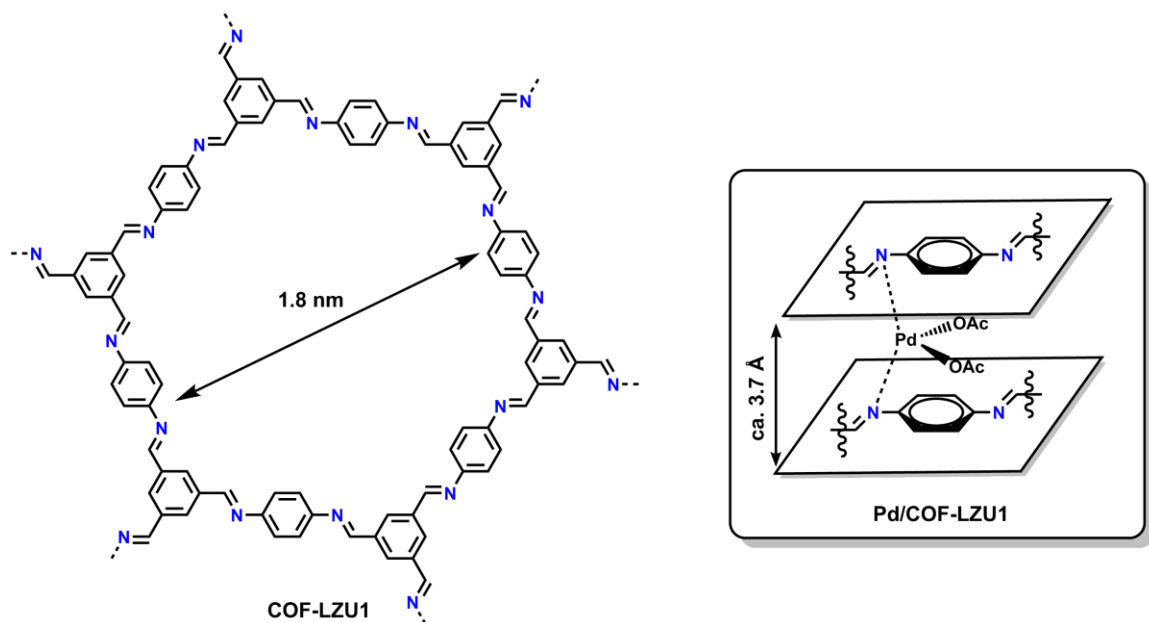


Figure 1.11 Schematic representation of imine-linked COF and its coordination with a Pd ion.

1.3.3.3 Semiconduction and Photoconduction

Whereas the strong covalent bonds in 2D COFs connect their backbone into hexagonal or tetragonal sheets, the out-of-plane π -interactions are the primary driving force in the formation of a layered structure. Owing to their $[\pi \cdots \pi]$ stacking alignment, COFs are promising porous platforms for organic semiconducting and photoconducting materials. A large electronic coupling between the p-orbitals of the eclipsed stacking layers can be induced in the frameworks. Via these preorganized and built-in pathways, the transport of charge carriers and photoexcited states (excitons) can be facilitated.

The investigations of a series of 2D COFs as construction of electronic and optoelectronic materials were demonstrated by Jiang and co-workers.⁸⁸ They have designed π -electronic 2D TP-COF consisting of interlocking hexagons made from

2,3,6,7,10,11-hexahydroxytriphenylene and pyrene-2,7-diboronic acid (Figure 1.12A). TP-COF is semiconducting, which enables hole transport and is capable of on-off switching of the electric current as demonstrated by the I - V curve measurements. In contrast to mostly p-type semiconducting COFs, the same group designed 2D-NiPc-BTDA-COF as an n-type semiconductor with electron mobilities as high as $0.6 \text{ cm}^2 \text{ V}^{-1} \text{ s}^{-1}$ (Figure 1.12B).⁸⁹ Notably, NiPc-BTDA-COF is extremely sensitive and yields prominent photocurrents upon irradiation with long wavelength visible light and near infrared photons. Therefore, NiPc-BTDA-COF represents a well-organized, thermally stable, and photoconductive n-channel semiconductor.

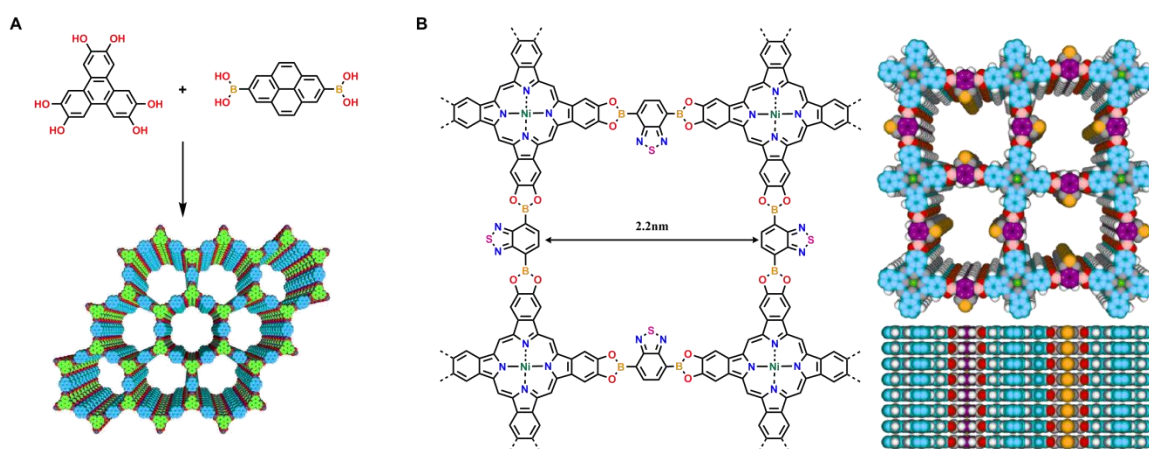


Figure 1.12 (A) Schematic representation of the synthesis of 2D TP-COF. (B) The chemical structure of NiPc-BTDA-COF (left); top and side views of a graphical representation of a 2×2 tetragonal grid showing the eclipsed stacking of 2D polymer sheets (right).

1.3.4 Conclusions and Outlook

In summary, COFs represent a newcomer in the field of crystalline porous organic polymeric materials. This field is blossoming because of their unique features, such as low density (especially when compared to MOFs), modular synthesis, permanent porosity, controllable pore size, and the diversity of available building blocks. The development of additional new synthetic strategies and new linkage systems will provide access to expand the family of COFs. Understanding of the thermodynamic behaviors of DCC during the condensation reactions would be necessary to consistently prepare high quality COF materials. The chemical stability of COFs can be enhanced by using a new approach, which is the formation of imine-linked networks that can undergo keto–enol tautomerism to yield COFs stable in boiling water, acids and bases. Enriching the complexity of the COF structures can be done through post-synthetic modifications. Due to the distinguished $[\pi \cdots \pi]$ stacking of frameworks, besides common applications for porous materials, COFs provide a promising application as semiconducting and photoconducting materials.

1.4 Crystalline Noncovalent Porous Organic Materials

Most crystalline porous materials with permanent pores are extended structures composed of directional covalent or coordination bonds, such as MOFs, COFs, and organic network polymers. In contrast, porous molecular crystals, in which interactions between individual molecular building blocks are weak and noncovalent, are relatively

rare. Discrete molecules tend to pack efficiently in the solid state, leaving as little void volume as possible, which leads to nonporous materials. During the past decade, several robust porous organic molecular crystals were discovered and their physical properties and porosity were exhaustively studied. Such molecular crystals, which may be either crystalline or amorphous, can be categorized as either intrinsically porous (containing permanent covalent cavities) or extrinsically porous (inefficiently packed).⁹⁰ Unlike porous materials with infinite networks, discrete molecules may be dissolved in common organic solvents which enable versatile chemical reactions in the solution or modification by recrystallization.

Crystalline porous molecules are desirable because their long-range molecular order allows the single crystal X-ray analysis of materials, which reveals the details of structural information and offers potential for fine structural control in applications. The biggest challenge is that the cavities or channels of molecular crystals tend to collapse while desolvating the crystals. As a result, a denser phase that may be either crystalline or amorphous remains. Moreover, the multiple potential interactions of organic molecules associating with one another in solid state make the prediction of the crystallographic structures and molecular packing difficult. Therefore, rational design and assembly of organic molecules into crystalline porous structures is still a challenging task. In this chapter, only the crystalline molecular crystals with permanent porosity are discussed.

1.4.1 Intrinsically Porous Organic Crystals

Intrinsic porosity results from the cavity-containing structures of discrete molecules, such as bowl-shaped calixarenes and porous organic cages. In 2002, Atwood and co-workers reported a hexagonal close-packed arrangement of calix[4]arene containing lattice voids that can occlude small, highly volatile molecules (Figure 1.13).⁹¹ They have demonstrated the storage of methane and Freon by interstitial van der Waals confinement. However, the uptake of liquid and gas phase of molecular guests was carried out by slow evaporation of acetone solution containing calix[4]arene and the target molecule, and introducing the gases under high pressure, respectively. They assumed that the guest could not easily escape and diffuse through the host lattice was because of the nonporous channels. For practical applications, porous molecular crystals should have accessible pores, permanent and high porosity, and adsorption of guests should occur under mild conditions.

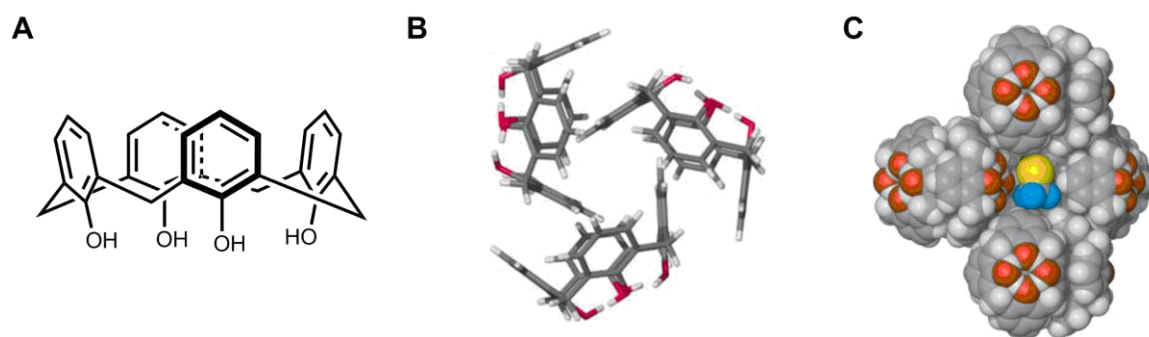


Figure 1.13 (A) Chemical structure of calix[4]arene. (B) Capped-stick representation of its crystal structure viewed along the threefold axis. (C) Space-filling representation of $\text{CF}_3\text{Br}@$ calix[4]arene. The interstitial void of the host lattice is

occupied by one molecule of CF_3Br . Only van der Waals contacts occur between host and guest atoms. Colors: C, gray; H, white; O, red; F, blue; and Br, yellow.

Cooper et al. demonstrated that covalently bonded organic cages can assemble into crystalline microporous materials (Figure 1.14).⁹² A series of porous materials was built from the noncovalent self-assembly of intrinsic porous molecular cages. By varying the chemical functionality of molecular cages, the three-dimensional connectivity between the cage windows can be modified to either non-porous or permanently porous structures. They showed that the design principles for modular synthesis of intrinsic molecular cages that led to guest-responsive porous organic crystals. Moreover, they also demonstrated that organic molecules, rather than infinite frameworks, can separate other organic molecules by size and shape.⁹³ This molecular organic cage was able to separate a common aromatic compound (mesitylene) from its structural isomer (4-ethyltoluene). They suggested that this phenomenon stemmed from the structure of the intrinsically porous cage molecule, which was itself synthesized from a derivative of mesitylene. They also performed a combination of atomistic simulations for individual cage molecules and solid-state molecular dynamics simulations.

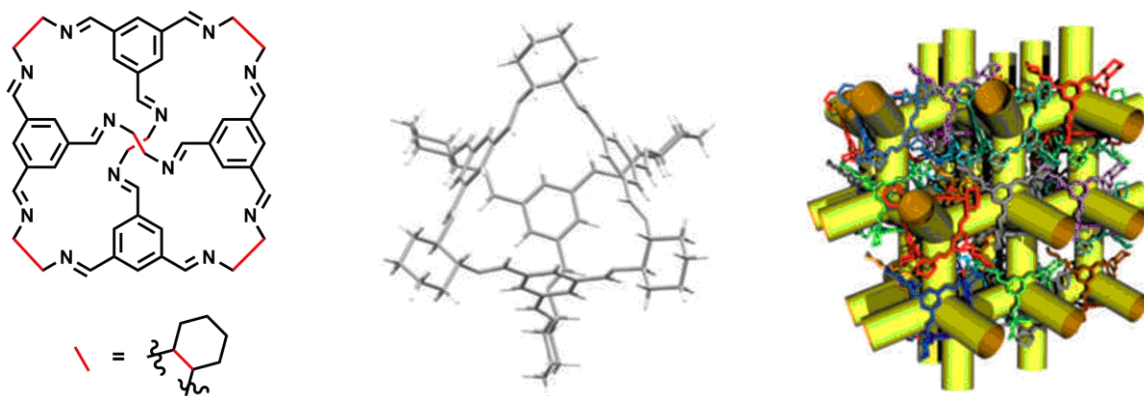


Figure 1.14 Molecular structure (left), crystal structure of individual molecule (middle), and crystal packing (right) of tetrahedral imine cage.

Owing to the relatively small molecular sizes of the cages, resulting porous molecular crystals are restricted to the microporous regime. Recently, Mastalerz et al. synthesized a shape-persistent cage by the reversible formation of 24 boronic ester units of 12 triptycene tetraol molecules and 8 triboronic acid molecules (Figure 1.15).⁹⁴ By single-crystal X-ray analysis, the cage compound has a cavity with an inner diameter of 2.6 nm and an outer diameter of 3.1 nm. The porous molecular crystal was stable after activation by removing solvent molecules inside the pores. As a result, the mesoporous material with a pore diameter of 2.3 nm has a BET surface area of $3,758 \text{ m}^2\text{g}^{-1}$, the highest among all kinds of molecular crystals to date.

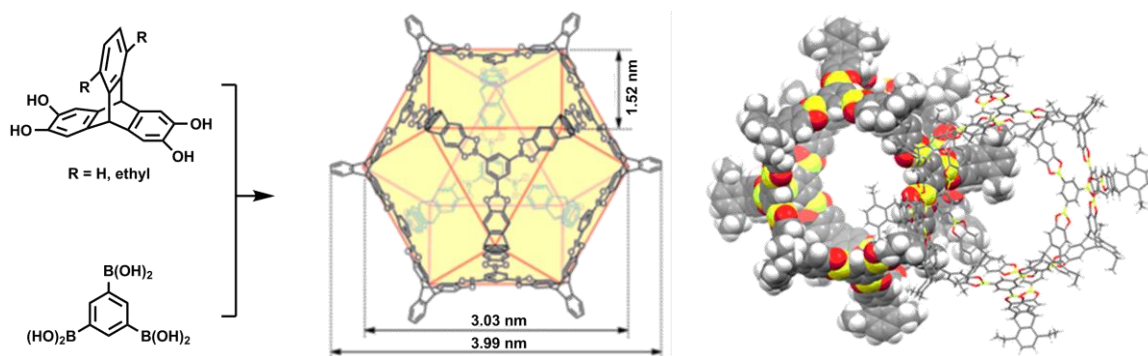


Figure 1.15 Left: the condensation of triptycene tetraol and triboric acid forms a cuboctahedral cage. Right: Space-filling and stick representation of molecular packing of the cage. Colors: C, gray; H, white; O, red; B, yellow.

1.4.2 Extrinsically Porous Organic Crystals

Extrinsic porosity arises purely from packing of small molecules without an intrinsic cavity, owing to their lack of topological self-complementarity. Sometimes, both intrinsic and extrinsic porosity can exist in the same porous molecular crystal, e.g., in the case of cavity-containing macrocycles.⁹⁵ One of the exhaustively studied extrinsically porous molecular crystals is *tris-o*-phenylenedioxycyclotriphosphazene (TPP), which features a phosphazene (P_3N_3) core with three orthogonal catechol rings (Figure 1.16A).⁹⁶ A structure with one-dimensional hexagonal-shaped pores was obtained by the crystallization of TPP and it was accessible to gases such as CO_2 and CH_4 .

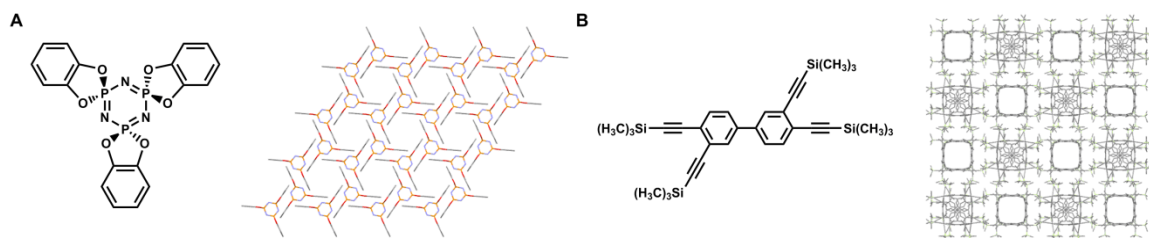


Figure 1.16 (A) Chemical structure of TPP and its extrinsically porous crystal structure. (B) Chemical structure of 4TMSEBP and its extrinsically porous crystal structure.

A useful approach for discovering potential porous organic molecules is to search the Cambridge Structural Database, or other crystallographic databases, for candidate structures. For example, materials with anomalously low crystallographic densities could be possible having certain degree of porosity. Based on this data mining strategy, McKeown and co-workers uncovered the porous nature of the crystalline material 3,3'-4,4'-*tetrakis*(trimethylsilylethynyl)biphenyl (4TMSEBP) (Figure 1.16B).⁹⁷ Crystalline 4TMSEBP was found to be stable to desolvation, and the desolvated material showed internal voids with diameters of 11 Å. Surprisingly, this structure apparently was mostly stabilized by self-complementary [C–H \cdots π] interactions, rather than the more commonly used weak interactions such as H-bonding, [$\pi\cdots\pi$] interactions, or donor-acceptor binding.

Hydrogen-bonding is widely exploited in the supramolecular chemistry for self-assembly. Zhong et al. assembled a hydrogen-bonded organic framework, HOF-8 that is not only thermally stable but also stable in water and common organic solvents (Figure 1.17).⁹⁸ Remarkably, desolvated HOF-8 exhibits high CO₂ adsorption as well as highly selective CO₂ and benzene adsorption at ambient temperature.

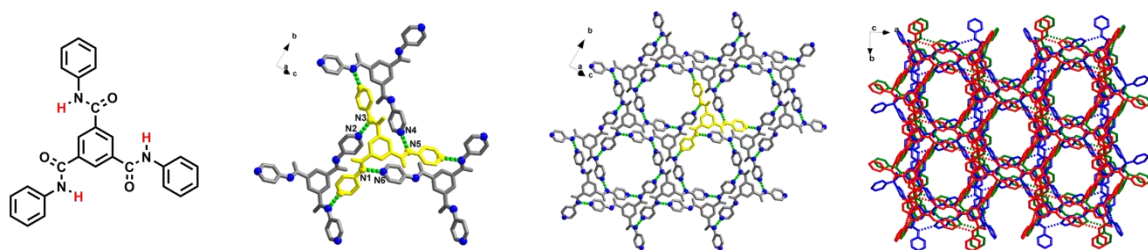


Figure 1.17 From left to right: molecular structure of organic building block; H-bonding interactions observed in HOF-8; 2D supramolecular layer structure of HOF-8; 3D supramolecular microporous structure of HOF-8.

Utilizing the concept of H-bonding self-assembly of versatile triptycene (Figure 1.18A), a triptycene trisbenzimidazolone (TTBI; Figure 1.18B) is shown to self-assemble through programmed hydrogen-bonding to form an extrinsically porous solid with a large pore volume, low density (0.755 g cm^{-3}) and a BET surface area, of $2,796 \text{ m}^2 \text{ g}^{-1}$.⁹⁹ This material from Mastalerz's group is the most porous extrinsic molecular crystal to date. The ribbon-like self-assembly of hydrogen-bonded benzimidazolone tapes define the one-dimensional pore channels in the crystal structure of TTBI. Interestingly, the porous solid is activated by multiple solvent exchanges—rather than the more common thermal desolvation—to avoid stress on the hydrogen-bonding pattern.

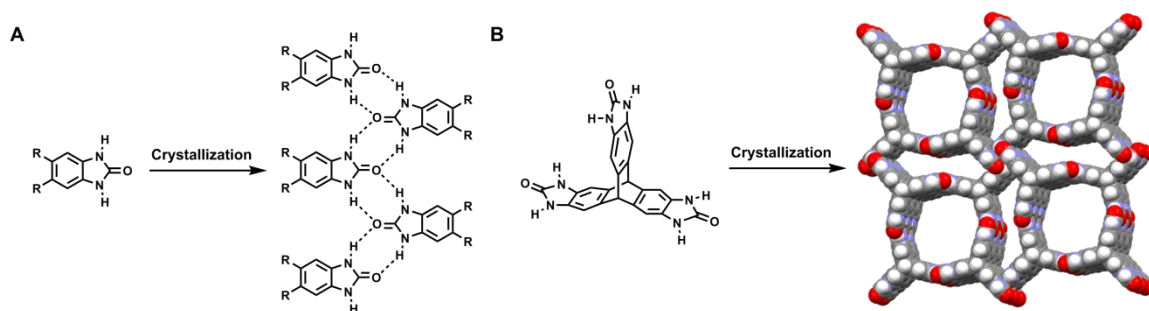


Figure 1.18 (A) Schematic representation of formation of ribbon-like structures in the

crystalline state by H-bonding of 4,5-disubstituted benzimidazolones. (C) Single crystal structure of porous molecular crystal made from triptycene trisbenzimidazolone. Colors: C, gray; H, white; O, red; N, blue.

1.4.3 Conclusions and Outlook

The field of porous organic molecular crystals has attracted much attention due to their solution processibility, modular synthesis, and high structural responsiveness to guest. However, compared to other crystalline porous materials (zeolites, MOF, and COFs), this research is still in its infancy. Molecular crystals can form either crystalline structures with voids or amorphous solids with interconnected disordered pores. Unlike other porous materials, it is very challenging to predict and design the structure and topology of molecular crystal. The lack of systematic studies and examples hampers the understanding of trends of molecular configuration for promoting the formation of cavities or lattice voids.

In general, the molecules with convergent shapes such as cups, macrocycles, and cages, are more likely candidates for building porous molecular crystals. To obtain extrinsically porous materials, careful and rational design of molecules is necessary to avoid efficient packing. It is possible to combine a number of different weak interactions for enhancing the stability of molecular crystals. Various chemical functionalities can be introduced into the pore by organic modification of the molecule or postsynthetic modification on crystals.

Organic molecular solids possessing permanent porosity are still rare. Mastalerz's group holds the record for highest surface area of both intrinsic and extrinsic porous molecular crystals with $3,758 \text{ m}^2\text{g}^{-1}$ and $2,796 \text{ m}^2\text{g}^{-1}$, respectively. These numbers are comparable to those of MOFs and COFs. These molecules retain significant porosity in the desolvated crystals with the combination of intrinsic and extrinsic porosity arising from inefficient molecular packing. In addition to high surface areas and pore volumes, porous molecular solids may have potential advantages over infinite networks in terms of solution processability and highly structural responsiveness to guests. Unlike porous networks, organic molecules can easily be dissolved and recrystallized, which is promising for their deposition on membranes or as thin films. The noncovalent packing of porous molecular solids indicates that discrete molecules have positional and conformational flexibility, which may lead to highly guest-responsive materials for molecular separation.

1.5 References

- [1] Bruce, D. W.; O'Hare D.; Walton, R. I. *Porous Materials*; John Wiley & Sons: Hoboken, NJ, 2010.
- [2] Akhtar, F.; Andersson, L.; Ogunwumi, S.; Hedin, N.; Bergström, L. *J. Eur. Ceramic Soc.* **2014**, *34*, 1643–1666.
- [3] Yilmaz, B.; Trukhan, N.; Müller, U. *Chin. J. Catal.* **2012**, *33*, 3–10.

- [4] Cronstedt, A. F.; Handl, A. *Stockholm* **1756**, 18, 120–125.
- [5] James, S. T. *Chem. Soc. Rev.* **2003**, 32, 276–288.
- [6] (a) Farrusseng, D. *Metal-Organic Frameworks: Applications from Catalysis to Gas Storage*; Wiley-VCH: Weinheim, Germany, 2011. (b) MacGillivray, L. R. *Metal-Organic Frameworks: Design and Applications*; Wiley: Hoboken, NJ, **2010**. (c) Special issue of *Chem. Soc. Rev.* **2009**, 38, 1201–1508. (d) Special issue of *Chem. Rev.* **2012**, 112, 673–1268.
- [7] Banerjee, R.; Phan, A.; Wang, B.; Knobler, C.; Furukawa, H.; O'Keeffe, M.; Yaghi, O. M. *Science* **2008**, 319, 939–943.
- [8] Stock, N.; Biswas, S. *Chem. Rev.* **2012**, 112, 933–969.
- [9] (a) Kappe, C. O. *Chem. Soc. Rev.* **2008**, 37, 1127–1139. (b) Kappe, C. O.; Pieber, B.; Dallinger, D. *Angew. Chem., Int. Ed.* **2009**, 52, 1088–1094.
- [10] Kim, M.; Garibay, S. J.; Cohen, S. M. *Inorg. Chem.* **2011**, 50, 729–731.
- [11] Mueller, U.; Puetter, H.; Hesse, M.; Wessel, H. *Patent* WO 2005/049892, 2005.
- [12] Czaja, A. U.; Trukhan, N.; Mueller, U. *Chem. Soc. Rev.* **2009**, 38, 1284–1293.
- [13] Friščić, T. *Chem. Soc. Rev.* **2012**, 41, 3493–3510.
- [14] Mason, T. J.; Peters, D. *Practical Sonochemistry: Power Ultrasound Uses and Applications*; Horwood Publishing: Chichester, 2003.

- [15] (a) Son, W.-J.; Kim, J.; Ahn, W.-S. *Chem. Commun.* **2008**, *44*, 6336–6338. (b) Kim, J.; Yang, S.-T.; Choi, S. B.; Sim, J.; Kim, J.; Ahn, W.-S. *J. Mater. Chem.* **2011**, *21*, 3070–3076. (c) Qiu, L.-G.; Li, Z.-Q.; Wu, Y.; Wang, W.; Xu, T.; Jiang, S. *Chem. Commun.* **2008**, *44*, 3642–3644.
- [16] Férey, G.; Serre, C. *Chem. Soc. Rev.* **2009**, *38*, 1380–1399.
- [17] (a) Cooper, E. R.; Andrews, C. D.; Wheatley, P. S.; Webb, P. B.; Wormald, P.; Morris, R. E. *Nature* **2004**, *430*, 1012–1016. (b) Parnham, E.; Morris, R. E. *Acc. Chem. Res.* **2007**, *40*, 1005–1013.
- [18] Loiseau, T.; Férey, G. *J. Fluorine Chem.* **2007**, *128*, 413–422.
- [19] Guillerme, V.; Gross, S.; Serre, C.; Devic, T.; Bauer, M.; Férey, G. *Chem. Commun.* **2010**, *46*, 767–769.
- [20] Jiang, H.-L.; Feng, D.; Wang, K.; Gu, Z.-Y.; Wei, Z.; Chen, Y.-P.; Zhou, H.-C. *J. Am. Chem. Soc.* **2013**, *135*, 13934–13938.
- [21] Deria, P.; Mondloch, J. E.; Tylianakis, E.; Ghosh, P.; Bery, W.; Snurr, R. Q.; Hupp, J. T.; Farha, O. K. *J. Am. Chem. Soc.* **2013**, *135*, 16801–16808.
- [22] Chen, T.-H.; Popov, I.; Kaveevivitchai, W.; Miljanić, O. Š. *Chem. Mater.* **2014**, doi: 10.1021/cm501657d.
- [23] Stoddart's carbohydrate-based MOFs, which incorporate γ -cyclodextrins as ligands, probably stand among the most complex organically functionalized materials of

the kind. See: Forgan, R. S.; Smaldone, R. A.; Gassensmith, J. J.; Furukawa, H.; Cordes, D. B.; Li, Q.; Wilmer, C. E.; Botros, Y. Y.; Snurr, R. Q.; Slawin, A. M. Z.; Stoddart, J. F. *J. Am. Chem. Soc.* **2012**, *134*, 406–417.

[24] Kaye, S. S.; Long, J. R. *J. Am. Chem. Soc.* **2008**, *130*, 806–807.

[25] Tanabe, K. K.; Cohen, S. M. *Chem. Soc. Rev.* **2011**, *40*, 498–519.

[26] Nguyen, J. G.; Cohen, S. M. *J. Am. Chem. Soc.* **2010**, *132*, 4560–4561.

[27] Deshpande, R. K.; Minnaar, J. L.; Telfer, S. G. *Angew. Chem., Int. Ed.* **2010**, *49*, 4598–4602.

[28] (a) Nguyen, H. G. T.; Weston, M. H.; Farha, O. K.; Hupp, J. T.; Nguyen, S. T. *CrystEngComm* **2012**, *14*, 4115–4118. (b) Tanabe, K. K.; Allen, C. A.; Cohen, S. M. *Angew. Chem., Int. Ed.* **2010**, *49*, 9730–9733.

[29] Vermeulen, N. A.; Karagiari, O.; Sarjeant, A. A.; Stern, C. L.; Hupp, J. T.; Farha, O. K.; Stoddart, J. F. *J. Am. Chem. Soc.* **2013**, *135*, 14916–14919.

[30] (a) Li, Q.; Zhang, W.; Miljanić, O. Š.; Sue, C.-H.; Knobler, C.; Zhao, Y.-L.; Liu, L.; Stoddart, J. F.; Yaghi, O. M. *Science* **2009**, *325*, 855–859. (b) Zhao, Y.-L.; Liu, L.; Zhang, W.; Sue, C.-H.; Li, Q.; Miljanić, O. Š.; Yaghi, O. M.; Stoddart, J. F. *Chem. Eur. J.* **2009**, *13*, 13356–13380.

[31] Zhang, Z.; Drapailo, A.; Matvieiev, Y.; Wojtas, L.; Zaworotko, M. J. *Chem. Commun.* **2013**, *49*, 8353–8355.

- [32] (a) Coskun, A.; Hmadeh, M.; Barin, G.; Gándara, F.; Li, Q.; Choi, E.; Strutt, N. L.; Cordes, D. B.; Slawin, A. M. Z.; Stoddart, J. F.; Sauvage, J.-P.; Yaghi, O. M. *Angew. Chem., Int. Ed.* **2012**, *51*, 2160–2163. (b) Li, Q.; Zhang, W.; Miljanić, O. Š.; Knobler, C. B.; Stoddart, J. F.; Yaghi, O. M. *Chem. Commun.* **2010**, *46*, 380–382.
- [33] Vukotic, V. N.; Harris, K. J.; Zhu, K.; Schurko, R. W.; Loeb, S. J. *Nat. Chem.* **2012**, *4*, 456–460.
- [34] Shimomura, S.; Higuchi, M.; Matsuda, R.; Yoneda, K.; Hijikata, Y.; Kubota, Y.; Mita, Y.; Kin, J.; Takata, M.; Kitagawa, S. *Nat. Chem.* **2010**, *2*, 633–637.
- [35] Li, J.-R.; Yu, J.; Lu, W.; Sun, L.-B.; Sculley, J.; Balbuena, P. B.; Zhou, H.-C. *Nat. Commun.* **2013**, *4*, 1538–1545.
- [36] (a) Lee, J. Y.; Farha, O. K.; Roberts, J.; Scheidt, K. A.; Nguyen, S. T.; Hupp, J. T. *Chem. Soc. Rev.* **2009**, *38*, 1450–1459. (b) Farrusseng, D.; Aguado, S.; Pinel, C. *Angew. Chem., Int. Ed.* **2009**, *48*, 7502–7513.
- [37] Yang, C.; Kaipa, U.; Mather, Q. Z.; Wang, X.; Nesterov, V.; Venero, A. F.; Omary, M. A. *J. Am. Chem. Soc.* **2011**, *133*, 18094–18097.
- [38] Padial, N. M.; Procopio, E. Q.; Montoro, C.; López, E.; Oltra, J. E.; Colombo, V.; Maspero, A.; Masciocchi, N.; Galli, S.; Senkovska, I.; Kaskel, S.; Barea, E.; Navarro, J. A. R. *Angew. Chem., Int. Ed.* **2013**, *52*, 8290–8294.
- [39] Hong, Y.; Lam, J. W. Y.; Tang, B. Z. *Chem. Soc. Rev.* **2011**, *40*, 5361–5388.

- [40] (a) Shustova, N. B.; Ong, T.-C.; Cozzolino, A. F.; Michaelis, V. K.; Griffin, R. G.; Dincă, M. *J. Am. Chem. Soc.* **2012**, *134*, 15061–15070. (b) Shustova, N. B.; McCarthy, B. D.; Dincă, M. *J. Am. Chem. Soc.* **2011**, *133*, 20126–20129.
- [41] Li, S.-L.; Xu, Q. *Energy Environ. Sci.* **2013**, *6*, 1656–1683.
- [42] Narayan, T. C.; Miyakai, T.; Seki, S.; Dincă, M. *J. Am. Chem. Soc.* **2012**, *134*, 12932–12935.
- [43] Sheberla, D.; Sun, L.; Blood-Forsythe, M. A.; Er, S.; Wade, C. R.; Brozek, C. K.; Aspuru-Guzik, A.; Dincă, M. *J. Am. Chem. Soc.* **2014**, *136*, 8859–8862.
- [44] (a) Talin, A. A.; Centrone, A.; Ford, A. C.; Foster, M. E.; Stavila, V.; Haney, P.; Kinney, R. A.; Szalai, V.; El Gabaly, F.; Yoon, H. P.; Léonard, F.; Allendorf, M. D. *Science* **2014**, *343*, 66–69. See also: (b) Kobayashi, Y.; Jacobs, B.; Allendorf, M. D.; Long, J. R. *Chem. Mater.* **2010**, *22*, 4120–4122.
- [45] Chui, S. S. Y.; Lo, S. M. F.; Charmant, J. P. H.; Orpen, A. G.; Williams, I. D. *Science* **1999**, *283*, 1148–1150.
- [46] Suh, M. P.; Park, H. J.; Prasad, T. K.; Lim, D.-W. *Chem. Rev.* **2012**, *112*, 782–835.
- [47] Peng, Y.; Krungleviciute, V.; Eryazici, I.; Hupp, J. T.; Farha, O. M.; Yildirim, T. *J. Am. Chem. Soc.* **2013**, *135*, 11887–11894.

- [48] Sumida, K.; Rogow, D. L.; Mason, J. A.; McDonald, T. M.; Bloch, E. D.; Herm, Z. R.; Bae, T.-H.; Long, J. R. *Chem. Rev.* **2012**, *112*, 724–781.
- [49] Farha, O. K.; Hupp, J. T. *Acc. Chem. Res.* **2010**, *43*, 1166–1175.
- [50] Furukawa, H.; Go, Y. B.; Ko, N.; Park, Y. K.; Uribe-Romo, F. J.; Kim, J.; O'Keeffe, M.; Yaghi, O. M. *Inorg. Chem.* **2011**, *50*, 9147–9152.
- [51] Chen, B.; Eddaoudi, M.; Hyde, S. T.; O'Keeffe, M.; Yaghi, O. M. *Science* **2001**, *291*, 1021–1023.
- [52] Farha, O. K.; Eryazici, I.; Jeong, N. C.; Hsuser, B. G.; Wilmer, C. E.; Sarjeant, A. A.; Snurr, R. Q.; Nguyen, S. T.; Yazaydin, A. Ö.; Hupp, J. T. *J. Am. Chem. Soc.* **2012**, *134*, 15016–15021.
- [53] Senkovska, I.; Kaskel, S. *Chem. Commun.* **2014**, *50*, 7089–7098.
- [54] Nelson, A. P.; Farha, O. M.; Mulfort, K. L.; Hupp, J. T. *J. Am. Chem. Soc.* **2009**, *131*, 458–460.
- [55] Yang, C.-X.; Chen, Y.-J.; Wang, H.-F.; Yan, X.-P. *Chem. Eur. J.* **2011**, *17*, 11734–11737.
- [56] Kitagawa, S.; Matsuda, R. *Coord. Chem. Rev.* **2007**, *251*, 2490–2509.
- [57] Li, J.-R.; Sculley, J.; Zhou, H.-C. *Chem. Rev.* **2012**, *112*, 869–932.

- [58] Britt, D.; Furukawa, H.; Wang, B.; Glover, T. G.; Yaghi, O. M. *Proc. Natl. Acad. Sci. U.S.A.* **2009**, *106*, 20637–20640.
- [59] Matsuda, R.; Kitaura, R.; Kitagawa, S.; Kubota, Y.; Belosludov, R. V.; Kobayashi, T. C.; Sakamoto, H.; Chiba, T.; Takata, M.; Kawazoe, Y.; Mita, Y. *Nature* **2005**, *436*, 238–240.
- [60] Mueller, U.; Schubert, M.; Teich, F.; Puetter, H.; Schierle-Arndt, K.; Pastre, J. *J. Mater. Chem.* **2006**, *16*, 626–630.
- [61] Kawamichi, T.; Haneda, T.; Kawano, M.; Fujita, M. *Nature* **2009**, *461*, 633–635.
- [62] Inokuma, Y.; Yoshioka, S.; Ariyoshi, J.; Arai, T.; Takada, K.; Matsunaga, S.; Rissanen, K.; Fujita, K. *Nature* **2013**, *495*, 461–466.
- [63] Alaerts, L.; Kirschhock, C. E. A.; Maes, M.; van der Veen, M. A.; Finsy, V.; Depla, A.; Martens, J. A.; Baron, G. V.; Jacobs, P. A.; Denayer, J. E. M.; De Vos, D. E. *Angew. Chem., Int. Ed.* **2007**, *46*, 4293–4296.
- [64] Fernandez, C. A.; Liu, J.; Thallapally, P. K.; Strachen, D. M. *J. Am. Chem. Soc.* **2012**, *134*, 9046–9049.
- [65] Ma, L.; Falkowski, J. M.; Abney, C.; Lin, W. *Nat. Chem.* **2010**, *2*, 838–843.
- [66] Xie, Z.; Ma, L.; deKrafft, K. E.; Jin, A.; Lin, W. *J. Am. Chem. Soc.* **2010**, *132*, 922–923.
- [67] Simon, P.; Gogotsi, Y. *Nat. Mater.* **2008**, *7*, 845–854.

- [68] Brown, J. W.; Henderson, B. L.; Kiesz, M. D.; Whalley, A. C.; Morris, W.; Grunder, S.; Deng, H.; Furukawa, H.; Zink, J. I.; Stoddart, J. F.; Yaghi, O. M. *Chem. Sci.* **2013**, *4*, 2858–2864.
- [69] (a) Deng, H.; Grunder, S.; Cordova, K. E.; Valente, C.; Furukawa, H.; Hmadeh, M.; Gándara, F.; Whalley, A. C.; Liu, Z.; Asahina, S.; Kazumori, H.; O’Keeffe, M.; Terasaki, O.; Stoddart, J. F.; Yaghi, O. M. *Science* **2012**, *336*, 1018–1023. (b) Grunder, S.; Valente, C.; Whalley, A. C.; Sampath, S.; Portmann, J.; Botros, Y. Y.; Stoddart, J. F. *Chem. Eur. J.* **2012**, *18*, 15632–15649.
- [70] (a) Kong, X.; Deng, H.; Yan, F.; Kim, J.; Swisher, J. A.; Smit, B.; Yaghi, O. M.; Reimer, J. A. *Science* **2014**, *341*, 882–885. (b) Deng, H.; Doonan, C. J.; Furukawa, H.; Ferreira, R. B.; Towne, J.; Knobler, C. B.; Wang, B.; Yaghi, O. M. *Science* **2010**, *327*, 846–850.
- [71] Feng, X.; Ding, X.; Jiang, D. *Chem. Soc. Rev.* **2012**, *41*, 6010–6022.
- [72] Jin, Y.; Wang, Q.; Taynton, P.; Zhang, W. *Acc. Chem. Res.* **2014**, *47*, 1575–1586.
- [73] (a) Jin, Y.; Yu, C.; Denman, R. J.; Zhang, W. *Chem. Soc. Rev.* **2013**, *42*, 6634–6654. (b) Ji, Q.; Lirag, R. C.; Miljanić, O. Š. *Chem. Soc. Rev.* **2014**, *43*, 1873–1884.
- [74] Côté, A. P.; Benin, A. I.; Ockwig, N. W. Matzger, A. J.; O’Keeffe, M.; Yaghi, O. M. *Science* **2005**, *310*, 1166–1170.
- [75] Spitler, E. L.; Dichtel, W. R. *Nat. Chem.* **2010**, *2*, 672–677.

- [76] Uribe-Romo, F. J.; Hunt, J. R.; Furukawa, H.; Klock, C.; O'Keeffe, M.; Yaghi, O. M. *J. Am. Chem. Soc.* **2009**, *131*, 4570–4571.
- [77] Uribe-Romo, F. J.; Doonan C. J.; Furukawa, H.; Oisaki, K.; Yaghi, O. M. *J. Am. Chem. Soc.* **2011**, *133*, 11478–11481.
- [78] Kuhn, P.; Antonietti, M.; Thomas, A. *Angew. Chem., Int. Ed.* **2008**, *47*, 3450–3453.
- [79] Beaudoin, D.; Maris, T.; Wuest, J. D. *Nat. Chem.* **2013**, *5*, 830–834.
- [80] Zhang, Y.-B.; Su, J.; Furukawa, H.; Yun, Y.; Gandara, F.; Duong, A.; Zou, X.; Yaghi, O. M. *J. Am. Chem. Soc.* **2013**, *135*, 16336–16339.
- [81] Campbell, N. L.; Clowes, R.; Ritchie, L. K.; Cooper, A. I. *Chem. Mater.* **2009**, *21*, 204–206.
- [82] Zwaneveld, N. A. A.; Pawlak, R.; Abel, M.; Catalin, D.; Gigmes, D.; Bertin, D.; Porte, L. *J. Am. Chem. Soc.* **2008**, *130*, 6678–6679.
- [83] Colson, J. W.; Woll, A. R.; Mukherjee, A.; Levendorf, M. P.; Spitler, E. L.; Shields, V. B.; Spencer, M. G.; Park, J.; Dichtel, W. R. *Science* **2011**, *332*, 228–231.
- [84] Nagai, A.; Guo, Z.; Feng, X.; Jin, S.; Chen, X.; Ding, X.; Jiang, D. *Nat. Commun.* **2011**, *2*, 536–543.
- [85] Kandambeth, S.; Mallick, A.; Lukose, B.; Mane, M. V.; Heine, T.; Banerjee, R. *J. Am. Chem. Soc.* **2012**, *134*, 19524–19527.

- [86] El-Kaderi, H. M.; Hunt, J. R.; Mendoza-Cortés, J. L.; Côté, A. P.; Taylor, R. E.; O'Keeffe, M.; Yaghi, O. M. *Science* **2007**, *316*, 268–272.
- [87] Ding, S. Y.; Gao, J.; Wang, Q.; Zhang, Y.; Song, W. G.; Su, C. Y.; Wang, W. J. *Am. Chem. Soc.* **2011**, *133*, 19816–19822.
- [88] Wan, S.; Guo, J.; Kim, J.; Ihee, H.; Jiang, D. *Angew. Chem., Int. Ed.* **2008**, *47*, 8826–8830.
- [89] Ding, X.; Chen, L.; Honsho, Y.; Feng, X.; Saengsawang, O.; Guo, J.; Saeki, A.; Seki, S.; Irle, S.; Ngase, S.; Parasuk, V.; Jiang, D. *J. Am. Chem. Soc.* **2011**, *133*, 14510–14513.
- [90] Holst, J. R.; Trewin, A.; Cooper, A. I. *Nat. Chem.* **2010**, *2*, 915–920.
- [91] Atwood, J. L.; Barbour, L. J.; Jerga, A. *Science* **2002**, *296*, 2367–2369.
- [92] Tozawa, T.; Jones, J. T. A.; Swamy, S. I.; Jiang, S.; Adams, D. J.; Shakespeare, S.; Clowes, R.; Bradshaw, D.; Hasell, T.; Chong, S. Y.; Tang, C.; Thompson, S.; Parker, J.; Trewin, A.; Bacsá, J.; Slawin, A. M. Z.; Steiner, A.; Cooper, A. I. *Nat. Mater.* **2009**, *8*, 973–978.
- [93] Mitra, T.; Jelfs, K. E.; Schmidtman, M.; Ahmed, A.; Chong, S. Y.; Adams, D. J.; Cooper, A. I. *Nat. Chem.* **2013**, *5*, 276–281.
- [94] Zhang, G.; Presly, O.; White, F.; Oppel, I. M.; Mastalerz, M. *Angew. Chem., Int. Ed.* **2014**, *53*, 1516–1520.

- [95] Tian, J.; Thallapally, P. K.; McGrail, B. P. *CrystEngComm* **2012**, *14*, 1909–1919.
- [96] Sozzani, P.; Bracco, S.; Comotti, A.; Ferretti, L.; Simonutti, R. *Angew. Chem., Int. Ed.* **2005**, *44*, 1816–1820.
- [97] Msayib, K. J.; Book, D.; Budd, P. M.; Chaukura, N.; Harris, K. D. M.; Helliwell, M.; Tedds, S.; Walton, A.; Warren, J. E.; Xu, M.; McKeown, N. B. *Angew. Chem., Int. Ed.* **2009**, *48*, 3273–3277.
- [98] Luo, X.-Z.; Jia, X.-J.; Deng, J.-H.; Zhong, J.-L.; Liu, H.-J.; Wang, K.-J.; Zhong, D.-C. *J. Am. Chem. Soc.* **2013**, *135*, 11684–11687.
- [99] Mastalerz, M.; Oppel, I. M. *Angew. Chem., Int. Ed.* **2012**, *51*, 5252–5255.

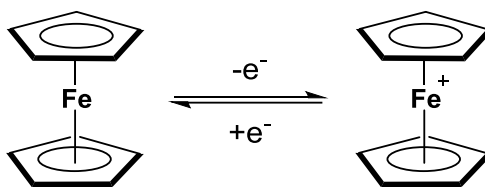
Chapter Two

Synthesis and Characterization of Ferrocene-based Boroxine Cyclophane

2.1 Introduction

Since the discovery of ferrocene in 1951 by Kealy and Pauson,¹ its organometallic chemistry had been exhaustively studied. After more than 60 years, ferrocene still plays an important role in catalysis, electrochemistry, polymer chemistry, bioorganometallic chemistry, and materials chemistry.² Ferrocene is a stable neutral molecule which can be readily oxidized to ferrocenium cation under either chemical or electrochemical conditions (Scheme 2.1). The well-developed synthetic chemistry of ferrocene and its accessible ferrocene/ferrocenium redox chemistry have led to its use in electrochemically active sensors³ for cationic, anionic, ion-paired, or neutral guests. The effect of

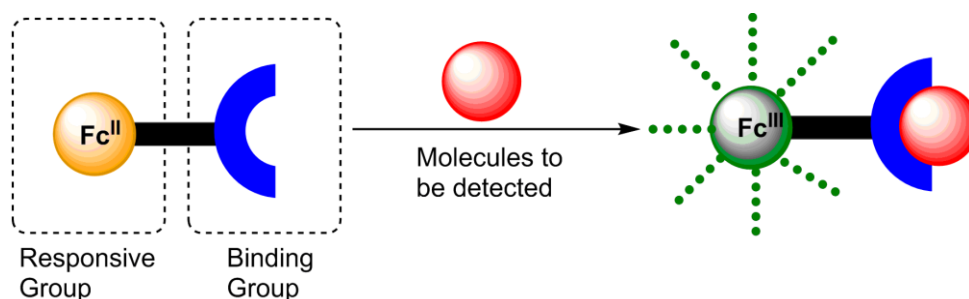
Scheme 2.1 Reduced (Left) and Oxidized (Right) States of Ferrocene



complexed guest is important, in that ionic guests induce a positive (cations) or negative (anions) potential shift in the oxidation potential of the ferrocene/ferrocenium couple (Scheme 2.2). Ferrocene receptors have been incorporated into nanoscale structures such as dendrimers, nanoparticles, thin film polymers, and self-assembled monolayers.²

The work described in this chapter has been previously published: Chen, T.-H.; Kaveevivitchai, W.; Bui, N.; Miljanić, O. Š. *Chem. Commun.* **2012**, 48, 2855–2857.

Scheme 2.2 One of the Electrochemical Recognition Binding Modes of Ferrocene (Fc)



Owing to the modular and porous character of MOFs and COFs, a new solid-state sensing mechanism of ferrocene via adsorbing or trapping the target molecules inside the cavities of such porous materials should be possible. The hybrid nature of MOFs, which includes both an organic ligand and a metal ion within a porous structure, enables a wide range of applications as sensors. Nevertheless, most of such proposed sensing behaviors are based on luminescence properties, and we reasoned that electrochemical sensors would potentially represent a largely complementary class. Because of its desirable properties, incorporation of ferrocene into porous materials is the subject of much interest. However, the incorporation of ferrocene into ordered solid-state porous materials is still a challenge. The free rotation of the two cyclopentadiene rings complicates the conformational profile of ferrocene derivatives, as building struts for porous materials typically have to be rigid.⁴

The redox properties of a series of coordination polymers based on ferrocenecarboxylic acid and zinc have been studied by Fan and co-workers.⁵ In order to obtain infinite porous network, polydentate ligands are necessary. The direct route—synthesis of extended structures based on ferrocene coordination polymers was

presumably first attempted by Chae and co-workers, who used 1,1'-ferrocenedicarboxylic acid as a building block to coordinate to Zn and Cu centers. Unfortunately, the two carboxylic acid groups were oriented convergently, forming clusters (Figure 2.1A).⁶ Instead of directly using ferrocene derivatives as building blocks, postsynthetic introduction was also attempted. Fischer and co-workers turned the MOF MIL-53(Al) (composed of Al and 1,4-benzenedicarboxylate) redox-active by functionalization of the bridging OH-group with 1,1'-ferrocene-dimethylsilane (Figure 2.1B).⁷ Marken and co-

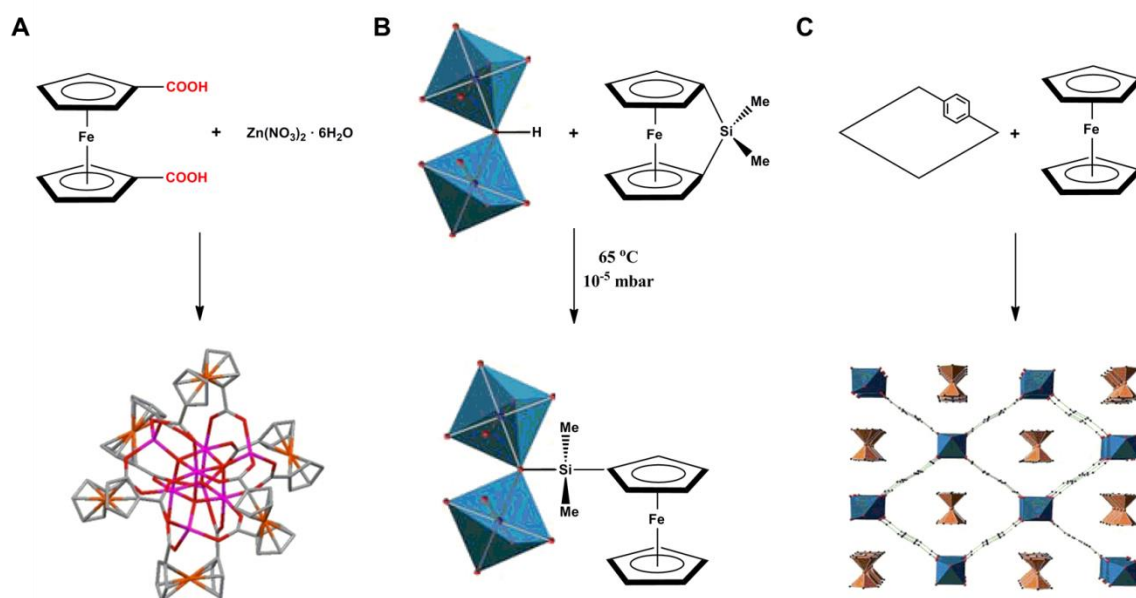


Figure 2.1 (A) Synthesis and the crystal structure of 1,1'-ferrocenedicarboxylate-zinc cluster (C, gray; O, red; Fe, orange; Zn, purple).⁶ (B) Ring-opening reaction of 1,1'-ferrocene-dimethylsilane with the bridging OH-group between two AlO_6 octahedra of MIL-53(Al) (O, red; Al, blue).⁷ (C) Incorporation of ferrocene into the channel of MIL-53(Al). Ferrocene guest molecules aligned along the channel of MIL-53(Al) network with the Fe–Cp centroid vectors aligned parallel in the *c*-direction.⁸

workers introduced ferrocenyl groups into MOFs by using amine-to-amide transformation.⁸ Organometallic host-guest chemistry of porous MOFs and COFs was furthered by Fischer and co-workers through the introduction of volatile ferrocene derivatives into MOF cavities using a solvent-free gas phase filtration method (Figure 2.1C).⁹ This method ensures full and homogeneous loading of the framework with organometallic molecules by avoiding any competition with solvent molecules typically used in liquid impregnation methods. Notably, all examples mentioned above have ferrocene occupy their cavities—thus leaving insufficient space for additional and possibly larger guests—meaning that their potential usefulness in sensing would be unlikely. To circumvent the problem, incorporating ferrocene into building struts, instead of inside the pores, of a porous framework was the primary goal of this project.

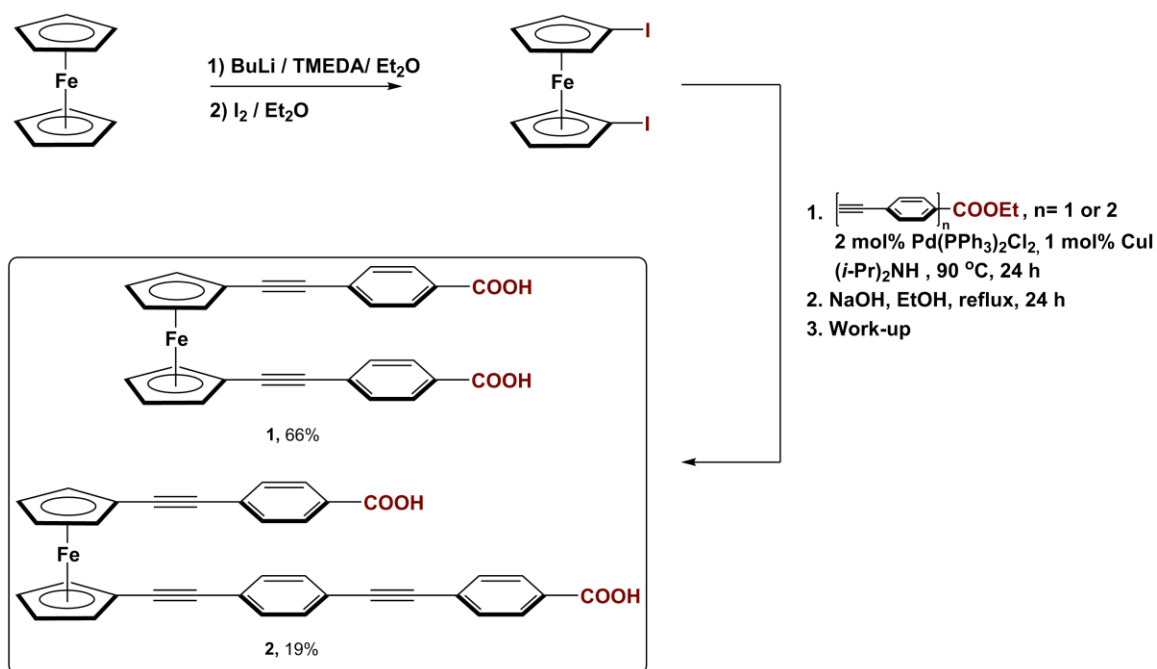
This chapter describes our attempts to prepare both ferrocene-based MOFs and COFs. As a part of our efforts toward ferrocene-based MOFs, we have synthesized extended ferrocene dicarboxylic acids as building struts but were unfortunately not able to incorporate them into crystalline materials. Our work on ferrocene-based COFs resulted, perhaps unexpectedly, in a novel discrete ferrocene-bridged boroxine cyclophane,¹⁰ which is the first crystallographically characterized example of a boroxine cyclophane.

2.2 Results and Discussion

2.2.1 Syntheses of Ferrocene-based MOF Precursors

The synthesis of extended ferrocene-containing carboxylic acids utilized Sonogashira coupling¹¹ of terminal alkynes and aryl iodides as the key reaction step. Lithiation and subsequent iodination of ferrocene produced 1,1'-diiodoferrocene, as described in the literature.¹² Then, Sonogashira reaction was used to couple this building block with the independently synthesized rigid linkers: ethyl-4-ethynylbenzoate or ethyl-4-[2-(4-ethynylphenyl)ethynyl]benzoate.¹³ Final hydrolysis afforded orange powders of carboxylic acids **1** and **2** with 66% and 19% yield, respectively (Scheme 2.3). Growing single crystals and determining their crystal structures are essential to obtaining structural characterization of MOFs. Based on the archetype structure of MOF-5, we chose zinc as the metal source to be tried first. The trials of synthesizing ferrocene-containing MOFs were started under solvothermal conditions. On account of their low solubility, acids **1** and **2** were suspended in mixtures of DMF, DEF, DMA, DMSO, EtOH, MeOH, or H₂O with various ratios and concentrations, and then heated in isothermal ovens with temperature settings ranging from 60 to 120 °C. However, both linkers were readily decomposed at high temperatures, limiting options in terms of solvothermal synthesis. We also tried to coordinate **1** and **2** to metals under hydrothermal conditions (in Teflon-lined autoclave vessels), and using slow vapor diffusion and biphasic diffusion of bases to deprotonate the acids for slowly crystallization. All of these reactions resulted in amorphous precipitates. The situation did not change when other metal ions (Mg²⁺, Al³⁺, Cd²⁺, Fe³⁺, Co²⁺, Ni²⁺, and Cu²⁺) were used.

Scheme 2.3 Syntheses of Compounds 1 and 2



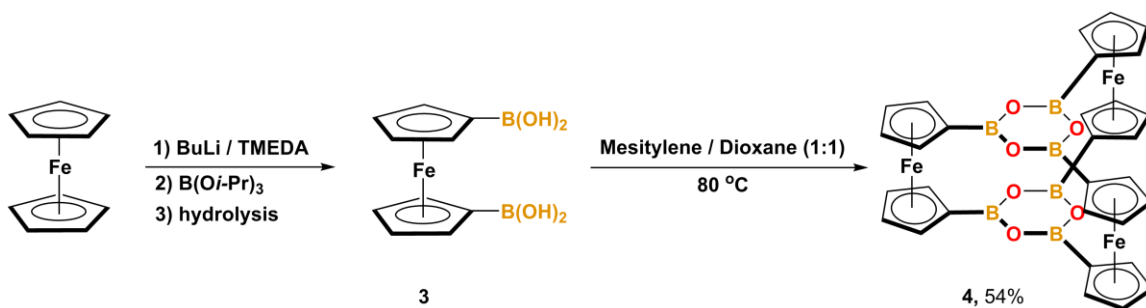
2.2.2 Synthesis of Triply Ferrocene-bridged Boroxine Cyclophane

Dynamic covalent functionalities are versatile groups in the construction of organic extended architectures due to their reversible nature, which facilitates self-assembly and self-correction. In recent years, the chemistry of six-membered boroxine rings (R₃B₃O₃)¹⁴ has undergone a period of renaissance stimulated by their use as precursors to COFs¹⁵ and high-performance polymer electrolytes,¹⁶ and as partners in cross-coupling reactions.¹⁷ The boronic acid-based reversible interaction system has been applied to various fields such as self-assembly, sensing, and separation science.¹⁸ Boroxines are also of interest in the studies of aromaticity,¹⁹ especially when contrasted with their more aromatic borazine and benzene analogs. Combinations of boronic acid

building blocks and ferrocene derivatives appear like a promising way for the preparation of new ferrocene-based materials.

Boronic acid is one of the well-known dynamic covalent functionality that favors the reversible thermodynamically controlled self-assembly and self-correction. Recent work on the synthesis of COFs provided experimental guidance for our synthesis of ferrocene–boroxine cluster **4**.²⁰ 1,1'-Ferrocenediboronic acid was thus synthesized through the lithation and borylation of ferrocene, following by hydrolysis.²¹ In an attempt to convert **3** into a COF, solvothermal dehydration conditions were used. A suspension of 1,1'-ferrocenediboronic acid **3** in a 1 : 1 mixture of mesitylene and dioxane was heated at 80 °C and yielded bright orange crystals within 24 h (Scheme 2.4 and Figure 2.2). These crystals were filtered, soaked in EtOH to remove unreacted starting material, and then washed with hot EtOH and *N,N*-dimethylformamide (DMF). After drying in vacuo at 150 °C, crystals of pure **4** were obtained in 54% yield.

Scheme 2.4 Syntheses of 1,1'-Ferrocenediboronic Acid **3** and Triply Ferrocene-bridged Boroxine Cyclophane **4**



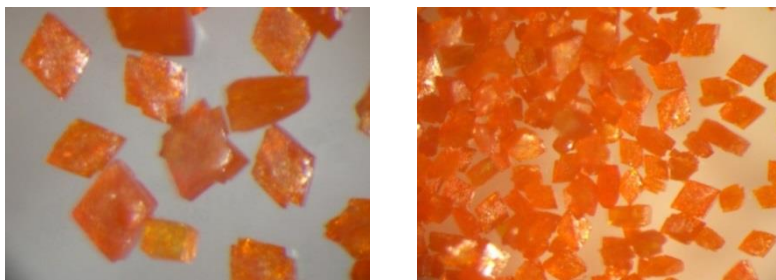


Figure 2.2 Photographs of crystals of compound **4**.

Compound **4** is insoluble in virtually all organic solvents, including ionic liquids. Its infrared spectrum reveals B–O bands at 1386 and 1353 cm^{-1} , indicative of the presence of boroxine, and no BO–H bands around 3300 cm^{-1} , suggesting that complete dehydration of **3** has occurred. A ^1H NMR spectrum (CDCl_3 , 25 $^\circ\text{C}$) shows two multiplets, as expected for 1,1'-disubstituted ferrocenes, at 4.52 and 4.66 ppm. Low solubility of **4** precluded us from obtaining a meaningful ^{13}C NMR spectrum. Boroxine cyclophane **4** is thermally highly robust, but hydrolytically very fragile. Its crystals do not melt or decompose until 300 $^\circ\text{C}$, and TGA (Figure 2.3) shows no mass loss until 463 $^\circ\text{C}$ —when a 95.2% mass loss occurs, presumably on account of the sublimation of **4** (orange residue could be observed in the venting tubing of TGA instrument). In contrast, hydrolysis occurs within minutes in water or wet solvents; the initial hydrolysis product is **3**, which is subsequently deborylated to pure ferrocene.²²

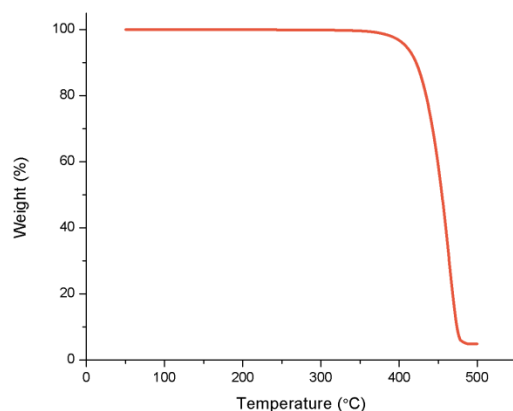


Figure 2.3 Thermogravimetric analysis of compound **4**.

2.2.3 Crystal Structure Analysis of Compound **4**

The conditions used in the synthesis of **4** reproducibly yield orange block-shaped single crystals suitable for X-ray diffraction. Compound **4** crystallizes in space group *C2*, with 16 molecules per unit cell. The crystal structure of **4** reveals the remarkably symmetric and highly rigid trigonal prism shown in Figure 2.4A (only one of the four crystallographically independent molecules is represented). The side view (Figure 2.4B) reveals an almost co-planar arrangement of all atoms in the two $\text{Cp}_3\text{B}_3\text{O}_3$ ligands ($\text{Cp} = \eta^5\text{-cyclopentadienyl}$), with slight bowing of the boroxine rings inward. Trigonal geometry of this molecule is best seen in the top view (Figure 2.4C): three Fe atoms define a virtually equilateral triangle, with Fe–Fe bond lengths averaging $7.12 (\pm 0.15) \text{ \AA}$ and Fe–Fe–Fe angles in the $58.0\text{--}61.3^\circ$ range. Despite the highly rigidified cyclophane structure of **4**, its boroxine and ferrocene elements minimally influence each other. All B–O bonds are between 1.36 and 1.39 \AA in length, falling well within the $1.29\text{--}1.47 \text{ \AA}$ range for all boroxine B–O bonds reported in the Cambridge Structural Database. Ferrocene units are

desymmetrized, but still largely undisturbed—all C–C bond lengths in all ferrocene nuclei fall within the narrow 1.39–1.45 Å window, close to parent ferrocene’s C–C bond lengths of 1.40 Å. Its two $\text{Cp}_3\text{B}_3\text{O}_3$ planes also represent an interesting and reversibly assembled ligand scaffold—particularly in light of the absence of a benzene analog. This boroxine-based cyclophane provided inspiration for the direction for future work: expansion of these results to other larger covalent organic polyhedra (COP).

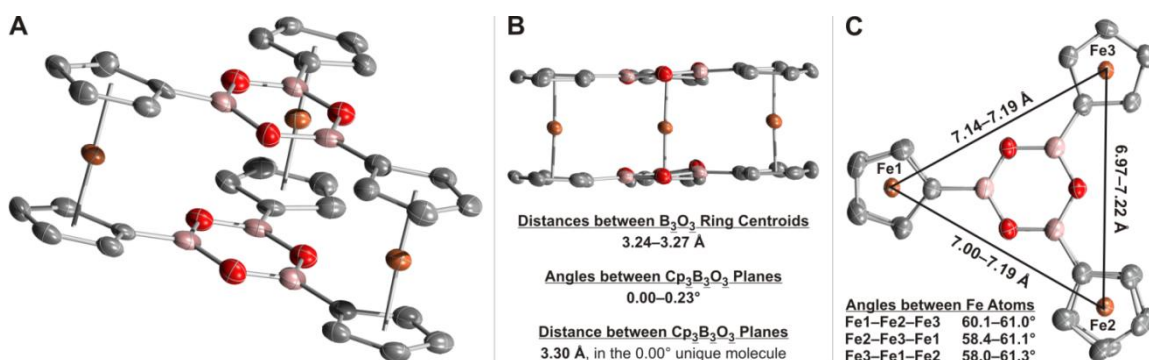


Figure 2.4 Crystal structure of ferrocene–boroxine cyclophane **4**—perspective view (A), side view (B), and top view (C). Selected structural features are highlighted. Hydrogen atoms are omitted for clarity and thermal ellipsoids are shown at 50% probability.

An analysis of the supramolecular organization of **4** within the crystal is presented in Figure 2.5. The asymmetric unit contains four molecules of **4**, organized in two pairs of molecules in a parallel orientation. Within each pair, two molecules of **4** are offset but very close to each other, with average distances between the adjacent $\text{Cp}_3\text{B}_3\text{O}_3$ planes of 2.97 and 3.11 Å. The offset arrangement allows a close packing fit of one pair with the other, perpendicularly oriented, pair. Two other short contacts are noteworthy: one α -hydrogen atom on one of the Cp rings of **4** establishes a $[\text{C}–\text{H}\cdots\text{O}]$ interaction (2.57 Å)²³

with an oxygen atom in the neighboring molecule's boroxine ring. In addition, one of the β -hydrogen atoms on one of the Cp rings engages in a $[\text{C}-\text{H}\cdots\pi]$ interaction with another Cp ring, characterized by a $\text{H}\cdots\text{Cp}$ (centroid) distance of 2.37 Å.

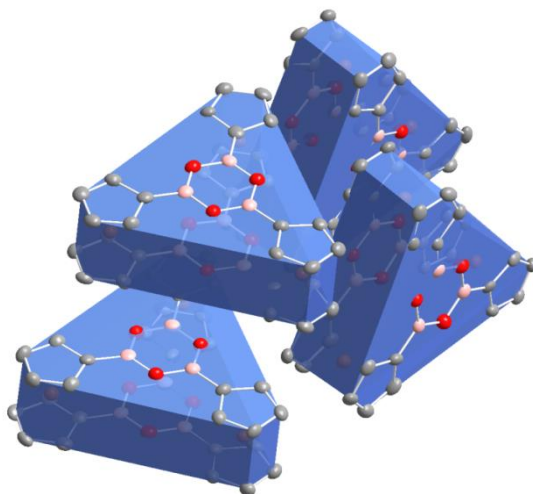


Figure 2.5 Asymmetric unit in the crystal structure of **4**. Hydrogen atoms omitted for clarity.

2.2.4 Testing of Compound **4** as an Anion Receptor

Boron is an electron deficient element which can be datively bonded by nitrogen, oxygen, and anions such as fluoride, chloride, and cyanide.²⁴ It is perhaps surprising that there are no examples of boroxine cyclophanes²⁵ reported in the literature—especially since such species have been suggested as superb receptors for halide anions.²⁶ Anion receptors combining redox-active ferrocene responder unit and boronic acid was previously reported by Shinkai and co-workers.²⁴ Fluorinated boron or boroxine-based anion receptors were reported and applied in lithium ion battery research.²⁷ Thus, the novel ferrocene-boroxine compound **4** has the potential to act as an anion receptor as well.

Experiments were carried out by stirring and heating the mixture of compound **4**, 18-crown-6, and KF or KCl in various solvents. However, in all cases, the rigid "box" structure was decomposed due to the destruction of the flat boroxine ring by strong anion-boron interaction which forms boronate anions.

2.2.5 Solid-state Cyclic Voltammetry of Compound **4**

Despite extensive experimentation, the low solubility of **4** precluded solution-phase cyclic voltammetry (CV) studies aimed at elucidating the level of electronic communication of ferrocene nuclei across the boroxine rings. Solid-state CV measurements, with the aid from Watchareeya Kaveevivitchai in Prof. Jacobson's group, revealed irreversible oxidation (Figure 2.6), with three distinct steps at 3.05, 3.30, and 3.50 V (relative to the Li/Li⁺ pair).²⁸ This result is consistent with previous solution-phase studies on tris(ferrocenyl)boroxines,²⁹ which also show three well-resolved oxidation peaks.

Theoretically, the three ferrocenyl groups in compound **4** are equivalent; therefore, oxidation of any of them in the neutral structure would occur at the same redox potential to produce a monocationic species. However, the removal of a second electron from another ferrocenyl group requires more energy than the first because of electrostatic repulsion³⁰ (the relatively short distance between these groups of about 7 Å allows significant through-space electrostatic interaction). As a result, the potential of oxidation of the second ferrocenyl group is more positive than the first, resulting in the splitting of

the CV waves into three distinct oxidation peaks from three corresponding ferrocenyl groups.

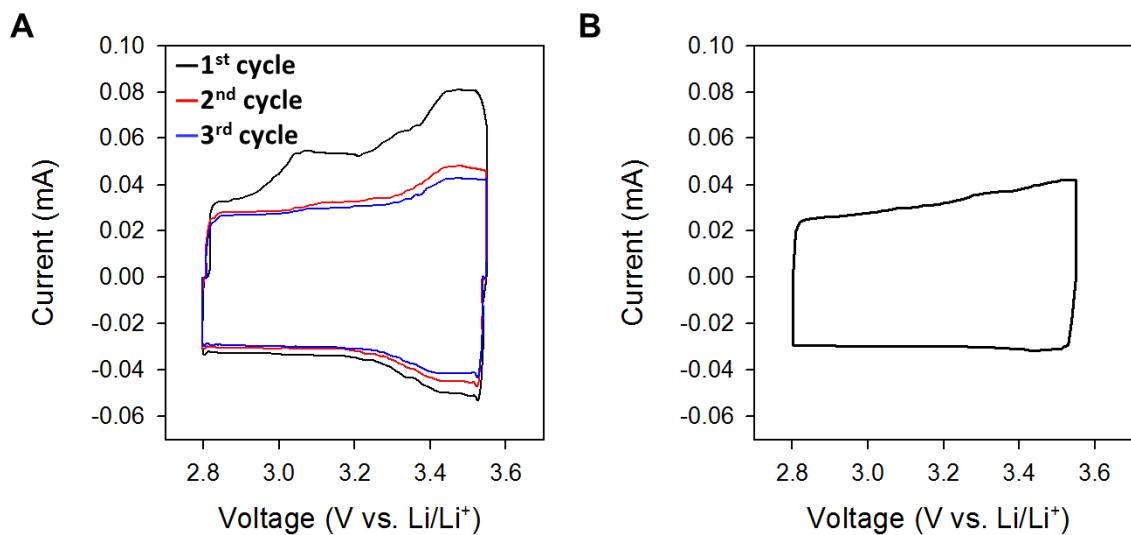


Figure 2.6 Solid-state cyclic voltammograms of (A) compound **4** (with polymer binder and carbon), and (B) a blank electrode (polymer binder and carbon only).

Oxidation of a ferrocenyl species requires an additional counteranion (PF_6^-) from the electrolyte to maintain the electroneutrality of the structure. The appearance of the CV waves therefore also depends on the strength of ion pairing between the ferrocenium cation and the electrolyte anion. The insertion of the bulky PF_6^- into such a rigid structure of the ferrocene boroxine box might be responsible for the irreversible electrochemical properties of compound **4**.

2.3 Conclusions and Outlook

In conclusion, we have prepared a trigonal prismatic ferrocene–boroxine ”box” by parallel positioning of two boroxine planes using 1,1'-substituted ferrocene as the scaffold. While the poor solubility of this structure precluded extensive solution-state characterization, **4** has a unique important structure which warrants further study. Synthesis of its (presumably) more soluble alkyl derivatives would allow detailed solution-phase electrochemistry studies. Greater solubility of derivatives of **4** would also permit investigations of the reversibility of cyclophane’s formation in the context of dynamic covalent chemistry,³¹ and possible desymmetrization via the formation of heteroboroxines.³²

No discernible cavity is present in the center of cyclophane **4**, and hence guest encapsulation proved impossible. Nevertheless, this cyclophane’s rigid trigonal prismatic structure and Lewis acidic character suggest that larger derivatives of **4** could present a uniquely preorganized platform for anion encapsulation.²⁶ This proposition could be tested by elongating **4** via the replacement of the 1,1'-disubstituted ferrocene linker with e.g. a 1,8-disubstituted anthracene connector.

Considered even more broadly, compound **4** is the minimal boroxine-based polyhedron and a progenitor of a broader class of reversibly assembled polyhedral structures in which the boroxine ring plays a role of the threefold symmetric connector.³³ Changing the angle between the boronic acid moieties could expand the scope of this self-assembly protocol to other polyhedra with trigonal symmetry—including tetrahedral

(4 boroxines), octahedra and truncated cubes (8 boroxines) or icosahedra (20 boroxines). These covalent organic polyhedral (COPs)³⁴ would conceptually relate to COFs in the same way as previously reported metal organic polyhedra (MOPs)³⁵ relate to MOFs. COPs could be useful both as reversibly formed molecular containers, and as synthons in the preparation of topologically sophisticated functional COFs.

2.4 Experimental Section

2.4.1 General Methods

All reactions were performed under nitrogen atmosphere in oven-dried glassware. Reagents were purchased from commercial suppliers and used without further purification. Solvents were used as received, except diethyl ether (Et₂O), which was dried over activated alumina in an mBraun solvent purification system.

NMR spectra were obtained on JEOL ECX-400 and ECA-500 spectrometers, with working frequencies (for ¹H and ¹³C nuclei) of 400 and 500 MHz, respectively. ¹H and ¹³C NMR chemical shifts are reported in ppm units relative to the residual signals of the solvents (¹H: CDCl₃, 7.26 ppm and DMSO-*d*₆, 2.50 ppm; ¹³C: DMSO-*d*₆, 39.5 ppm). ¹¹B NMR shifts are given relative to external BF₃·Et₂O standard. All NMR spectra were recorded at 25 °C. Infrared spectra were recorded on a Perkin-Elmer Spectrum 100 FT-IR spectrophotometer using Pike MIRacle Micrometer pressure clamp. UV-Vis spectra were recorded on a Perkin-Elmer Lambda 25 UV-Vis spectrophotometer. Microanalyses were

conducted by Intertek USA, Inc. TGA was carried out on a TA Instruments Hi-Res TGA 2950 thermogravimetric analyzer.

2.4.2 Syntheses of Compound 1–4

Synthesis of Compound 1

A mixture of 1,1'-diiodoferrocene¹¹ (4.00 g, 9.10 mmol), ethyl-4-ethynylbenzoate¹² (4.08 g, 22.8 mmol), PdCl₂(PPh₃)₂ (0.25 g, 0.36 mmol), CuI (0.034 g, 0.18 mmol), and degassed (*i*-Pr)₂NH (75 mL) were combined in a 250 mL Schlenk flask and heated at reflux at 90 °C for overnight. After cooling, solvents were removed under reduced pressure and the crude solid was purified by column chromatography, eluting with a hexane/ethyl acetate (9:1) mixture to collect the product. After removal of the solvent, orange-red solid (3.15 g, 6.00 mmol, 66%) was obtained. The red solid (1.50 g, 2.80 mmol) was mixed with NaOH (0.28 g, 7.1 mmol) in 100 mL EtOH and kept at reflux overnight. After cooling, the mixture was dissolved by adding water and washed with dichloromethane. The aqueous layer was collected and acidified until pH 2 by adding CF₃COOH. The suspension was filtered and washed with ethanol. After removal of solvent under reduced pressure, orange-red solid (1.34 g, 5.90 mmol, 98%) was obtained. IR: 2982 (b, $\tilde{\nu}_{\text{COO-H}}$), 2200 (m, $\tilde{\nu}_{\text{C}\equiv\text{C}}$), 1683 (s, $\tilde{\nu}_{\text{C=O}}$), 1602 (s, $\tilde{\nu}_{\text{C=C}}$), 1420 (s, $\tilde{\nu}_{\text{C=C}}$), 1279 (s, $\tilde{\nu}_{\text{C-C}}$) cm⁻¹. ¹H NMR (DMSO-*d*₆): δ 4.47 (m, 4H, C_{ferrocene}-H), 4.69 (m, 4H, C_{ferrocene}-H), 7.39 (d, *J*=8.1 Hz, 4H, C=CH), 7.76 (d, *J*=8.1 Hz, 4H, C=CH) ppm, 13.08 (s, 2H, COOH) ppm. ¹³C NMR (DMSO-*d*₆): δ 166.63, 130.95, 129.64, 129.29,

127.19, 90.19, 86.25, 72.76, 71.05, 66.23 ppm. HRMS (ESI⁻ mode): Calculated for FeC₂₈H₁₈O₄: 473.98. Found: 473.07.

Synthesis of Compound 2

A mixture of 1,1'-diiodoferrocene¹¹ (0.79 g, 1.8 mmol), ethyl-4-[2-(4-ethynylphenyl)ethynyl]benzoate¹² (1.23 g, 4.50 mmol), PdCl₂(PPh₃)₂ (0.05 g, 0.07 mmol), CuI (0.01 g, 0.04 mmol), and degassed (*i*-Pr)₂NH (30 mL) was placed into a 100 mL Schlenk flask and kept at reflux (90 °C) overnight. After cooling, solvents were removed under reduced pressure and the crude solid was purified by column chromatography, eluting with a hexane/ethyl acetate (9:1) mixture to collect the product. After removal of the solvent, the monosubstituted iodoferrocene compound was obtained as an orange-red solid (0.42 g, 0.72 mmol, 23%). A mixture of this red solid (0.42 g, 0.72 mmol), ethyl-4-ethynylbenzoate¹² (0.19 g, 1.1 mmol), PdCl₂(PPh₃)₂ (0.01 g, 0.01 mmol), CuI (0.01 g, 0.01 mmol), and degassed (*i*-Pr)₂NH (30 mL) was placed in a 100 mL Schlenk flask and kept at reflux (90 °C) overnight. Red solid precipitated out and was collected by filtration and washed with water, and orange-red solid (0.38 g, 0.60 mmol, 84%) was obtained. The red solid (0.20 g, 0.32 mmol) was mixed with NaOH (0.03 g, 0.8 mmol) in 10 mL EtOH and kept at reflux overnight. After cooling, the mixture was dissolved by adding water and washed with dichloromethane. The aqueous layer was collected and acidified until pH 2 by adding CF₃COOH. The suspension was filtered and washed with EtOH. After removal of solvent under reduced pressure, orange-red solid (0.18 g, 0.31 mmol, 97%) was obtained. IR: 2850 (b, $\tilde{\nu}_{\text{COO-H}}$), 2203 (m, $\tilde{\nu}_{\text{C}\equiv\text{C}}$), 1682 (s, $\tilde{\nu}_{\text{C=O}}$), 1605 (s, $\tilde{\nu}_{\text{C=C}}$), 1424 (s, $\tilde{\nu}_{\text{C=C}}$), 1281 (s, $\tilde{\nu}_{\text{C-C}}$) cm⁻¹. ¹H NMR (DMSO-*d*₆): δ 4.47 (m, 4H, C_{ferrocene}-H),

4.68 (m, 4H, C_{ferrocene}-H), 7.36 (d, 2H, $J=8.6$ Hz, C=CH), 7.39 (d, $J=8.1$ Hz, 2H, C=CH) ppm, 7.40 (d, $J=8.1$ Hz, 2H, C=CH), 7.68 (d, 2H, $J=8.6$ Hz, C=CH), 7.78 (d, $J=8.1$ Hz, 2H, C=CH), 7.96 (d, $J=8.6$ Hz, 2H, C=CH), 13.08 (s, 2H, COOH) ppm. HRMS (ESI⁻ mode): Calculated for FeC₃₆H₂₂O₄: 574.02. Found: 573.13.

Synthesis of Compound 3

A mixture of butyllithium (1.6 M solution in hexane, 37.5 mL, 60.0 mmol) and *N,N,N',N'*-tetramethyl-ethane-1,2-diamine (9.0 mL, 60 mmol) in Et₂O (50 mL) was added to a stirred solution of ferrocene (5.00 g, 26.9 mmol) in Et₂O (100 mL) in a 250 mL Schlenk flask. After overnight stirring at 20 °C, the suspension was added slowly via cannula to a 500 mL Schlenk flask which contained a stirred and cooled (−78 °C) solution of triisopropylborate (14.7 mL, 65.0 mmol) in Et₂O. The mixture was allowed to warm up to 20 °C over 1 h, and stirring was continued overnight. After hydrolysis with 10% aqueous KOH solution, the organic layer was extracted with H₂O. The combined aqueous layers were acidified with 10% H₂SO₄ in an ice bath and kept at 20 °C for 24 h. The precipitate was filtered and washed with water and Et₂O and air dried to yield pure **3** (2.50 g, 34%). IR: 3315 (s, $\tilde{\nu}_{\text{O-H}}$), 1469 (s, $\tilde{\nu}_{\text{C=C}}$), 1393 (s, $\tilde{\nu}_{\text{O-B}}$), 1334 (s, $\tilde{\nu}_{\text{O-B}}$), 1322 (s, $\tilde{\nu}_{\text{C-C}}$) cm^{−1}. ¹H NMR (DMSO-*d*₆): δ 4.17 (m, 4H, C_{ferrocene}-H), 4.34 (m, 4H, C_{ferrocene}-H), 7.48 (s, 4H, O-H) ppm. ¹³C NMR (DMSO-*d*₆): δ 64.81, 71.65, 73.66 ppm. ¹¹B NMR (DMSO-*d*₆): δ 29.07 ppm. Spectral data are identical to those previously reported in the literature.²¹

Synthesis of Compound 4

A 20 mL vial was charged with 1,1'-ferrocenediboronic acid (**3**, 30 mg, 0.11 mmol), mesitylene (5 mL), and 1,4-dioxane (5 mL). The resulting suspension was sonicated for 1 h at 20 °C, and was then placed into an oven at 80 °C for 1 d. Orange crystals were formed after this treatment. The supernatant was decanted and the crystals were soaked in EtOH to dissolve unreacted starting material and impurities. The resulting crystals were then filtered and washed with DMF and hot EtOH. After drying for 1 d in an 150 °C vacuum oven, 14.2 mg (54%) of single crystals of **4** was isolated. UV-Vis (CHCl₃): λ_{max} (log ϵ) = 448 (4.51) nm (lower limit of the extinction coefficient, on account of low solubility). IR: 1474 (s, $\tilde{\nu}_{\text{C}=\text{C}}$), 1386 (s, $\tilde{\nu}_{\text{O}-\text{B}}$), 1353 (s, $\tilde{\nu}_{\text{O}-\text{B}}$), 1322 (s, $\tilde{\nu}_{\text{C}-\text{C}}$) cm⁻¹. ¹H NMR (CDCl₃): δ 4.66 (m, 12H), 4.52 (m, 12H). ¹¹B NMR (CDCl₃): δ 28.81. Anal. calcd for C₃₀H₂₄Fe₃B₆O₆: C 50.50, H 3.37; Found: C 50.56, H 3.16.

2.4.3 ^1H and ^{13}C NMR Spectra of Compound 1–4³⁶

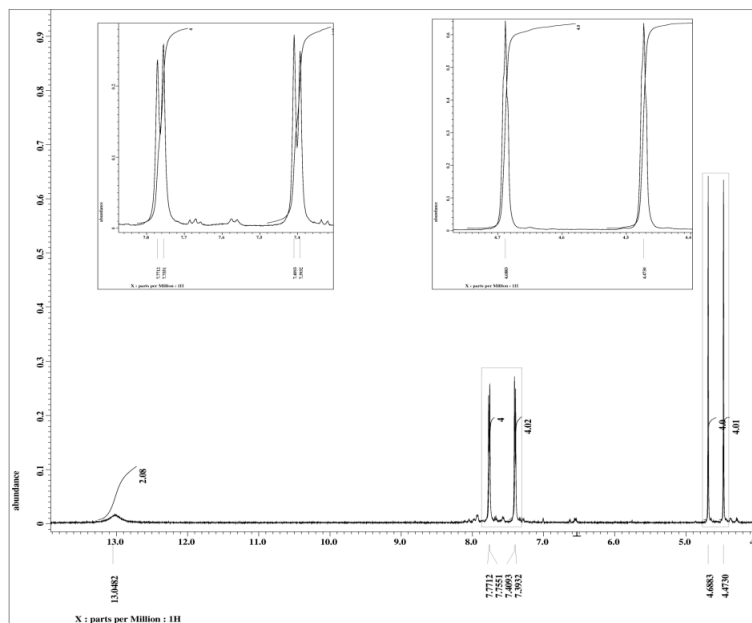


Figure 2.7 ^1H NMR spectrum of compound 1.

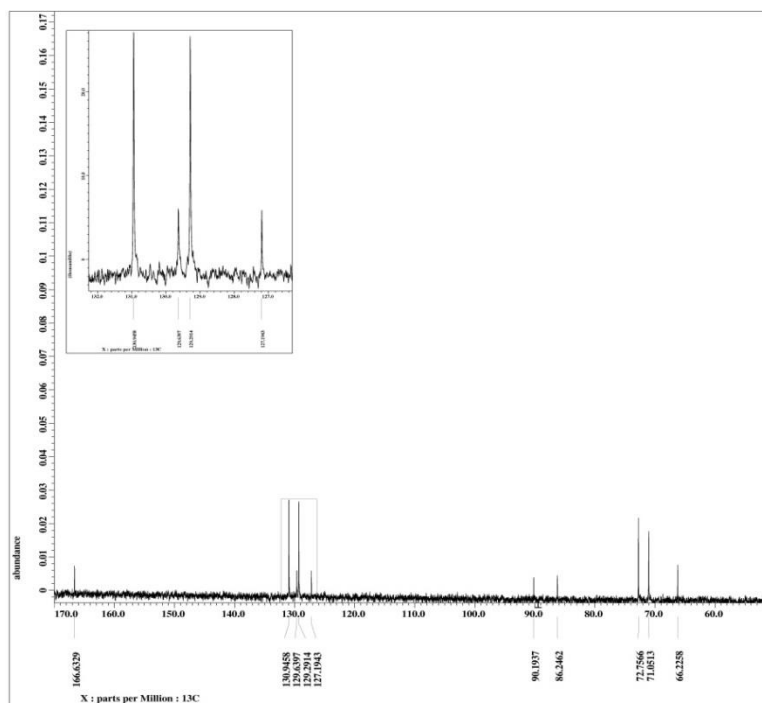


Figure 2.8 ^{13}C NMR spectrum of compound 1.

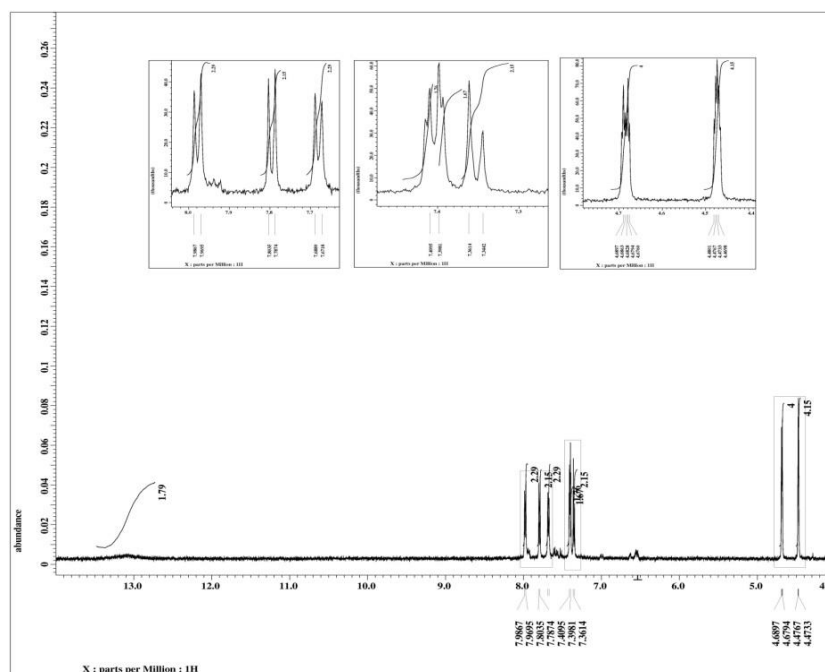


Figure 2.9 ^1H NMR spectrum of compound 2.

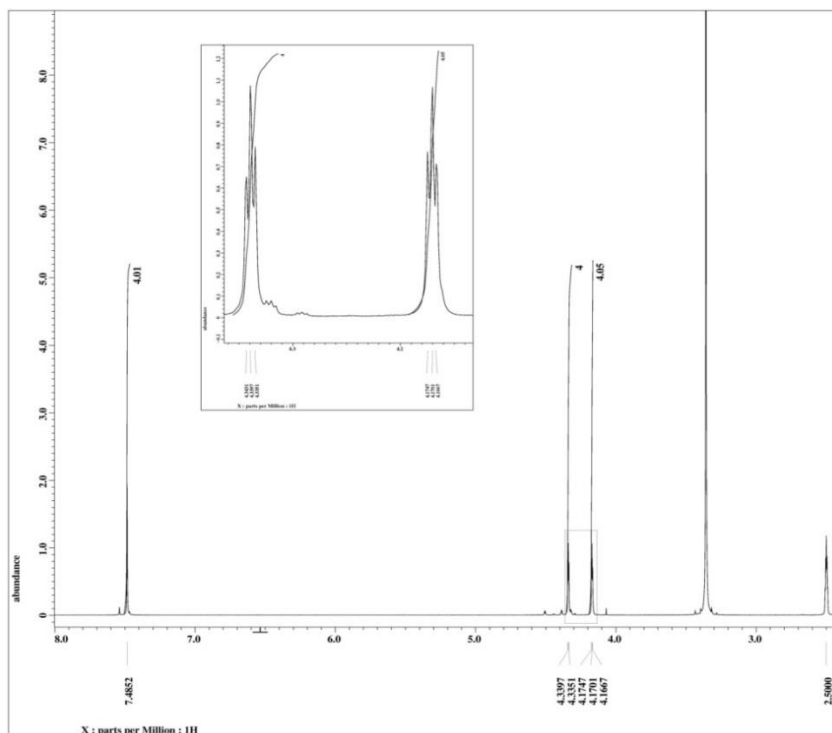


Figure 2.10 ^1H NMR spectrum of 1,1'-ferrocenediboronic acid 3.

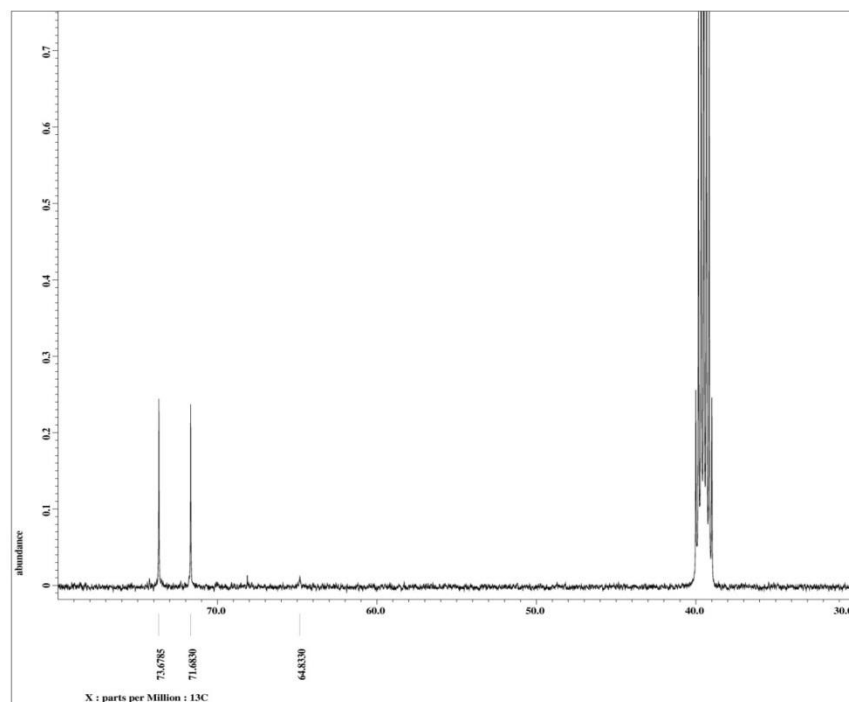


Figure 2.11 ^{13}C NMR spectrum of 1,1'-ferrocenediboronic acid **3**.

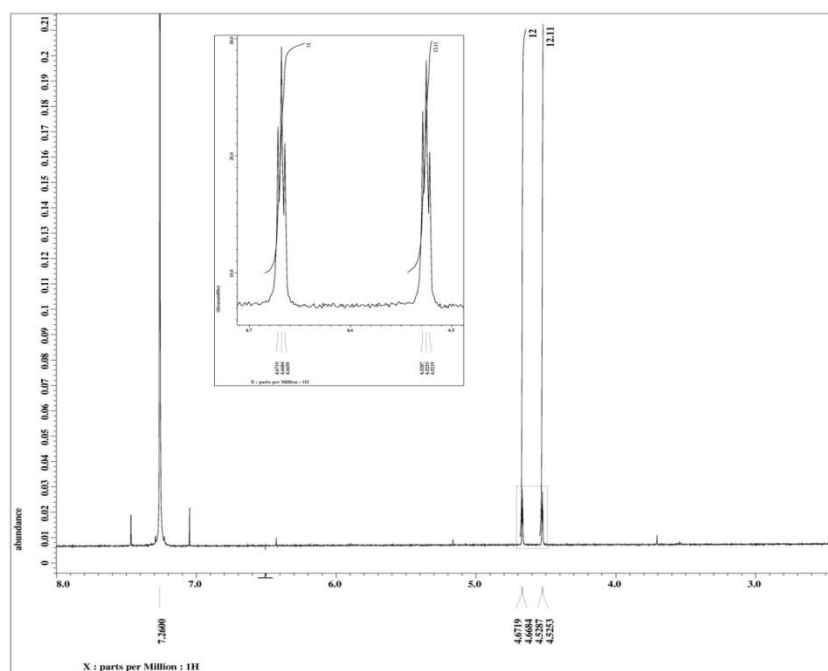


Figure 2.12 ^1H NMR spectrum of compound **4**.

2.4.4 Fourier-transform Infrared Spectra of Compound 1–4

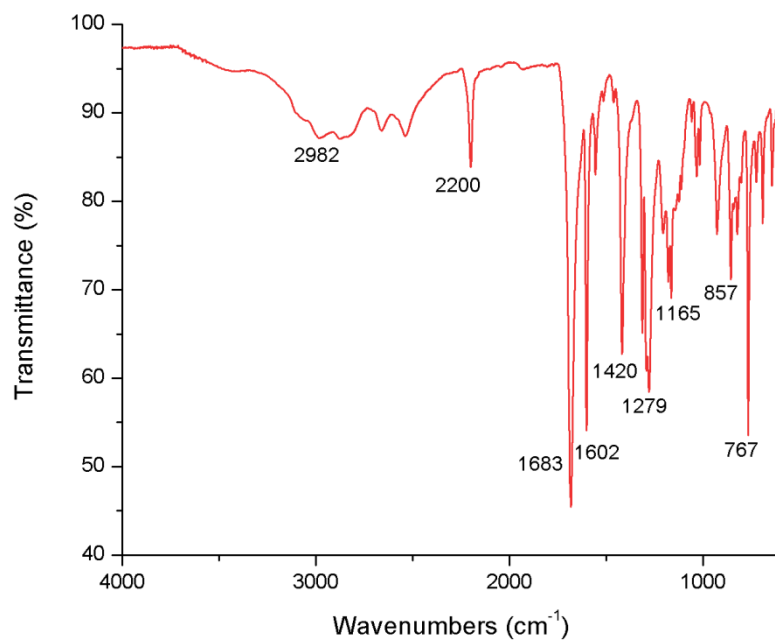


Figure 2.13 Fourier-transform infrared spectrum of compound 1.

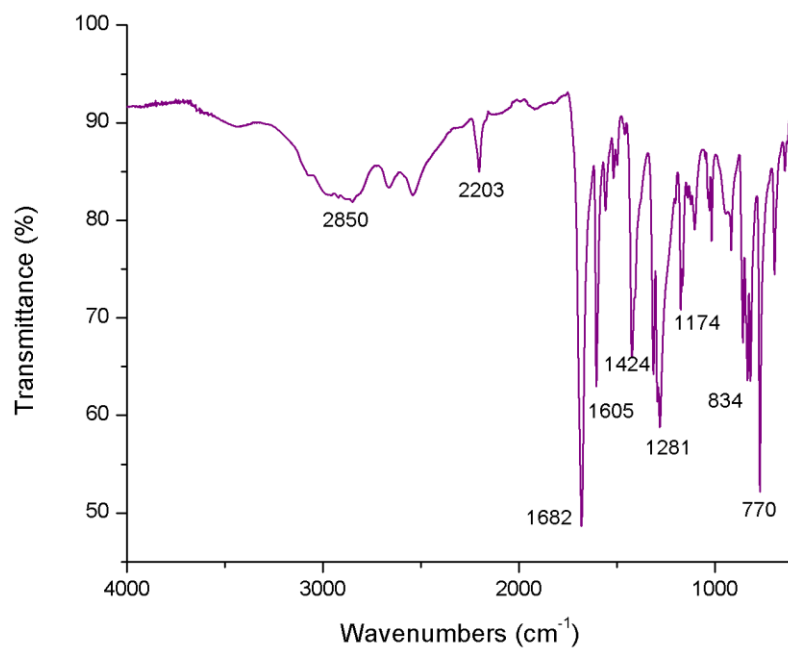


Figure 2.14 Fourier-transform infrared spectrum of compound 2.

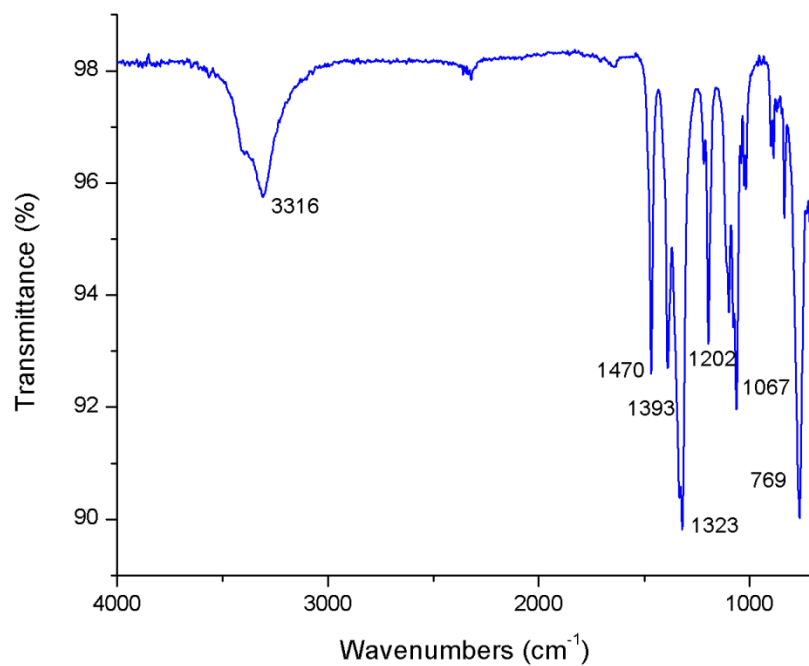


Figure 2.15 Fourier-transform infrared spectrum of compound **3**.

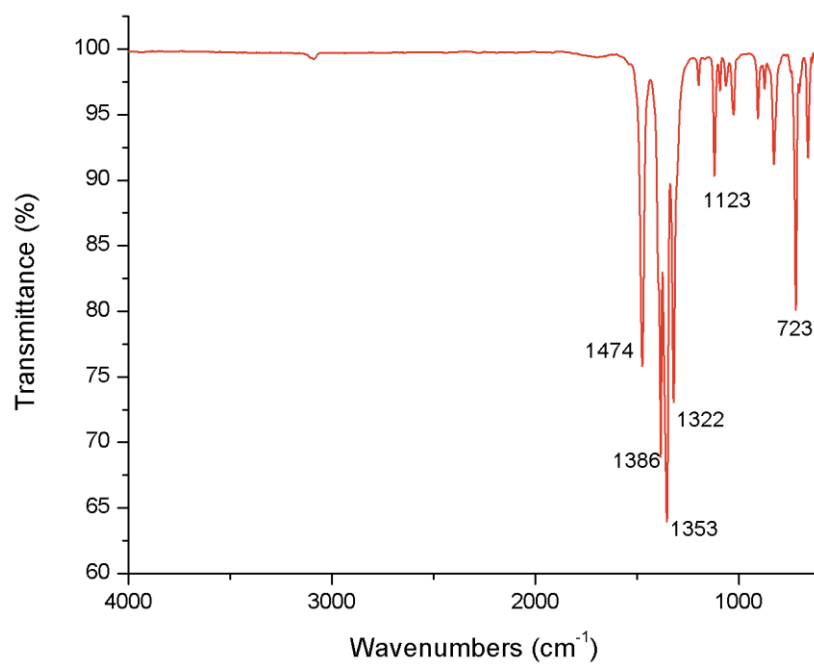


Figure 2.16 Fourier-transform infrared spectrum of compound **4**.

2.4.5 X-ray Crystallographic Analysis of Compound 4

Table 2.1 Crystallographic Data of Compound 4

Empirical formula	$\text{C}_{30}\text{H}_{24}\text{B}_6\text{O}_6\text{Fe}_3$	
Formula weight	712.90	
Temperature	193(2) K	
Wavelength	0.71073 Å	
Crystal system	Monoclinic	
Space group	$C2$	
Unit cell dimensions	$a = 21.8605(9)$ Å	$\alpha = 90^\circ$
	$b = 19.4421(8)$ Å	$\beta = 96.620(1)^\circ$
	$c = 25.7885(10)$ Å	$\gamma = 90^\circ$
Volume	$10887.4(8)$ Å ³	
Z	16	
Density (calculated)	1.740 Mg/m^3	
Absorption coefficient	1.626 mm^{-1}	
$F(000)$	5760	
Crystal size	$0.30 \times 0.15 \times 0.05 \text{ mm}^3$	
Theta range for data collection	1.41° to 25.04°	
Index ranges	$-26 \leq h \leq 25, -23 \leq k \leq 17, 0 \leq l \leq 30$	
Reflections collected	28076	
Independent reflections	17093 [$R_{\text{int}} = 0.0671$]	
Completeness to $\theta = 25.04^\circ$	99.9%	

Absorption correction	Empirical
Max. and min. transmission	0.9959 and 0.5538
Refinement method	Full-matrix least-squares on F^2
Data / restraints / parameters	9438 / 145 / 1621
Goodness-of-fit on F^2	0.955
Final R indices [$I > 2\sigma(I)$]	$R_1 = 0.0398$, $wR_2 = 0.0915$
a indices (all data)	$R_1 = 0.0777$, $wR_2 = 0.1128$
Absolute structure parameter	0.037(17)
Largest diff. peak and hole	0.514 and $-0.344 \text{ e}^-/\text{\AA}^3$

2.4.6 Solid-State Cyclic Voltammetry of Compound **4**

Cyclic voltammetry of compound **4** was performed using a Macpile potentiostat in the potential range of 2.80 to 3.55 V (vs. Li/Li⁺) with a scan rate of 1 mV/s. The experiments were carried out using two-electrode SwagelokTM-type cells. The working electrodes were prepared by mixing 10 wt% of polyvinylidene fluoride (PVDF) binder, 10 wt% of the active material, and 80 wt% of carbon black (a conducting additive) in an agate mortar. Celgard 2400 was used as the separator and pure lithium foil (Aldrich) was used as the counter electrode. The electrolyte consisted of a solution of 1.0 M LiPF₆ in ethylene carbonate (EC)/dimethyl carbonate (DMC) mixture (1:1 w/w). The cells were assembled inside an argon-filled glove box.

2.5 References

- [1] Kealy, T. J.; Pauson, P. L. *Nature* **1951**, *168*, 1039–1040.
- [2] Heinze, K.; Lang, H. *Organometallics* **2013**, *32*, 5623–5625.
- [3] Štěpnička, P. *Ferrocenes: Ligands, Materials and Biomolecules*; Wiley, 2008.
- [4] Peri, D.; Ciston, J.; Gándara, F.; Zhao, Y.; Yaghi, O. M. *Inorg. Chem.* **2013**, *52*, 13818–13820.
- [5] Zhang, E.; Hou, H.; Meng, X.; Liu, Y.; Fan, Y. *Cryst. Growth Des.* **2009**, *9*, 903–913.
- [6] Kim, Y. S.; Kim, J.; Kim, D.; Chae, H. K. *Chem. Lett.* **2007**, *36*, 150–151.
- [7] Meilikhov, M.; Yusenko, K.; Fischer, R. A. *J. Am. Chem. Soc.* **2009**, *131*, 9644–9645.
- [8] Halls, J. E.; Hernan-Gomez, A.; Burrows, A. D.; Marken, F. *Dalton Trans.* **2012**, *41*, 1475–1480.
- [9] (a) Meilikhov, M.; Yusenko, K.; Fischer, R. A. *Dalton Trans.* **2010**, *39*, 10990–10999. (b) Kalidindi, S. B.; Yusenko, K.; Fischer, R. A. *Chem. Commun.* **2011**, *47*, 8506–8508.
- [10] Chen, T.-H.; Kaveevivitchai, W.; Bui, N.; Miljanić, O. Š. *Chem. Commun.* **2012**, *48*, 2855–2857.

- [11] Sonogashira, K.; Tohda, Y.; Hagihara, N. *Tetrahedron Lett.* **1975**, 4467–4470.
- [12] Kovar, R. F.; Rausch, M. D.; Rosenberg, H. *Organomet. Chem. Syn.* **1971**, *1*, 173–181.
- [13] Belema, M.; Nguyen, V. N.; Zusi, F. C. *Tetrahedron Lett.* **2004**, *45*, 1693–1697.
- [14] (a) Korich, A. L.; Iovine, P. M. *Dalton Trans.* **2010**, *39*, 1423–1431. (b) Westcott, S. A. *Angew. Chem., Int. Ed.* **2010**, *49*, 9045–9046.
- [15] For selected examples, see: (a) Spitler, E. L.; Giovino, M. R.; White, S. L.; Dichtel, W. R. *Chem. Sci.* **2011**, *2*, 1588–1593. (b) Spitler, E. L.; Dichtel, W. R. *Nat. Chem.* **2010**, *2*, 672–677. (c) El-Kaderi, H. M.; Hunt, J. R.; Mendoza-Cortés, J. L.; Côté, A. P.; Taylor, R. E.; O’Keeffe, M.; Yaghi, O. M. *Science* **2007**, *316*, 268–272. (d) Côté, A. P.; Benin, A. I.; Ockwig, N. W.; Matzger, A. J.; O’Keeffe, M.; Yaghi, O. M. *Science* **2005**, *310*, 1166–1170. (e) Tilford, R. W.; Gemmill, W. R.; zur Loye, H.-C.; Lavigne, J. J. *Chem. Mater.* **2006**, *18*, 5296–5301.
- [16] (a) Forsyth, M.; Sun, J.; Zhou, F.; MacFarlane, D. R. *Electrochim. Acta* **2003**, *48*, 2129–2136. (b) Yang, Y.; Inoue, T.; Fujinami, T.; Mehta, M. A. *Solid State Ionics* **2001**, *140*, 353–359. (c) Mehta, M. A.; Fujinami, T.; Inoue, S.; Matsushita, K.; Miwa, T.; Inoue, T. *Electrochim. Acta* **2000**, *45*, 1175–1180.
- [17] For selected examples, see: (a) Nishimura, T.; Kasai, A.; Nagaosa, M.; Hayashi, T. *Chem. Commun.* **2011**, *47*, 10488–10490. (b) Graham, T. J. A.; Shields, J. D.; Doyle, A. G. *Chem. Sci.* **2011**, *2*, 980–984. (c) Xu, L.; Li, B.-J.; Wu, Z.-H.; Lu, X.-Y.; Guan, B.-T.;

Wang, B.-Q.; Zhao, K.-Q.; Shi, Z.-J. *Org. Lett.* **2010**, *12*, 884–887. (d) Song, Z. Z.; Wong, H. N. C.; Yang, Y. *Pure Appl. Chem.* **1996**, *68*, 723–726.

[18] Nishiyabu, R.; Kubo, Y.; James, T. D.; Fossey, J. S. *Chem. Commun.* **2011**, *47*, 1124–1150.

[19] (a) Schleyer, P. v. R.; Jiao, H.; van Eikema Hommes, N. J.; Malkin, R. V. G.; Malkina, O. L. *J. Am. Chem. Soc.* **1997**, *119*, 12669–12670. (b) Pierrefixe, S. C. A. H.; Bickelhaupt, F. M. *Aust. J. Chem.* **2008**, *61*, 209–215. (c) Novak, I.; Kovač, B. *Chem. Phys. Lett.* **2007**, *440*, 70–72. (d) Fowler, P. W.; Steiner, E. *J. Phys. Chem. A* **1997**, *101*, 1409–1413.

[20] Feng, X.; Ding, X.; Jiang, D. *Chem. Soc. Rev.* **2012**, *41*, 6010–6022.

[21] (a) Knapp, R.; Rehahn, M. *J. Organomet. Chem.* **1993**, *452*, 235–240. (b) Kamounah, F. S.; Christensen, J. B. *J. Chem. Res. (S)* **1997**, 150.

[22] Spicer, C. D.; Davis, B. G. *Chem. Commun.* **2013**, *49*, 2747–2749.

[23] All C–H bond lengths have been normalized to a neutron-diffraction determined internuclear distance of 1.083 Å. See: (a) Steiner, T. *Angew. Chem., Int. Ed.* **2002**, *41*, 48–76. (b) Allen, F. H.; Kennard, O.; Watson, D. G.; Brammer, L.; Orpen, A. G.; Taylor, R.; *J. Chem. Soc. Perkin Trans. 2* **1987**, S1–S19.

[24] (a) Korich, A.; Iovine, P. M. *Dalton Trans.* **2010**, *39*, 1423–1431. (b) Wade, C. R.; Broomsgrove, A. E. J.; Aldridge, S.; Gabbai, F. P. *Chem. Rev.* **2010**, *110*, 3958–3984. (c)

Yamamoto, H.; Ori, A.; Ueda, K.; Dusemund, C.; Shinkai, S. *Chem. Commun.* **1996**, 407–408.

[25] Gleiter, R.; Hopf, H. *Modern Cyclophane Chemistry*; Wiley-VCH: Weinheim, 2005.

[26] Mascal, M. *Angew. Chem., Int. Ed.* **2006**, 45, 2890–2893.

[27] (a) West, W.; Blanco, M.; Whitacre, J. F.; Leifer, M.; Smart, M.; Greenbaum, S.; Bugga, R.; Reddy, V. P.; Narayanan, S. R. *J. Electrochem. Soc.* **2007**, 154, A929–A936.

(b) Nair, N. G.; Blanco, M.; West, W.; Weise, F. C.; Greenbaum, S.; Reddy, V. P. *J. Phys. Chem. A* **2009**, 113, 5918–5926.

[28] Attempts to chemically oxidize compound **4** produced inconclusive results: while crystals changed color to greenish (as expected for ferrocenium species), no significant improvements in solubility were noticed, thus precluding the solution-phase characterization of these (presumably) oxidized species.

[29] (a) Bats, J. W.; Ma, K.; Wagner, M. *Acta Crystallogr. Sect. C* **2002**, 58, m129–m132. (b) Thilagar, P.; Chen, J.; Lalancette, R. A.; Jäkle, F. *Organometallics* **2011**, 30, 6734–6741. (c) Braunschweig, H.; Bera, H.; Stellwag, S.; Schwarz, S.; Hemberger, Y.; Radacki, K. *Z. Anorg. Allg. Chem.* **2007**, 633, 2314–2320. (d) Tamura, K.; Akutagawa, N.; Satoh, M.; Wada, J.; Masuda, T. *Macromol. Rapid Commun.* **2008**, 29, 1944–1949. (e) Park, K.-S.; Schougaard, S. B.; Goodenough, J. B. *Adv. Mater.* **2007**, 19, 848–851.

- [30] Diallo, A. K.; Absalon, C.; Ruiz, J.; Astruc, D. *J. Am. Chem. Soc.* **2011**, *133*, 629–641.
- [31] (a) Reek, J. N. H.; Otto, S. *Dynamic Combinatorial Chemistry*; Wiley-VCH: Weinheim, Germany, 2010. (b) Miller, B. L. *Dynamic Combinatorial Chemistry in Drug Discovery, Bioorganic Chemistry, and Materials Science*; Wiley: Hoboken, NJ, 2010. (c) Corbett, P. T.; Leclaire, J.; Vial, L.; West, K. R.; Wietor, J.-L.; Sanders, J. K. M.; Otto, S. *Chem. Rev.* **2006**, *106*, 3652–3711. (d) Rowan, S. J.; Cantrill, S. J.; Cousins, G. R. L.; Sanders, J. K. M.; Stoddart, J. F. *Angew. Chem., Int. Ed.* **2002**, *41*, 898–952.
- [32] Iovine, P. M.; Gyselbrecht, C. R.; Perttu, E. K.; Click, C.; Neuwelt, A.; Loera, J.; DiPasquale, A. G.; Rheingold, A. L.; Kua, J. *Dalton Trans.* **2008**, 3791–3794.
- [33] Mastalerz, M.; Oppel, I. M. *Angew. Chem., Int. Ed.* **2012**, *51*, 5252–5255.
- [34] (a) Jones, J. T. A.; Hasell, T.; Wu, X.; Bacsa, J.; Jelfs, K. E.; Schmidtman, M.; Chong, S.; Adams, Y. D. J.; Trewin, A.; Schiffman, F.; Cora, F.; Slater, B.; Steiner, A.; Day, G. M.; Cooper, A. I. *Nature* **2011**, *474*, 367–371. (b) Tozawa, T.; Jones, J. T. A.; Swamy, S.; Jiang, I. S.; Adams, D. J.; Shakespeare, S.; Clowes, R.; Bradshaw, D.; Hasell, T.; Chong, S. Y.; Tang, C.; Thompson, S.; Parker, J.; Trewin, A.; Bacsa, J.; Slawin, A. M. Z.; Steiner, A.; Cooper, A. I. *Nat. Mater.* **2009**, *8*, 973–978.
- [35] (a) Tranchemontagne, D. J.; Ni, Z.; O’Keeffe, M.; Yaghi, O. M. *Angew. Chem., Int. Ed.* **2008**, *47*, 5136–5147. (b) Lu, Z.; Knobler, C. B.; Furukawa, H.; Wang, B.; Liu, G.; Yaghi, O. M. *J. Am. Chem. Soc.* **2009**, *131*, 12532–12533. (c) Perry IV, J. J.; Perman,

J. A.; Zaworotko, M. J. *Chem. Soc. Rev.* **2009**, 38, 1400–1417. (d) Perttu, E. K.; Arnold, M.; Iovine, P. M. *Tetrahedron Lett.* **2005**, 46, 8753–8756.

[36] Meaningful ^{13}C NMR spectra of compounds **2** and **4** could not be obtained due to their low solubility.

Chapter Three

Syntheses and Properties of Perfluorinated Metal-Organic Frameworks

3.1 Introduction

3.1.1 Fluorinated Metal-Organic Frameworks

Since Plunkett's accidental discovery of Teflon in 1938,¹ the field of fluoropolymers has blossomed into a mature research area.² Fluoropolymers' appeal in industrial and household applications comes from their desirable physical properties—hydrophobicity and low friction coefficients—combined with high thermal and chemical stability, which is largely a consequence of the strong C–F bond (110–120 kcal mol^{−1}). With the advent of MOFs as a class of three-dimensional coordination polymers, much interest has been devoted to amalgamating these two polymer classes to produce *fluorinated MOFs*. Such materials would combine the superior characteristics of fluoropolymers with MOFs' appealing properties: high porosities and surface areas, crystallographic order, thermal stability, and modular synthesis. However, efforts to develop extensively fluorinated MOFs have been significantly hampered by the paucity of synthetic routes to extensively fluorinated ligands—such as aromatic carboxylates or tetrazolates—for incorporation into MOFs. Banerjee^{3,4,5,6} and others⁷ have synthesized and studied H₂ and CO₂ adsorption in partially fluorinated MOFs constructed from 4,4'-

The work described in this chapter has been previously published: Chen, T.-H.; Popov, I.; Zenasni, O.; Daugulis, O.; Miljanić, O. Š. *Chem. Commun.* **2013**, 49, 6846–6848.

(hexafluoro-isopropylidene)bis(benzoic acid) (**1** in Figure 3.1) and 3-fluoronicotinic acid (**2**).⁸ Cheetham and co-workers studied MOFs derived from perfluorinated aliphatic dicarboxylates (tetrafluorosuccinate—**3** and hexafluoroglutarate—**4**),⁹ tetrafluoro-terephthalate (**5**)^{10,11,12,13} and tetrafluoroisophthalate (**6**).^{11,13} Among non-carboxylate fluorinated ligands, Long used a bistriazole derived from perfluorophenyl (**7**),^{14,15} while Omary used 3,5-bis(trifluoromethyl)-1,2,4-triazolate linker (derived from **8** in Figure 3.1) to prepare two silver-based MOFs that are highly hydrophobic. Omary also demonstrated that fluorinated MOFs selectively adsorb small hydrocarbon molecules (without adsorbing water),^{16,17} suggesting that they could be used in the treatment of oil spills and hydrocarbon storage.¹⁸

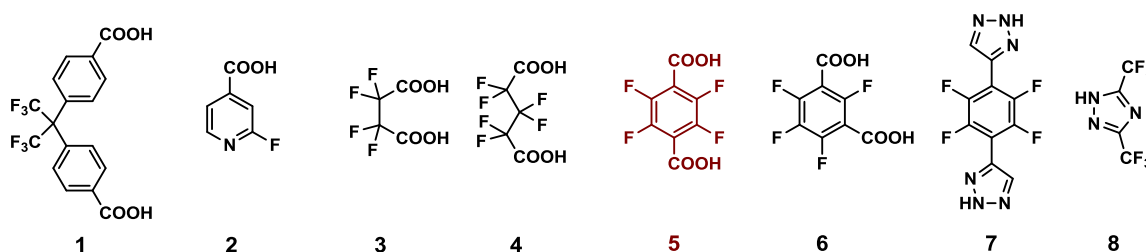


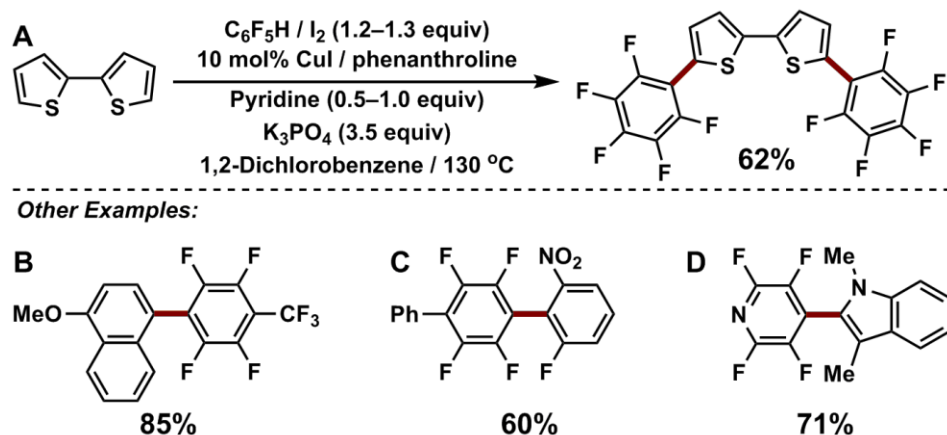
Figure 3.1 Examples of fluorinated linkers employed in MOF synthesis. Perfluoroterephthalic acid (**5**, shown in red) is the most commonly used connector. Absence of preparative strategies to fluorinated carboxylic acids has prohibited exploration of larger ligands and different topologies.

3.1.2 Copper-catalyzed C–H Bond Functionalization

The last decade has witnessed an explosive development of C–H bond functionalization methodologies.¹⁹ The most common functional groups in chemistry are

C–C and C–H bonds, but selective one-step conversion of C–H bonds to other functional groups is usually not possible. Consequently, methods for selective functionalization of C–H bonds may result in shorter synthetic sequences, increased efficiency of chemical transformations, and ability to attain unique product regioselectivity. By decreasing the amount of synthetic steps that are needed to synthesize the desired final product, the overall process becomes less labor-intensive and more environmentally friendly due to the decreased amount of disposable waste and solvents.

Scheme 3.1 Copper-catalyzed Dehydrogenative Cross-coupling Protocols Developed by Daugulis' Group



Daugulis and co-workers developed a general method for selective, dehydrogenative arene C–H bond cross-coupling. This is currently the most general procedure for arene cross-coupling (Scheme 3.1).²⁰ The methodology allows for cross-coupling of virtually any combination of five- and six-membered-ring heterocycles and electron-poor arenes. Furthermore, electron-rich arenes can be cross-coupled with electron-poor arenes and acidic heterocycles. The formation of homocoupling products is

minimal. Daugulis' group has successfully cross-coupled five-membered ring heterocycle with an electron-deficient arene (Scheme 3.1A), electron-poor arene with electron-rich arene (Scheme 3.1B), two electron-deficient arenes (Scheme 3.1C), and six-membered ring heterocycle with a five-membered ring heterocycle (Scheme 3.1D). With thisprecedented diversity of possible coupling partners, Daugulis group applied copper-catalyzed C–H bond functionalization to the preparation of ligands for MOFs.

In this chapter, with a series of large, perfluorinated and rigid aromatic carboxylic acids and tetrazoles in hand, we demonstrate that these novel ligands can be reticulated into MOFs under solvothermal conditions. We propose to name these new materials **MOFFs**, highlighting their fluorinated character.

3.2 Results and Discussion

3.2.1 Syntheses and Crystal Structure Analyses of MOFFs

Ilya Popov from Prof. Daugulis' group has prepared the first examples of extensively fluorinated MOF linkers **9–24** (Figure 3.2) using copper-catalyzed C–H bond functionalization methodology.²¹ Then I attempted to incorporate these compounds into single-crystalline MOFs with a high degree of fluorination. Parts of these results were published.²² Herein, only significant results from **MOFFs 1–6** are discussed.

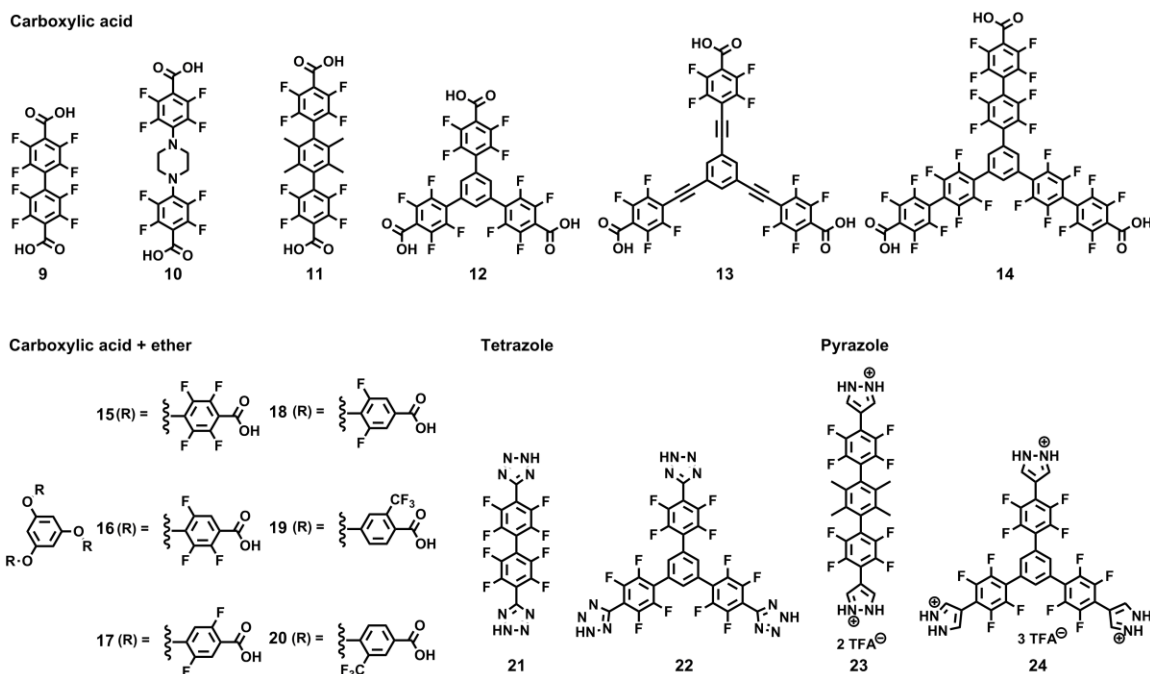


Figure 3.2 Examples of extensively fluorinated linkers synthesized by Ilya Popov in Prof. Daugulis' labs, catalogued by coordination functional groups.²¹

With linker **9** in hand, we proceeded to develop synthetic conditions for its incorporation into single-crystalline MOFs. Ligand **9** was combined with $\text{Cu}(\text{NO}_3)_2 \cdot 2.5 \text{H}_2\text{O}$ in a 1:18:1 mixture of DMF, MeOH and H_2O . After 4 d of heating at 40 °C, greenish-blue plate-shaped crystals of **MOFF-1** were isolated. Their structural analysis using single crystal X-ray diffraction revealed an infinite two-dimensional network (Figure 3.3), in which pairs of Cu atoms form paddlewheel-shaped $\text{Cu}_2(\text{COO})_4$ clusters that are capped with one MeOH molecule at each Cu. This structure permits formulating the obtained material as $\text{Cu}^{2+}(\mathbf{9}-2\text{H}^+)(\text{MeOH})$. Two-dimensional sheets of **MOFF-1** organize into a three-dimensional crystal through parallel offset stacks, in which the $\text{Cu}_2(\text{COO})_4$ cluster of one layer fits into the void space of the adjacent layers. The two-

dimensional grid structure of this MOF is similar to that of its non-fluorinated analog MOF-118,²³ but the two frameworks differ in their three-dimensional organization: while MOF-118 presents a rare interpenetrated square grid network, **MOFF-1** is composed of parallel stacked two-dimensional layers.

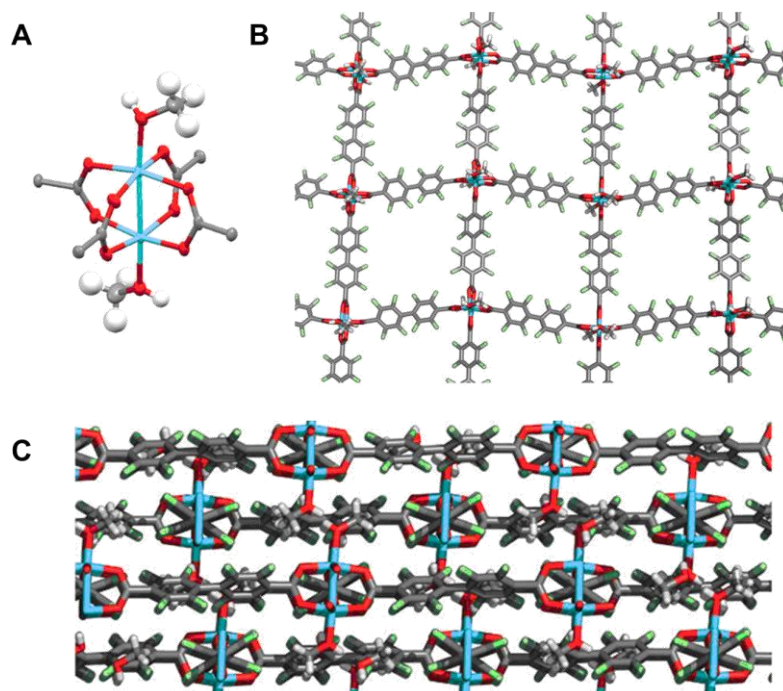


Figure 3.3 X-ray crystal structure of **MOFF-1**, $\text{Cu}^{2+}(\mathbf{9}-2\text{H}^+)(\text{MeOH})$. (A) Secondary building unit; (B) representative segment of the two-dimensional layer structure; (C) side-on view of interlayer orientation. Element colors: C, gray; Cu, cyan; O, red; F, lime; and H, white.

In the presence of a bifunctional pillaring ligand 1,4-diazabicyclo[2.2.2]octane (DABCO), diacid **9** was converted into a pillared three-dimensional Cu-based framework **MOFF-2**. Specifically, heating a solution of ligand **9**, DABCO and $\text{Cu}(\text{NO}_3)_2 \cdot 2.5 \text{H}_2\text{O}$ in a 3:18:1 mixture of DMF, MeOH and H_2O at 60 °C for 2 d resulted in greenish single

crystals. Their analysis using X-ray diffraction revealed (Figure 3.4) the expected constitution $\text{Cu}^{2+}(\mathbf{9}-2\text{H}^+)(\text{DABCO})_{0.5}$ and the pillared arrangement of layers mediated by DABCO connectors. The structure is two-fold interpenetrated, in contrast to its non-fluorinated constitutional analog DMOF-1-bpdc.²⁴

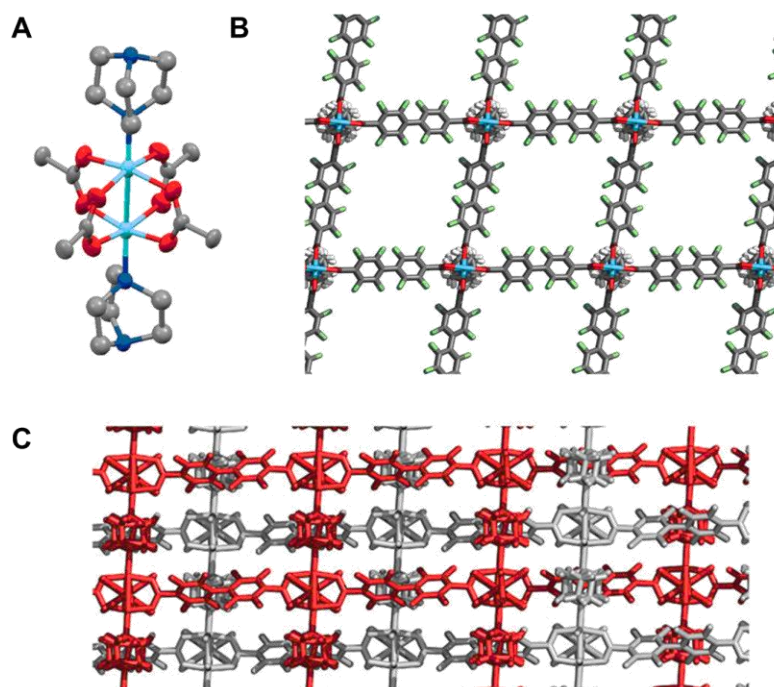


Figure 3.4 X-ray crystal structure of **MOFF-2**, $\text{Cu}^{2+}(\mathbf{9}-2\text{H}^+)(\text{DABCO})_{0.5}$. The disorder in the DABCO ligand is apparent. (A) Secondary building unit; (B) view along the one-dimensional channels in the structure; (C) side-on view of the interpenetrated framework, where two independent nets are shown in different colors. Element colors: C, gray; Cu, cyan; O, red; N, blue; F, lime; and H, white.

The linker **21** was used to demonstrate that perfluorinated tetrazolate-based linkers can also be coordinated into MOFs. A solution of **21** and $\text{CuCl}_2 \cdot 2\text{H}_2\text{O}$ in DMF was heated at 70 °C for 4 d. Blue rod-shaped single crystals that resulted were analyzed

using X-ray diffraction, revealing (Figure 3.5) a porous three-dimensional structure of **MOFF-3**. In this structure, octahedral Cu atoms are coordinated to peripheral tetrazolate nitrogens in four separate molecules of **21**, and an H₂O molecule acts as a bridge between each pair of adjacent Cu centers. This structure is analogous to Long's previously reported example of Cu-bistetrazolate MOFs,²⁵ and it also changes significantly upon heating as the coordinated H₂O molecules are removed.

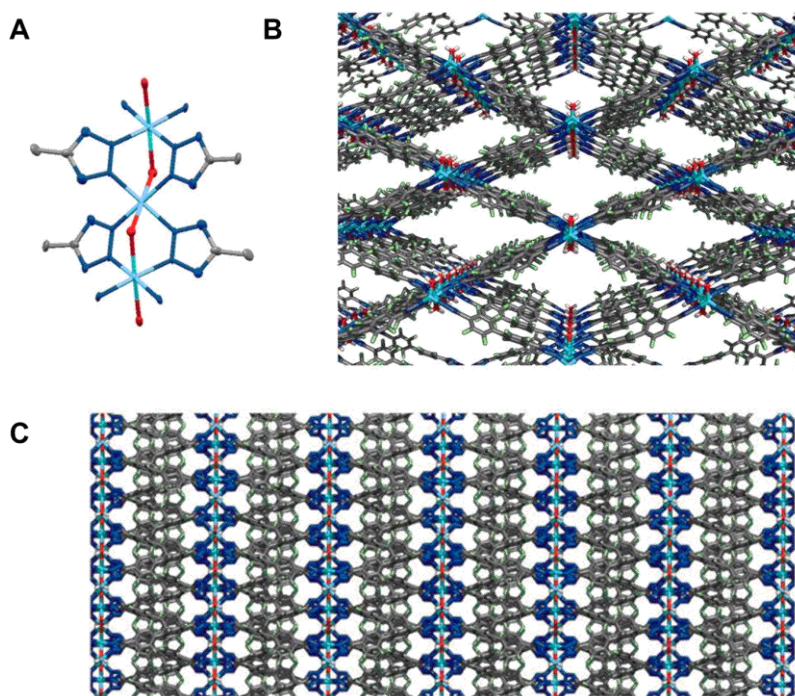


Figure 3.5 X-ray crystal structure of **MOFF-3**, Cu²⁺(**21**-2H⁺)(H₂O). (A) Secondary building unit; (B) view along the one-dimensional channels in the structure; (C) view of the structure perpendicular to the orientation of the channels. Element colors: C, gray; Cu, cyan; O, red; N, blue; F, lime; and H, white.

Ligand **13** was the first triangular ligand to be tested as a MOF linker in this work. A suspension of **13** and Cu(NO₃)₂·2.5H₂O in MeOH was heated at 40 °C for 1 d. Green

block-shaped single crystals that were formed were analyzed by X-ray diffraction, revealing (Figure 3.6) the structure of **MOFF-4** as a one-dimensional infinite chain in which two of the three carboxylic acid groups are complexed to Cu within H₂O-capped paddlewheel clusters. The third –COOH group remained uncoordinated, despite the presence of excess Cu in the reaction mixture. The originally trigonal linker bends into a square geometry, which was permitted by the flexibility within the triple bonds—evidenced by the decreased C–C≡C angles which ranged between 173.5° and 175.0°. ²⁶

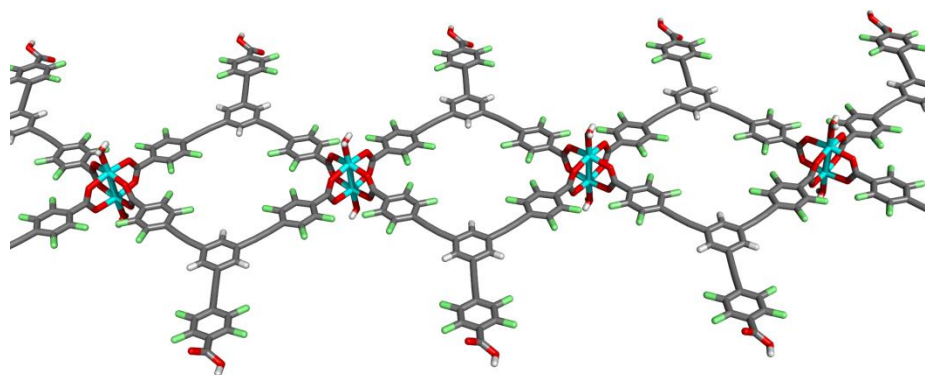


Figure 3.6 Segment of the X-ray crystal structure of **MOFF-4**, formulated as $\text{Cu}^{2+}(\mathbf{13}-2\text{H}^+)(\text{H}_2\text{O})$. MeOH molecules hydrogen-bonded to the uncoordinated –COOH group have been omitted for clarity. Element colors: C, gray; H, white; F, lime; O, red; and Cu, cyan.

Ligand **12** was combined with $\text{Cu}(\text{NO}_3)_2 \cdot 2.5\text{H}_2\text{O}$ in a mixture of DMF and EtOH. After 4 d at 60 °C, greenish-blue crystals of **MOFF-5** were isolated. Because the massive disorder of the solvent in the cavities yielded poor-quality diffraction data, using the in-house $\text{CuK}\alpha$ radiation diffractometer, the highest resolution we could obtain was ~ 2 Å,

which was insufficient to obtain a structure solution. Thus, a stronger synchrotron radiation source was required to complete this crystal structure. With the assistance from Dr. Yu-Sheng Chen (ChemMatCARS, Advanced Photon Source, Argonne National Laboratory) and Dr. Yu-Chun Chuang (National Synchrotron Radiation Research Center, Taiwan), we were able to analyze its single crystal structure. Single crystal synchrotron diffraction analysis revealed a three-dimensional network with a large cubic unit cell $a = b = c = 47.326(5)$ Å (Figure 3.7), in which pairs of Cu atoms form paddlewheel-shaped $\text{Cu}_2(\text{COO})_4$ clusters that are capped with one molecule of H_2O at each Cu. This structure permits formulating the obtained material as $\text{Cu}^{2+}_3(\mathbf{12}-3\text{H}^+)_2(\text{H}_2\text{O})_3$. Six $\text{Cu}_2(\text{COO})_4$ clusters are connected by four linkers **12** to form a small octahedral 23.7 Å-wide cage with four open 13.3 Å equilateral triangular faces. Eight small cages build up a cubic unit cell containing a 33.5 Å-wide large cage with six open 13.3 Å-wide square faces. The void volume of the material preliminarily calculated by *Mercury CSD 3.3*²⁷ is 77%, which is comparable to its non-fluorinated analogue MOF-143.²⁸ To the best of our knowledge, **MOFF-5** is the first example of a mesoporous perfluorinated MOF.

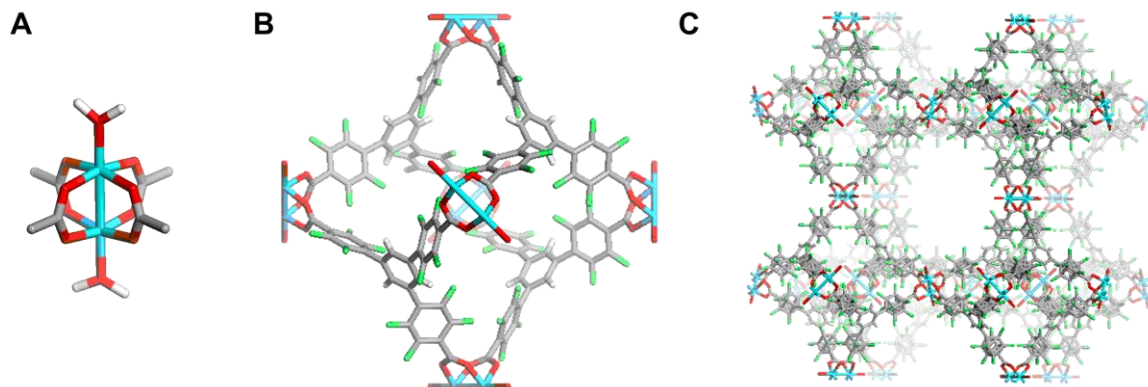


Figure 3.7 Synchrotron X-ray crystal structure of **MOFF-5**, $\text{Cu}^{2+}_3(\mathbf{12}-3\text{H}^+)_2(\text{H}_2\text{O})_3$. (A) Secondary building unit; (B) small cage (intrinsically disordered atoms are omitted for clarity) formed by SBU and ligand **12**; (C) infinite 3D frameworks built from small cages. Element colors: C, gray; H, white; F, lime green; O, red; and Cu, cyan.

Tetrazole-based ligand **22** was combined with $\text{CuCl}_2 \cdot 2\text{H}_2\text{O}$ in a mixture of *N,N*-diethylformamide (DEF), MeOH, and H_2O . After 7 d at 70 °C, green cubic crystals of **MOFF-6** were isolated. Single crystal synchrotron diffraction analysis revealed a three-dimensional network with a cubic unit cell (Figure 3.8). The SBU is composed of a square planar $[\text{Cu}_4\text{Cl}]^{7+}$ cluster, bridged by eight tetrazolates of eight discrete ligand **22**, each Cu is additionally coordinated by one H_2O . This structure permits formulating the obtained material as $[\text{Cu}_4\text{Cl}]_3(\mathbf{22}-3\text{H}^+)_8(\text{H}_2\text{O})_{12}$. Six $[\text{Cu}_4\text{Cl}]^{7+}$ are connected by eight linkers **22** to form a small octahedral 29.0 Å-wide cavity with ligand **22** on each face. Eight small cages build up a cubic unit cell containing a 34.1 Å-wide cave with six open 13.6 Å square faces. The void volume of **MOFF-6** preliminarily calculated by *Mercury CSD 3.3* is 73%.

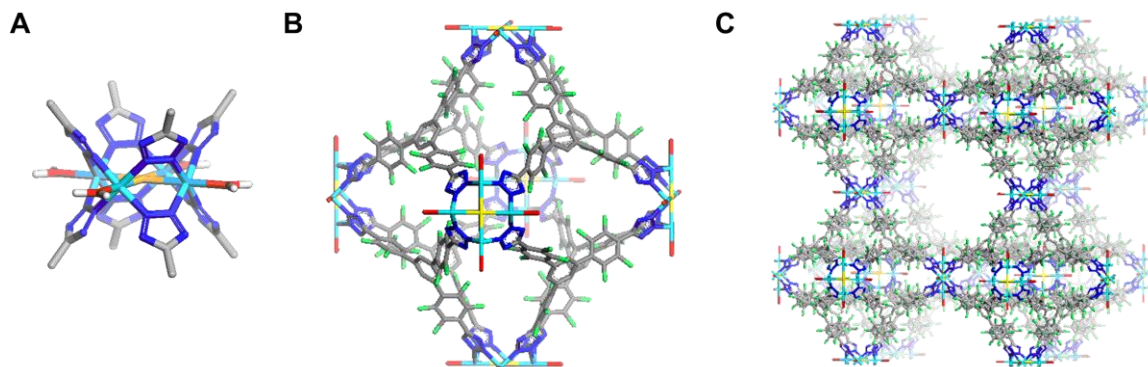


Figure 3.8 Synchrotron X-ray crystal structure of **MOFF-6**, $[\text{Cu}_4\text{Cl}]_3(\mathbf{22}-3\text{H}^+)_8(\text{H}_2\text{O})_{12}$. (A) Secondary building unit; (B) small cage (crystallographically intrinsic disordered atoms are omitted for clarity) formed by SBU and ligand **22**; (C) infinite 3D frameworks built by small cages. Element colors: C, gray; H, white; F, lime green; O, red; Cu, cyan; N, blue; Cl, yellow.

3.2.2 Thermogravimetric Analyses of MOFFs

Thermal stabilities of **MOFFs 1–6** were evaluated using TGA (Figure 3.9). **MOFF-1** shows a relatively featureless TGA trace, suggesting that the initial slow loss of coordinated and encapsulated solvent overlaps with the more rapid weight loss caused by framework decomposition occurring at around 220 °C.²⁹ **MOFF-2** does not crystallize with solvent and thus shows no weight loss until it starts to rapidly decompose at around 270 °C. For **MOFF-3**, loss of solvent (14.5% weight) occurs under 80 °C; the desolvated framework then remains stable until ~230 °C, when final decomposition begins. **MOFF-4** and **-5**, comprising with different triangular carboxylate ligands, similar TGA traces are

observed: no clear decomposition step is observed until ~200 °C, and then the materials slowly decompose to 15% and 27% of the starting weight, respectively. As for **MOFF-6**, with triangular tetrazolate-based ligand, presents a unique trace with only 40% weight loss at 500 °C (60% at 800 °C, see Chapter 3.4.6). Overall, decomposition temperatures for these MOFs are comparable to those for similar non-fluorinated networks, suggesting that the cleavage of the strong C–F bond ($110\text{--}120\text{ kcal mol}^{-1}$) is unlikely during framework decomposition.

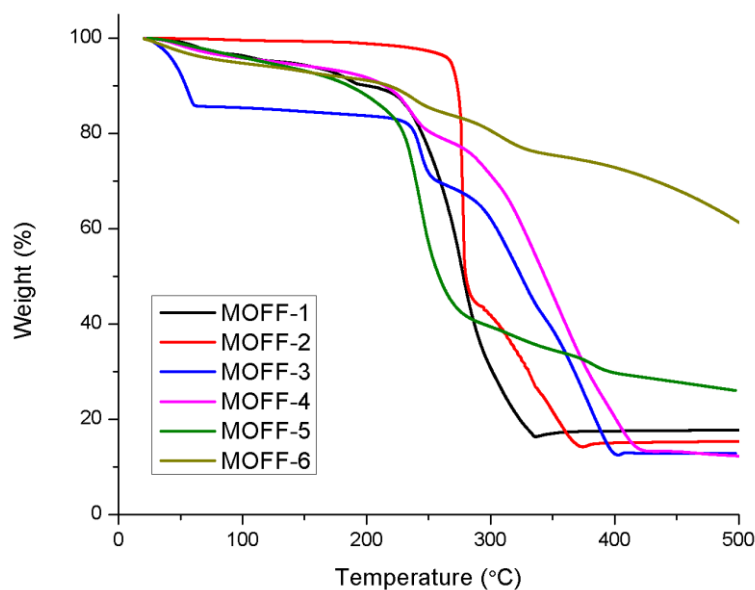


Figure 3.9 Comparison of TGA traces of **MOFFs 1–6**.

3.2.3 Gas and Vapor Adsorption of MOFFs

Nitrogen sorption within the pores of **MOFF-1** and **MOFF-2** was characterized by typical type I isotherms—with the corresponding BET surface areas of 580 and 444 m^2g^{-1} , respectively. In contrast, **MOFF-3** showed hysteric uptake of N_2 , perhaps indicative of its breathing behavior (Figure 3.10). Owing to this unique character, we

additionally tested the adsorption of O₂ and CO₂ within **MOFF-3**. The hysteretic adsorption of N₂ and O₂ indicates a flexible structure, similar to Long's previous results.³⁰ Negligible adsorption of N₂ and O₂ in the low pressure range implies the completely closed 1D channels in **MOFF-3**. Remarkably, negligible adsorption of CO₂ (293 K) even at 1000 mbar shows the selective adsorption of **MOFF-3**. This unusual behavior could be capitalized upon if we could prepare MOFs which maintain hysteretic adsorption profiles, but have a greater surface area and higher capacity for adsorption. The porosity measurement was not conducted on **MOFF-4** due to its negligible accessible voids from crystal structure. The gas adsorption measurements on mesoporous **MOFF-5** and **-6** were challenging because the results strongly depend on the activation methods. SCD drying was the best method we tried so far and the BET surface areas were 510 and 2,045 m²g⁻¹, respectively. Although these two numbers could be possibly optimized by drying in SCD for longer time or other methods, BET surface area over 2,000 m²g⁻¹ is the highest among those of all fluorinated MOFs to date.

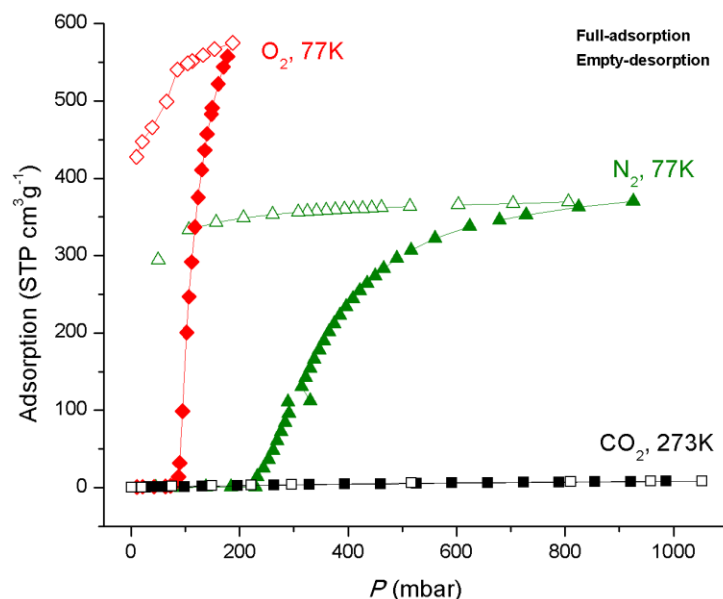


Figure 3.10 Adsorption isotherms for N₂ (77 K), O₂ (77 K), and CO₂ (293 K) sorption within **MOFF-3**.

The water vapor adsorption studies provide evidence for the superhydrophobic behavior of the prepared **MOFFs** (Figure 3.11). These revealed that **MOFFs 1–3** adsorb negligible amounts of water, even at 90% relative humidity ($< 2 \text{ kgm}^{-3}$)—which is comparable to the very low water adsorption of Omary’s perfluorinated FMOF-1.¹⁶ Since other large perfluorinated ligands are expected to be hydrophobic, this direct-synthesis route to highly hydrophobic MOFs appears to be broadly applicable and complementary to Cohen’s postsynthetic functionalization approach³¹ to superhydrophobic MOFs. **MOFF-4** has negligible accessible voids and **MOFF-5** and **-6** are fragile in the presence of moisture.³² Therefore, water vapor adsorption is meaningless for these materials.

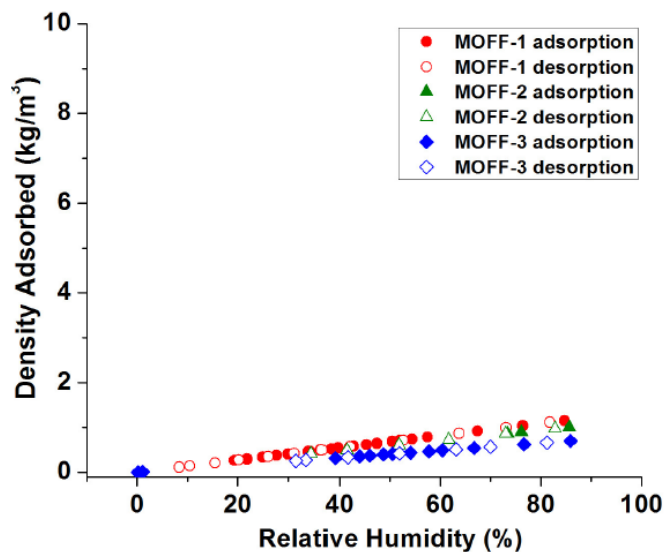


Figure 3.11 Adsorption of H₂O vapor in **MOFFs 1–3** at 293 K.

3.2.4 Advancing Contact Angle Measurements of MOFFs

To evaluate the hydrophobic/hydrophilic characteristics of **MOFFs 1–4**, with the aid from Dr. Oussama Zenasni, we performed contact angle measurements with H₂O (Table 3.1). **MOFF-5** and **-6** were not tested because the structures of mesoporous frameworks were not stable in the presence of water. Samples of **MOFF-1** are wettable by H₂O if air-dried, which is probably caused by the coordinated hydrophilic molecules of MeOH. Upon oven-drying, these solvent molecules are removed and the residual framework becomes water-repellent (H₂O contact angle of $108 \pm 2^\circ$), as do oven-dried **MOFF-3** (H₂O contact angle of $134 \pm 1^\circ$) and **MOFF-4** (H₂O contact angle of $143 \pm 2^\circ$). The most hydrophobic material among these new fluorinated MOFs is **MOFF-2**, with a H₂O contact angle of $151 \pm 1^\circ$. As **MOFF-2** crystallizes without included solvent molecules, its structure and hydrophobicity are unaffected upon drying.

Table 3.1 Advancing Contact Angle Measurements of **MOFFs**.

MOF	contact angle with:		
	water	<i>n</i>-hexadecane	<i>cis</i>-perfluorodecalin
MOFF-1, air-dried	~0°	~0°	~0°
MOFF-1, oven-dried	108 ± 2°	~0°	~0°
MOFF-2, oven-dried	151 ± 1°	~0°	~0°
MOFF-3, oven-dried	134 ± 1°	~0°	~0°
MOFF-3, SCD-dried	135 ± 2°	~0°	~0°
MOFF-4, oven-dried	143 ± 2°	~0°	~0°

3.3 Conclusions and Outlook

In summary, we have utilized C–H bond functionalization to access novel perfluorinated aromatic linkers, which were in turn reticulated into highly hydrophobic, extensively fluorinated metal–organic frameworks. The preparative route to ligands presented here is simple and general, and other extensively fluorinated ligands (and the derived MOFs) could be generated through straightforward adaptation of our protocol. As the extended aromatic ligands shown here open up pathways to highly porous fluorinated MOFs, it should be possible to explore and capitalize upon unique adsorption and binding properties anticipated for these materials. These new fluorinated precursors have > 300 times higher acidities than their non-fluorinated counterparts,³³ and can be coordinated

into MOFs at temperatures as low as 40 °C—which could be of interest in the effort to produce high-resolution patterned MOF arrays on surfaces.³⁴

3.4 Experimental Section

3.4.1 General Methods

Schlenk flasks or vials with PTFE/Liner caps were used as reaction vessels for the synthesis of precursors, while standard scintillation vials were used as vessels for the synthesis of **MOFFs**. Infrared spectra were recorded on a Perkin-Elmer Spectrum 100 FT-IR spectrophotometer using Pike MIRacle Micrometer pressure clamp. Microanalyses were conducted by Intertek USA, Inc. TGA were carried out on a TA Instruments TGA 2050 thermogravimetric analyzer with a temperature ramping rate of 2 °C/min under the flow of N₂ gas. PXRD data were collected at 25 °C on a Phillips X'pert Pro diffractometer (**MOFFs 1–3**). Capillary PXRD measurements (**MOFFs 4–6**) were performed on a Bruker DUO platform diffractometer equipped with a 4K CCD APEX II detector and an Incoatec 30 Watt Cu microsource with compact multilayer optics. Simulated PXRD patterns were calculated with the *Material Studio* software package³⁵ employing the structure model from the obtained single crystal data.

The following starting materials and solvents were obtained from the respective commercial sources and used without further purification: *n*-hexadecane, *cis*-perfluorodecalin, Cu(NO₃)₂·2.5H₂O, and CuCl₂·2H₂O (JT Baker); water (Milli-Q, deionized). All the solvents for synthesizing **MOFFs** were obtained from commercial

sources and used without further purification. Polished Silicon (100) wafers were purchased from Silicon Inc. and rinsed with absolute EtOH (Aaper Alcohol and Chemical Co) before use. All the gases for gas adsorption analysis were purchased from Matheson Tri-Gas Inc.

3.4.2 Syntheses of MOFFs

Synthesis of MOFF-1

Ligand **3** (30 mg, 0.077 mmol) and $\text{Cu}(\text{NO}_3)_2 \cdot 2.5\text{H}_2\text{O}$ (18 mg, 0.077 mmol) were added to a 20 mL glass scintillation vial. Solvents DMF (0.3 mL), MeOH (5.4 mL), and H_2O (0.3 mL) were added to the solids, and the mixture was sonicated until dissolved. The vial was capped and placed into an oven at 40 °C for 4 d. The resulting greenish-blue crystals were washed with MeOH and dried in a 120 °C vacuumed oven for 1d. Yield calculated from the evacuated sample was 81% (32 mg) based on Cu. FT-IR (neat): $\tilde{\nu}$ = 1605 (s), 1460 (s), 1384 (s), 1269 (w), 1005 (m), 978 (s), 811 (m), 774 (m), 720 (s) cm^{-1} . CHN anal. calcd (%) for $\text{C}_{28}\text{F}_{16}\text{O}_8\text{Cu}_2$: C 37.54; Found: C 37.06.

Synthesis of MOFF-2

Ligand **3** (75 mg, 0.19 mmol), 1,4-diazabicyclo[2.2.2]octane (DABCO, 11 mg, 0.098 mmol) and $\text{Cu}(\text{NO}_3)_2 \cdot 2.5\text{H}_2\text{O}$ (45 mg, 0.19 mmol) were added to a 20 mL glass scintillation vial. Solvents DMF (1 mL), MeOH (6 mL), and H_2O (0.3 mL) were added to the solids, and the mixture was sonicated until dissolved. The vial was capped and placed into an oven at 60 °C for 2 d. The resulting greenish crystals were washed with MeOH and dried under reduced pressure. Yield calculated from evacuated sample was 77% (74

mg) based on Cu. FT-IR (neat): $\tilde{\nu}$ = 1663 (s), 1630 (m), 1472 (s), 1408 (s), 999 (m), 980 (s), 802 (w), 774 (s), 720 (s) cm^{-1} . CHN anal. calcd (%) for $\text{C}_{34}\text{H}_{12}\text{N}_2\text{F}_{16}\text{O}_8\text{Cu}_2$: C 40.51, H 1.20, N 2.78; Found: C 40.56, H 0.98, N 2.85.

Synthesis of MOFF-3

Ligand **4** (50 mg, 0.12 mmol) and $\text{CuCl}_2 \cdot 2\text{H}_2\text{O}$ (20 mg, 0.12 mmol) were added to a 20 mL glass scintillation vial. Solvent DMF (5 mL) was added to the solids, and the mixture was sonicated until dissolved. The vial was capped and placed into an oven at 70 °C for 4 d. The resulting blue crystals were washed with DMF. The activated crystals were obtained by heating them in a 120 °C oven for 1 d under reduced pressure. Yield calculated from evacuated sample was 26% (16 mg) based on Cu. FT-IR (neat): $\tilde{\nu}$ = 1642 (s), 1493 (m), 1469 (s), 1420 (w), 1387 (w), 1266 (w), 1108 (s), 999 (s), 971 (s), 874 (s), 725 (s) cm^{-1} . CHN anal. calcd (%) for $\text{C}_{14}\text{N}_8\text{F}_8\text{Cu}$: C 33.88, N 22.60; Found: C 34.80, N 21.75.

Synthesis of MOFF-4

Ligand **10** (10 mg, 0.014 mmol) and $\text{Cu}(\text{NO}_3)_2 \cdot 2.5\text{H}_2\text{O}$ (16 mg, 0.068 mmol) were added to a 4 mL glass scintillation vial. MeOH (0.5 mL) was added to the solids, and the mixture was sonicated for 10 min. The vial was capped and placed into an oven at 40 °C for 1 d. The resulting green crystals were washed with MeOH without drying. Yield calculated from evacuated sample was 93% (12 mg) based on ligand **10**. FT-IR (neat): $\tilde{\nu}$ = 2233 (w), 1727 (w), 1654 (m), 1624 (m), 1478 (s), 1402 (s), 1081 (w), 990 (s),

884 (w), 832 (w), 759 (s) cm^{-1} . Anal. calcd (%) for $\text{C}_{33}\text{H}_4\text{F}_{12}\text{O}_6\text{Cu}$: C 50.25, H 0.51; Found: C 49.65, H 0.61.

Synthesis of MOFF-5

Ligand **12** (20 mg, 0.031 mmol) and $\text{Cu}(\text{NO}_3)_2 \cdot 2.5\text{H}_2\text{O}$ (36 mg, 0.15 mmol) were added to a 20 mL glass scintillation vial. Solvents DMF (4 mL) and EtOH (4 mL) were added to the solids, then the mixture was sonicated until dissolved and degassed with N_2 for 1 min. The vial was capped and placed into an oven at 60 °C for 4 d. The resulting greenish-blue crystals were activated by SCD drying (Chapter 3.4.9). Yield calculated from the evacuated sample was 75% (18 mg) based on ligand **12**. FT-IR (neat): $\tilde{\nu}$ = 1598 (s), 1470 (s), 1374 (s), 984 (s), 756 (s), 675 (s) cm^{-1} . CHN anal. calcd (%) for $\text{C}_{18}\text{H}_2\text{CuF}_8\text{O}_5$: C 42.06, H 0.39; Found: C 41.55, H 0.96.

Synthesis of MOFF-6

Ligand **22** (20 mg, 0.028 mmol) and $\text{CuCl}_2 \cdot 2\text{H}_2\text{O}$ (24 mg, 0.14 mmol) were added to a 20 mL glass scintillation vial. Solvents DEF (4 mL), MeOH (0.04 mL) and H_2O (0.04 mL) were added to the solids, and the mixture was sonicated until dissolved. The vial was capped and placed into an oven at 70 °C for 7 d. The resulting green crystals were activated by SCD drying (Chapter 3.4.9). Yield calculated from the evacuated sample was 66% (16 mg) based on ligand **22**. FT-IR (neat): $\tilde{\nu}$ = 1605 (m), 1493 (s), 1408 (s), 977 (s), 895 (s), 835 (s), 678 (s) cm^{-1} . CHN anal. calcd (%) for $\text{C}_{72}\text{H}_8\text{ClCu}_4\text{F}_{32}\text{N}_{32}\text{O}_4$: C 37.87, H 0.35, N 19.64; Found: C 35.81, H 0.67, N 18.40.³⁵

3.4.3 X-ray Crystallographic Analyses of MOFFs

X-ray Crystallographic Analysis of MOFF-1

The measurement was performed by Dr. Antonio DiPasquale (University of California, Berkeley). A blue plate 0.10×0.10×0.04 mm in size was mounted on a Cryoloop with Paratone oil. Data were collected in a nitrogen gas stream at 100(2) K using phi and omega scans. Crystal-to-detector distance was 40 mm and exposure time was 10 s per frame using a scan width of 0.5°. Data collection was 99.8% complete to 25.00° in θ . A total of 27288 reflections were collected covering the indices, $-20 \leq h \leq 20$, $-18 \leq k \leq 18$, $-18 \leq l \leq 19$. 6865 reflections were found to be symmetry independent, with an R_{int} of 0.0272. Indexing and unit cell refinement indicated a primitive, monoclinic lattice. The space group was found to be $P2/c$ (No. 13). The data were integrated using the Bruker SAINT software program and scaled using the SADABS software program. Solution by direct methods (SIR-2011) produced a complete heavy-atom phasing model consistent with the proposed structure. All non-hydrogen atoms were refined anisotropically by full-matrix least-squares (SHELXL-97). All hydrogen atoms were placed using a riding model. Their positions were constrained relative to their parent atom using the appropriate HFIX command in SHELXL-97.

Table 3.2 Crystallographic Data of **MOFF-1**

Empirical formula	$\text{C}_{32}\text{H}_{16}\text{Cu}_2\text{F}_{16}\text{O}_{12}$
Formula weight	1023.53
Temperature	100(2) K

Wavelength	0.71073 Å	
Crystal system	Monoclinic	
Space group	<i>P2/c</i>	
Unit cell dimensions	$a = 16.7149(9)$ Å	$\alpha = 90^\circ$
	$b = 15.1584(8)$ Å	$\beta = 112.098(2)^\circ$
	$c = 15.9373(8)$ Å	$\gamma = 90^\circ$
Volume	3741.4(3) Å ³	
<i>Z</i>	4	
Density (calculated)	1.817 Mg/m ³	
Absorption coefficient	1.278 mm ⁻¹	
<i>F</i> (000)	2024	
Crystal size	0.10×0.10×0.04 mm ³	
θ range for data collection	1.31° to 25.39°	
Index ranges	$-20 \leq h \leq 20, -18 \leq k \leq 18, -18 \leq l \leq 19$	
Reflections collected	27288	
Independent reflections	6865 [<i>R</i> (int) = 0.0272]	
Completeness to $\theta = 25.00^\circ$	99.8%	
Absorption correction	Semi-empirical from equivalents	
Max. and min. transmission	0.9507 and 0.8829	
Refinement method	Full-matrix least-squares on F^2	
Data / restraints / parameters	6865 / 0 / 573	
Goodness-of-fit on F^2	1.091	

Final R indices [$I > 2\sigma(I)$]	$R_1 = 0.0394$, $wR_2 = 0.1050$
R indices (all data)	$R_1 = 0.0488$, $wR_2 = 0.1110$
Largest diff. peak and hole	0.846 and $-0.808 \text{ e}/\text{\AA}^3$

X-ray Crystallographic Analysis of MOFF-2

The measurement was performed by Dr. James Korp (UH). A green prism $0.30 \times 0.25 \times 0.25$ mm in size was mounted on a Cryoloop with Paratone oil. Data were collected at 298(2) K using phi and omega scans. Crystal-to-detector distance was 60 mm and exposure time was 40 s per frame using a scan width of 0.3° . Data collection was 99.8% complete to 25.00° in θ . A total of 13682 reflections were collected covering the indices, $-25 \leq h \leq 25$, $0 \leq k \leq 21$, $0 \leq l \leq 10$. 3310 reflections were found to be symmetry independent, with a R_{int} of 0.0631. Indexing and unit cell refinement indicated a C-centered, monoclinic lattice. The space group was found to be $C2/c$ (No. 15). All measurements were made with a Siemens SMART platform diffractometer equipped with a 4K CCD APEX II detector. A hemisphere of data (1271 frames at 6 cm detector distance) was collected using a narrow-frame algorithm with scan widths of 0.30% in omega and an exposure time of 40 s/frame. The data were integrated using the Bruker-Nonius SAINT program, with the intensities corrected for Lorentz factor, polarization, air absorption, and absorption due to variation in the path length through the detector faceplate. A psi scan absorption correction was applied based on the entire data set. Redundant reflections were averaged. Final cell constants were refined using 2215 reflections having $I > 10\sigma(I)$, and these, along with other information pertinent to data collection and refinement. The Laue symmetry was determined to be $2/m$, and from the

systematic absences noted the space group was shown to be either Cc or $C2/c$. The data crystal was found to be twinned, consisting of two major domains. A twinned integration was performed on the two separate domains to correct for overlap. Final least squares refinement was done using the independent structure factors measured from each domain, with a normalizing scale factor between them. The asymmetric unit consists of one Cu atom, one fluorinated dicarboxylate ligand, and one-half of a DABCO molecule situated about a two-fold axis. The dicarboxylate was found to be disordered over two slightly different orientations, and this was treated by use of ideal rigid body refinement. The DABCO was found to be disordered over three different orientations, and this was treated using distance constraints based on literature values. The dicarboxylate ligand was refined anisotropically using restraints to make the $U(ij)$ components approximate isotropic behavior. DABCO was refined isotropically. The final difference density map showed one very large peak of about $4.5 \text{ e}^-/\text{\AA}^3$ located on the two-fold axis between equivalent Cu atoms, and another smaller but significant peak of about $1.5 \text{ e}^-/\text{\AA}^3$ between Cu and DABCO. The distance between these peaks is 2.7 \AA , virtually identical to the distance between the refined Cu atom and its two-fold relative. This larger density was included in the final refinement as atom C25X in order to improve the least squares model, however since it does not make chemical sense to belong to the structure it was omitted from all other calculations. Because the distance between the "ghost peaks" coincides with the observed $[\text{Cu}\cdots\text{Cu}]$ separation, they are presumed to be the locations of Cu atoms in the very minor third and fourth orientations of the unit cell which could not be identified during twin analysis due to very weak scattering.

Table 3.3 Crystallographic Data of **MOFF-2**

Empirical formula	$\text{C}_{34}\text{H}_{12}\text{Cu}_2\text{F}_{16}\text{N}_2\text{O}_8$	
Formula weight	1007.54	
Temperature	298(2) K	
Wavelength	0.71073 Å	
Crystal system	Monoclinic	
Space group	$C2/c$	
Unit cell dimensions	$a = 23.065(5)$ Å	$\alpha = 90^\circ$
	$b = 19.498(4)$ Å	$\beta = 94.91(3)^\circ$
	$c = 9.529(2)$ Å	$\gamma = 90^\circ$
Volume	$4269.7(16)$ Å ³	
<i>Z</i>	4	
Density (calculated)	1.567 Mg/m ³	
Absorption coefficient	1.113 mm ⁻¹	
<i>F</i> (000)	1984	
Crystal size	$0.30 \times 0.25 \times 0.25$ mm ³	
θ range for data collection	1.37° to 23.60°	
Index ranges	$-25 \leq h \leq 25, 0 \leq k \leq 21, 0 \leq l \leq 10$	
Reflections collected	13682	
Independent reflections	3310 [$R(\text{int}) = 0.0631$]	
Completeness to $\theta = 25.00^\circ$	99.8%	
Absorption correction	Empirical	

Max. and min. transmission	0.7449 and 0.5664
Refinement method	Full-matrix least-squares on F^2
Data / restraints / parameters	1752 / 261 / 345
Goodness-of-fit on F^2	1.030
Final R indices [$I > 2\sigma(I)$]	$R_1 = 0.0551$, $wR_2 = 0.1586$
R indices (all data)	$R_1 = 0.1031$, $wR_2 = 0.1972$
Largest diff. peak and hole	0.577 and -0.621 e/\AA^3

X-ray Crystallographic Analysis of MOFF-3

The measurement was performed by Dr. Antonio DiPasquale (University of California, Berkeley). A blue block-shaped crystal $0.12 \times 0.06 \times 0.04$ mm in size was mounted on a Cryoloop with Paratone oil. Data were collected in a nitrogen gas stream at 100(2) K using phi and omega scans. Crystal-to-detector distance was 40 mm and exposure time was 20 s per frame using a scan width of 1.0° . Data collection was 99.8% complete to 25.00° in θ . A total of 37915 reflections were collected covering the indices, $-19 \leq h \leq 17$, $-37 \leq k \leq 36$, $-15 \leq l \leq 16$. 5907 reflections were found to be symmetry independent, with an R_{int} of 0.0693. Indexing and unit cell refinement indicated a C-centered, monoclinic lattice. The space group was found to be $C2/m$ (No. 12). The data were integrated using the Bruker SAINT software program and scaled using the SADABS software program. Solution by direct methods (SIR-97) produced a complete heavy-atom phasing model consistent with the proposed structure. All non-hydrogen atoms were refined anisotropically by full-matrix least-squares (SHELXL-97). All hydrogen atoms were placed using a riding model. Their positions were constrained

relative to their parent atom using the appropriate HFIX command in SHELXL-97. SQUEEZE was used to treat the diffuse solvent contribution in the crystal. Its use has been noted in the CIF file.

Table 3.4 Crystallographic Data of **MOFF-3**

Empirical formula	$\text{C}_{14}\text{H}_2\text{CuF}_8\text{N}_8\text{O}$	
Formula weight	513.78	
Temperature	100(2) K	
Wavelength	0.71073 Å	
Crystal system	Monoclinic	
Space group	$C2/m$	
Unit cell dimensions	$a = 15.8991(10)$ Å	$\alpha = 90^\circ$
	$b = 31.5712(18)$ Å	$\beta = 115.357(3)^\circ$
	$c = 13.8721(8)$ Å	$\gamma = 90^\circ$
Volume	$6292.3(6)$ Å ³	
<i>Z</i>	8	
Density (calculated)	1.085 Mg/m^3	
Absorption coefficient	0.756 mm^{-1}	
F(000)	2008	
Crystal size	$0.12 \times 0.06 \times 0.04 \text{ mm}^3$	
θ range for data collection	1.56° to 25.43°	
Index ranges	$-19 \leq h \leq 17, -37 \leq k \leq 36, -15 \leq l \leq 16$	

Reflections collected	37915
Independent reflections	5907 [$R(\text{int}) = 0.0693$]
Completeness to $\theta = 25.00^\circ$	99.8%
Absorption correction	Semi-empirical from equivalents
Max. and min. transmission	0.9704 and 0.9148
Refinement method	Full-matrix least-squares on F^2
Data / restraints / parameters	5907 / 4 / 303
Goodness-of-fit on F^2	1.119
Final R indices [$I > 2\sigma(I)$]	$R_1 = 0.0753$, $wR_2 = 0.2272$
R indices (all data)	$R_1 = 0.0896$, $wR_2 = 0.2346$
Largest diff. peak and hole	1.809 and -0.897 e/\AA^3

X-ray Crystallographic Analysis of MOFF-4

The measurement was performed by Dr. Antonio DiPasquale (University of California, Berkeley). A green prism-shaped crystal $0.12 \times 0.04 \times 0.04$ mm in size was mounted on a Cryoloop with Paratone oil. Data were collected in a nitrogen gas stream at 100(2) K using phi and omega scans. Crystal-to-detector distance was 40 mm and exposure time was 10 s per frame using a scan width of 0.5° . Data collection was 99.7% complete to 25.00° in θ . A total of 25777 reflections were collected covering the indices, $-11 \leq h \leq 12$, $-13 \leq k \leq 13$, $-21 \leq l \leq 21$. 6587 reflections were found to be symmetry independent, with an R_{int} of 0.0818. Indexing and unit cell refinement indicated a primitive, triclinic lattice. The space group was found to be $P\bar{1}$ (No. 2). The data were integrated using the Bruker SAINT software program and scaled using the SADABS

software program. Solution by direct methods (SIR-97) produced a complete heavy-atom phasing model consistent with the proposed structure. All non-hydrogen atoms were refined anisotropically by full-matrix least-squares (SHELXL-97). All hydrogen atoms were placed using a riding model. Their positions were constrained relative to their parent atom using the appropriate HFIX command in SHELXL-97.

Table 3.5 Crystallographic Data of **MOFF-4**

Empirical formula	$\text{C}_{33}\text{H}_{17}\text{Cu}_2\text{F}_{12}\text{N}_2\text{O}_9$	
Formula weight	940.57	
Temperature	100(2) K	
Wavelength	0.71073 Å	
Crystal system	Triclinic	
Space group	$P\bar{1}$	
Unit cell dimensions	$a = 12.3131(5)$ Å	$\alpha = 103.699(2)^\circ$
	$b = 12.9609(5)$ Å	$\beta = 102.109(2)^\circ$
	$c = 18.1518(7)$ Å	$\gamma = 92.277(2)^\circ$
Volume	$2739.58(19)$ Å ³	
<i>Z</i>	2	
Density (calculated)	1.140 Mg/m ³	
Absorption coefficient	0.854 mm ⁻¹	
<i>F</i> (000)	934	
Crystal size	$0.10 \times 0.04 \times 0.04$ mm ³	

θ range for data collection	1.62° to 25.47°
Index ranges	$-14 \leq h \leq 14, -15 \leq k \leq 15, -21 \leq l \leq 21$
Reflections collected	24772
Independent reflections	9879 [$R(\text{int}) = 0.0434$]
Completeness to $\theta = 25.00^\circ$	98.5%
Absorption correction	Semi-empirical from equivalents
Max. and min. transmission	0.9666 and 0.9195
Refinement method	Full-matrix least-squares on F^2
Data / restraints / parameters	9879 / 0 / 527
Goodness-of-fit on F^2	0.998
Final R indices [$I > 2\sigma(I)$]	$R_1 = 0.0574, wR_2 = 0.1569$
R indices (all data)	$R_1 = 0.0816, wR_2 = 0.1695$
Largest diff. peak and hole	1.203 and $-0.512 \text{ e}/\text{\AA}^3$

X-ray Crystallographic Analysis of MOFF-5

The experiment was performed at ChemMatCARS beamline at Advanced Photon Source in Argonne National Laboratory. The diffraction data was collected on a Bruker D8 diffractometer with an APEX-II CCD detector using using phi scans. Data collection was 99.6% complete to 12.74° in θ . A total of 56600 reflections were collected covering the indices, $-34 \leq h \leq 41, -42 \leq k \leq 36, -41 \leq l \leq 41$. Indexing and unit cell refinement indicated a P -centered, cubic lattice. The space group was found to be $Fm\bar{3}m$ (No. 225). The data were integrated using the Bruker SAINT software program and scaled using the

SADABS software program. Solution by direct methods produced a complete heavy-atom phasing model consistent with the proposed structure. All non-hydrogen atoms were refined anisotropically by full-matrix least-squares (SHELXL-97). All hydrogen atoms were placed using a riding model. Their positions were constrained relative to their parent atom using the appropriate HFIX command in SHELXL-97. The PLATON program, SQUEEZE function, was used to remove disordered solvent.

Table 3.6 Crystallographic Data of **MOFF-5**

Empirical formula	$\text{C}_{18}\text{H}_2\text{CuF}_8\text{O}_5$
Formula weight	513.74
Temperature	293(2) K
Wavelength	0.49594 Å
Crystal system	Cubic
Space group	$Fm\bar{3}m$
Unit cell dimensions	$a = b = c = 47.326(5) \text{ Å}$ $\alpha = \beta = \gamma = 90^\circ$
Volume	$106,002(21) \text{ Å}^3$
<i>Z</i>	48
Density (calculated)	0.386 Mg/m^3
Absorption coefficient	0.102 mm^{-1}
<i>F</i> (000)	12048
θ range for data collection	0.60° to 12.74°
Index ranges	$-34 \leq h \leq 41$, $-42 \leq k \leq 36$, $-41 \leq l \leq 41$

Reflections collected	56600
Independent reflections	1974 [$R(\text{int}) = 0.1576$]
Completeness to $\theta = 12.74^\circ$	99.6%
Absorption correction	Semi-empirical from equivalents
Refinement method	Full-matrix least-squares on F^2
Data / restraints / parameters	1974 / 0 / 109
Goodness-of-fit on F^2	1.357
Final R indices [$I > 2\sigma(I)$]	$R_1 = 0.1130$, $wR_2 = 0.3203$
R indices (all data)	$R_1 = 0.1409$, $wR_2 = 0.3448$
Largest diff. peak and hole	0.379 and $-0.389 \text{ e}/\text{\AA}^3$

X-ray Crystallographic Analysis of MOFF-6

The experiment was performed at ChemMatCARS beamline at Advanced Photon Source in Argonne National Laboratory. A green cubic single crystal was mounted on a glass fiber and cooled to 100K using Cyrojet (Oxford instrumentation). The diffraction data was collected on a Bruker D8 diffractometer with an APEX-II CCD detector using phi scans. Crystal-to-detector distance was 110 mm and exposure time was 0.4 s per frame using a scan width of 0.5° . Data collection was 99.9% complete to 12.79° in θ . A total of 140824 reflections were collected covering the indices, $-19 \leq h \leq 30$, $-28 \leq k \leq 30$, $-24 \leq l \leq 30$. Indexing and unit cell refinement indicated a P -centered, cubic lattice. The space group was found to be $Pm\bar{3}m$ (No. 221). The data were integrated using the Bruker SAINT software program and scaled using the SADABS software program. Solution by direct methods produced a complete heavy-atom phasing model consistent

with the proposed structure. All non-hydrogen atoms were refined anisotropically by full-matrix least-squares (SHELXL-97). All hydrogen atoms were placed using a riding model. Their positions were constrained relative to their parent atom using the appropriate HFIX command in SHELXL-97. The PLATON program, SQUEEZE function, was used to remove disordered solvent.

Table 3.7 Crystallographic Data of **MOFF-6**

Empirical formula	$\text{C}_{72}\text{H}_8\text{ClCu}_4\text{F}_{32}\text{N}_{32}\text{O}_4$
Formula weight	2282.71
Temperature	100(2) K
Wavelength	0.41328 Å
Crystal system	Cubic
Space group	$Pm\bar{3}m$
Unit cell dimensions	$a = b = c = 28.881(6) \text{ Å} \quad \alpha = \beta = \gamma = 90^\circ$
Volume	$24091(9) \text{ Å}^3$
Z	3
Density (calculated)	0.472 Mg/m^3
Absorption coefficient	0.061 mm^{-1}
$F(000)$	3351
Crystal size	$0.15 \times 0.15 \times 0.15 \text{ mm}^3$
θ range for data collection	0.71° to 12.79°
Index ranges	$-19 \leq h \leq 30, -28 \leq k \leq 30, -24 \leq l \leq 30$

Reflections collected	140824
Independent reflections	3061 [$R(\text{int}) = 0.1696$]
Completeness to $\theta = 12.79^\circ$	99.9%
Absorption correction	Semi-empirical from equivalents
Refinement method	Full-matrix least-squares on F^2
Data / restraints / parameters	3061 / 60 / 131
Goodness-of-fit on F^2	1.642
Final R indices [$I > 2\sigma(I)$]	$R_1 = 0.1325$, $wR_2 = 0.3908$
R indices (all data)	$R_1 = 0.1504$, $wR_2 = 0.4051$
Largest diff. peak and hole	0.579 and $-0.612 \text{ e}/\text{\AA}^3$

3.4.4 Fourier-Transform Infrared Spectra of MOFFs

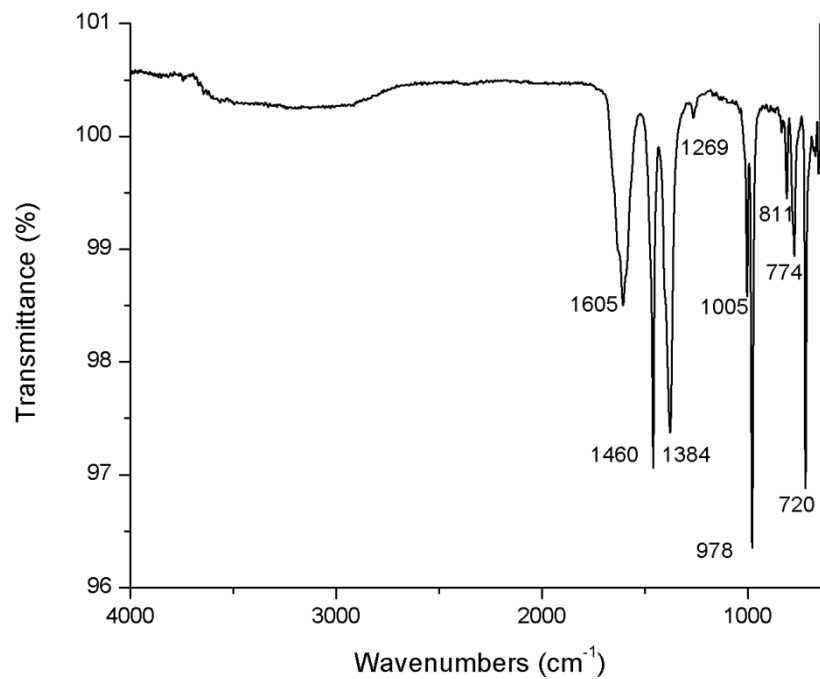


Figure 3.12 Fourier-transform infrared spectrum of **MOFF-1**.

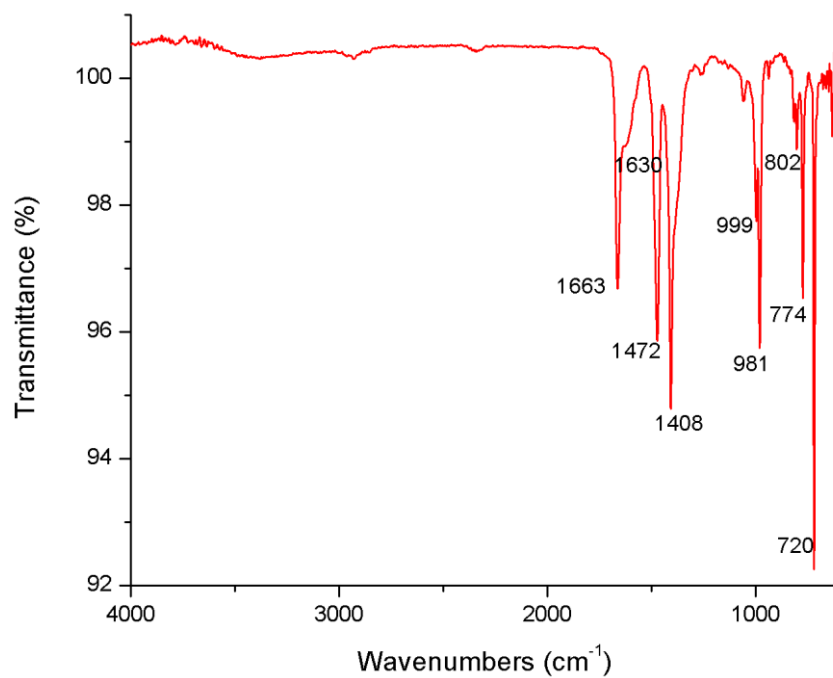


Figure 3.13 Fourier-transform infrared spectrum of **MOFF-2**.

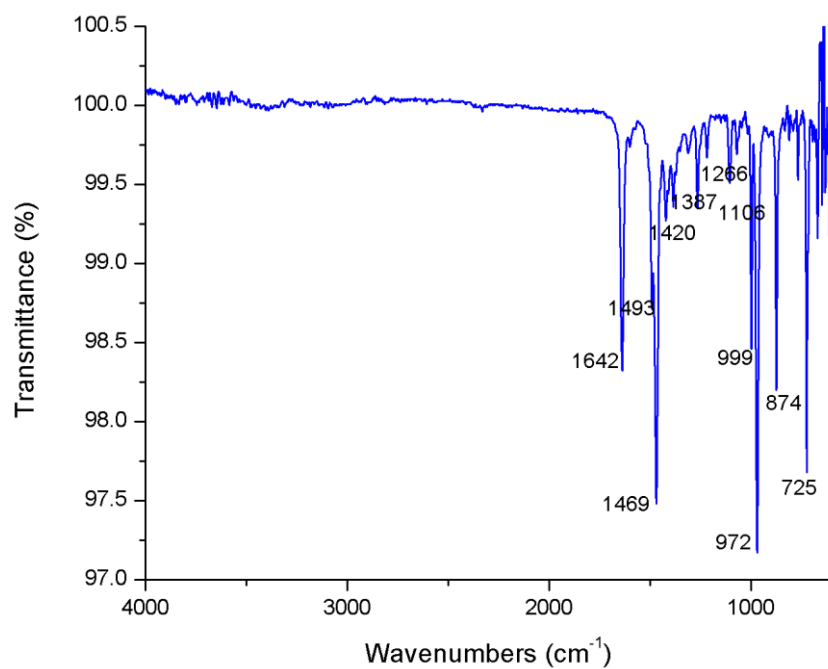


Figure 3.14 Fourier-transform infrared spectrum of **MOFF-3**.

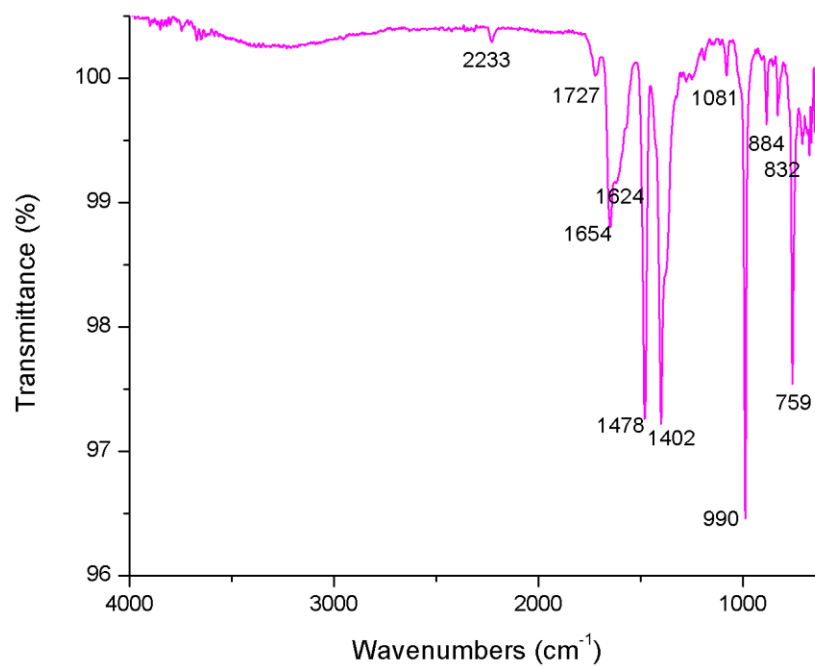


Figure 3.15 Fourier-transform infrared spectrum of **MOFF-4**.

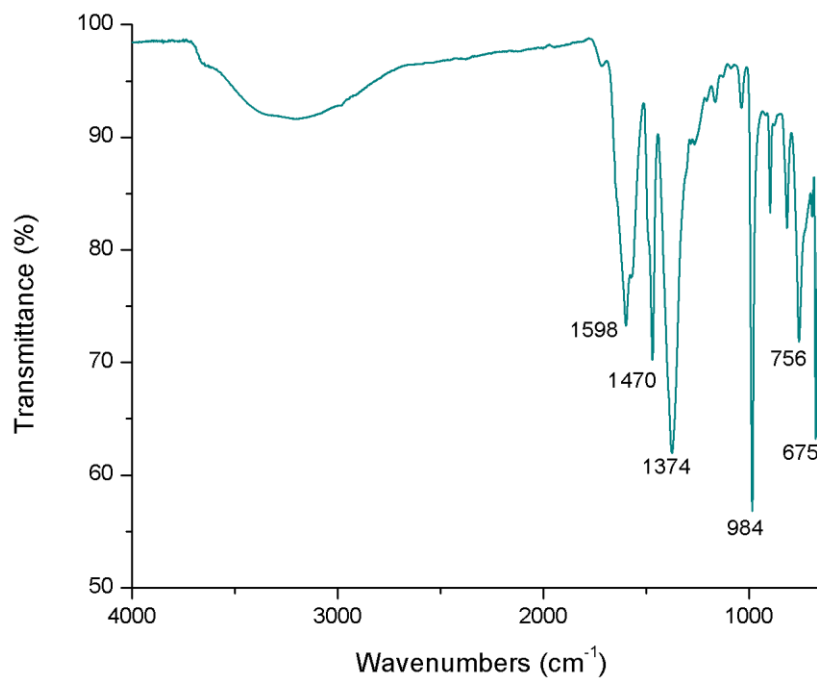


Figure 3.16 Fourier-transform infrared spectrum of **MOFF-5**.

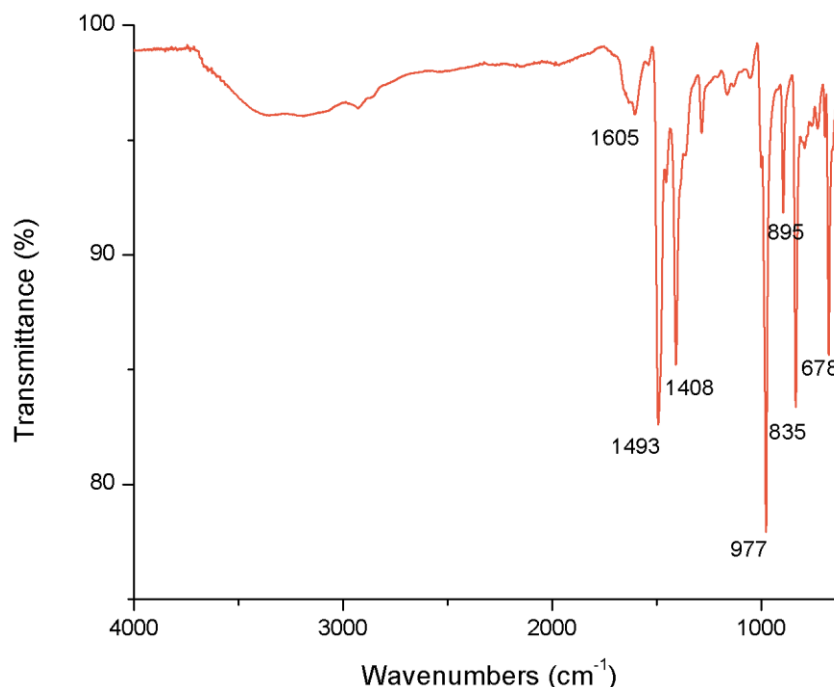


Figure 3.17 Fourier-transform infrared spectrum of **MOFF-6**.

3.4.5 Powder X-ray Diffraction Patterns of MOFFs

Sample Activation. Samples of **MOFFs 1–3** were dried in a 120 °C vacuum oven for 24 h. For **MOFF-3**, in order to retain the H₂O terminal groups in the channels, SCD drying was also performed (Chapter 3.4.9). For **MOFF-4**, no activation was performed due to its negligible accessible pores. Although the SCD drying was applied to mesoporous **MOFF-5** and **-6**, the fragile frameworks did not retain the long-range crystallographically ordered structure and exhibit amorphous PXRD patterns, which are not presented here. However, by using an improved drying procedure it may be possible to retain the MOF's crystalline structure after activation.

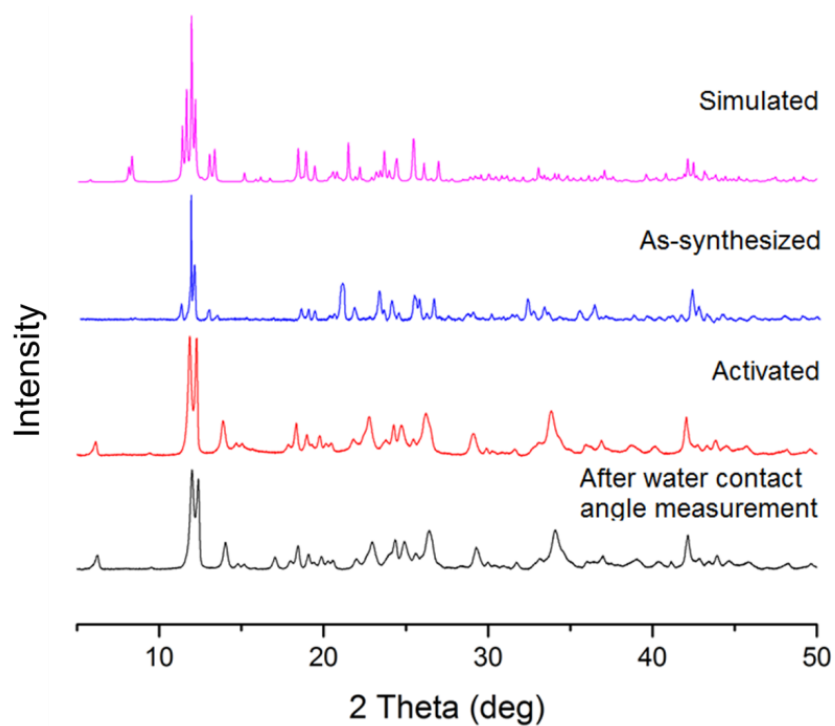


Figure 3.18 Powder X-ray diffraction pattern of **MOFF-1**.

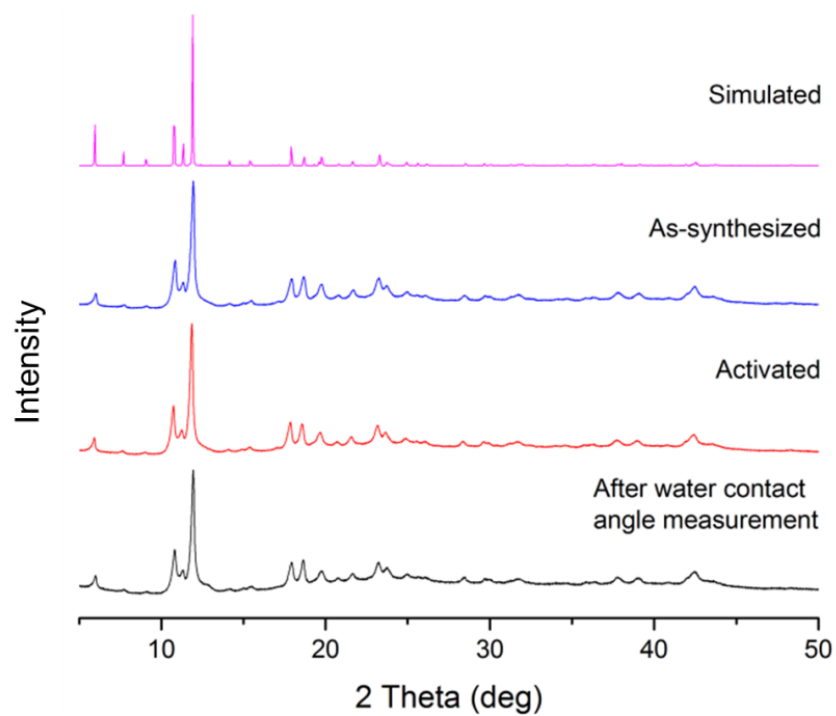


Figure 3.19 Powder X-ray diffraction pattern of **MOFF-2**.

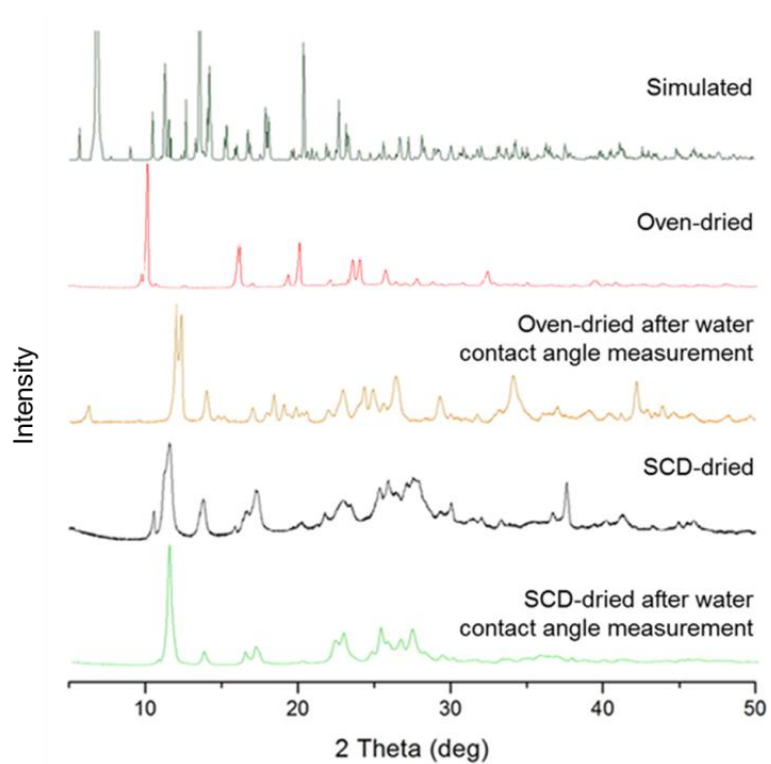


Figure 3.20 Powder X-ray diffraction pattern of **MOFF-3**.

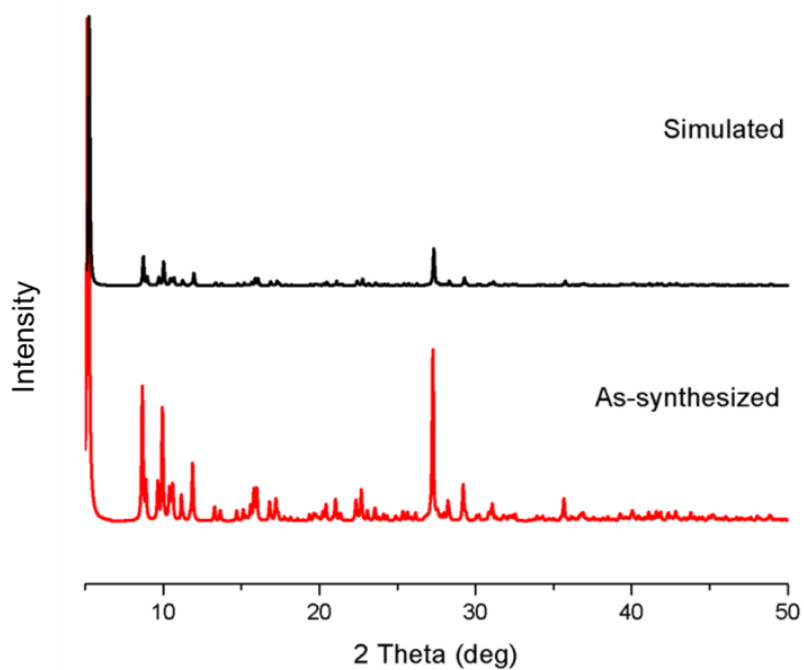


Figure 3.21 Powder X-ray diffraction pattern of **MOFF-4**.

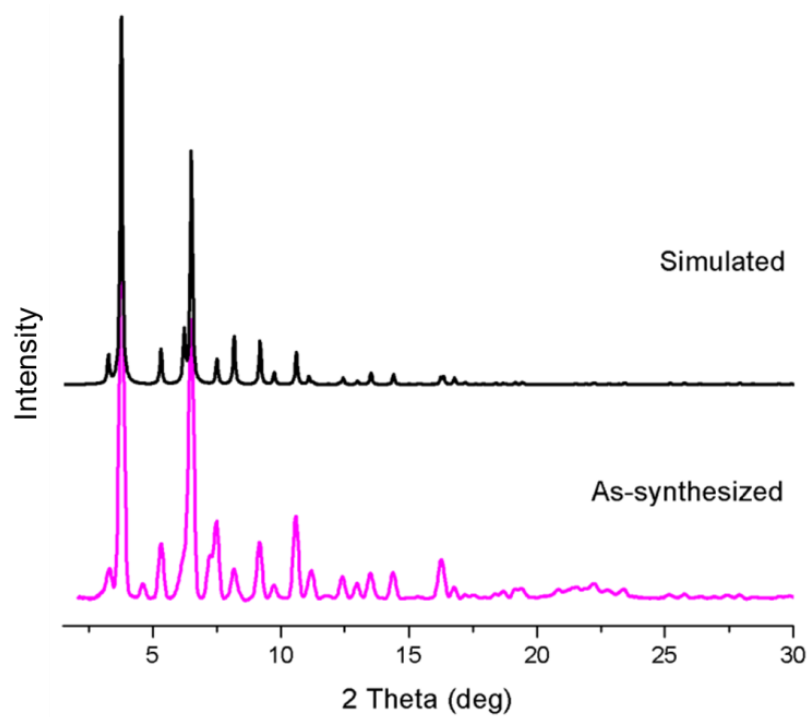


Figure 3.22 Powder X-ray diffraction pattern of **MOFF-5**.

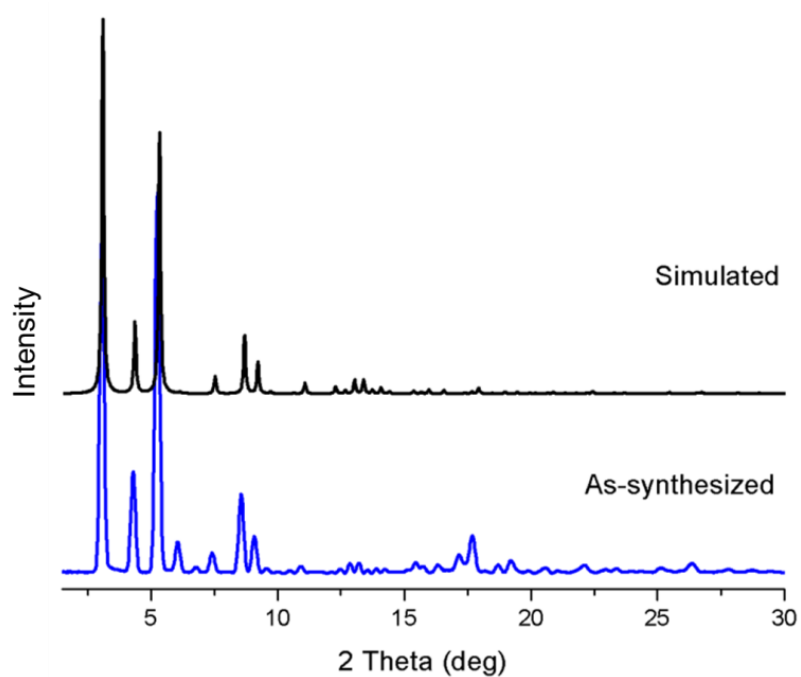


Figure 3.23 Powder X-ray diffraction pattern of **MOFF-6**.

3.4.6 Thermogravimetric Analyses of MOFFs

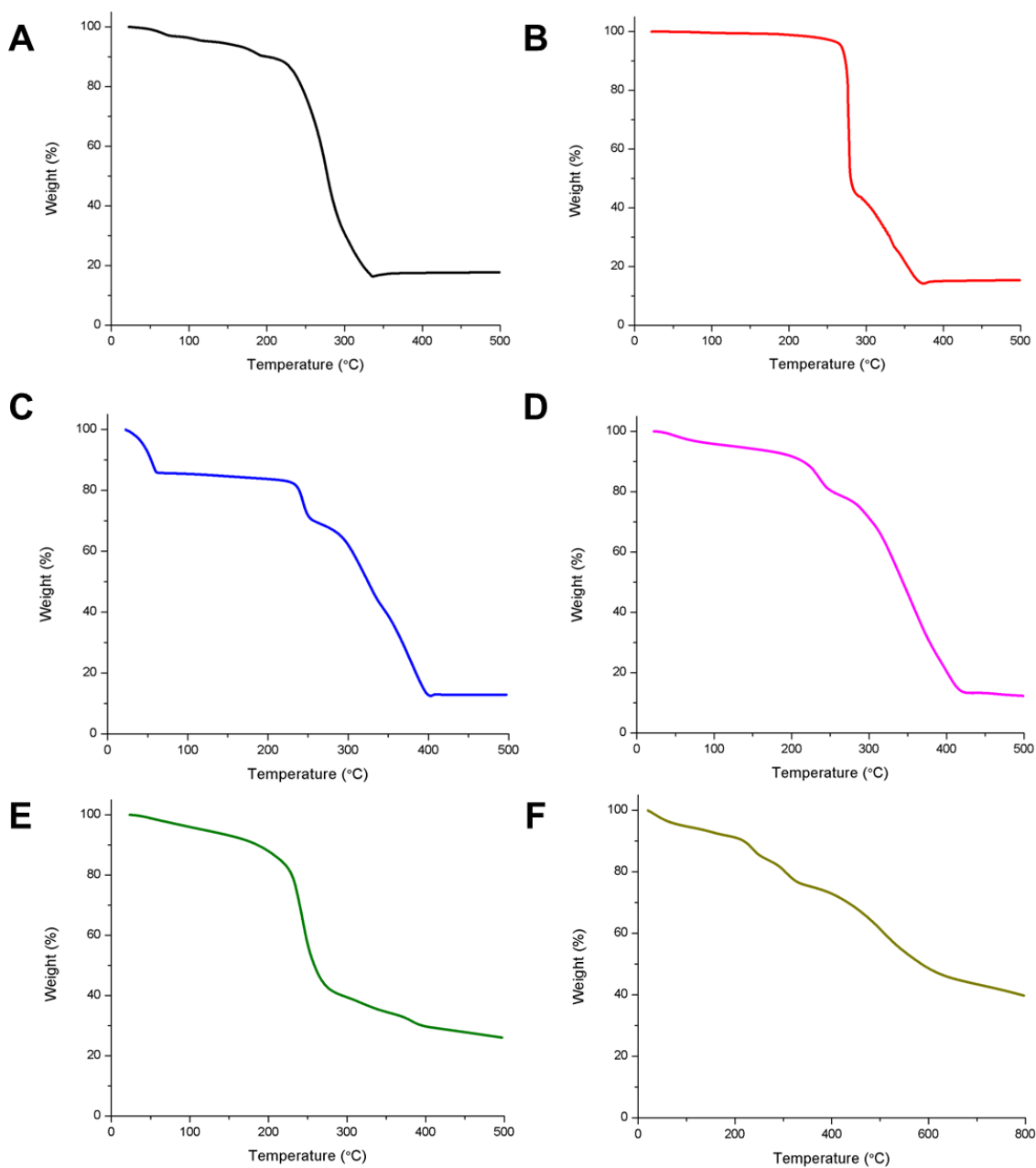


Figure 3.24 TGA traces of (A) **MOFF-1**, (B) **MOFF-2**, (C) **MOFF-3**, (D) **MOFF-4**, (E) **MOFF-5**, and (F) **MOFF-6**.

3.4.7 Gas and Water Vapor Adsorption Isotherms

A Micromeritics ASAP 2020 Surface Area and Porosity Analyzer was used to measure N₂, O₂, CO₂, and H₂O adsorption isotherms. Oven-dried sample tubes equipped with TranSeals™ (Micromeritics) were evacuated and tared. Samples (100-300 mg) were transferred to the sample tube, which was then capped by a TranSeal™. Samples were heated to 150 °C (**MOFFs 1–3**) or 35 °C (**MOFF-5** and **-6**) under high vacuum (10^{-3} – 10^{-4} Torr) and held until the outgas rate was less than 2 mTorr/minute. The evacuated sample tubes were weighed again, and the sample mass was determined by subtracting the mass of the previously tared tubes. N₂ isotherms were measured using a liquid nitrogen bath (77 K). H₂O isotherms were measured at 293 K with temperature control provided by Neslab LT-50DD refrigerated circulating bath. Ultra high purity grade (99.999% purity) N₂, O₂, CO₂, and He, oil-free valves and gas regulators were used for all free space corrections and measurements. Relative pressure (P/P_o) range for BET analysis was taken from 5×10^{-5} to 0.1. Nitrogen adsorption was not performed on **MOFF-4**; H₂O adsorption was performed on **MOFFs 1-3**; O₂ and CO₂ adsorptions were performed on **MOFF-3** only (Figure 3.10).

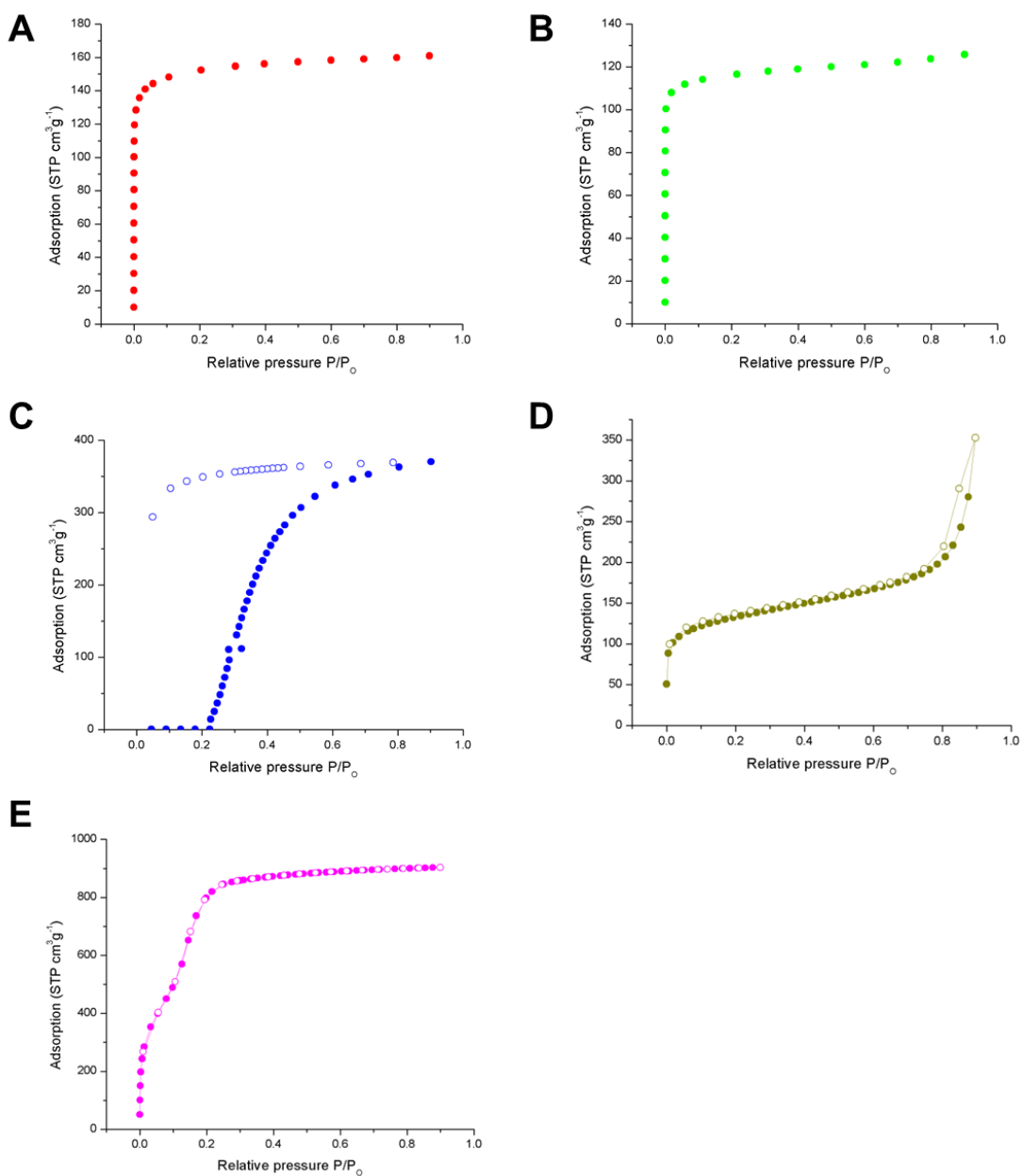


Figure 3.25 N_2 (77 K) adsorption isotherms of (A) **MOFF-1**, (B) **MOFF-2**, (C) **MOFF-3**, (D) **MOFF-5**, and (E) **MOFF-6**.

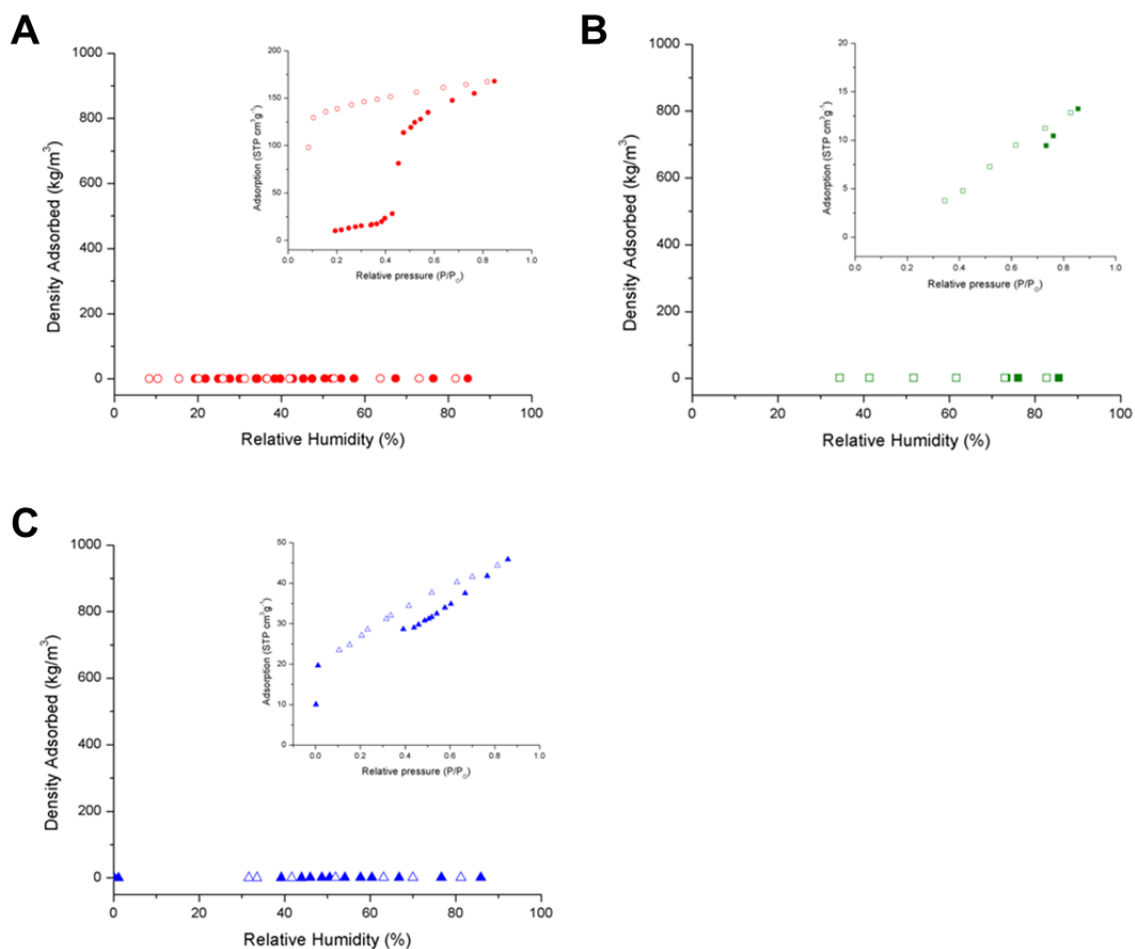


Figure 3.26 H₂O vapor (293 K) adsorption isotherms (density adsorbed (kg/m³) versus relative humidity (%)) of (A) **MOFF-1**, (B) **MOFF-2**, and (C) **MOFF-3**. Inserts: quantity adsorbed (STP cm³g⁻¹) versus relative pressure (P/P_0).

3.4.8 Advancing Contact Angle Measurements

Before the measurements, all MOFFs were dried in a 120 °C vacuum oven for 24 h. In addition, **MOFF-1** was air-dried, and **MOFF-3** was SCD-dried in order to retain their terminal MeOH and H₂O groups, respectively. **MOFF-5** and **-6** were not tested because the structures of mesoporous frameworks were not stable in the presence of water. The finely ground **MOFFs** crystals were pressed between two Silicon (100) slides that had been previously rinsed with absolute EtOH and dried in a stream of nitrogen gas. After removing the upper slide, the exposed crystal surface was used for conducting contact angle measurements. A ramé-hart model 100 contact angle goniometer was employed to measure the contact angle of water, *n*-hexadecane and cis-perfluorodecalin on the **MOFFs**. The contacting liquids were dispensed on the surface of the **MOFFs** using a Matrix Technologies micro-Electrapette 25 at the slowest speed of 1 µL/s. The measurements were performed at 293 K, with the pipet tip remaining in contact with the drop. The reported data for each sample were the average of three measurements obtained from three different slides for each **MOFF** with advancing contact angles (θ_a) recorded for both edges of the drop.

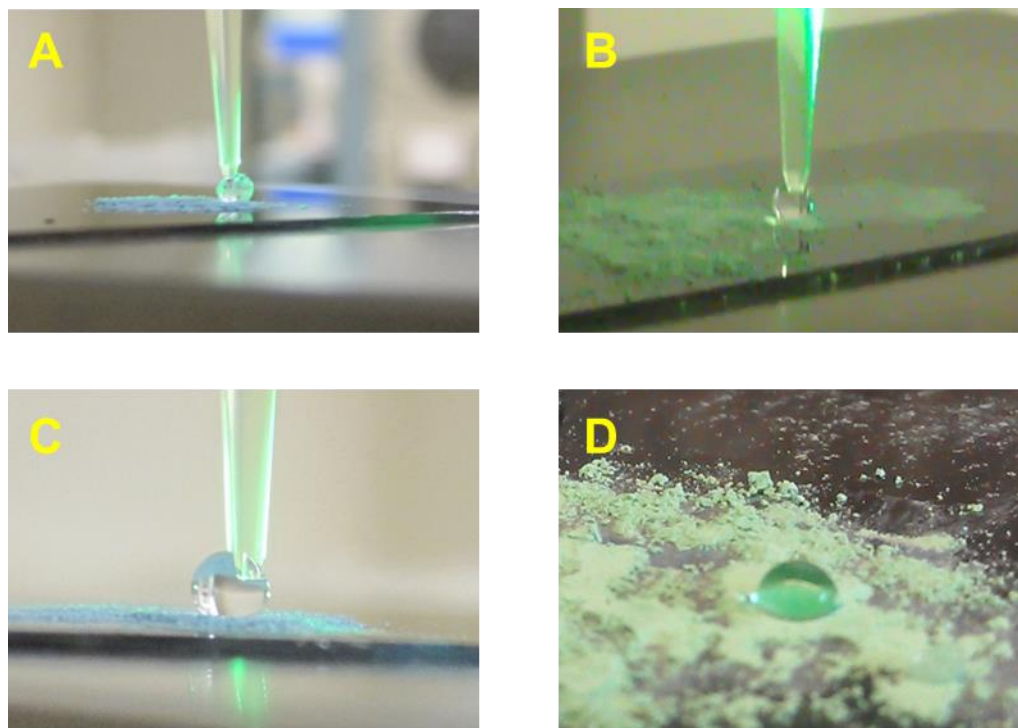


Figure 3.27 Pictures of oven-dried (A) **MOFF-1**, (B) **MOFF-2**, (C) **MOFF-3**, and (D) **MOFF-4** after a drop of water was placed onto the samples.

3.4.9 Supercritical CO₂ Activation of MOFF-5 and -6

Absolute EtOH was added to the crystals after the mother liquor was decanted. The EtOH was then decanted and replaced daily for 3 d and the crystals were left in ethanol until the next step. Approximately 60 mg of crystals were transferred into a Tousimis Samdri-PVT-3D super-critical CO₂ dryer. Excess EtOH was decanted, the temperature was lowered to 0 °C, and the chamber was filled with supercritical CO₂ (ultrahigh grade CO₂ with a siphon tube from Matheson Tri-Gas Inc. was used). The sample was soaked for a total of 48 h, venting for 10 min for 10 times. Full exchange of EtOH for liquid CO₂ in the pores of the crystals was signaled by a color change. The chamber was then heated to 40 °C and the pressure in the chamber was above 1300 psi.

The supercritical CO₂ was bled off for 24 h until the chamber was at ambient pressure. The chamber was opened and the sample was quickly sealed and taken into an argon atmosphere glove box for further manipulations. Dried crystals were transferred into a pre-weighed glass sample tube. The tube was sealed and quickly transferred to a system providing 10⁻⁴ Torr dynamic vacuum. The sample was kept under vacuum at 35 °C for 15 h and then used for gas adsorption measurements.

3.5 References

- [1] Plunkett, R. J. *The History of Polytetrafluoroethylene: Discovery and Development*, pp. 261–266 in "High Performance Polymers: Their Origin and Development. Proceedings of the Symposium on the History of High Performance Polymers at the American Chemical Society Meeting held in New York, April 15–18, 1986", Seymour R. B.; Kirshenbaum G. S. (Eds.), Elsevier: New York, 1986.
- [2] (a) Scheirs, J. *Modern Fluoropolymers: High Performance Polymers for Diverse Applications*; Wiley: Hoboken, NJ, 1997. (b) Wall, L. A. *Fluoropolymers*; Wiley: New York, NY, 1972.
- [3] Pachfule, P.; Dey, C.; Panda, T.; Vanka, K.; Banerjee, R. *Cryst. Growth Des.* **2010**, *10*, 1351–1363.
- [4] Pachfule, P.; Dey, C.; Panda, T.; Banerjee, R. *CrystEngComm* **2010**, *12*, 1600–1609.

- [5] Pachfule, P.; Das, R.; Poddar, P.; Banerjee, R. *Inorg. Chem.* **2011**, *50*, 3855–3865.
- [6] Pachfule, P.; Das, R.; Poddar, P.; Banerjee, R. *Cryst. Growth Des.* **2011**, *11*, 1215–1222.
- [7] (a) Pan, L.; Sander, M. B.; Huang, X.; Li, J.; Smith, M.; Bittner, E.; Bockrath, B.; Johnson, J. K. *J. Am. Chem. Soc.* **2004**, *126*, 1308–1309. (b) Wang, X.; Liu, L.; Conato, M.; Jacobson, A. J. *Cryst. Growth Des.* **2011**, *11*, 2257–2263.
- [8] Pachfule, P.; Chen, Y.; Jiang, J.; Banerjee, R. *Chem. Eur. J.* **2012**, *18*, 668–694.
- [9] Hulvey, Z.; Wragg, D. S.; Lin, Z.; Cheetham, A. K. *Dalton Trans.* **2009**, 1131–1135.
- [10] Hulvey, Z.; Sava, D. A.; Eckert, J.; Cheetham, A. K. *Inorg. Chem.* **2011**, *50*, 403–405.
- [11] Hulvey, Z.; Furman, J. D.; Turner, S. A.; Tang, M.; Cheetham, A. K. *Cryst. Growth Des.* **2010**, *10*, 2041–2043.
- [12] Hulvey, Z.; Falcao, E. H. L.; Eckert, J.; Cheetham, A. K. *J. Mater. Chem.* **2009**, *19*, 4307–4309.
- [13] Hulvey, Z.; Ayala, E.; Furman, J. D.; Forster, P. M.; Cheetham, A. K. *Cryst. Growth Des.* **2009**, *9*, 4759–4765.
- [14] Sumida, K.; Foo, M. L.; Horike, S.; Long, J. R. *Eur. J. Inorg. Chem.* **2010**, 3739–3744.

- [15] For a related fluorinated tetrazolate MOF linker, see also: Pachfule, P.; Chen, Y.; Sahoo, S. C.; Jiang, J.; Banerjee, R. *Chem. Mater.* **2011**, *23*, 2908–2916.
- [16] Yang, C.; Kaipa, U.; Mather, Q. Z.; Wang, X.; Nesterov, V.; Venero, A. F.; Omary, M. A. *J. Am. Chem. Soc.* **2011**, *133*, 18094–18097.
- [17] Yang, C.; Wang, X.; Omary, M. A. *J. Am. Chem. Soc.* **2007**, *129*, 15454–15455.
- [18] Halford, B. *Chem. Eng. News* **2011**, *89*, 37.
- [19] (a) Colby, D. A.; Bergman, R. G.; Ellman, J. A. *Chem. Rev.* **2010**, *110*, 624–655.
(b) Chen, X.; Engle, K. M.; Wang, D.-H.; Yu, J.-Q. *Angew. Chem., Int. Ed.* **2009**, *48*, 5094–5115. (c) Lyons, T. W.; Sanford, M. S. *Chem. Rev.* **2010**, *110*, 1147–1169.
- [20] (a) Do, H.-Q.; Daugulis, O. *J. Am. Chem. Soc.* **2008**, *130*, 1128–1129. (b) Do, H.-Q.; Daugulis, O. *J. Am. Chem. Soc.* **2008**, *130*, 15185–15192. (c) Do, H.-Q.; Daugulis, O.; Shabashov, D. *Acc. Chem. Res.* **2009**, *42*, 1074–1086. (d) Do, H.-Q.; Daugulis, O. *J. Am. Chem. Soc.* **2011**, *133*, 13577–13586.
- [21] Popov, I. *Synthetic and Methodological Studies in Copper and Palladium-Catalyzed Carbon-Carbon and Carbon-Heteroatom Bond Formation*; PhD Thesis, University of Houston, 2014.
- [22] Chen, T.-H.; Popov, I.; Zenasni, O.; Daugulis, O.; Miljanić, O. Š. *Chem. Commun.* **2013**, *49*, 6846–6848.

- [23] Furukawa, H.; Kim, J.; Ockwig, N. W.; O’Keeffe, M.; Yaghi, O. M. *J. Am. Chem. Soc.* **2008**, *130*, 11650–11661.
- [24] (a) Dau, P. V.; Kim, M. S.; Garibay, J. F.; Munch, H. L.; Moore, C. H.; Cohen, S. M. *Inorg. Chem.* **2012**, *51*, 5671–5676. (b) Seki, K. *Chem. Commun.* **2001**, 1496–1497.
- [25] Dincă, M.; Yuand, A. F.; Long, J. R. *J. Am. Chem. Soc.* **2006**, *128*, 8904–8913.
- [26] Zhu, N.; Tobin, G.; Schmitt, W. *Chem. Commun.* **2012**, *48*, 3638–3640.
- [27] Freely available for Linux, MacOSX and Windows operating systems, from: <http://www.ccdc.cam.ac.uk/Solutions/CSDSystem/Pages/Mercury.aspx>.
- [28] Furukawa, H.; Go, Y. B.; Ko, N.; Park, Y. K.; Uribe-Romo, F. J.; Kim, J.; O’Keeffe, M.; Yaghi, O. M. *Inorg. Chem.* **2011**, *50*, 9147–9152.
- [29] Calculations of **MOFFs**’ percent weight loss only roughly correlate with the amount of solvent observed in the crystal structure. The electron densities associated with the disordered solvent (present within MOFF pores) were subtracted using the SQUEEZE routine and their weight contributions to the crystals were not quantified.
- [30] Dincă, M.; Long, J. R. *Angew. Chem., Int. Ed.* **2008**, *47*, 6766–6779.
- [31] (a) Nguyen, J. G.; Cohen, S. M. *J. Am. Chem. Soc.* **2010**, *132*, 4560–4561. (b) Wade, C.; Corrales-Sanchez, R. T.; Narayan T.; Dincă, M. *Energy Environ. Sci.* **2013**, *6*, 2172–2177.
- [32] Cychosz, K. A.; Matzger, A. J. *Langmuir* **2010**, *26*, 17198–17202.

- [33] Jiang, D.; Burrows, D. A.; Edler, K. J. *CrystEngComm* **2011**, *12*, 6916–6919.
- [34] Zacher, D.; Schmidt, R.; Wöll, C.; Fischer, R. A. *Angew. Chem., Int. Ed.* **2011**, *50*, 176–199.
- [35] The large deviation (> 1%) between calculated and obtained elemental analysis is presumably due to the incompletely removed guest molecules remaining in the collapsed structure of MOF.

Chapter Four

Synthesis, Characterization, and Applications of a Perfluorinated Noncovalent Organic Framework

4.1 Introduction

Crystallographically ordered porous materials such as MOFs and COFs are characterized by high thermal stability, exceptional surface areas, and—perhaps most importantly—highly modular syntheses which allow facile modification of pore sizes, shapes, surface functionalities, and polarities. While this strategy allows superior control over pore properties, it comes with a price. As extended crystalline materials, MOFs and COFs are essentially impossible to recrystallize or dissolve without decomposition, and thus the scope of their solution-phase characterization and processability is limited. Significant advances have been made in the ability to deposit MOFs and COFs controllably on surfaces,^{1,2,3} but considerable benefits could still come from the ability to construct robust porous structures—analogueous to COFs and MOFs—from discrete small molecules. In principle, that should be a straightforward task: there is no fundamental correlation between infinite structures and porosity. Nevertheless, highly porous crystal structures of discrete molecules are rare and difficult to predict *a priori*;⁴ furthermore, even when a small molecule can be organized into a porous structure, such structures are typically fragile after solvent removal and thus unsuitable for applications.

In recent years, work by Chen,^{5,6} Cooper,⁷ Mastalerz,⁸ and others^{9,10,11} has resulted in molecular crystals characterized by high porosity. These noncovalently held structures can be intrinsically or extrinsically porous. In the former case, the molecule itself contains a large pore—typically within a macrocycle or a molecular capsule. Organization of these within the crystal then results in an extended structure which replicates individual molecules' porosities. In the latter case, the monomer molecule itself is inherently nonporous, and all porosity comes as the consequence of its crystal packing. Using intrinsic strategy, materials with surface areas over 3,500 m² g⁻¹ have been constructed by Mastalerz and co-workers;^{8f} the same research group also prepared extrinsically porous molecular crystals with surface areas in excess of 3,000 m² g⁻¹.^{8b,8c} However, some of these highly porous molecular crystals are still using hydrolytically sensitive imine and boronate ester functionalities and are thus rather fragile.¹² Thus, structurally, thermally, and hydrolytically stable porous molecular crystals are still rare and further research on them is warranted.

Various noncovalent interactions such as hydrogen bonding, charge–charge, donor–acceptor, $[\pi \cdots \pi]$, van der Waals, and hydrophilic/hydrophobic interactions are often used to form highly complex and symmetrical supramolecular architectures.¹³ Rational design of the molecule which possesses multiple sites for directional and strong supramolecular interactions could be a key step toward a stable structure. Stacking between aromatic rings is a common interaction for building 3D structures from 2D sheets and is observed in, e.g., graphite and COFs. With our previous work on perfluorinated aromatic compounds (Chapter 3), we established a general strategy for

placing both electron-deficient and electron-rich components into the same molecule, which was a promising lead for the creation of favorable $[\pi \cdots \pi]$ interaction.¹⁴

Recently, Fujita and co-workers used hydrophobic metal-organic cage to capture polyfluorinated aliphatic and aromatic compounds in aqueous solution.¹⁵ It was expected that solid-state fluororous porous materials will be more useful for storage and capture of fluororous compounds. For instance, fluororous pollutants such as chlorofluorocarbons (CFCs, also known as Freons), and their intermediate replacements hydrochlorofluorocarbons (HCFCs), are ozone-depleting substances and potent contributors to the greenhouse effect, influencing global climate. CFCs have been phased out in both industrialized and developing nations, with a total global ban on production achieved in 2010 due to the Montreal Protocol.¹⁶ However, their first-stage replacements HCFCs still can accumulate in the lower atmosphere and deplete ozone.¹⁷

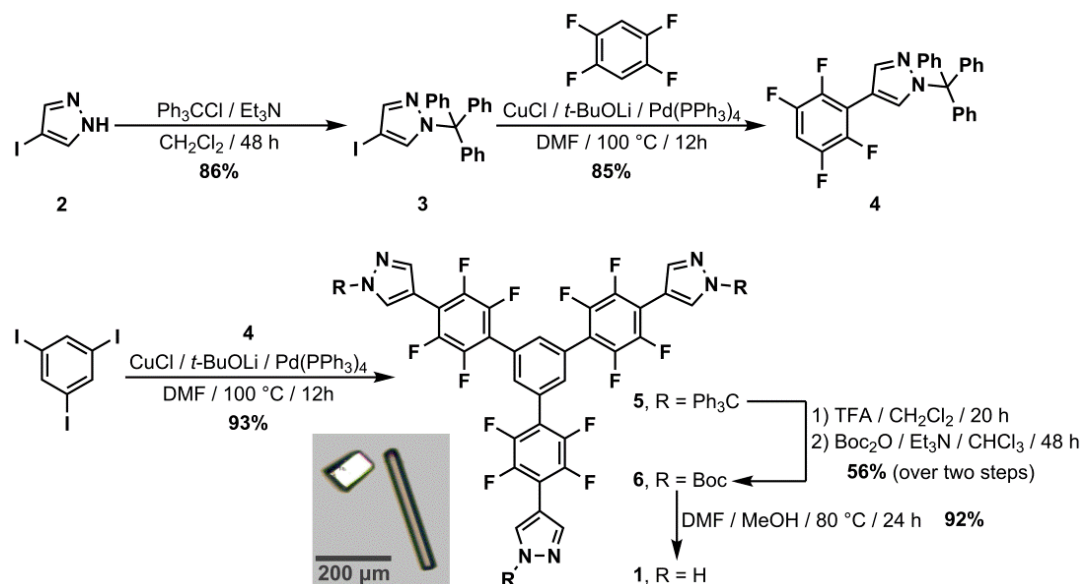
In this chapter, we present the synthesis and characterization of a trispyrazole **1** (Scheme 4.1) which organizes into a highly robust supramolecular structure with high extrinsic porosity, through a combination of $[\pi \cdots \pi]$ stacking¹⁸ and hydrogen bonding.¹⁹ Its porosity and gas binding ability rank highly among the other noncovalently connected materials presented to date. In addition, **1** also captures as much as three quarters of its own weight in hydrocarbon and fluorocarbon analytes, which should be of interest both in fuel processing and the capture of potent greenhouse species.

4.2 Results and Discussion

4.2.1 Synthesis of Compound 1

The synthesis of **1** commenced with the commercially available 4-iodopyrazole (**2** in Scheme 4.1). Compounds **2–6** were prepared by Ilya Popov from Prof. Olafs Daugulis' group (UH). The masking of the N–H bond in **2** with a trityl (Ph₃C–) group gave compound **3**, which was subjected to a palladium-catalyzed coupling with an excess of 1,2,4,5-tetrafluorobenzene, to produce intermediate **4**. In **4**, only one of the two C–H bonds of tetrafluorobenzene was replaced with a functionalized pyrazole moiety. Another palladium-catalyzed coupling followed, combining 3.3 equivalents of **4** with 1,3,5-triiodobenzene and resulting in the trigonal precursor **5**. The trityl groups in **5** were removed by acidic treatment, and subsequently replaced with *tert*-butoxycarbonyl (Boc) groups. Heating of a solution of **6** in DMF and MeOH for one day at 80 °C resulted in single crystals of compound **1**; crystals are formed before the solution is cooled to room temperature. This protocol utilized previously reported protocols for the in situ deprotection of Boc group²⁰ and concurrent binding to metals.²¹

Scheme 4.1 Synthesis of Compound 1



4.2.2 Crystal Structure Analysis of Compound 1

Single-crystal X-ray diffraction data on **1** was obtained with the use of synchrotron radiation. The asymmetric unit contains parts of two crystallographically distinct molecules, one of which has a C₂ axis dissecting it. Several aspects of this structure are shown in Figure 4.1. The three arms of **1** twist in a propeller-like fashion out of the plane of the central ring, forming angles of 33.7, 33.8 and 46.3° (in the more symmetric molecule of **1**, all three angles are 32.8°). Each molecule of **1** establishes short contacts with twelve of its neighbors: six [N–H⋯N] hydrogen bonds, which create a hexagonal two-dimensional lattice, and six [π⋯π] stacking arrangements which propagate these layers into the third dimension. Pyrazoles at the end of each arm of **1** establish hydrogen bonds with two adjacent molecules (Figure 4.1, left).²² These bonds are close to each other in length (N⋯H distances vary between 1.81 and 1.91 Å;²³ N⋯N

distances vary between 2.78(1) and 2.854(9) Å. Control of inter-layer relationships is achieved through $[\pi\cdots\pi]$ stacking of the electron-poor tetrafluorinated aromatic rings with the relatively electron-rich pyrazoles (Figure 4.1, center), but this relationship is highly unsymmetric. In each molecule of **1**, the most deplanarized of the three arms engages in the predicted $[\pi\cdots\pi]$ stacking with its "top" and "bottom" neighbors (shown in yellow in Figure 4.1, center). These AB stacks are symmetric, with centroid–centroid distances between the pyrazole and tetrafluorobenzene rings being 3.68 Å for the pair closer to the central benzene of black molecule in Figure 4.1, center, and 3.69 Å for the pair further away from the center (centroid–centroid distances are quoted because ring planes are not parallel and thus interplanar distance cannot be determined, *vide infra*). The angle between the adjacent planes of pyrazole and tetrafluorobenzene rings is 11.2° (for the inner pair) and 9.7° (for the outer pair). A more peculiar situation is observed with the other two "arms" of black molecule. In these, the top and the bottom neighbors are no longer equivalent. One (shown in red in Figure 4.1, center) establishes a pair of $[\pi\cdots\pi]$ stacking interactions characterized by centroid–centroid distances of 3.42 and 3.50 Å and interplanar angles of 10.3 and 11.4°, respectively, for the inner and outer pairs. But the other neighbor (shown in blue in Figure 4.1, center) establishes an oddly slipped $[\pi\cdots\pi]$ stacking, in which centroids of tetrafluorobenzene and pyrazole rings reside quite far from each other at 5.28 Å. In fact, the closest two rings are two tetrafluorobenzenes, with centroid–centroid distance of 4.08 Å, and essentially parallel arrangement of the planes (interplanar angle of 0.49°). This arrangement—which is repeated in the third arm of **1**—is caused by the steric mismatch of the central benzene ring with the "pyrazole triad" that resides above it in the next layer, and so one arm of the molecule must

sacrifice favorable $[\pi\cdots\pi]$ stacking interactions to accommodate this dimensional difference.

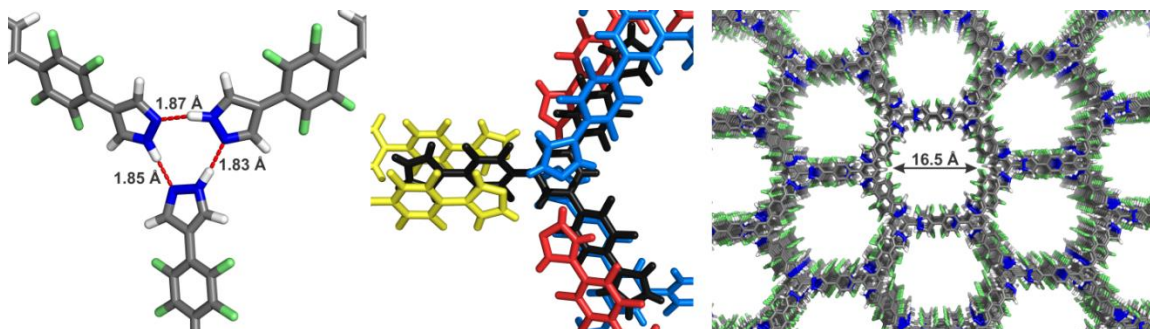


Figure 4.1 Crystal structure of compound **1**. Three pyrazoles come together in each of the layers (left) forming a triplet of hydrogen bonds. Each compound **1** engages in $[\pi\cdots\pi]$ stacking interactions with six of its neighbors, wherein electron-rich pyrazoles stack with electron-poor tetrafluorobenzene rings (center). Overall, a hexagonal network results, with infinite fluorine-lined channels protruding throughout the structure along the crystallographic *c*-axis (right).

Overall, a three-dimensional network results, with infinite one-dimensional channels protruding throughout the crystal along the crystallographic *c*-axis; these channels are lined with fluorines and have a diameter of approx. 16.5 Å. Layers of this crystal structure can be described as having **hnb** topology²⁴ with two distinct kinds of vertices, edges, and faces; adjacent layers are offset so that two faces of different kinds stack with each other. All structural elements of **1** are essential in producing the infinite porous structure: pyrazole is needed to establish the hydrogen bonding pattern within the two-dimensional layers, while the electron-poor perfluorinated ring can favorably $[\pi\cdots\pi]$ stack with the relatively electron-rich pyrazole.

4.2.3 Stability of Compound 1

Compound **1** is colorless and remarkably stable to solvents, acids, and bases. Visual inspection of the crystals shows no signs of crystal decomposition or dissolution in off-the-shelf dichloromethane, hexanes, toluene, or acetone for at least 30 days. Furthermore, after crystals of **1** treated with these solvents were dried and subjected to PXRD analysis, their PXRD patterns (Figure 4.2) were virtually identical to those of the original samples. Similar analysis confirmed the material to be stable to deionized water at 25 °C for at least 30 days, and at 100 °C for at least 7 days. Compound **1** also tolerated acids (1M HCl) and bases (2M NaOH) at 25 °C for at least 30 days. It is sparingly soluble in DMSO at 25 °C, but its solubility in this solvent considerably increases with temperature.

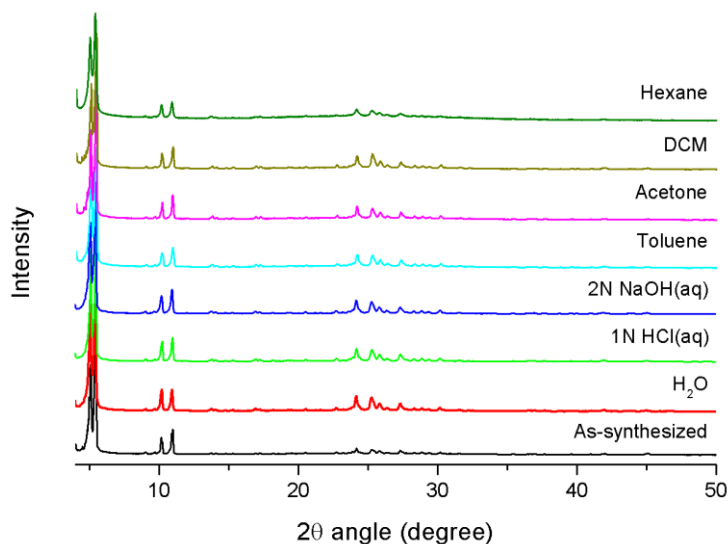


Figure 4.2 PXRD patterns of compound **1** after treatment with various solvents and drying. All crystals were soaked in the corresponding solvent, filtered, heated at 80 °C and dried in vacuo prior to PXRD analysis.

While many organic molecules form crystal structures with large apparent empty spaces, those spaces are typically occupied by solvent molecules, and tend to collapse upon solvent removal.^{7b} Compound **1** is different in that respect. Its single-crystal X-ray structure—refined from the data collected at 100 K—revealed significant electron density within the pores attributed to disordered solvent. However, all of that solvent appears to leave the pores within minutes at 25 °C without any observable loss of crystallinity. TGA (Figure 4.3A) of **1** was performed in both air (red trace in Figure 4.3A) and nitrogen (blue trace), confirming the absence of solvent in the as-synthesized crystal. After air-drying, heating of this material does not result in any weight loss up until 360 °C, significantly above the boiling points of all the solvents used in the synthesis. We speculate that the perfluorinated material associates only very weakly with the hydrophilic solvents—DMF, MeOH and residual H₂O—used in its synthesis. At 360 °C, compound **1** losses ~11% of its weight under both nitrogen and air. Oddly, the material recovered from the TGA experiment that was heated slightly above 360 °C shows almost exactly the same elemental analysis (within 3% for all elements) as the pristine nCOF. This observation could suggest partial sublimation, but it is unclear why this should result in a relatively sharp 11% weight loss observed. Isolation of minor amounts of the sublimed products from the TGA vent tubing and their characterization by NMR suggested a complex mixture of products. Overall, TGA of **1** is complicated by its relatively low sublimation point (vs. MOFs and COFs), and multiple apparent decomposition pathways. Slightly above 400 °C, the second stage of weight-loss begins; in a nitrogen-based TGA experiment, about 50% of the original weight remains even at 900 °C, while in air the entire sample is consumed below 600 °C.

To probe the structural changes that occur with heating, we also performed variable-temperature PXRD study of **1**; results, shown in Figure 4.3B, suggest that the crystal phase does not change until at least 250 °C. At higher temperatures, the PXRD pattern changes dramatically and irreversibly, but the material still appears largely crystalline, although the broad peak in PXRD pattern baseline may suggest a contribution from an amorphous phase. Differential scanning calorimetry (DSC) measurements show a sharp peak at 285 °C, consistent with a phase change. The discrepancy between the apparent decomposition temperatures obtained from TGA and PXRD measurements could be rationalized by the possibility that the phase change observed by PXRD is not associated with weight loss.

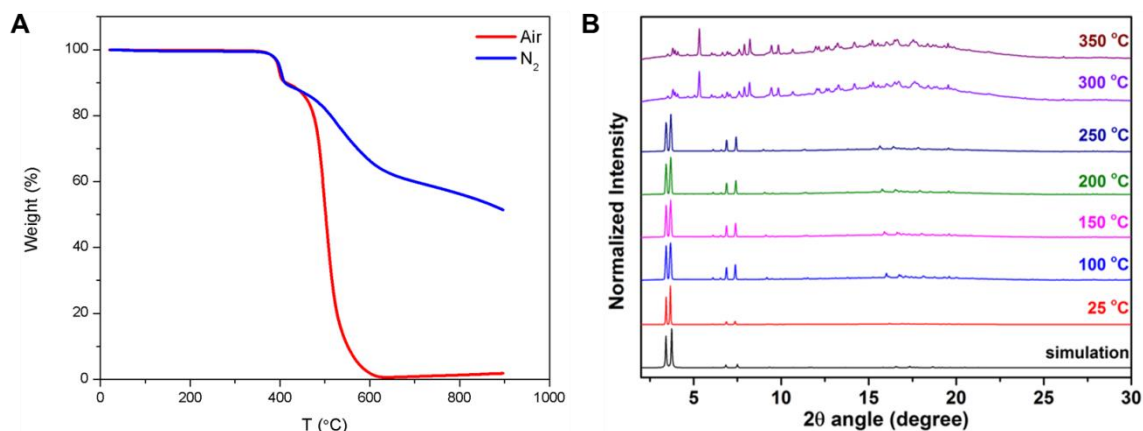


Figure 4.3 Thermal stability of compound **1**. (A) TGA in nitrogen (blue trace) and air (red trace) shows no weight loss until 360 °C, suggesting that no solvent was included in the crystal structure of **1**. Between 360 and 400 °C, compound **1** loses ~11% of its weight regardless of the carrier gas. Beyond 400 °C, slow decomposition of the material ensues under nitrogen, and much faster one under air. (B) Variable

temperature PXRD revealed no change in structure until at least 250 °C. Beyond that temperature, an irreversible phase change occurs. Structure of this new crystalline phase could not be determined.

Compound **1** can be sublimed in high vacuum (0.03 mmHg) at 250 °C during the course of 48 hours. The obtained material is crystalline, but its PXRD pattern matches neither the one of the as-synthesized sample of **1**, nor the one observed after **1** was heated to > 300 °C; this new phase is also completely nonporous. This finding, along with the irreversible thermal phase change observed by variable temperature PXRD (Figure 4.3B), suggests that the porous structure of **1** is a kinetic rather than a thermodynamic product.

4.2.4 Sorption Properties of Compound **1**

Gas sorption within the pores of **1** was probed using nitrogen, oxygen and CO₂ as guests. Based on the nitrogen adsorption isotherm (Figure 4.4A), the BET surface area of **1** was determined to be 1,159 m² g⁻¹, and the pore volume was estimated at 51%. These values agree reasonably well with those calculated from crystal structure data using *CrystalExplorer* and *PLATON*²⁵ software packages: 1,481 m² g⁻¹ and 56%, respectively.²⁶ Using nonlocal density functional theory (NLDFT), pores were estimated to be ~11 Å in diameter; this result is significantly lower than that measured from the crystal structure, but existing models may not be well-suited for fluorine-lined pores such as those of our nCOF. Uptake of CO₂ at 195 K is ~270 cm³ g⁻¹ (Figure 4.4A), a value among the highest observed for noncovalently connected structures. On the other hand, even at 90% relative humidity, crystals of **1** take up a negligible amount of H₂O vapor,

consistent with their highly hydrophobic character (Figure 4.4B). Hydrophobic behavior²⁷ was also confirmed by contact angle measurements with H₂O, which revealed a contact angle of $132 \pm 1^\circ$. We²⁸ and others²⁹ have previously observed similar hydrophobicity in MOFs constructed from fluorinated ligands.

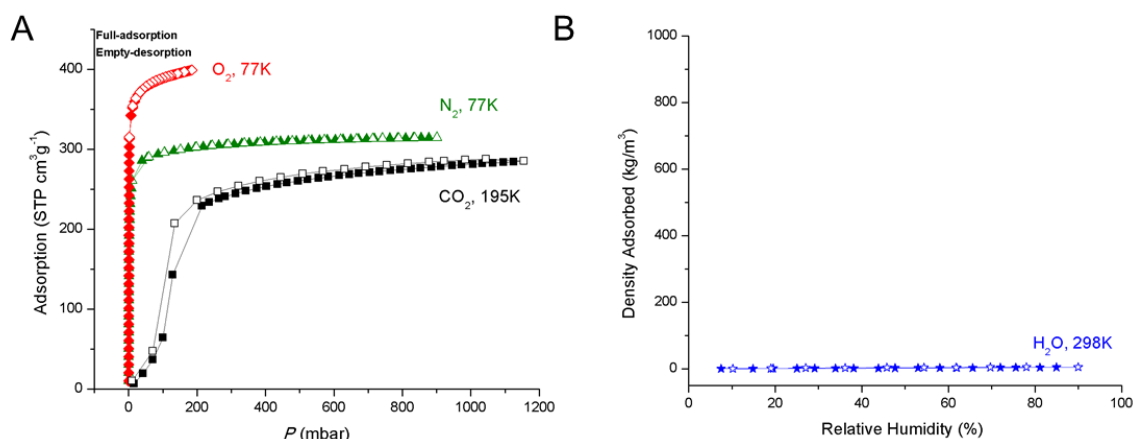


Figure 4.4 Gas sorption in crystals of compound **1**. (A) Uptake of N₂ (77 K), O₂ (77 K) and CO₂ (195 K); (B) negligible uptake of H₂O vapor (298 K)—even at 90% relative humidity.

Adsorption of liquid guests within the pores of **1** was followed by TGA with the help from Watchareeya Kaveevivitchai in Prof. Allan J. Jacobson's group.^{30,31} We have focused on fluorocarbons, hydrocarbons^{29a} and Freons³² as guests. The experimental design is illustrated in Figure 4.5A on the example of perfluorohexane (C₆F₁₄). Crystals of **1** were placed into the thermogravimetric balance and then heated to 120 °C, at which temperature they were kept for 1 h. The objective of this step was to remove any residual solvent and/or volatile guests from the pores of **1**. The heating was then discontinued and the material was allowed to cool down to 25 °C. At that point, the flow of carrier gas was

switched from pure nitrogen to nitrogen that was allowed to pass over a reservoir containing the liquid guest of interest. Using this methodology, we determined uptake capacities for several hydrocarbon and halogenated hydrocarbon guests shown in Table 4.1. In the case of fluorinated guests, the uptake is very fast: compound **1** gets saturated with 75 wt% of perfluorohexane in less than 20 seconds (Figure 4.5B). Reversibility of this process was confirmed by performing over 20 adsorption/desorption cycles with perfluorohexane as the guest (Figure 4.5C); no loss of capacity was observed. At room temperature, all of the examined guests can be removed completely and within minutes from the pores of **1** if vacuum is applied. However, if vacuum is not applied, fluorinated guests will remain in the pores of **1** even after the flow of guest-enriched nitrogen is stopped; this behavior, along with the very fast uptake, suggests high fluorophilicity of **1**. The last three guests in Table 4.1 are of particular interest because of their high greenhouse potential, which is hundreds to thousands of times more severe than that of CO₂.³³ The high weight sorption percentages profit from the absence of metals in the lightweight structure of **1**.

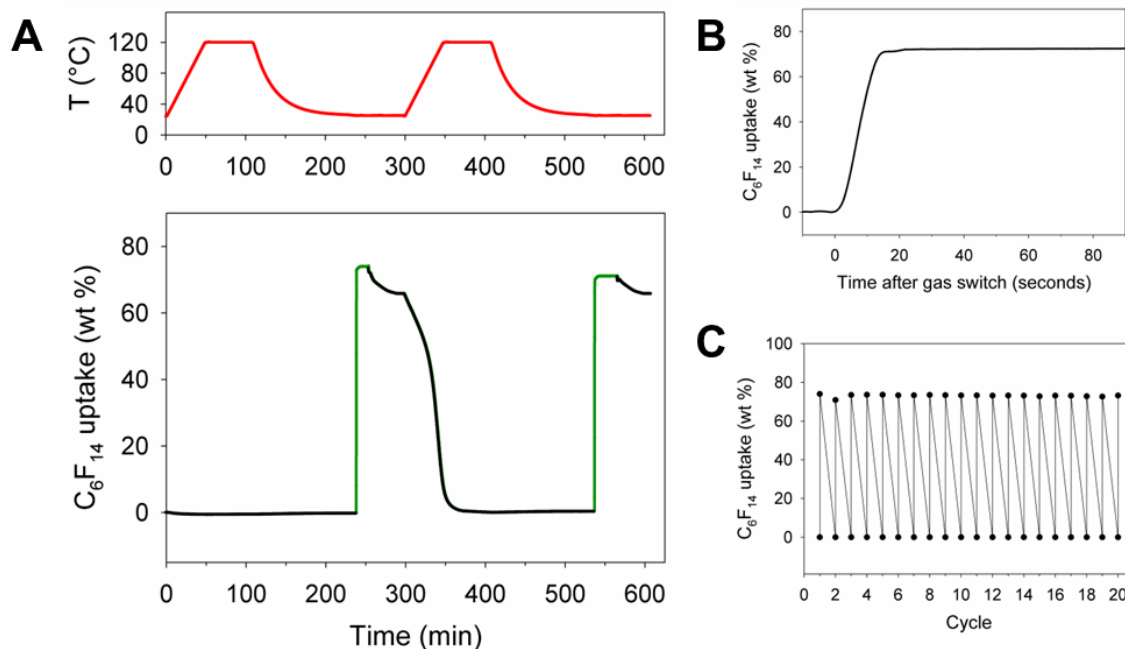


Figure 4.5 Sorption of perfluorohexane (C_6F_{14}) in crystals of **1**. (A) Crystals of **1** take up close to 75% of their own weight in perfluorohexane. Top chart shows the temperature program used, while the bottom one illustrates the uptake of the guest as the function of time. In the bottom chart, the black lines indicate the parts of the program when **1** was exposed only to nitrogen stream, while the green line describes the section of the program when nitrogen carrying C_6F_{14} vapors was passed over **1**. (B) Very steep adsorption of perfluorohexane, which is essentially complete in < 20 seconds. (C) Weight uptake percentages during 20 adsorption/desorption cycles performed on a single sample of compound **1**.

Table 4.1 Sorption Capacities and Other Characteristics of Guest Adsorbed within the Pores of Compounds **1**

Guest species	Boiling point [°C]	20-Year greenhouse gas potential (vs. CO ₂)	Adsorption in 1		
			Weight % ^a	In moles, per mole of 1 ^b	Desorption temperature [°C]
Toluene	110	—	30.6 (29.7)	2.39	62
Hexane	68	—	27.7 (27.4)	2.31	52
Cyclohexane	81	—	25.7 (25.6)	2.20	61
Chloroform	61	—	52.5 (53.4)	3.17	62
Dichloromethane	40	31	49.8 (49.6)	4.22	45
Perfluorohexane	56	6,600	74.0 (73.6)	1.58	62
CFC-113 (Cl ₂ FC–CClF ₂)	48	6,540	65.6 (64.9)	2.52	62
HCFC-225ca (CF ₃ CHF ₂ CHCl ₂)	51	429	58.0 (58.0)	2.06	63

^a Values in parenthesis indicate weight adsorption capacities observed in the second attempt.

^b Molar values were calculated using weight adsorption data from the first attempt.

4.3 Conclusions and Outlook

In conclusion, we have synthesized and exhaustively characterized extensively fluorinated trispyrazole **1**, which assembles into a porous organic structure held together through an unusual, but highly robust combination of hydrogen bonding and $[\pi \cdots \pi]$ stacking. This material is lightweight, thermally and hydrolytically stable, and is a superb adsorbent for hydrocarbons and their halogenated derivatives, many of which are potent greenhouse gases.

This study opens up several questions.³⁴ Can the arms of **1** be extended to yield an isorecticular series³⁵ of more porous structures? Can pyrazole be replaced with other functionalities that could allow the dissection and fine tuning of hydrogen bonding and $[\pi \cdots \pi]$ stacking effects? Can the structure of **1** be postsynthetically^{36,37} modified through nucleophilic aromatic substitutions of fluorines attached to the aromatic rings with other nucleophiles? Can different kinds of interactions be involved in the formation of framework for enhancing the properties of materials? Exploring these questions will be the future work in our group.

4.4 Experimental Section

4.4.1 General Methods

¹H and ¹⁹F NMR spectra were recorded on JEOL ECA-500 or ECX-400P spectrometers using the peaks of TMS or residual solvent as standards. Trifluorotoluene (PhCF₃, $\delta = -63.72$ ppm) was used as the internal standard in ¹⁹F NMR spectra. Melting points were measured in a Barnstead International Mel-TEMP[®] apparatus, and are uncorrected. Infrared spectra were recorded on a Perkin-Elmer Spectrum 100 FT-IR spectrophotometer using Pike MIRacle Micrometer pressure clamp. Microanalyses were conducted by Intertek USA, Inc. TGA were carried out on a TA Instruments TGA 2050 thermogravimetric analyzer at a temperature ramping rate of 2 °C/min under the flow of N₂ and air gas. Differential scanning calorimetry measurement was performed on a Mettler Toledo gas controller DSC system. Crystalline sample was placed in an

aluminum crucible, heated up to 300 °C and then cooled down to −150 °C at a rate of 20 °C/min under N₂.

The following starting materials and solvents were obtained from the respective commercial sources and used without further purification: DMF (TCI America); Perfluorohexane, 1,1,2-trichlorotrifluoroethane (CFC-113), 3,3-dichloro-1,1,1,2,2-pentafluoropropane (HCFC-225ca), 2,3,5,6-tetrafluorophenol, triflic anhydride and triflic acid (SynQuest Labs); MeOH, toluene, *n*-hexane, dichloromethane, chloroform, cyclohexane (Aldrich); water (Milli-Q, deionized). All the gases used for gas adsorption measurements were purchased from Matheson Tri-Gas Inc.

4.4.2 Synthesis, Sublimation, and Stability Testing of Compound 1

The starting materials and precursors of compound **1** shown in Scheme 4.1 were prepared by Ilya Popov.³⁸ Compound **6** (0.20 g, 0.20 mmol) was added to a 100 mL glass bottle. Solvents DMF (20 mL) and MeOH (20 mL) were added to the solid and the mixture was sonicated for 10 min. The bottle was capped and placed into an 80 °C oven for 1 d. The resulting colorless rod-shape crystals (mp > 350 °C) were washed with MeOH and air-dried. The yield of **1** was 92% (0.13 g), calculated from the dried sample. ¹H NMR (500 MHz, DMSO-*d*₆) δ 13.54 (s, 3H), 8.36 (s, 3H), 8.03 (s, 3H), 7.95 (s, 3H) ppm. ¹⁹F NMR (470 MHz, DMSO-*d*₆) δ −141.5 to −141.6 (m, 6F), −144.7 to −144.9 (m, 6F) ppm. FT-IR : 3469 (m, $\tilde{\nu}_{\text{N-H}}$), 3213 (s, $\tilde{\nu}_{\text{N=C-H}}$), 3147 (s, $\tilde{\nu}_{\text{N-C-H}}$), 2966 (m, $\tilde{\nu}_{\text{C=C-H}}$), 1653 (m, $\tilde{\nu}_{\text{C=N}}$), 1570 (s, $\tilde{\nu}_{\text{C=C}}$), 1491 (s), 1427 (s), 1394 (s), 1342 (m), 1219 (m), 1155 (m), 1025 (s), 980 (s), 962 (s), 949 (m), 804 (s) cm^{−1}. CHN anal. calcd (%) for

$\text{C}_{33}\text{F}_{12}\text{H}_{12}\text{N}_6$: C 54.99, H 1.68, N 11.66; Found: C 54.61, H 1.46, N 11.56. HRMS (Cl^+ mode): Calculated for $\text{C}_{33}\text{H}_{12}\text{F}_{12}\text{N}_6$: 720.0932. Found: 720.0926.

Compound **1** could be sublimed using the following procedure. A sample of compound **1** was placed in a 30 cm long quartz tube. The tube was connected to a vacuum source (0.03 mmHg) and the bottom half of the tube was heated in a 250 °C oven with 1 °C/min heating rate. White microcrystalline solid was collected from the wall of the tube above the oven after 48 h. The solid was ground in a mortar and its powder X-ray diffraction pattern was compared to the sample obtained by solvothermal synthesis (Figure 4.6).

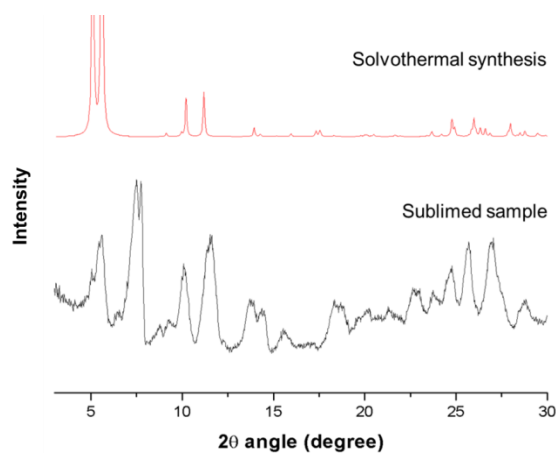


Figure 4.6 Comparison of PXRD patterns of compound **1** from solvothermal synthesis and sublimed sample.

Stability of compound **1** to various solvents was tested by exposing a handful of crystals to the given solvent and observing them under a microscope over time. If—under given conditions—no visible signs of crystal decomposition or dissolution were observed, compound **1** was deemed stable to those conditions. Using this methodology, we have

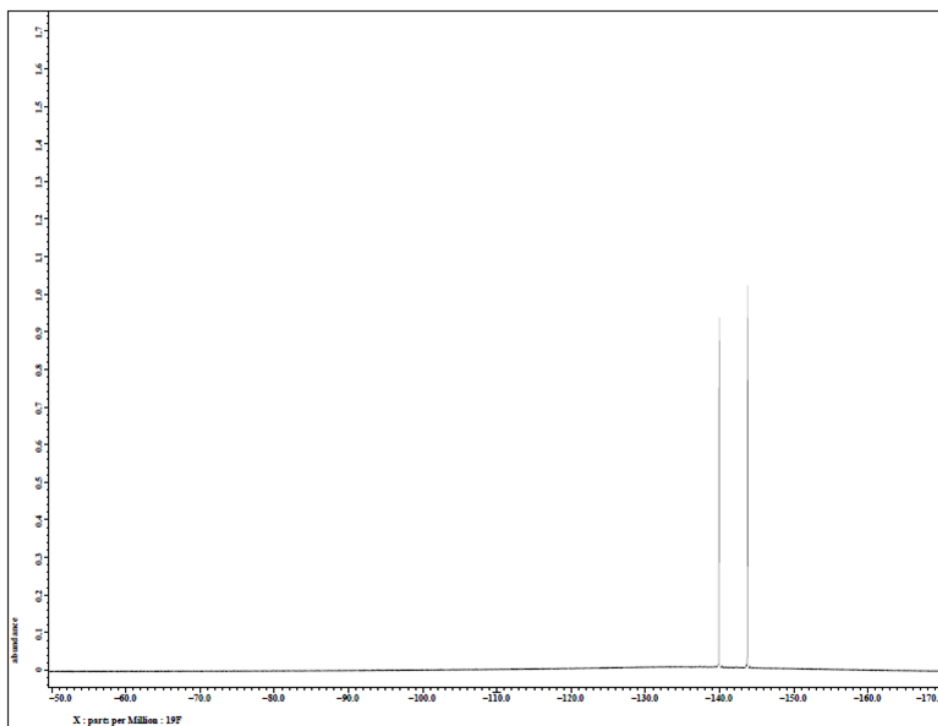


Figure 4.8 ^{19}F NMR spectrum of compound **6**.

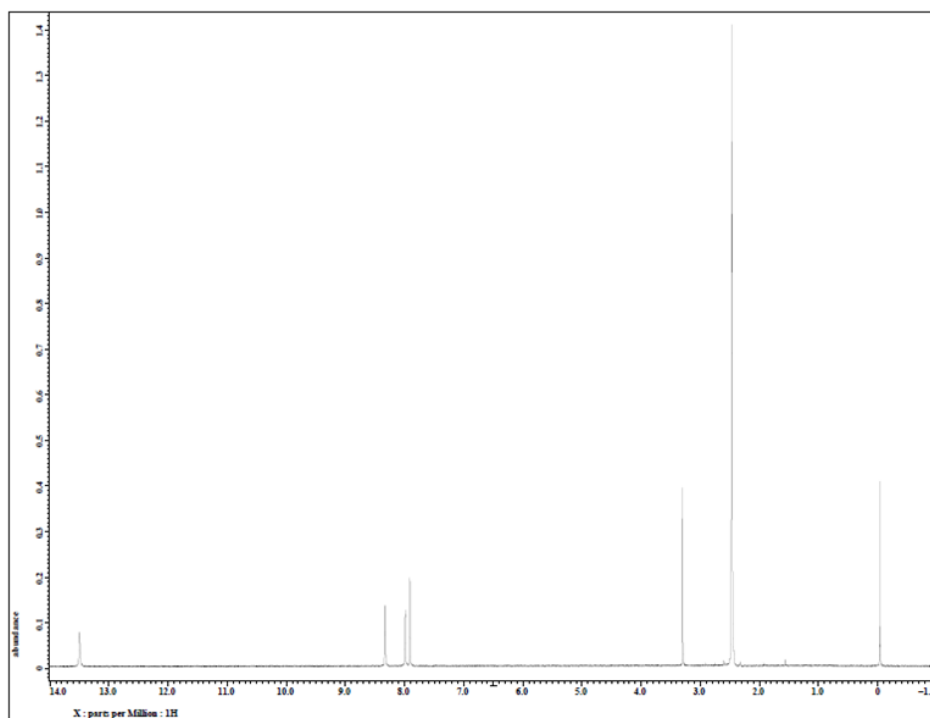


Figure 4.9 ^1H NMR spectrum of compound **1**.

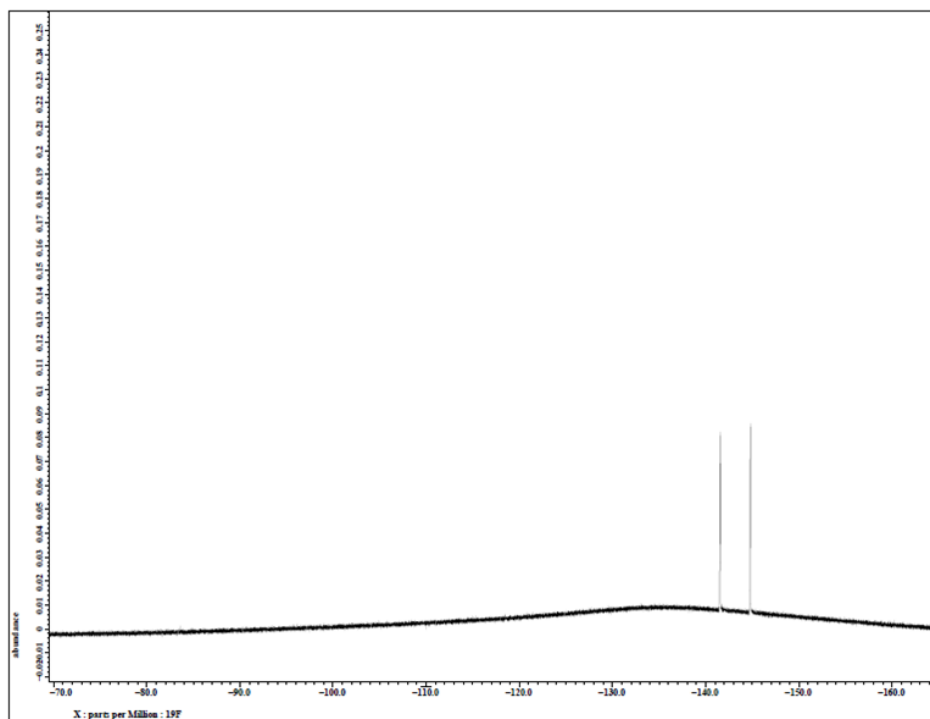


Figure 4.10 ^{19}F NMR spectrum of compound **1**.

4.4.4 X-ray Crystallographic Analysis of Compound **1**

The X-ray diffraction data was collected at ChemMatCARS beamline at Advanced Photon Source in Argonne National Laboratory and refined by Dr. Yu-Chun Chuang (National Synchrotron Radiation Research Center, Taiwan). A colorless rod-shaped crystal measuring 0.10×0.10×0.04 mm in size was mounted on a glass fiber and cooled to 100 K using Cryojel (Oxford instrumentation). The diffraction data was collected on a Bruker D8 diffractometer with an APEX-II CCD detector using phi scans. Crystal-to-detector distance was 110 mm and the exposure time was 0.3 s per frame using a scan width of 0.5°. Data collection was 89.2% complete to 13.96° in θ . A total of 31825 reflections were collected covering the indices: $-11 \leq h \leq 21$, $-40 \leq k \leq 32$ and $-25 \leq l \leq 21$. A total of 10079 reflections were found to be symmetry independent, with an R_{int} of

0.0604. Indexing and unit cell refinement indicated a *C*-centered, monoclinic lattice. The space group was found to be *C2/c* (No. 15). The data were integrated using the Bruker SAINT software package and scaled using the SADABS software program. Solution by direct methods produced a complete heavy-atom phasing model consistent with the proposed structure. All non-hydrogen atoms were refined anisotropically by full-matrix least-squares (SHELXL-97). All hydrogen atoms were placed using a riding model. Their positions were constrained relative to their parent atom using the appropriate HFIX command in SHELXL-97. The SQUEEZE function in the PLATON program was used to remove disordered solvent.

Table 4.2 Crystallographic Data of Compound **1**

Empirical formula	$\text{C}_{33}\text{H}_{12}\text{F}_{12}\text{N}_6$	
Formula weight	720.49	
Temperature	100(2) K	
Wavelength	0.41328 Å	
Crystal system	Monoclinic	
Space group	<i>C2/c</i>	
Unit cell dimensions	$a = 19.314(9)$ Å	$\alpha = 90^\circ$
	$b = 34.639(16)$ Å	$\beta = 113.164(4)^\circ$
	$c = 22.045(10)$ Å	$\gamma = 90^\circ$
Volume	13560 (11) Å ³	
<i>Z</i>	12	
Density (calculated)	1.059 Mg/m ³	

Absorption coefficient	0.013 mm^{-1}
$F(000)$	4320
Crystal size	$0.10 \times 0.10 \times 0.04 \text{ mm}^3$
θ range for data collection	0.68° to 13.96°
Index ranges	$-11 \leq h \leq 21$, $-40 \leq k \leq 32$, $-25 \leq l \leq 21$
Reflections collected	31825
Independent reflections	10079 [$R(\text{int}) = 0.0604$]
Completeness to $\theta = 13.96^\circ$	89.2%
Absorption correction	Semi-empirical from equivalents
Max. and min. transmission	0.9987 and 0.9994
Refinement method	Full-matrix least-squares on F^2
Data / restraints / parameters	10079 / 353 / 645
Goodness-of-fit on F^2	1.261
Final R indices [$I > 2\sigma(I)$]	$R_1 = 0.1572$, $wR_2 = 0.4553$
R indices (all data)	$R_1 = 0.2510$, $wR_2 = 0.4912$
Extinction coefficient	$0.015(2)$
Largest diff. peak and hole	0.849 and $-0.501 \text{ e/\AA}^{-3}$

4.4.5 Fourier-transform Infrared Spectra

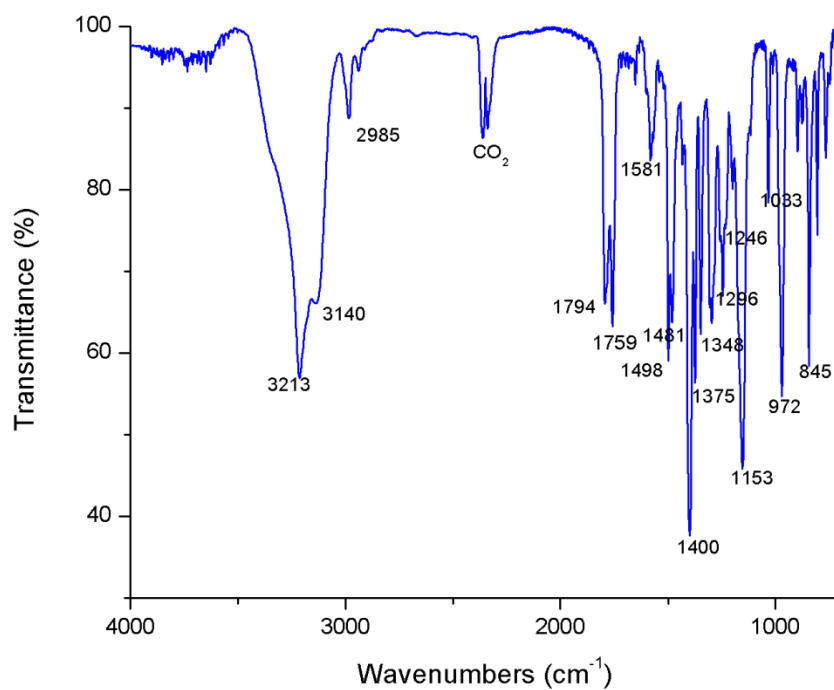


Figure 4.11 Fourier-transform infrared spectrum of compound **6**.

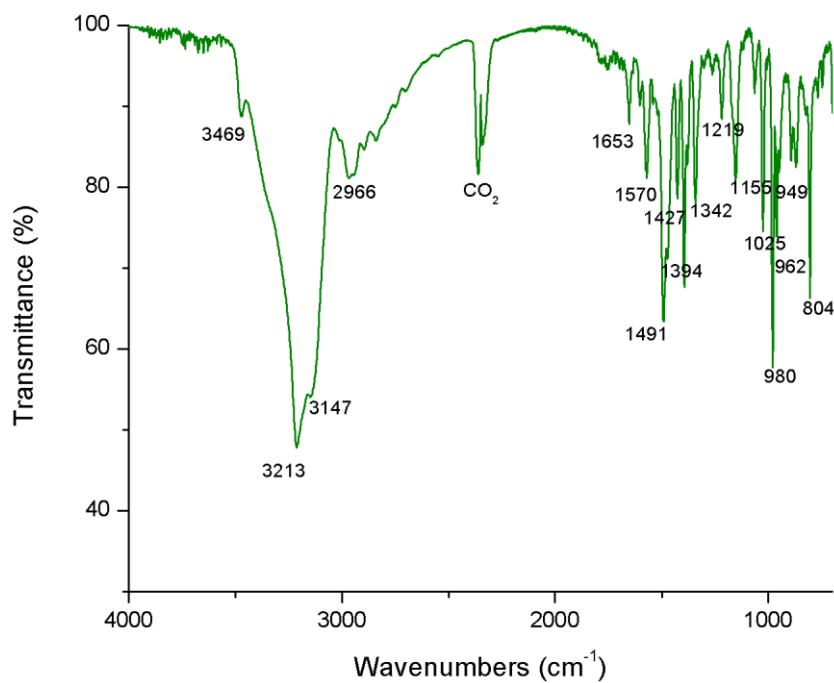


Figure 4.12 Fourier-transform infrared spectrum of compound **1**.

4.4.6 Differential Scanning Calorimetry Analysis of Compound 1

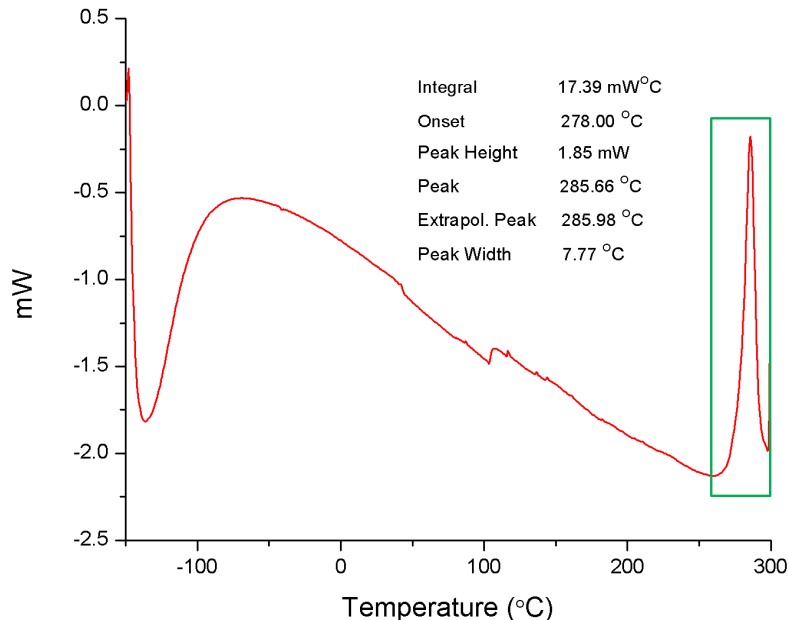


Figure 4.13 Differential scanning calorimetry analysis of compound **1**.

4.4.7 Powder X-ray Diffraction Patterns of Compound 1

The synchrotron powder X-ray diffraction data of compound **1** were collected at the BL01C2 beamline at the National Synchrotron Radiation Research Center in Taiwan. The wavelength of the incident X-rays was 1.033 Å and the diffraction patterns were recorded with a Mar345 IP detector, positioned approx. 306 mm from the sample. The powder sample was packed in a glass capillary (0.3 mm diameter) and each pattern was exposed for 60 s. In-situ temperature-dependent diffraction data on compound **1** were collected in a stream of hot air at temperatures of 25, 100, 150, 200, 250, 300, and 350 °C, with a heating rate of 10 °C/min. Every set point of the temperature gradient was sustained for 10 min to ensure the temperature balance in the entire powder sample. The one-dimensional powder diffraction profile was converted using GSAS-II package with

cake-type integration, where the diffraction angles were calibrated according to Bragg positions of LaB₆ standard from NIST.³⁹ Simulated PXRD patterns were calculated with the Material Studio software package⁴⁰ employing the structure model from the obtained single crystal data. Powder X-ray diffraction (PXRD) data of sublimed compound **1** was collected at 25 °C on a Phillips X'pert Pro diffractometer with CuK α radiation.

4.4.8 Gas Adsorption Isotherms

A Micromeritics ASAP 2020 Surface Area and Porosity Analyzer was used to measure N₂, O₂, CO₂, and H₂O adsorption isotherms. Oven-dried sample tubes equipped with seal frit (Micromeritics) were evacuated and tared. Samples of **1** weighing between 100 and 200 mg were transferred to the sample tube, which was then capped by a seal frit. Samples were heated to 120 °C under high vacuum (10^{-3} – 10^{-4} Torr) for 15 h. The evacuated sample tubes were weighed again, and the sample mass was determined by subtracting the mass of the previously tared tubes. Isotherms for the sorption of N₂ and O₂ were measured using a liquid nitrogen bath (77 K). Isotherm for the sorption of CO₂ was measured using a dry ice/isopropanol bath (195 K). Water vapor adsorption isotherm was measured at 298 K using a water bath. Ultra high purity grade (99.999%) gases—N₂, O₂, CO₂ and He—as well as oil-free valves and gas regulators were used for all free space corrections and measurements. Relative pressure (P/P_o) range for BET analysis was taken from 5×10^{-5} to 0.1.

4.4.9 Thermogravimetric Vapor Adsorption

The schematic setup of thermogravimetric adsorption apparatus is shown in Figure 4.14. From Figure 4.15–22, colorless rod-shaped crystals of compound **1** were first heated on a thermobalance of the TA Instruments TGA 2050 thermogravimetric analyzer under N₂ flow to 120 °C (red lines). They were then held at this temperature for 60 min to ensure complete activation. Once no further weight change was observed (black ines), the temperature was reduced to 25 °C at 5 °C/min and held at 25 °C. The N₂ flow was then switched (green line) to a second N₂ gas stream that was saturated with the vapor of adsorbate at 25 °C (saturation was achieved by passing the N₂ gas stream through a bubbler containing the liquid adsorbate. After the weight reached a plateau, the adsorbate vapor/N₂ flow was switched back to pure N₂ flow (black lines) at the same temperature (25 °C).

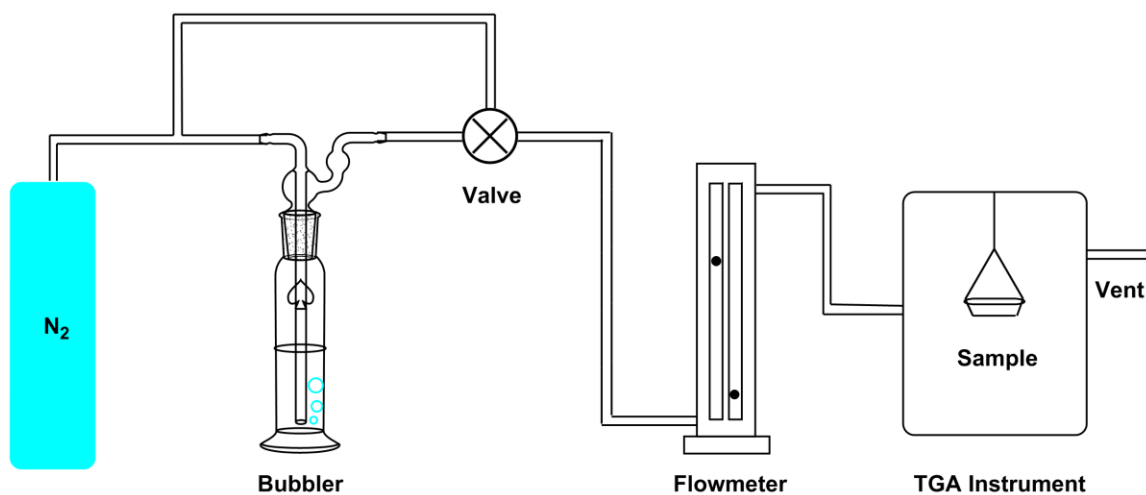


Figure 4.14 A schematic diagram of the apparatus for the thermogravimetric analysis of adsorption.

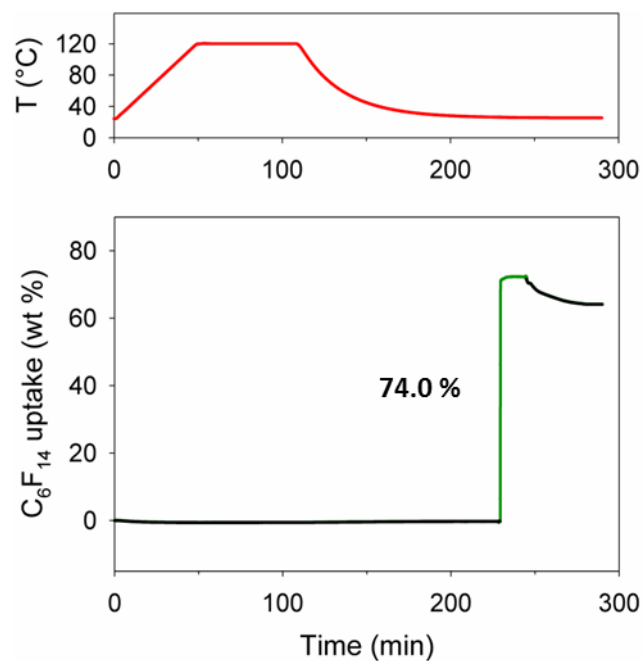


Figure 4.15 Thermogravimetric analysis of adsorption of perfluorohexane (C_6F_{14}) in **1**.

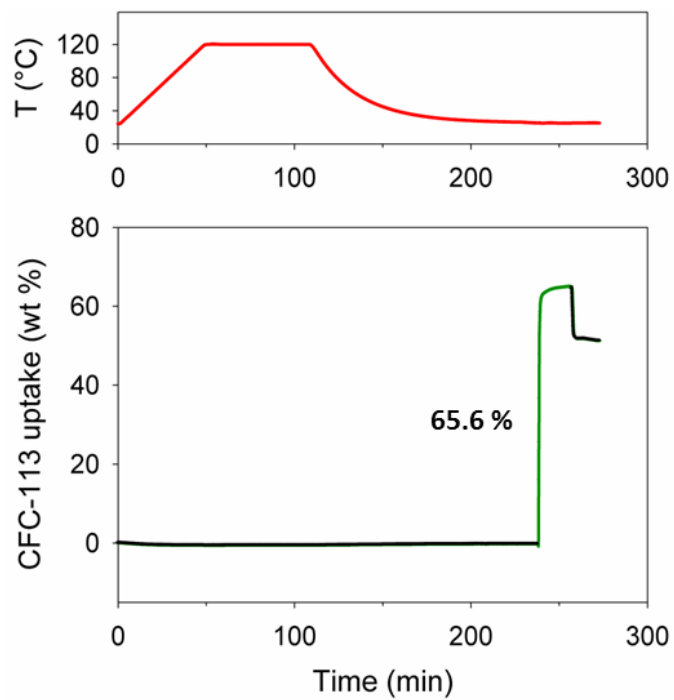


Figure 4.16 Thermogravimetric analysis of adsorption of CFC-113 ($Cl_2FC-CClF_2$) in **1**.

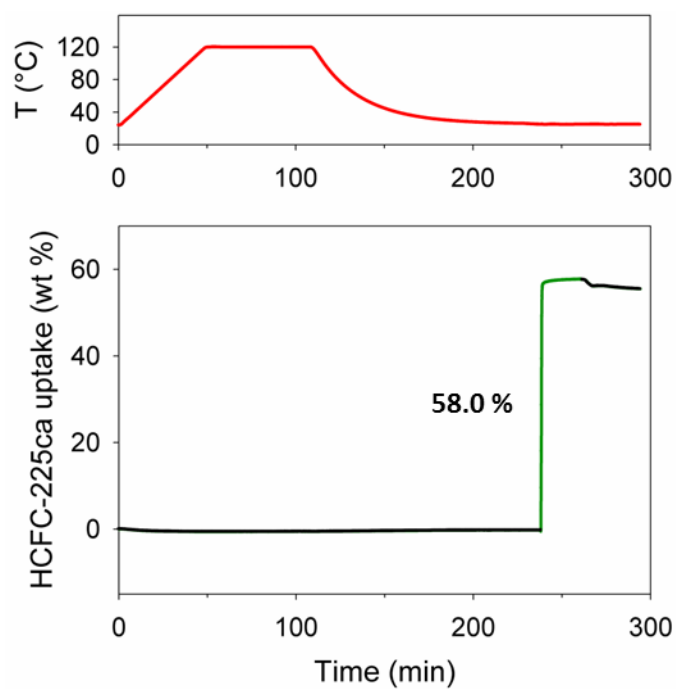


Figure 4.17 Thermogravimetric analysis of adsorption of HCFC-225ca ($\text{CF}_3\text{CHF}_2\text{CHCl}_2$) in **1**.

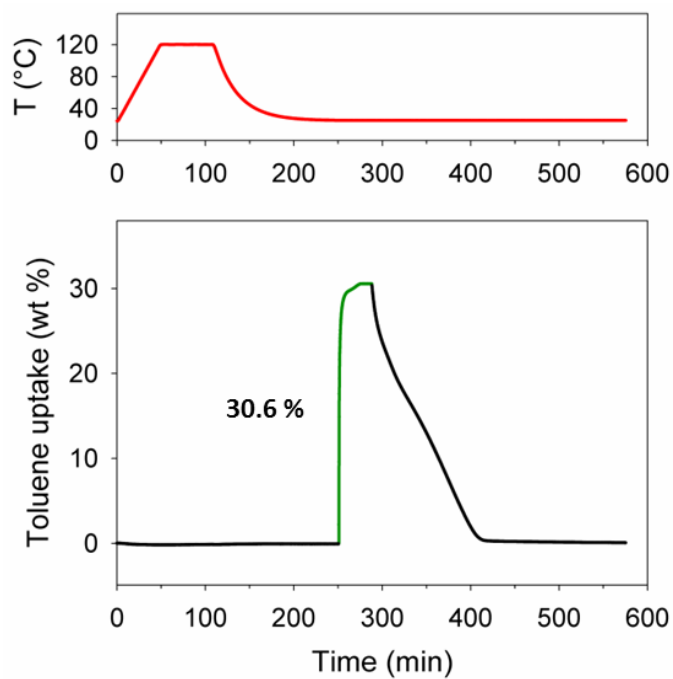


Figure 4.18 Thermogravimetric analysis of adsorption of toluene in **1**.

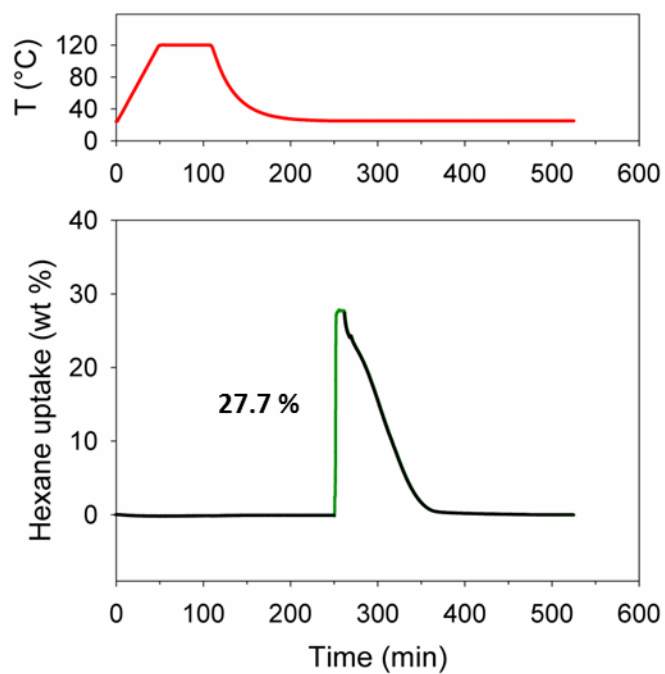


Figure 4.19 Thermogravimetric analysis of adsorption of *n*-hexane in **1**.

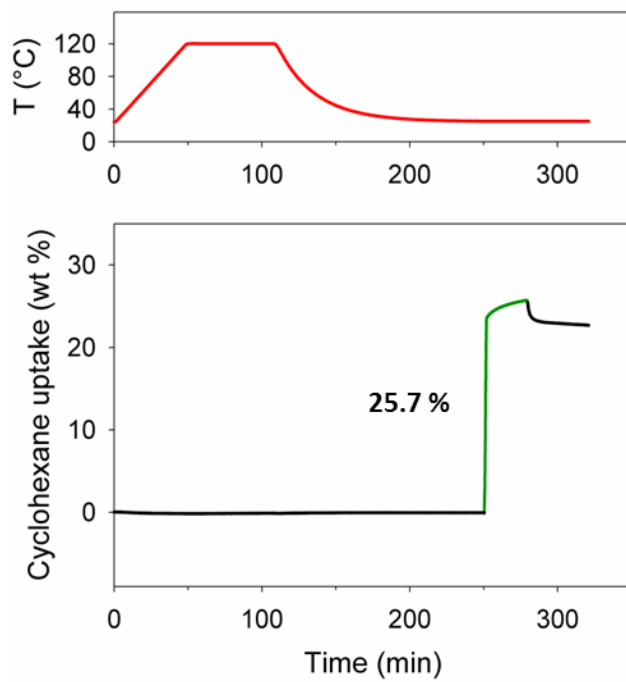


Figure 4.20 Thermogravimetric analysis of adsorption of cyclohexane in **1**.

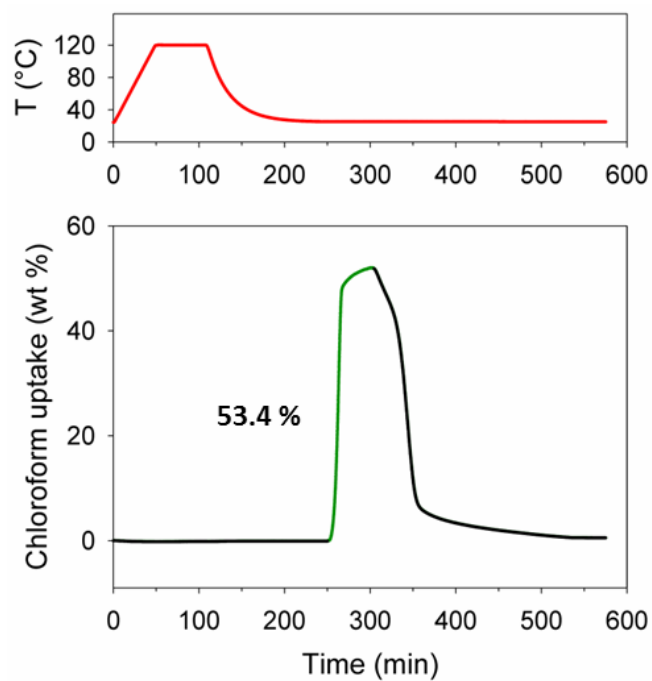


Figure 4.21 Thermogravimetric analysis of adsorption of chloroform in **1**.

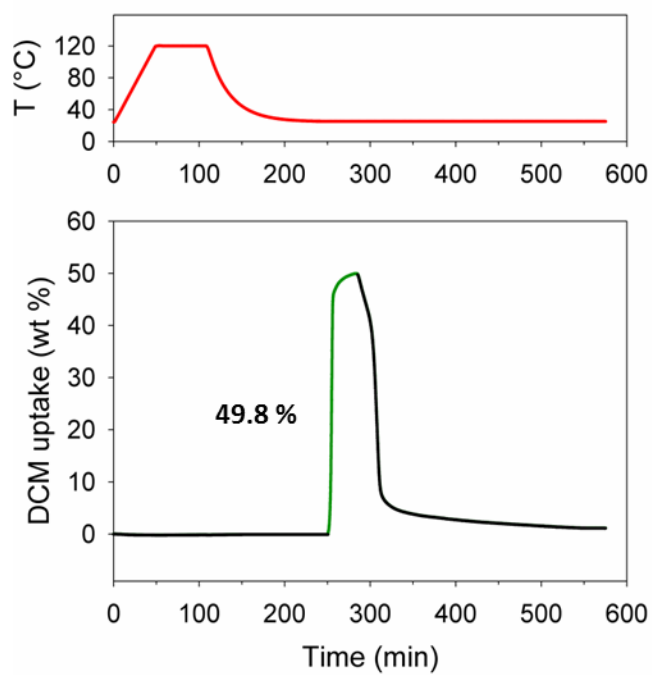


Figure 4.22 Thermogravimetric analysis of adsorption of dichloromethane in **1**.

4.4.10 Advancing Water Contact Angle Measurements

Finely ground crystals of compound **1** were pressed between two Si(100) slides that had been previously rinsed with absolute EtOH and dried in a stream of N₂ gas. After removing the upper slide, the exposed crystal surface was used for conducting contact angle measurements. A ramé-hart model 100 contact angle goniometer was employed to measure the contact angle of H₂O and compound **1**. The contacting liquid was dispensed on the surface of compound **1** using a Matrix Technologies micro-Electrapette 25 at the slowest speed of 1 μ L/s. The measurements were performed at 293 K, with the pipet tip remaining in contact with the drop. The reported data for each sample were the average of three measurements obtained from three different slides for compound **1** with advancing contact angles (θ_a) recorded for both edges of the drop.



Figure 4.23 Picture of compound **1** after a drop of water was placed onto the sample.

4.5 References

- [1] Wade, C. R.; Li, M.; Dincă, M. *Angew. Chem., Int. Ed.* **2013**, 52, 13377–13381.

- [2] Conato, M. T.; Jacobson, A. J. *Microporous Mesoporous Mater.* **2013**, *175*, 107–115.
- [3] Colson, W. J.; Woll, A. R.; Mukherjee, A.; Levendorf, M. P.; Spitler, E. L.; Shields, V. B.; Spencer, M. G.; Park, J.; Dichtel, W. R. *Science* **2011**, *332*, 228–231.
- [4] Aoyama, Y. *Top. Curr. Chem.* **1998**, *198*, 131–161.
- [5] He, Y.; Xiang, S.; Chen, B. *J. Am. Chem. Soc.* **2011**, *133*, 14570–14573.
- [6] Li, P.; He, Y.; Guang, J.; Weng, L.; Zhao, J. C.-G.; Xiang, S.; Chen, B. *J. Am. Chem. Soc.* **2014**, *136*, 547–549.
- [7] (a) Jones, J. T. A.; Hasell, T.; Wu, X.; Bacsá, J.; Jelfs, K. E.; Schmidtman, M.; Chong, S. Y.; Adams, D. J.; Trewin, A.; Schiffman, F.; Cora, F.; Slater, B.; Steiner, A.; Day, G. M.; Cooper, A. I. *Nature* **2011**, *474*, 367–371. (b) Cooper, A. I. *Angew. Chem., Int. Ed.* **2012**, *51*, 7892–7894. (c) Hasell, T.; Zhang, H.; Cooper, A. I. *Adv. Mater.* **2012**, *24*, 5732–5737.
- [8] (a) Zhang, G.; Mastalerz, M. *Chem. Soc. Rev.* **2014**, *43*, 1934–1947. (b) Mastalerz, M.; Oppel, I. M. *Angew. Chem., Int. Ed.* **2012**, *51*, 5252–5255. (c) Schneider, M. W.; Oppel, I. M.; Ott, H.; Lechner, L. G.; Hauswald, H.-J.; Stoll, R.; Mastalerz, M. *Chem. Eur. J.* **2012**, *18*, 836–847. (d) Mastalerz, M.; Schneider, M. W.; Oppel, I. M.; Presly, O. *Angew. Chem., Int. Ed.* **2011**, *50*, 1046–1050. (e) Zhang, G.; Presly, O.; White, F.; Oppel, I. M.; Mastalerz, M. *Angew. Chem., Int. Ed.* **2014**, *53*, 5126–5130. (f) Zhang, G.; Presly, O.; White, F.; Oppel, I. M.; Mastalerz, M. *Angew. Chem., Int. Ed.* **2014**, *53*, 1516–1520.

- (g) Brutschy, M.; Schneider, M. W.; Mastalerz, M.; Waldvogel, S. R. *Adv. Mater.* **2012**, *24*, 6049–6052.
- [9] Luo, X.-Z.; Jia, X.-J.; Deng, J.-H.; Zhong, J.-L.; Liu, H.-J.; Wang, K.-J.; Zhong, C. *J. Am. Chem. Soc.* **2013**, *135*, 11684–11687.
- [10] Yang, W.; Greenaway, A.; Lin, X.; Matsuda, R.; Blake, A. J.; Wilson, C.; Lewis, W.; Hubberstey, P.; Kitagawa, S.; Champness, N. R.; Schröder, M. *J. Am. Chem. Soc.* **2010**, *132*, 14457–14469.
- [11] Brunet, P.; Simard, M.; Wuest, J. D. *J. Am. Chem. Soc.* **1997**, *119*, 2727–2738.
- [12] Jin, Y.; Yu, C.; Denman, R. J.; Zhang, W. *Chem. Soc. Rev.* **2013**, *42*, 6634–6654.
- [13] Chakrabarty, R.; Mukherjee, P. S.; Stang, P. J. *Chem. Rev.* **2012**, *111*, 6810–6918.
- [14] Pace, C. J.; Gao, J. *Acc. Chem. Res.* **2013**, *46*, 907–915.
- [15] Takezawa, H.; Murase, T.; Resnati, G.; Metrangolo, P.; Fujita, M. *J. Am. Chem. Soc.* **2014**, *136*, 1786–1788.
- [16] Scientific Assessment of Ozone Depletion: 2010, Global Ozone Research and Monitoring Project Report No. 52 (World Meteorological Organization, 2011).
- [17] Laube, J. C.; Newland, M. J.; Hogan, C.; Brenninkmeijer, C. A. M.; Fraser, P. J.; Martinerie, P.; Oram, D. E.; Reeves, C. E.; Röckmann, T.; Schwander, J.; Witrant, E.; Sturges, W. T. *Nat. Geosci.* **2014**, *7*, 266–269.

- [18] Meyer, E. A.; Castellano, R. K.; Diederich, F. *Angew. Chem., Int. Ed.* **2003**, *42*, 1210–1250.
- [19] (a) Kawade, V. A.; Kumbhar, A. S.; Erxleben, A.; Pachfule, P.; Banerjee, R. *CrystEngComm* **2011**, *13*, 5289–5291. (b) Wei, W.; Li, W.; Wang, X.; He, J. *Cryst. Growth Des.* **2013**, *13*, 3843–3846.
- [20] Deshpande, R. K.; Minnaar, J. L.; Telfer, S. G. *Angew. Chem., Int. Ed.* **2010**, *49*, 4598–4602.
- [21] (a) Procopio, E. Q.; Padial, N. M.; Masciocchi, N.; Galli, S.; Oltra, J. E.; Barea, E.; Navarro, J. A. R. *CrystEngComm* **2013**, *15*, 9352–9355. (b) Padial, N. M.; Procopio, E. Q.; Montoro, C.; López, E.; Oltra, J. E.; Colombo, V.; Maspero, A.; Masciocchi, N.; Galli, S.; Senkovska, I.; Kaskel, S.; Barea, E.; Navarro, J. A. R. *Angew. Chem., Int. Ed.* **2013**, *52*, 8290–8294.
- [22] (a) Foces-Foces, C.; Llamas-Saiz, A. L.; Claramunt, R. M.; López, C.; Elguero, J. *J. Chem. Soc., Chem. Commun.* **1994**, 1143–1145. (b) Maspero, A.; Giovenzana, G. B.; Masciocchi, N.; Palmisano, G.; Comotti, A.; Sozzani, P.; Irene Bassanetti, I.; Nardo, L. *Cryst. Growth Des.* **2013**, *13*, 4948–4956.
- [23] Lengths of N–H bonds involved in hydrogen bonding have been normalized to values obtained from neutron diffraction. See: Steiner, T. *Angew. Chem., Int. Ed.* **2002**, *41*, 48–76.

- [24] O'Keeffe, M.; Peskov, M. A.; Ramsden, S. J.; Yaghi, O. M. *Acc. Chem. Res.* **2008**, *41*, 1782–1789.
- [25] Peng, Y.; Krungleviciute, V.; Eryazici, I.; Hupp, J. T.; Farha, O. K.; Yildirim, T.; *J. Am. Chem. Soc.* **2013**, *135*, 11887–11894.
- [26] Turner, M. J.; McKinnon, J. J.; Jayatilaka, D.; Spackman, M. A. *CrystEngComm* **2011**, *13*, 1804–1813.
- [27] Nguyen, J. G.; Cohen, S. M. *J. Am. Chem. Soc.* **2010**, *132*, 4560–4561.
- [28] Chen, T.-H.; Popov, I.; Zenasni, O.; Daugulis, O.; Miljanić, O. Š. *Chem. Commun.* **2013**, *49*, 6846–6848.
- [29] (a) Yang, C.; Kaipa, U.; Mather, Q. Z.; Wang, X.; Nesterov, V.; Venero, A. F.; Omary, M. A. *J. Am. Chem. Soc.* **2011**, *133*, 18094–18097. (b) Yang, C.; Wang, X.; Omary, M. A. *J. Am. Chem. Soc.* **2007**, *129*, 15454–15455.
- [30] Wang, X.; Liu, L.; Jacobson, A. J. *Angew. Chem., Int. Ed.* **2006**, *45*, 6499–6503.
- [31] Ingleson, M. J.; Barrio, J. P.; Bacsá, J.; Dickinson, C.; Park, H.; Rosseinsky, M. J. *Chem. Commun.* **2008**, *44*, 1287–1289.
- [32] (a) Atwood, J. L.; Barbour, L. J.; Jerga, A. *Science* **2002**, *296*, 2367–2369. (b) Tanada, S.; Kawasaki, N.; Nakamura, T.; Abe, I. *J. Colloid Interf. Sci.* **1996**, *183*, 143–147. (c) Senkovska, I.; Barea, E.; Navarro, J. A. R.; Kaskel, S. *Micropor. Mesopor. Mat.* **2012**, *156*, 115–120.

- [33] IPCC Fourth Assessment Report, Climate Change 2007: Net Global Radiative Forcing, Global Warming Potentials and Patterns of Forcing. Available online at http://www.ipcc.ch/publications_and_data/ar4/wg1/en/tssts-2-5.html.
- [34] Mastalerz, M. *Chem. Eur. J.* **2012**, *18*, 10082–10091.
- [35] Eddaoudi, M.; Kim, J.; Rosi, N.; Vodak, D.; Wachter, J.; O'Keeffe, M.; Yaghi, O. *M. Science* **2002**, *295*, 469–472.
- [36] Tanabe, K. K.; Cohen, S. M. *Chem. Soc. Rev.* **2011**, *40*, 498–519.
- [37] Schneider, M. W.; Oppel, I. M.; Griffin, A.; Mastalerz, M. *Angew. Chem., Int. Ed.* **2013**, *52*, 3611–3615.
- [38] Only the compound **1** and **6** used in the reactions carried out by the author are shown, other compounds synthesized by Ilya Popov refer to "Popov, I. *Synthetic and Methodological Studies in Copper and Palladium-Catalyzed Carbon-Carbon and Carbon-Heteroatom Bond Formation*; PhD Thesis, University of Houston, 2014". ¹³C Spectra were not included since they are not informative: due to the poor solubility of the prepared compounds and extensive coupling between ¹³C and ¹⁹F nuclei, low intensities and many missing peaks were apparent.
- [39] Toby, B. H.; Von Dreele, R. B. *J. Appl. Cryst.* **2013**, *46*, 544–549.
- [40] *Materials Studio* program, version 5.5; Accelrys, San Diego, CA, 2011.

Chapter Five

Shape-Persistent Dehydrobenzannulene Macrocycles: Incorporation into Metal-Organic Frameworks and Host-Guest Chemistry with Fluoroarenes

5.1 Introduction

High internal surface area is one of the important features of MOFs, especially for gas storage applications, and has been pursued for decades.¹ Other than gas storage, mesoporous MOFs are also being explored for applications in catalysis, separation, or capture of guest molecules.² However, mesoporous MOFs are considerably more difficult to obtain than microporous ones. As the size of the organic linker increases, once the guest molecules (typically the solvent of synthesis, synthetic components, or by-products) are removed, the structural integrity of the resulting frameworks decreases, that often results in collapse of the pore structure and loss of crystallinity. Interpenetration and catenation are also frequent problems in the design of MOFs with mesopores; the process of self-assembly avoids the formation of large regions of empty space by generating multiple copies of the MOF which mechanically interlock with each other (and are thus rendered inseparable).³

Macrocyclic molecules are widely studied in supramolecular chemistry as molecular cages, nanosized reaction vessels, switches and shuttles, liquid crystals, catalysts, and sensors.⁴ To date, two classes of macrocyclic linkers have been used in the synthesis of MOF synthesis: (1) catenanes, pseudorotaxanes, and rotaxanes⁵ and (2)

azamacrocycles.⁶ Pseudorotaxane linkers enabled the resulting MOF to show specific stereoelectronic host-guest interactions,⁵ essential for the creation of solid-state molecular switches and molecular machines based on mechanically interlocked molecules. Flexible azamacrocyclic ligands were used to enhance guest-binding affinity for CO₂ via its chemospecific interactions with amines.⁶ Despite this important progress, the macrocycles included into these MOFs were not shape-persistent and hence likely flexed into a conformation which did not have a significant void within the center of the macrocycles. Thus, the development of MOFs based on shape-persistent macrocycles is still an underexplored area, which could yield unusual new materials with exceptional topologies, and increased surface areas and pore sizes.

Shape-persistent aryleneethynylene macrocycles have attracted much attention in recent years because they feature a large, supramolecular building blocks that generate solution-based π -stacked structures, noncollapsible nanoporous solids, and tubular ordered fluid phases.⁷ Their π -conjugated systems can exhibit unique optical and electronic behaviors. Moreover, π -conjugated redox-active macrocycles have potential applications in organic electronic devices and switches.⁸ Shape-persistent macrocycles generally have a regular repeating unit with much fewer degrees of conformational freedom compared to flexible macrocycles. In the synthesis of MOFs, their rigid backbones could give rise to large molecular surfaces and prevent interpenetration. Most importantly, they guarantee the minimum pore size of the resultant MOF by their own interior pores, which can be synthetically engineered. The difficult preparation of macrocycles (high cost, low yields, and multiple steps) has been improved by the

development of C–C cross-coupling reactions and DCC.⁹ Site-specific substitution with functional groups can be accomplished on both the interior and exterior of macrocycles as well. All these properties make shape-persistent macrocycles attractive—and now viable—building blocks for the synthesis of MOFs.

Para-fused phenylene-ethynylene macrocycles were shown to accommodate guest molecules such as toluene, hexamethylbenzene, and fullerenes via $[C-H\cdots\pi]$ and $[\pi\cdots\pi]$ interactions, as proven by single crystal X-ray structures.¹⁰ The host-guest chemistry of flexible macrocyclic linkers incorporated into MOFs has been studied but the substantial applications based on the voids of macrocycles are still limited.^{5,6} This chapter describes our preliminary work on the syntheses of metal-macrocyclic frameworks, denoted as **MCMOFs** to stress the shape-persistent macrocyclic nature of linker **1** (Figure 5.1), which was used in their synthesis. Furthermore, we also describe the solid-state host-guest chemistry of compound **2** (Figure 5.1), an ester derivative of **1**, by studying the crystal structures of polyfluorobenzenes encapsulated in the central cavity of **2**.

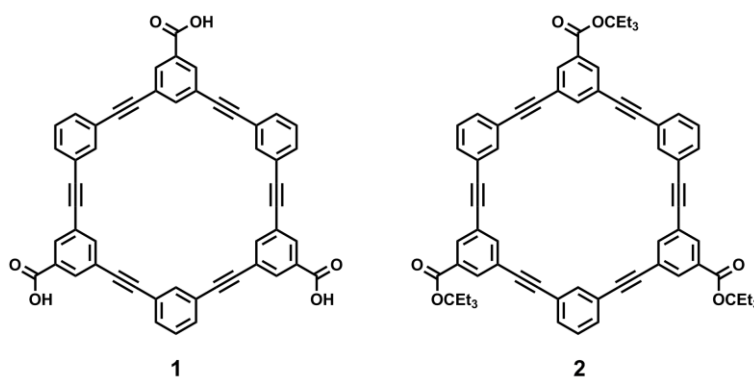


Figure 5.1 Shape-persistent macrocyclic ligand **1** used in the syntheses of **MCMOFs**, and **2** for the studies of host-guest chemistry.

5.2 Results and Discussion

5.2.1 Syntheses and Crystal Structure Analyses of MCMOFs

A rigid macrocyclic ligand is anticipated to be a good precursor for increasing the porosity and preventing the interpenetration or catenation within MOFs. Based on well-studied phenylacetylene macrocycle family established by Moore,¹¹ a novel macrocyclic triacid ligand **1** and its ester derivative **2** were synthesized by Ilya Popov from Prof. Daugulis' group (Figure 5.1).¹² Macrocycle **1** has an 11.74-Å-wide central void, which serves as a predesigned pore and reduce the interpenetration or catenation in an extended network. A mixture of macrocycle **1** and $\text{Zn}(\text{NO}_3)_2 \cdot 6\text{H}_2\text{O}$ in *N,N*-dimethylacetamide (DMA) was heated at 100 °C for 1 d and yellowish single crystals of **Zn-MCMOF** were isolated. **Zn-MCMOF** has a large cubic unit cell ($a = b = c = 33.261(4)$ Å) with a large amount of massively disordered included solvent, which made its analysis impossible by the in-house diffractometer. With the assistance from Dr. Yu-Sheng Chen (ChemMatCARS, Advanced Photon Source, Argonne National Laboratory) and Dr. Yu-Chun Chuang (National Synchrotron Radiation Research Center, Taiwan), we were able to analyze the single crystal structure of **Zn-MCMOF**. The single crystal synchrotron analysis reveals an unprecedented three-dimensional network, whose chemical formula is $[\text{Zn}_3(\mathbf{1}-3\text{H}^+)_2(\text{H}_2\text{O})_2]$ (Figure 5.2). The SBU is built from three aligned Zn and six carboxylate groups from six discrete molecules of **1** (Figure 5.2A). The middle Zn in the SBU is octahedrally coordinated to three oxygens from six discrete carboxylates, and other two Zn atoms are tetrahedrally coordinated by one H_2O and three oxygens from three discrete carboxylates. The phenylacetylene macrocyclic linkers are inclined to

$[\pi\cdots\pi]$ stack with each other and two molecules form a unique complex building block with six carboxylate groups (Figure 5.2B). The two offset-stacked macrocycles are not entirely parallel, and are presented in a twisted asymmetric hexagonal geometry due to the flexible acetylene backbones. The distance between the two stacked macrocycles is 3.64 Å (measured as the distance between their centroids of voids, Figure 5.2 C). The SBU is connected by the complex macrocyclic linkers to form a novel infinite three-dimensional mesoporous framework. From the view along the *a*-axis (Figure 5.2D) and the space diagonal line of the unit cell (Figure 5.2E), ca. 25-Å-wide 1D channels are shown and they are connected to each other to form an infinite framework.

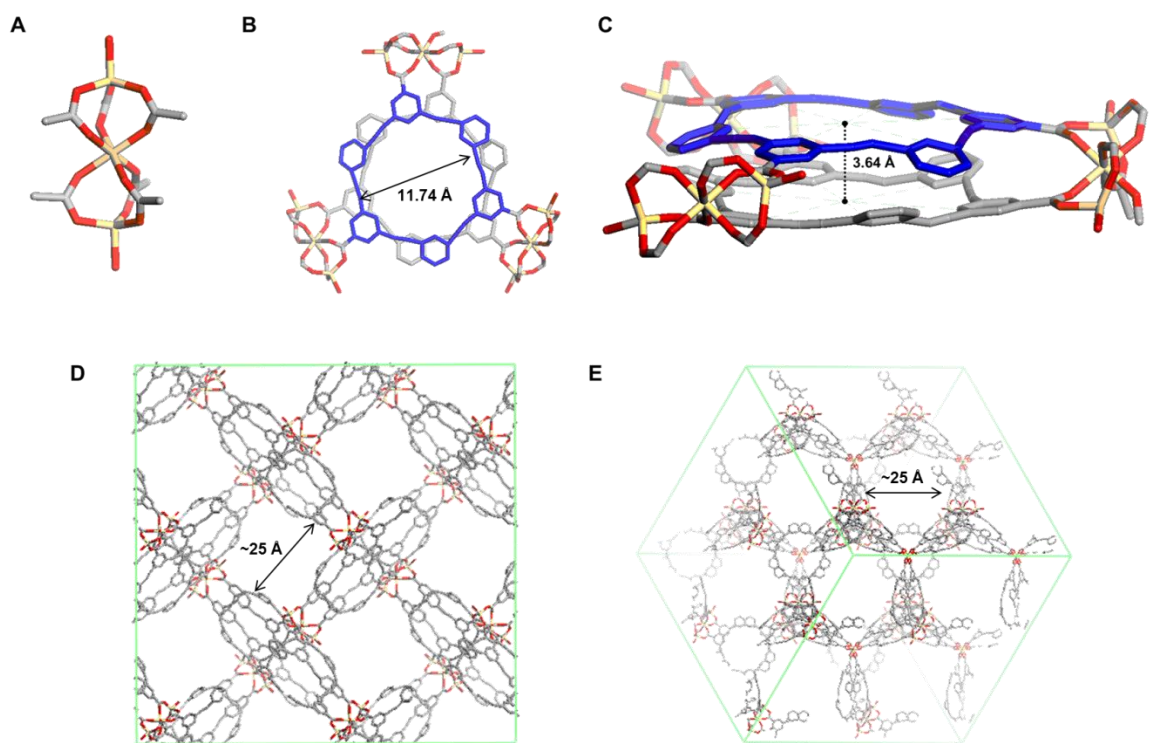


Figure 5.2 Single crystal synchrotron structure of **Zn-MCMOF**. (A) Secondary building unit; (B) top view of $[\pi\cdots\pi]$ stacking of two macrocyclic linkers; (C) side view of $[\pi\cdots\pi]$ stacking of two macrocyclic linkers, the distance between the

centroids of two macrocycles is 3.64 Å; (D) 1D mesoporous channels viewed along the *a*-axis; (E) 1D mesoporous channels viewed along the space diagonal line of the cubic unit cell. Green lines: unit cell edges. Element colors: C, gray; Zn, yellow; O, red; and hydrogen is omitted for clarity.

Besides the proposed high porosity of **MCMOF**, **Zn-MCMOF** is hydrolytically vulnerable. Therefore, it is necessary to explore the material with higher hydrolytic, thermal, and chemical stability. Zirconium-based MOFs are hydrolytically and thermally more stable compared to other MOFs.¹³ Using the SBU precursor approach mentioned in Chapter 1.2.1.3, we were able to synthesize **Zr-MCMOF**. First, anhydrous ZrCl₄ and large excess amount of benzoic acid were dissolved in DEF and heated at 80 °C for 1 d in order to obtain [Zr₆O₄(OH)₄(benzoate)₁₂] cluster. The solution containing the cluster was added onto the solid compound **1** (**1** : Zr⁴⁺ = 1 : 5) as shown in Figure 5.3A, and the resulting mixture was placed in an oven at 100 °C for 4 d to obtain colorless prismatic crystals. Single crystal X-ray analysis reveals another unprecedented and remarkable structure with 1D channels whose diameter is determined by the diameter of macrocycle **1**, along the *c*-axis of the trigonal unit cell. (Figure 5.3A). The constitution of this complexes can be formalized as [Zr₆O₄(OH)₄(**1**-3H⁺)(benzoate)₉(DEF)₃]. Interestingly, not all the benzoates on the prepared cluster precursor are replaced by bridging linkers because of the rigid and bulky macrocycle **1** (Figure 5.3B). Three benzoates from each [Zr₆O₄(OH)₄(benzoate)₁₂] are respectively replaced by one **1**-3H⁺, whose segments are highlighted green, and one DEF molecule. Notably, only one oxygen from each carboxylate group of the macrocycles coordinates to Zr, while the other one forms a

hydrogen bond with the adjacent μ_3 -OH, with the measured [O \cdots H] distance of 1.80 Å. The symmetric [Zr₆O₄(OH)₄] cluster adopts an asymmetric structure due to the three discrete coordinating macrocycle **1**, which tend to stay coplanar. As a result, orthogonal to the plane of macrocycles, three benzoates of each end of SBU form a small angle concavity on one end and a large one on the other end. The three-benzoate-concavity with larger angle allows the insertion of the smaller angle one from another SBU (Figure 5.3C). There is a [C–H $\cdots\pi$] interaction (distance is 3.40 Å) between C–H of benzoate of the smaller concavity and the centroid of benzene ring of the larger concavity. Therefore, the SBUs are aligned one-dimensionally via weak noncovalent interactions. Bridged by **1**–3H⁺, a two-dimensional infinite network is formed through metal-ligand bonding. Remarkably, the macrocycles still prefer to [$\pi\cdots\pi$] stack in pairs (centroid-centroid distance of adjacent two macrocycles is 3.46 Å). From Figure 5.3D, one 2D layer is attached by another upside-down 2D layer and thus forms a 2D double-layer sheet by [$\pi\cdots\pi$] stacking. The pairs of macrocycles are packing in a staggered orientation, with their connected SBUs interdigitating each other. The 2D double-layer sheets then pack on the top or bottom of another one via the [C–H $\cdots\pi$] interactions mentioned above, constructing a 3D framework with 1D channels. The distance between two pairs of [$\pi\cdots\pi$] stacked macrocycles is measured as 11.61 Å and that forms accessible small cages for guest molecules. Moreover, this porous material is constructed by four different interactions: metal-ligand bonding, hydrogen bonding, [C–H $\cdots\pi$] and [$\pi\cdots\pi$] interactions. Specifically, looking along the 1D channels formed by the rigid macrocycle **1**, the hydrogens of backbones are fixed toward to the center of pores, which are unlike most MOFs' pores built from linkers with rotatable benzene rings. Taking all the structural

features into account, **Zr-MCMOF** is expected to display unique host-guest interaction and induce the application on the separation of structural isomers (e.g. *o*-, *m*-, *p*-xylene, and ethylbenzene).

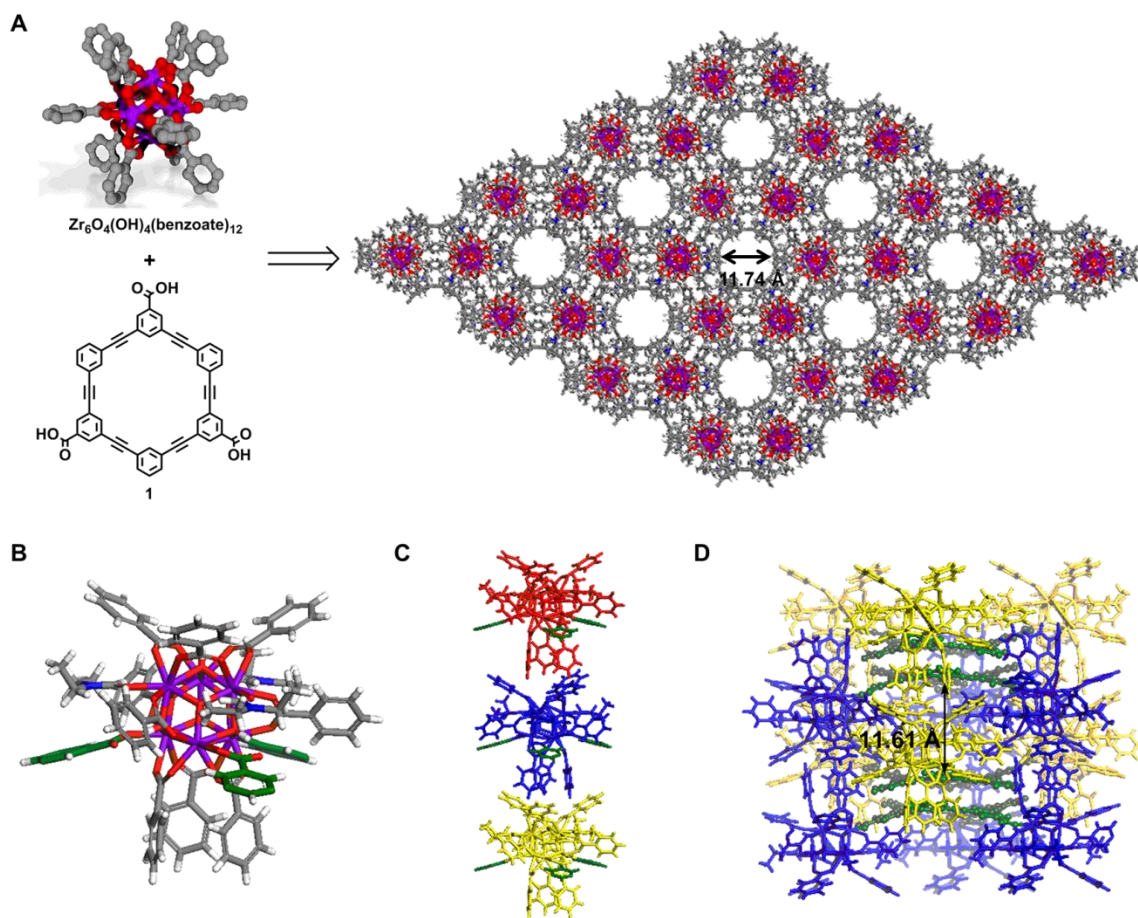


Figure 5.3 Synthesis and single crystal X-ray structure of **Zr-MCMOF**. (A) Reaction of pre-prepared $[\text{Zr}_6\text{O}_4(\text{OH})_4(\text{benzoate})_{12}]$ cluster (hydrogen atoms omitted for clarity) and macrocycle **1** gives rise to **Zr-MCMOF** with 1D channels. (B) SBUs, the segments of **1-3H⁺** are highlighted green. (C) The one-dimensional packing of SBUs through $[\text{C}-\text{H}\cdots\pi]$ interaction. (D) The 11.61-Å-tall small cage formed by two pairs

of $[\pi \cdots \pi]$ stacked macrocycles. Element colors: C, gray; Zr, purple; O, red; N, blue; and H, white.

5.2.2 Characterization of MCMOFs

Thermal stabilities of **Zn-** and **Zr-MCMOF** were evaluated using TGA under N₂ with 2 °C/min heating rate. Both materials showed poorly resolved decomposition steps, but **Zr-MCMOF** is thermally more stable (> 100 °C) than **Zn-MCMOF** (Figure 5.4A). Up to 800 °C, these two materials still retained 66.5 and 53.8 wt% of their initial weight, respectively. On both **Zn-** and **Zr-MCMOF** we performed N₂ adsorption (77 K) measurements to obtain BET surface areas of 510 and 317 m²/g, respectively. The latter was activated by heating in a vacuum oven at 120 °C and the surface area measured is consistent with that calculated from its microporous structure.¹⁴ However, **Zn-MCMOF** gave a much lower number than expected for a mesoporous MOF, especially with void volume of 82% calculated by *Mercury CSD 3.3*.¹⁵ Although the material was activated by SCD drying (Chapter 5.4.9), it still lost its crystallinity (Figure 5.4B). Interestingly, after soaking the activated material back into DMA, its crystallinity restored, indicating the flexibility of the structure. It might be possible to increase the porosity of **Zn-MCMOF** using a different activation method. Despite the amorphous activated structure, its BET surface area more than 500 m²/g is already higher than many microporous MOFs. Amorphous yet porous MOFs have recently been of interest.¹⁶ Along with its reversible structure proved by solvent removal and uptake, pressure-induced amorphization for porosity modification, gas storage, or trapping guests could be applied.¹⁷ Therefore, the potential application of flexible **Zn-MCMOF** will be further explored in our lab.

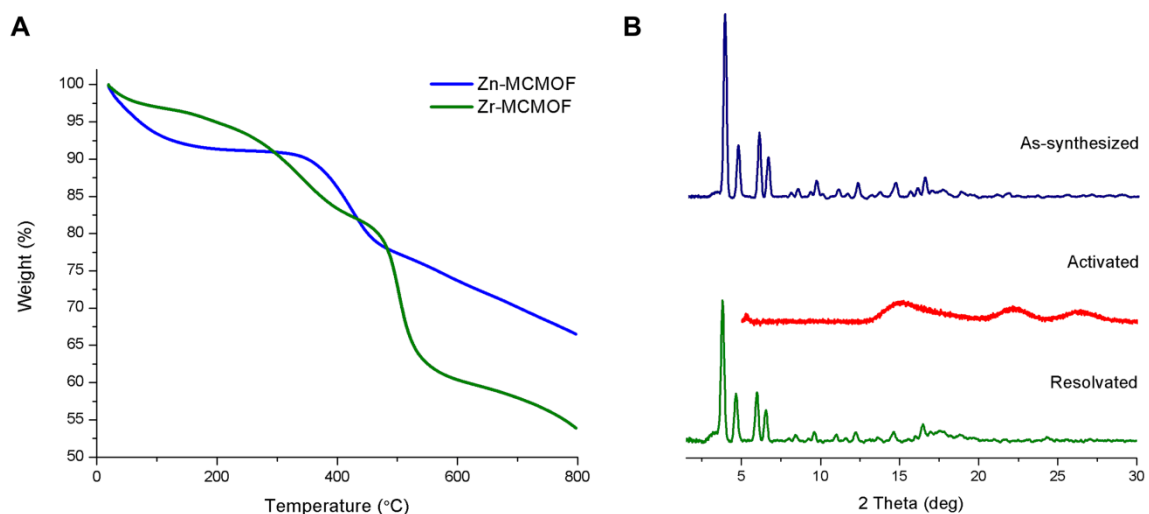


Figure 5.4 (A) TGA traces of **Zn-** and **Zr-MCMOF**. (B) The PXRD patterns of the reversible crystallinity of **Zn-MCMOF**.

5.2.3 Host-Guest Chemistry of Macrocycle **2**

Before the exploration of **MCMOFs** for potential applications, the investigation of the proposed host-guest chemistry of macrocycles was performed on macrocycle **2**, the ester derivative of macrocycle **1**. This small molecule serves as an important model for the host-guest chemistry of **MCMOFs**, without the problems associated with unpredictable topologies or activation of **MCMOFs**. A single crystal of macrocycle **2** was formed by slowly mixing the biphasic EtOH and **2**/DCM solution for a week. The crystal structure reveals a trigonal unit cell with space group $P3_121$ and $Z = 6$. The macrocycles do not pack in either eclipsed or staggered conformation as in the X-ray structure of **MCMOFs** (Figure 5.5A). Instead, the closest pair of macrocycle **2** has only one benzene ring from each molecule overlapping each other. The measured distance of

centroid-centroid of the benzene rings is 3.76 Å, which matches the $[\pi\cdots\pi]$ interaction distance.

Considering the rigid pore size of macrocycle **2** and the ease for single crystal X-ray analysis, we chose symmetric polyfluorobenzenes: hexafluorobenzene, 1,2,4,5-tetrafluorobenzene, 1,3,5-trifluorobenzene, and 1,4-difluorobenzene, as guest molecules for performing cocrystallization. Typically, the cocrystals of fluorobenzenes@**2** were prepared by slowly mixing the fluoroarene phase with a solution of macrocycle **2** in DCM in vials or NMR tubes for 7 d. The crystal structure of hexafluorobenzene@**2** shows a monoclinic unit cell with space group of $P2_1/c$ and $Z = 4$. The host-guest interaction of shape-persistent macrocycles is then exhibited by the fact of hexafluorobenzene being trapped in the void of macrocycle **2** (Figure 5.5B). Notably, hexafluorobenzene can perfectly fit into macrocycle **2**, not only because of the shape and volume of the pore, but also because of the $[\text{C}-\text{H}\cdots\text{F}-\text{C}]$ hydrogen bonds, with average distance of 2.58 Å and CHF angle of 140.6°. ¹⁸ The macrocycles containing guest molecules still prefer to pack in pairs, but interestingly, only half of the molecule overlaps with the other. The packing is directed by two factors: (1) the $[\pi\cdots\pi]$ interaction between the relatively electron-poor hexafluorobenzene and electron-rich benzene rings of **2** (centroid-centroid distance is 3.84 Å); ¹⁹ (2) the mutual avoidance of sterically bulky *t*-heptyl groups.

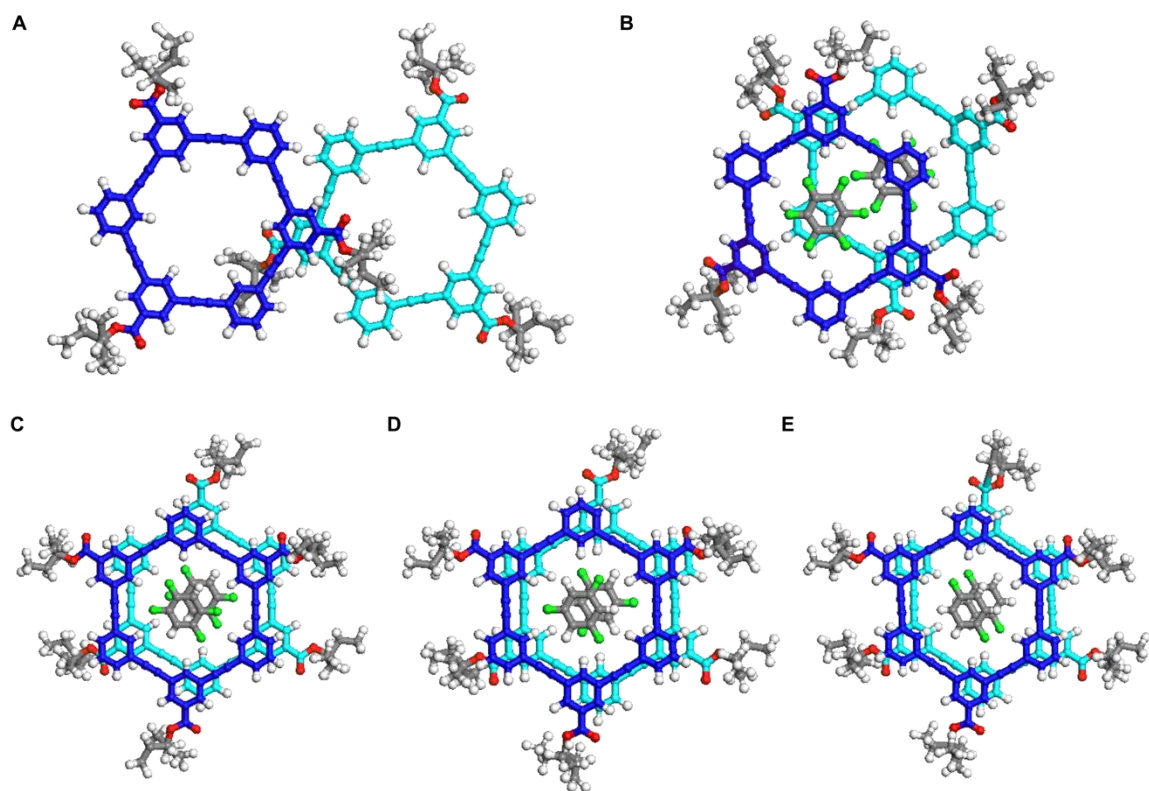


Figure 5.5 Single crystal X-ray structures of (A) macrocycle **2**; (B) hexafluorobenzene@**2**; (C) 1,2,4,5-tetrafluorobenzene@**2**; (D) 1,3,5-trifluorobenzene@**2**; (E) 1,4-difluorobenzene@**2**. Two different colors blue and cyan are applied to distinguish the two discrete macrocycle **2** molecules. Element colors: C, gray; O, red; F, lime; and H, white.

The crystal structures of 1,2,4,5-tetrafluorobenzene@**2**, 1,3,5-trifluorobenzene@**2**, and 1,4-difluorobenzene@**2** have the same monoclinic unit cell and space group of $P2_1/n$ and $Z = 4$. They display similar guest molecule trapping and pair-packing of macrocycles (Figure 5.5C–E). However, their packing is different than that of the previous two examples. The pair of guest molecules@**2** has a staggered packing with a slight offset. In these three complexes, the average $[\pi \cdots \pi]$ distance between centroids of every two

adjacent fluorobenzenes is 3.55 Å and each benzene ring of **2** has an average distance of 3.73 Å to the adjacent one of the other macrocycle **2**. The average distance of [C–H···F–C] hydrogen bonds is 2.69 Å and CHF angle is 146.9°. From the above five examples, it is clear that via $[\pi\cdots\pi]$ interaction, macrocycle **2** forms a pair of complex similar to the one in **MCMOFs** mentioned above. Suitable size and shape of guest molecules with interactive functional groups can be trapped in the void of macrocycles. As a proof of concept, the shape-persistent macrocycles in solid-state porous materials could be applied for separation or capture of guest molecules.

5.3 Conclusions and Outlook

As we proposed, the use of rigid macrocyclic linker led to isolation of extended structure with novel topologies that are devoid of interpenetration and catenation. Interestingly, the $[\pi\cdots\pi]$ stacking of macrocycles produces a new family of **MCMOFs**; it was demonstrated that different metals give different coordination geometries and the resulting framework is not predictable from our limited understanding of these systems. Second, the discovery of the unprecedented structure of **Zn-MCMOF** opens up a new route to MOFs of extremely high porosity, wherein the porosity is pre-engineered in the structure of the linker.

The **Zr-MCMOF** exhibits a unique microporous framework with 1D channels and small cages. The rigid tunnels with hydrogens facing the center of void are expected to show special host-guest interaction. Furthermore, the rare examples of host-guest

chemistry of shape-persistent macrocycles presented in this Chapter provide a promising application for guest molecule separation of **MCMOFs**.

In addition, the phenyleneacetylene macrocycles used in **MCMOFs** might also be fluorescent and exhibit non-linear optical (NLO) properties. Reticulating these materials into MOFs will yield porous frameworks with perhaps unprecedented optical properties, and we will investigate those in-house as well as collaboratively. From a fundamental perspective, our work will explore the importance of π -interactions in crystal engineering of MOFs, which is an emerging area of interest.¹⁹

In summary, the use of linkers with predesigned pore is expected to increase the likelihood of obtaining MOFs with accessible pores without interpenetration and catenation. The expected high surface area from mesoporous **MCMOFs** may be useful as materials for applications in gas storage, guest separations, and analysis. Moreover, either phenyl or acetylene group can be used to extend the structure; Snurr and Hupp suggested that introducing acetylene to replace phenyl group can effectively boost MOFs' accessible surface areas.²⁰

5.4 Experimental Section

5.4.1 General Methods

Standard scintillation vials were used as vessels for the synthesis of **MCMOFs**. Infrared spectra were recorded on a Perkin-Elmer Spectrum 100 FT-IR spectrophotometer using Pike MIRacle Micrometer pressure clamp. Microanalyses were conducted by Intertek USA, Inc. TGA were carried out on a TA Instruments TGA 2050 thermogravimetric analyzer at a temperature ramping rate of 2 °C/min under the flow of N₂ gas. PXRD data were collected at 25 °C on a Phillips X'pert Pro diffractometer. Capillary PXRD measurements were performed on a Bruker DUO platform diffractometer equipped with a 4K CCD APEX II detector and an Incoatec 30 Watt Cu microsource with compact multilayer optics. Simulated PXRD patterns were calculated with the Material Studio software package²¹ employing the structure model from the single crystal data obtained.

The following starting materials and solvents were obtained from their respective commercial sources and used without further purification: hexafluorobenzene, 1,2,4,5-tetrafluorobenzene, 1,3,5-trifluorobenzene, and 1,4-difluorobenzene (SynQuest Labs); Zn(NO₃)₂·6H₂O and anhydrous ZrCl₄ (Alfa Aesar). All the solvents for syntheses of **MCMOFs** and cocrystallization of macrocycle **2** and guest molecules were obtained from commercial sources and used without further purification. All the gases for gas adsorption analysis and SCD were purchased from Matheson Tri-Gas Inc.

5.4.2 Syntheses of MCMOFs

Synthesis of Zn-MCMOF

Compound **1** (20 mg, 0.027 mmol) and $\text{Zn}(\text{NO}_3)_2 \cdot 6\text{H}_2\text{O}$ (14 mg, 0.047 mmol) were added to a 20 mL glass scintillation vial. DMA (8 mL) was added to the solids, and the mixture was sonicated for 10 min. The vial was capped and placed into an oven at 100 °C for 1 d and yellowish crystals were obtained. After cooling, the liquid was decanted and replaced with fresh DMA three times. The crystals isolated were soaked in EtOH for 3 d and fresh EtOH was replaced each day. SCD drying was then performed on wet crystals and the activated sample with 87% (20 mg) yield based on macrocycle **1** was obtained. FT-IR (neat): $\tilde{\nu}$ = 3605 (b), 3063 (b), 1699 (w), 1557 (s), 1434 (s), 1393 (s), 890 (s), 788 (s), 679 (s) cm^{-1} . CHN anal. calcd (%) for $\text{C}_{102}\text{H}_{42}\text{O}_{14}\text{Zn}_3$: C 72.53, H 2.49; Found: C 70.33, H 2.77.²²

Synthesis of Zr-MCMOF

Anhydrous ZrCl_4 (0.20 g, 0.86 mmol) and benzoic acid (7.3 g, 60 mmol) were mixed in DEF (20 mL) and sonicated until dissolved. Due to the large amount of solid starting material, the volume of solution became 30 mL after dissolving all compounds. The solution was capped and placed in an oven at 80 °C for 1 d. After cooling down, the solution (2.4 mL) was added to macrocycle **1** (10 mg, 0.014 mmol) in a 8 mL glass scintillation vial and capped. The mixture was sonicated for 10 min and placed into an oven at 100 °C for 4 d. The resulting colorless crystals were washed with DEF and MeOH, and dried under reduced pressure. Yield calculated from evacuated sample was

51 % (10 mg) based on macrocycle **1**. FT-IR (neat): $\tilde{\nu}$ = 1595 (m), 1539 (m), 1403 (s), 1176 (w), 787 (m), 716 (s), 645 (s) cm^{-1} . CHN anal. calcd (%) for $\text{C}_{129}\text{H}_{58}\text{N}_3\text{O}_{35}\text{Zr}_6$: C 56.17, H 2.12, N 1.52; Found: C 53.62, H 2.25, N 0.48.²²

5.4.3 Cocrystallization of Macrocycle **2** and Guest Molecules

Crystallization of Macrocycle **2**

A 2 mL glass scintillation vial containing 1 mL EtOH was added a solution of macrocycle **2** (5.0 mg, 5.0 μmol)/DCM (1 mL) into the bottom of vial via a Pasteur pipet. The vial containing the biphasic solution was capped with a septum, that a syringe neddle (dimension 30G) sticking through it. The vial was then placed on a stable stage without disturbing, and colorless prismatic crystals were obtained after 7 d.

Crystallization of Hexafluorobenzene@**2**

To a 2 mL glass scintillation vial containing a solution of macrocycle **2** (5.0 mg, 5.0 μmol) in DCM (0.5 mL) was added hexafluorobenzene (1.5 mL). Hexafluorobenzene was carefully injected to the bottom of the vial via a Pasteur pipet. The vial containing the biphasic solution was capped and placed on a stable stage without disturbing, and colorless rod-shape crystals were obtained after 7 d.

Crystallization of 1,2,4,5-Tetrafluorobenzene@**2**

To a 2 mL glass scintillation vial containing a solution of macrocycle **2** (5.0 mg, 5.0 μmol) in DCM (0.5 mL) was added 1,2,4,5-tetrafluorobenzene (1.5 mL). Tetrafluorobenzene was added to the bottom of the vial via a Pasteur pipet. The vial

containing the biphasic solution was capped and placed on a stable stage without disturbing, and colorless rod-shape crystals were obtained after 7 d.

Crystallization of 1,3,5-Trifluorobenzene@2

To an NMR tube containing a solution of macrocycle **2** (5.0 mg, 5.0 μmol) in DCM (0.5 mL) was slowly added 1,3,5-trifluorobenzene (0.5 mL). Trifluorobenzene was added onto the top of the solution surface along the wall of NMR tube. The tube containing the biphasic solution was capped and a syringe needle (dimension 30G) was stucked through the cap. The NMR tube was placed vertically on a stable stage without disturbing, and colorless rod-shape crystals were obtained after 7 d.

Crystallization of 1,4-Difluorobenzene@2

To an NMR tube containing a solution of macrocycle **2** (5.0 mg, 5.0 μmol) in DCM (0.5 mL) was slowly added 1,4-difluorobenzene (0.5 mL). Difluorobenzene was added onto the top of the solution surface along the wall of the NMR tube. The tube containing the biphasic solution was capped and a syringe needle (dimension 30G) was stucked through the cap. The NMR tube was placed vertically on a stable stage without disturbing, and colorless rod-shape crystals were obtained after 7 d.

5.4.4 X-ray Crystallographic Analyses

X-ray Crystallographic Analysis of Zn-MCMOF

The structure data collection was performed at ChemMatCARS beamline at the Advanced Photon Source of the Argonne National Laboratory. The crystal structure was

refined by Dr. Yu-Chun Chuang from National Synchrotron Radiation Research Center, Taiwan. The diffraction data was collected on a Bruker D8 diffractometer with an APEX-II CCD detector using ϕ scans. Data collection was 99.9% complete to 11.25° in θ . A total of 147936 reflections were collected covering the indices, $-26 \leq h \leq 25$, $-24 \leq k \leq 26$, $-26 \leq l \leq 26$. Indexing and unit cell refinement indicated a *P*-centered, cubic lattice. The space group was found to be *P4₁32* (No. 210). The data were integrated using the Bruker SAINT software program and scaled using the SADABS software program. Solution by direct methods produced a complete heavy-atom phasing model consistent with the proposed structure. All non-hydrogen atoms were refined anisotropically by full-matrix least-squares (SHELXL-97). All hydrogen atoms were placed using a riding model. Their positions were constrained relative to their parent atom using the appropriate HFIX command in SHELXL-97. The PLATON program, SQUEEZE function, was used to remove disordered solvent.

Table 5.1 Crystallographic Data of **Zn-MCMOF**

Empirical formula	C ₁₀₂ H ₄₂ O ₁₄ Zn ₃
Formula weight	1687.47
Temperature	293(2) K
Wavelength	0.49594 Å
Crystal system	Cubic
Space group	<i>P4₁32</i>
Unit cell dimensions	$a = b = c = 33.261(4)$ Å $\alpha = \beta = \gamma = 90^\circ$
Volume	36796(8) Å ³

Z	4
Density (calculated)	0.305 Mg/m ³
Absorption coefficient	0.072 mm ⁻¹
<i>F</i> (000)	3424
θ range for data collection	0.60° to 11.25°
Index ranges	$-26 \leq h \leq 25$, $-24 \leq k \leq 26$, $-26 \leq l \leq 26$
Reflections collected	147936
Independent reflections	3141 [<i>R</i> (int) = 0.1088]
Completeness to $\theta = 11.25^\circ$	99.9%
Absorption correction	Semi-empirical from equivalents
Refinement method	Full-matrix least-squares on <i>F</i> ²
Data / restraints / parameters	3141 / 29 / 126
Goodness-of-fit on <i>F</i> ²	1.12
Final <i>R</i> indices [<i>I</i> > 2σ(<i>I</i>)]	<i>R</i> ₁ = 0.0648, w <i>R</i> ₂ = 0.1774
<i>R</i> indices (all data)	<i>R</i> ₁ = 0.0892, w <i>R</i> ₂ = 0.1879
Absolute structure parameter	0.06(8)
Largest diff. peak and hole	0.118 and −0.384 e/Å ³

X-ray Crystallographic Analysis of Zr-MCMOF

Measurements were performed by Dr James Korp (UH) using a Bruker DUO platform diffractometer equipped with a 4K CCD APEX II detector and an Incoatec 30 Watt Cu microsource with compact multilayer optics. A hemisphere of data (2713 frames

at 4 cm detector distance) was collected using a narrow-frame algorithm with scan widths of 0.50% in omega and an exposure time of 25 s/frame. The data were integrated using the Bruker-Nonius SAINT program, with the intensities corrected for Lorentz factor, polarization, air absorption, and absorption due to variation in the path length through the detector faceplate. The data were scaled, and an absorption correction was applied using SADABS. Redundant reflections were averaged. Final cell constants were refined using 7541 reflections having $I > 10\sigma(I)$. The Laue symmetry was determined to be $\bar{3}m1$, and from the systematic absences noted the space group was shown to be either $P3c1$ or $P\bar{3}c1$. The structure consists of complex Zr_6 clusters linked into 2D polymeric sheets by large macrocyclic rings. All of the solvent sites are heavily disordered, and the identities of some solvent species are impossible to determine precisely. Most of the solvent identities and occupancies in this model are just estimates, and should not be relied on. They represent just one possibility out of many. Some of the solvent sites are not fully occupied, either due to some loss during crystal handling or because the disorder is so severe that some solvent locations cannot be identified. It's also quite possible that some heavily disordered water has been omitted.

Table 5.2 Crystallographic Data of **Zr-MCMOF**

Empirical formula	$C_{140.75}H_{132}N_{5.50}O_{37.50}Zr_6$
Formula weight	3047.84
Temperature	113(2) K
Wavelength	1.5418 Å
Crystal system	Trigonal

Space group	$P\bar{3}c1$	
Unit cell dimensions	$a = 24.0688(3) \text{ \AA}$	$\alpha = 90^\circ$
	$b = 24.0688(3) \text{ \AA}$	$\beta = 90^\circ$
	$c = 30.1366(5) \text{ \AA}$	$\gamma = 120^\circ$
Volume	$15119.4(4) \text{ \AA}^3$	
Z	4	
Density (calculated)	1.339 Mg/m^3	
Absorption coefficient	3.886 mm^{-1}	
$F(000)$	6220	
Crystal size	$0.20 \times 0.20 \times 0.10 \text{ mm}^3$	
θ range for data collection	2.12° to 66.63°	
Index ranges	$-24 \leq h \leq 0, 0 \leq k \leq 28, 0 \leq l \leq 35$	
Reflections collected	103552	
Independent reflections	9606 [$R(\text{int}) = 0.0263$]	
Absorption correction	Empirical	
Max. and min. transmission	0.7528 and 0.5646	
Refinement method	Full-matrix least-squares on F^2	
Data / restraints / parameters	8908 / 47 / 619	
Goodness-of-fit on F^2	1.119	
Final R indices [$I > 2\sigma(I)$]	$R_1 = 0.0386, wR_2 = 0.1230$	
R indices (all data)	$R_1 = 0.0450, wR_2 = 0.1344$	
Largest diff. peak and hole	1.089 and -0.611 e/\AA^3	

X-ray Crystallographic Analysis of Macrocycle 2

The measurement was performed by Dr. James Korp (UH) using a Bruker DUO platform diffractometer equipped with a 4K CCD APEX II detector and an Incoatec 30 Watt Cu microsource with compact multilayer optics. A hemisphere of data (2713 frames at 4 cm detector distance) was collected using a narrow-frame algorithm with scan widths of 0.50% in omega and an exposure time of 40 s/frame. The data were integrated using the Bruker-Nonius SAINT program, with the intensities corrected for Lorentz factor, polarization, air absorption, and absorption due to variation in the path length through the detector faceplate. The data were scaled, and an absorption correction was applied using SADABS. Redundant reflections were averaged. Final cell constants were refined using 7891 reflections having $I > 10\sigma(I)$. The Laue symmetry was determined to be $\bar{3}m1$, and from the systematic absences noted the space group was shown to be either $P3_121$ or $P3_221$. The asymmetric unit consists of one main molecule in a general location, and three solvent sites each located on a two-fold axis. Two of the *t*-heptyl groups were found to be disordered over two different orientations, and this was treated by the use of mild distance constraints. Each of the three solvent sites consisted of a massively disordered mixture of methylene chloride and water, in an approximate ratio of 2:1 total occupancy. The methylene chlorides were treated as ideal rigid bodies, with occupancies estimated by comparison of isotropic displacement parameters. A small amount of water could not be located at one of the three sites, however all sites are presumed to be fully occupied for purposes of calculations such as formula weight, density, etc. No attempt was made to include hydrogen atoms on any of the solvent water molecules.

Table 5.3 Crystallographic Data of Macrocycle **2**

Empirical formula	$\text{C}_{73}\text{H}_{69.90}\text{Cl}_2\text{O}_{6.95}$	
Formula weight	1129.29	
Temperature	123(2) K	
Wavelength	1.54178 Å	
Crystal system	Trigonal	
Space group	$P3_121$	
Unit cell dimensions	$a = 23.6003(3)$ Å	$\alpha = 90.00^\circ$
	$b = 23.6003(3)$ Å	$\beta = 90.00^\circ$
	$c = 19.7136(3)$ Å	$\gamma = 120.00^\circ$
Volume	$9508.9(2)$ Å ³	
<i>Z</i>	6	
Density (calculated)	1.183 Mg/m ³	
Absorption coefficient	1.338 mm ⁻¹	
<i>F</i> (000)	3585	
Crystal size	$0.30 \times 0.25 \times 0.25$ mm ³	
θ range for data collection	2.16° to 66.62°	
Index ranges	$-28 \leq h \leq 14$, $0 \leq k \leq 28$, $0 \leq l \leq 23$	
Reflections collected	65395	
Independent reflections	11107 [$R(\text{int}) = 0.0242$]	
Absorption correction	Semi-empirical from equivalents	
Max. and min. transmission	0.7528 and 0.6445	

Refinement method	Full-matrix least-squares on F^2
Data / restraints / parameters	11093 / 24 / 752
Goodness-of-fit on F^2	1.044
Final R indices [$I > 2\sigma(I)$]	$R_1 = 0.0464$, $wR_2 = 0.1261$
R indices (all data)	$R_1 = 0.0488$, $wR_2 = 0.1296$
Largest diff. peak and hole	0.483 and -0.362 e/\AA^3

X-ray Crystallographic Analysis of Hexafluorobenzene@2

The measurement was performed by Dr. Sergey Belyakov (Latvian Institute of Organic Synthesis) using Bruker-Nonius KappaCCD diffractometer equipped with a fine-focus sealed tube with MoK_α radiation ($\lambda = 0.71073 \text{ \AA}$). A hemisphere of data (516 frames at 36 mm detector distance) was collected using φ and ω scan method with an exposure time of 65 s/frame. The data were integrated using the Nonius KappaCCD SUPERGUI program, with the intensities corrected for Lorentz and polarization factors; no absorption correction was performed. Redundant reflections were averaged. Final cell constants were refined using 5453 reflections having $I > 3\sigma(I)$. The Laue symmetry was determined to be $2/m$, and from the systematic absences noted the space group was shown unambiguously to be $P2_1/c$.

Table 5.4 Crystallographic Data of Hexafluorobenzene@2

Empirical formula	$\text{C}_{79}\text{H}_{68}\text{Cl}_2\text{F}_6\text{O}_6$
Formula weight	1298.23
Temperature	173(2) K
	207

Wavelength	0.71073 Å	
Crystal system	Monoclinic	
Space group	$P2_1/c$	
Unit cell dimensions	$a = 10.8228(3)$ Å	$\alpha = 90.00^\circ$
	$b = 28.4588(7)$ Å	$\beta = 98.1522(13)^\circ$
	$c = 21.9360(6)$ Å	$\gamma = 90.00^\circ$
Volume	6688.1(3) Å ³	
Z	4	
Density (calculated)	1.289 Mg/m ³	
Absorption coefficient	0.168 mm ⁻¹	
$F(000)$	2712	
Crystal size	0.38×0.03×0.02 mm ³	
θ range for data collection	0.9° to 27.5°	
Index ranges	$0 \leq h \leq 14, 0 \leq k \leq 36, -28 \leq l \leq 28$	
Reflections collected	15099	
Independent reflections	5453 [$R(\text{int}) = 0.045$]	
Absorption correction	Semi-empirical from equivalents	
Refinement method	Full-matrix least-squares on F^2	
Data / restraints / parameters	5358 / 68 / 443	
Goodness-of-fit on F^2	1.739	
Final R indices [$I > 2\sigma(I)$]	$R_1 = 0.144, wR_2 = 0.366$	
R indices (all data)	$R_1 = 0.428, wR_2 = 0.421$	

Largest diff. peak and hole 1.371 and $-0.611 \text{ e}/\text{\AA}^3$

X-ray Crystallographic Analysis of 1,2,4,5-Tetrafluorobenzene@2

The measurement was performed by Dr. James Korp (UH) using Bruker DUO platform diffractometer equipped with a 4K CCD APEX II detector and an Incoatec 30 Watt Cu microsource with compact multilayer optics. A hemisphere of data (2,713 frames at 4 cm detector distance) was collected using a narrow-frame algorithm with scan widths of 0.50% in omega and an exposure time of 40 s/frame. The data were integrated using the Bruker-Nonius SAINT program, with the intensities corrected for Lorentz factor, polarization, air absorption, and absorption due to the variation in the path length through the detector faceplate. The data were scaled, and an absorption correction was applied using SADABS. Redundant reflections were averaged. Final cell constants were refined using 8,125 reflections having $I > 10\sigma(I)$. The Laue symmetry was determined to be $2/m$, and from the systematic absences noted the space group was shown unambiguously to be $P2_1/n$. Two of the *t*-heptyl groups were found to be disordered over two different orientations, and this was treated by use of mild distance constraints. The tetrafluorobenzene guest molecule was also found to be very slightly disordered. The main orientation is present approximately 90% of the time, with two other possible orientations of the fluorines present approximately 5% each. This combination results in about 95% total occupancy for sites F1–F4, and 10% total occupancy for the alternative positions which were called F5 and F6.

Table 5.5 Crystallographic Data of Tetrafluorobenzene@2

Empirical formula	$\text{C}_{78}\text{H}_{68}\text{F}_4\text{O}_6$	
Formula weight	1177.32	
Temperature	123(2) K	
Wavelength	1.54178 Å	
Crystal system	Monoclinic	
Space group	$P2_1/n$	
Unit cell dimensions	$a = 7.6495(4)$ Å	$\alpha = 90.00^\circ$
	$b = 22.7639(10)$ Å	$\beta = 94.466(2)^\circ$
	$c = 36.5143(16)$ Å	$\gamma = 90.00^\circ$
Volume	6339.0(5) Å ³	
Z	4	
Density (calculated)	1.234 Mg/m ³	
Absorption coefficient	0.686 mm ⁻¹	
$F(000)$	2480	
Crystal size	0.40×0.12×0.10 mm ³	
θ range for data collection	2.29° to 66.62°	
Index ranges	$-8 \leq h \leq 8, 0 \leq k \leq 27, 0 \leq l \leq 43$	
Reflections collected	43547	
Independent reflections	11027 [$R(\text{int}) = 0.0237$]	
Absorption correction	Semi-empirical from equivalents	
Refinement method	Full-matrix least-squares on F^2	

Data / restraints / parameters	10731/ 14/ 784
Goodness-of-fit on F^2	0.992
Final R indices [$I > 2\sigma(I)$]	$R_1 = 0.0541$, $wR_2 = 0.1532$
R indices (all data)	$R_1 = 0.0628$, $wR_2 = 0.1599$
Largest diff. peak and hole	0.456 and -0.621 e/\AA^3

X-ray Crystallographic Analysis of 1,3,5-Trifluorobenzene@2

The measurement was performed by Dr. James Korp (UH) using Bruker DUO platform diffractometer equipped with a 4K CCD APEX II detector and an Incoatec 30 Watt Cu microsource with compact multilayer optics. A hemisphere of data (2713 frames at 4 cm detector distance) was collected using a narrow-frame algorithm with scan widths of 0.50% in omega and an exposure time of 25 s/frame. The data were integrated using the Bruker-Nonius SAINT program, with the intensities corrected for Lorentz factor, polarization, air absorption, and absorption due to variation in the path length through the detector faceplate. The data were scaled, and an absorption correction was applied using SADABS. Redundant reflections were averaged. Final cell constants were refined using 8140 reflections having $I > 10\sigma(I)$. The Laue symmetry was determined to be $2/m$, and from the systematic absences noted the space group was shown unambiguously to be $P2_1/n$. Two of the *t*-heptyl groups were found to be disordered over two different orientations, and this was treated by use of mild distance constraints.

Table 5.6 Crystallographic Data of 1,3,5-Trifluorobenzene@2

Empirical formula	$\text{C}_{78}\text{H}_{69}\text{F}_3\text{O}_6$	
Formula weight	1159.33	
Temperature	113(2) K	
Wavelength	1.54718 Å	
Crystal system	Monoclinic	
Space group	$P2_1/n$	
Unit cell dimensions	$a = 7.6480(41)$ Å	$\alpha = 90.00^\circ$
	$b = 22.7572(3)$ Å	$\beta = 94.246(1)^\circ$
	$c = 36.5575(5)$ Å	$\gamma = 90.00^\circ$
Volume	6345.26(15) Å ³	
Z	4	
Density (calculated)	1.214 Mg/m ³	
Absorption coefficient	0.654 mm ⁻¹	
$F(000)$	2448	
Crystal size	0.40×0.10×0.08 mm ³	
θ range for data collection	2.29° to 62.42°	
Index ranges	$-8 \leq h \leq 8, 0 \leq k \leq 26, 0 \leq l \leq 41$	
Reflections collected	41749	
Independent reflections	10379 [$R(\text{int}) = 0.1301$]	
Absorption correction	Semi-empirical from equivalents	
Refinement method	Full-matrix least-squares on F^2	

Data / restraints / parameters	10072 / 12 / 762
Goodness-of-fit on F^2	1.005
Final R indices [$I > 2\sigma(I)$]	$R_1 = 0.0628$, $wR_2 = 0.1712$
R indices (all data)	$R_1 = 0.0700$, $wR_2 = 0.1824$
Largest diff. peak and hole	0.433 and -0.409 e/Å ³

X-ray Crystallographic Analysis of 1,4-Difluorobenzene@2

The measurement was performed by Dr. James Korp (UH) using Bruker DUO platform diffractometer equipped with a 4K CCD APEX II detector and an Incoatec 30 Watt Cu microsource with compact multilayer optics. A hemisphere of data (2713 frames at 4 cm detector distance) was collected using a narrow-frame algorithm with scan widths of 0.50% in omega and an exposure time of 40 s/frame. The data were integrated using the Bruker-Nonius SAINT program, with the intensities corrected for Lorentz factor, polarization, air absorption, and absorption due to variation in the path length through the detector faceplate. The data were scaled, and an absorption correction was applied using SADABS. Redundant reflections were averaged. Final cell constants were refined using 8159 reflections having $I > 10\sigma(I)$. The Laue symmetry was determined to be $2/m$, and from the systematic absences noted the space group was shown unambiguously to be $P2_1/n$. Two of the *t*-heptyl groups were found to be disordered over two different orientations, and this was treated by use of mild distance constraints.

Table 5.7 Crystallographic Data of 1,4-Difluorobenzene@2

Empirical formula	$\text{C}_{78}\text{H}_{70}\text{F}_2\text{O}_6$	
Formula weight	1141.34	
Temperature	113(2) K	
Wavelength	1.54178 Å	
Crystal system	Monoclinic	
Space group	$P2_1/n$	
Unit cell dimensions	$a = 7.5333(1)$ Å	$\alpha = 90.00^\circ$
	$b = 22.7598(4)$ Å	$\beta = 93.686(1)^\circ$
	$c = 36.8754(7)$ Å	$\gamma = 90.00^\circ$
Volume	6309.44(18) Å ³	
Z	4	
Density (calculated)	1.202 Mg/m ³	
Absorption coefficient	0.626 mm ⁻¹	
$F(000)$	2416	
Crystal size	0.40×0.08×0.06 mm ³	
θ range for data collection	2.28° to 66.53°	
Index ranges	$-8 \leq h \leq 8, 0 \leq k \leq 26, 0 \leq l \leq 43$	
Reflections collected	43173	
Independent reflections	10995 [$R(\text{int}) = 0.0234$]	
Absorption correction	Semi-empirical from equivalents	
Refinement method	Full-matrix least-squares on F^2	

Data / restraints / parameters	10715 / 12 / 758
Goodness-of-fit on F^2	1.024
Final R indices [$I > 2\sigma(I)$]	$R_1 = 0.0438$, $wR_2 = 0.1145$
R indices (all data)	$R_1 = 0.0540$, $wR_2 = 0.1255$
Largest diff. peak and hole	0.366 and -0.408 e/Å ³

5.4.5 Fourier-transform Infrared Spectra of MCMOFs

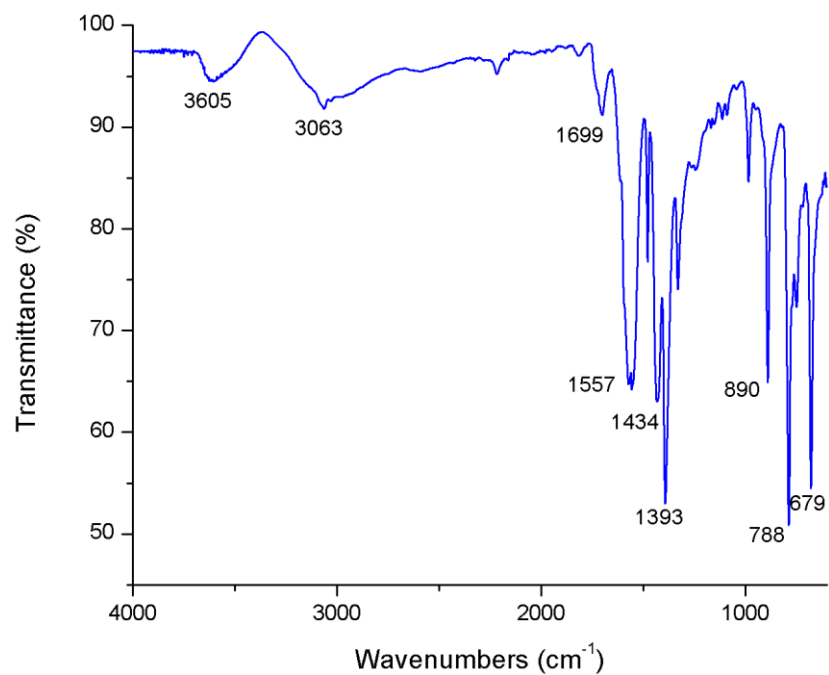


Figure 5.6 Fourier-transform infrared spectrum of **Zn-MCMOF**.

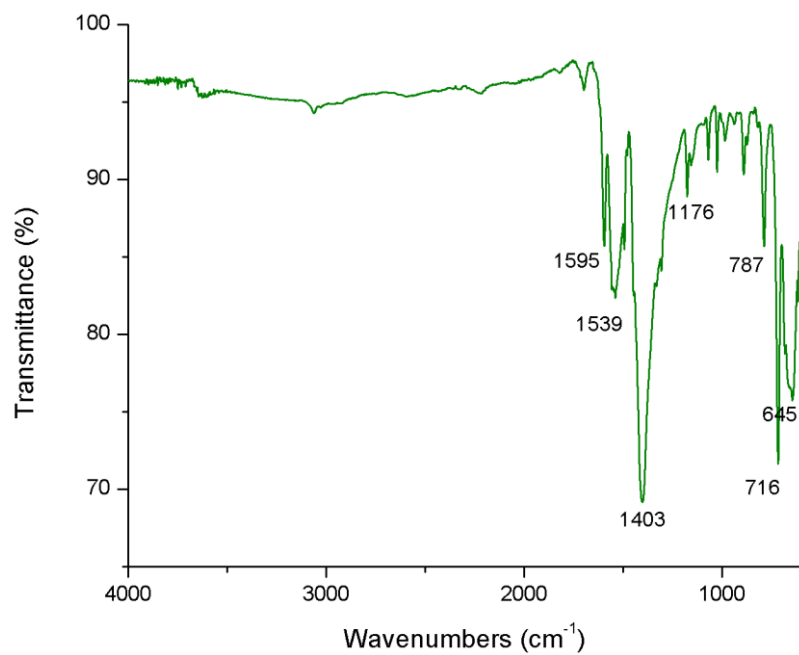


Figure 5.7 Fourier-transform infrared spectrum of **Zr-MCMOF**.

5.4.6 Powder X-ray Diffraction Patterns of MCMOFs

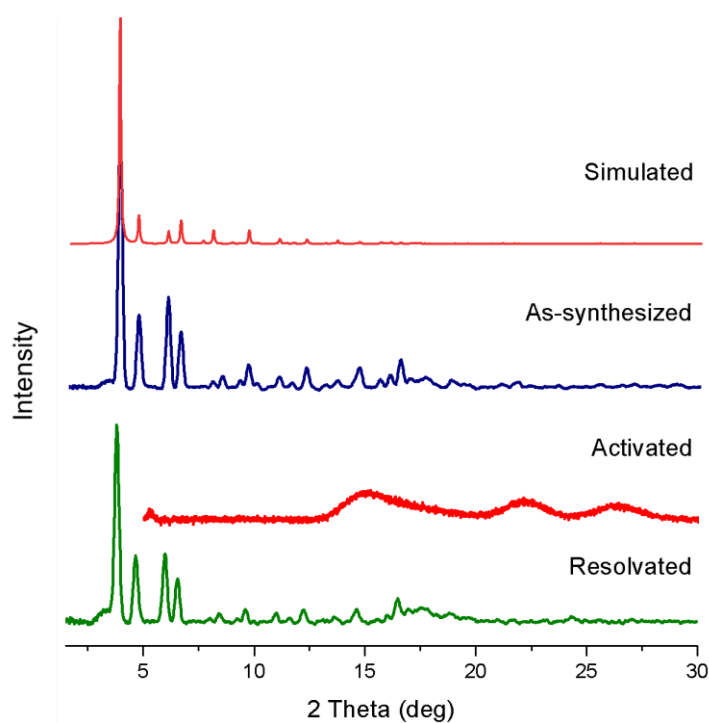


Figure 5.8 Powder X-ray diffraction pattern of **Zn-MCMOF**.

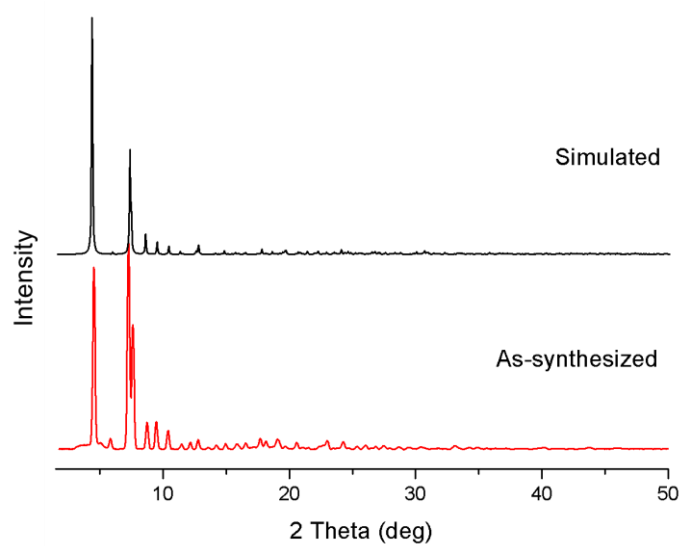


Figure 5.9 Powder X-ray diffraction pattern of **Zr-MCMOF**.

5.4.7 Gas Sorption Isotherms

A Micromeritics ASAP 2020 Surface Area and Porosity Analyzer was used to measure N₂ adsorption isotherms. Oven-dried sample tubes equipped with TranSeals™ (Micromeritics) were evacuated and tared. Samples (100–300 mg) were transferred to the sample tube, which was then capped by a TranSeal™. Samples were heated to 120 °C under high vacuum (10^{-3} – 10^{-4} Torr) and held until the outgas rate was less than 2 mTorr/minute. The evacuated sample tubes were weighed again, and the sample mass was determined by subtracting the mass of the previously tared tubes. N₂ isotherms were measured using a liquid nitrogen bath (77 K). Ultra high purity grade (99.999% purity) N₂ and He, oil-free valves, and gas regulators were used for all free space corrections and measurements. Relative pressure (P/P_o) range for BET analysis was taken from $5 \cdot 10^{-5}$ to 0.1.

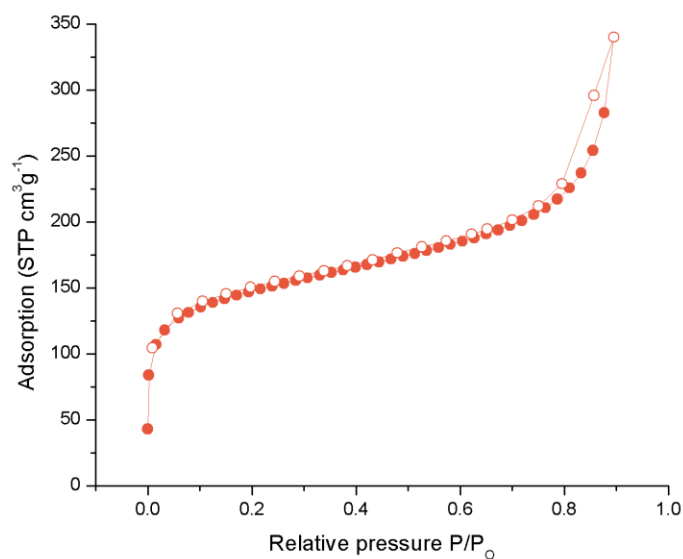


Figure 5.10 N₂ (77 K) adsorption isotherm of Zn-MCMOF.

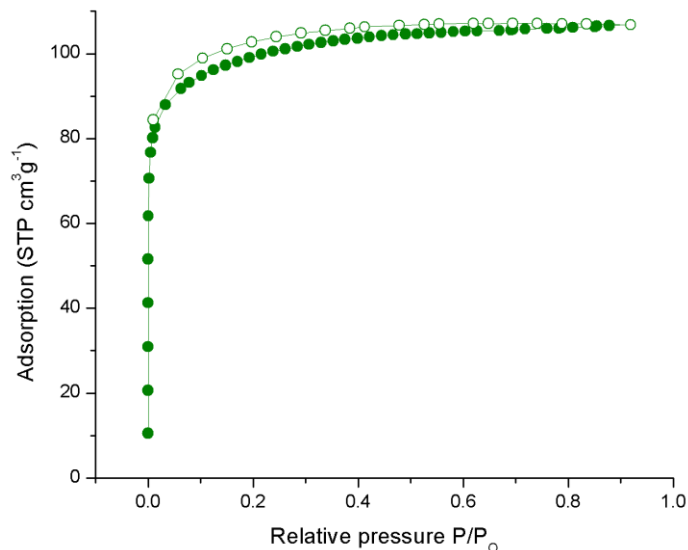


Figure 5.11 N_2 (77 K) adsorption isotherm of **Zr-MCMOF**.

5.4.8 Supercritical CO_2 Activation of **Zn-MCMOF**

Absolute EtOH was added to the crystals of **Zn-MCMOF** after the mother liquor was decanted. The EtOH was then decanted and replaced daily for 3 d and the crystals were left in EtOH until the next step. Approximately 60 mg of crystals were transferred into a Tousimis Samdri-PVT-3D super-critical CO_2 dryer. Excess EtOH was decanted, the temperature was lowered to 0 °C, and the chamber was filled with liquid CO_2 (ultrahigh grade CO_2 with a siphon tube from Matheson Tri-Gas Inc. was used). The sample was soaked for 48 h total, venting for 10 min for 10 times. The chamber was then heated to 40 °C and the pressure in the chamber was above 1300 psi. The supercritical CO_2 was bled off for 24 h until the chamber was at ambient pressure. The chamber was opened and the sample was quickly sealed and taken into an Ar atmosphere glove box for further manipulations. Dried crystals were transferred into a pre-weighed glass sample tube. The tube was sealed and quickly transferred to a system providing 10^{-4} Torr

dynamic vacuum. The sample was kept under vacuum at 120 °C for 15 h then used for gas adsorption measurements.

5.5 References

- [1] Farha, O. M.; Eryazici, I.; Jeong, N. C.; Hauser, B. G.; Wilmer, C. E.; Sarjeant, A. A.; Snurr, R. Q.; Nguyen, S. T.; Yazaydin, A. Ö.; Hupp, J. T. *J. Am. Chem. Soc.* **2012**, *134*, 15016–15021.
- [2] (a) Lan, Y.-Q.; Jiang, H.-L.; Li, S.-L.; Xu, Q. *Adv. Mater.* **2011**, *43*, 5015–5020. (b) Feng, D.; Gu, Z.-Y.; Li, J.-R.; Jiang, H.-L.; Wei, Z.; Zhou, H.-C. *Angew. Chem., Int. Ed.* **2012**, *51*, 10307–10310.
- [3] (a) Klein, N.; Senkovska, I.; Gedrich, K.; Stoeck, U.; Henschel, A.; Mueller, U.; Kaskel, S. *Angew. Chem., Int. Ed.* **2009**, *48*, 9954–9957. (b) Koh, K.; Wong-Foy, A. G.; Matzger, A. J. *Angew. Chem., Int. Ed.* **2008**, *47*, 677–680. (c) Park, Y. K.; Choi, S. B.; Kim, H.; Kim, K.; Won, B.-H.; Choi, K.; Choi, J.-S.; Ahn, W.-S.; Won, N.; Kim, S.; Jung, D. H.; Choi, S.-H.; Kim, G.-H.; Cha, S.-S.; Jhon, Y. H.; Yang, J. K.; Kim, J. *Angew. Chem., Int. Ed.* **2007**, *46*, 8230–8233. (d) Liu, C.; Li, T.; Rosi, N. L. *J. Am. Chem. Soc.* **2012**, *134*, 18886–18888. (e) Furukawa, H.; Ko, N.; Go, Y. B.; Aratani, N.; Choi, S. B.; Choi, E.; Yazaydin, A. Ö.; Snurr, R. Q.; O’Keeffe, M.; Kim, J.; Yaghi, O. M. *Science* **2010**, *329*, 424–428.

- [4] Davis, F., Higson, S. *Macrocycles: Construction, Chemistry and Nanotechnology Applications*; Wiley: A John Wiley and Sons, Ltd., Publication, 2011.
- [5] (a) Li, Q.; Zhang, W.; Miljanić, O. Š.; Sue, C.-H.; Zhao, Y.-L.; Liu, L.; Knobler, C. B.; Stoddart, J. F.; Yaghi, O. M. *Science* **2009**, *325*, 855–859. (b) Zhao, Y.-L.; Liu, L.; Zhang, W.; Sue, C.-H.; Li, Q.; Miljanić, O. Š.; Yaghi, O. M.; Stoddart, J. F. *Chem. Eur. J.* **2009**, *15*, 13356–13380. (c) Li, Q.; Zhang, W.; Miljanić, O. Š.; Knobler, C. B.; Stoddart, J. F.; Yaghi, O. M. *Chem. Commun.* **2010**, *46*, 380–382. (d) Vukotic, V. N.; Harris, K. J.; Zhu, K.; Schurko, R. W.; Loeb, S. J. *Nat. Chem.* **2012**, *4*, 456–460.
- [6] (a) Ortiz, G.; Brandes, S.; Rousselin, Y.; Guillard, R. *Chem. Eur. J.* **2011**, *17*, 6689–6695. (b) Gao, W.-Y.; Niu, Y.; Chen, Y.; Wojtas, L.; Cai, J.; Chen, Y.-S.; Ma, S. *CrystEngComm* **2012**, *14*, 6115–6117. (c) Tashiro, S.; Kubota, R.; Shionoya, M. *J. Am. Chem. Soc.* **2012**, *134*, 2461–2464.
- [7] Zang, L.; Che, Y.; Moore, J. S. *Acc. Chem. Res.* **2008**, *41*, 1596–1608.
- [8] (a) Iyoda, M.; Yamakawa, J.; Rahman, M. J. *Angew. Chem., Int. Ed.* **2011**, *50*, 10522–10553. (b) Gong, B.; Shao, Z. *Acc. Chem. Res.* **2013**, *46*, 2856–2866.
- [9] Zhang, W.; Moore, J. S. *Angew. Chem., Int. Ed.* **2006**, *45*, 4416–4439.
- [10] (a) Kawase, T.; Tanaka, K.; Fujiwara, N.; Darabi, H. R.; Oda, M. *Angew. Chem., Int. Ed.* **2003**, *42*, 1624–1628. (b) Kawase, T.; Seirai, Y.; Darabi, H. R.; Oda, M.; Sarakai, Y.; Tashiro, K. *Angew. Chem., Int. Ed.* **2003**, *42*, 1621–1624.
- [11] Venkataraman, D.; Lee, S.; Zhang, J.; Moore, J. S. *Nature* **1994**, *371*, 591–593.

- [12] Popov, I. *Synthetic and Methodological Studies in Copper and Palladium-Catalyzed Carbon-Carbon and Carbon-Heteroatom Bond Formation*; PhD Thesis, University of Houston, 2014.
- [13] Cavka, J. H.; Jakobsen, S.; Olsbye, U.; Guillou, N.; Lamberti, C.; Bordiga, S.; Lillerud, K. P. *J. Am. Chem. Soc.* **2008**, *130*, 13850–13851.
- [14] Walton, K. S.; Snurr, R. Q. *J. Am. Chem. Soc.* **2007**, *129*, 8552–8556.
- [15] Freely available for Linux, MacOSX and Windows operating systems, from: <http://www.ccdc.cam.ac.uk/Solutions/CSDSystem/Pages/Mercury.aspx>.
- [16] Bennett, T. D.; Cheetham, A. K. *Acc. Chem. Res.* **2014**, *47*, 1555–1562.
- [17] (a) Chapman, K. W.; Halder, G. J.; Chupas, P. J. *J. Am. Chem. Soc.* **2009**, *131*, 17546–17547. (b) Chapman, K. W.; Sava, D. F.; Halder, G. J.; Chupas, P. J.; Nenoff, T. M. *J. Am. Chem. Soc.* **2011**, *133*, 18583–18585. (c) Ohara, K.; Marti-Rujas, J.; Haneda, T.; Kawano, M.; Hashizume, D.; Izumi, F.; Fujita, M. *J. Am. Chem. Soc.* **2009**, *131*, 3860–3861. (d) Hu, Y.; Kazemian, H.; Rohani, S.; Huang, Y. N.; Song, Y. *Chem. Commun.* **2011**, *47*, 12694–12696. (e) Moggach, S. A.; Bennett, T. D.; Cheetham, A. K. *Angew. Chem., Int. Ed.* **2009**, *48*, 7087–7089. (f) Cairns, A. B.; Goodwin, A. L. *Chem. Soc. Rev.* **2013**, *42*, 4881–4893.
- [18] (a) Lu, N.; Ley, R. M.; Cotton, C. E.; Chung, W.-C.; Francisco, J. S.; Negishi, E. *J. Phys. Chem. A* **2013**, *117*, 8256–8262. (b) Dunitz, J. D.; Taylor, R. *Chem. Eur. J.* **1997**, *3*, 90–98. (c) Zhang, G.; He, W.; Chen, D. *Mol. Phys.* **2013**, *111*, 1–9.

- [19] Tiekink, E. R. T., Zukerman-Schpector, J. *The Importance of Pi-Interactions in Crystal-Engineering: Frontiers in Crystal Engineering*; Wiley: A John Wiley and Sons, Ltd., Publication, 2012.
- [20] Farha, O. K.; Wilmer, C. E.; Eryazici, I.; Hauser, B. G.; Parilla, P. A.; O'Neill, K.; Sarjeant, A. A.; Nguyen, T. S.; Snurr, R. Q.; Hupp, J. T. *J. Am. Chem. Soc.* **2012**, *134*, 9860–9863.
- [21] *Materials Studio program*, version 5.5; Accelrys, San Diego, CA, **2011**.
- [22] The large deviation (> 1%) between calculated and obtained elemental analysis is presumably due to the incompletely removed guest molecules remaining in the collapsed structure of MOF.

Chapter Six

Procedure for the Production of 3D Models of Crystal Structures¹

6.1 Introduction

Printing can be defined as the translation of information into a physical form that can be easily multiplied. Printing has a long history of over 2,000 years, which has been intricately connected to the development of modern society. Since 3D visualizing technology has been explosively developed in the past few decades, the demand for 3D printing is dramatically increasing. 3D printing or additive manufacturing is a process of making a three-dimensional solid object of virtually any shape from a digital model. The first working 3D printer was created in 1984 by Charles W. Hull of 3D Systems Corp.² However, it was not until the mid-2000s that the 3D printing technology dropped in price sufficiently to allow wide commercial exploitation. At the time of this writing in 2014, low-end 3D printers cost around \$1000 and were thus affordable even to a hobbyist. 3D printing has been touted as ushering “the third industrial revolution”—that of mass customization, wherein virtually any consumer object could be tailored to a previously unprecedented level.³

3D printable models can be created or designed by computer-aided software packages or via 3D scanning of an existing physical object. Modeling 3D items from

The work described in this chapter has been previously published: Chen, T.-H.; Lee, S.; Flood, A. H.; Miljanić, O. Š. *CrystEngComm* **2014**, *16*, 5488–5493.

scratch could be manipulated from 2D images by digital sculpting or inputting geometric data for 3D computer graphics. 3D scanning is a process of analyzing and collecting data of real object as digital data for printing. The 3D printing technology is used for both prototyping and distributed manufacturing with applications in architecture, industrial design, automotive, aerospace, military, engineering, dental and medical industries, biotechnology (human tissue replacement), fashion, footwear, jewelry, education, geographic information systems, and many other fields.² These technologies will likely revolutionize numerous fields of human activity; as just one example, prosthetic medicine could soon count on implants perfectly matching each individual patient. 3D printing is beginning to affect chemical research as well: Cronin *et al.* have recently reported the creation of customized 3D-printed “reactionware”, the composition and shape of which allow its active participation in the reaction and analysis of products.⁴

Chemistry is full of concepts that require three-dimensional understanding, and representing those in two-dimensional PowerPoint slides, journal articles, or on chalkboards inevitably leads to a loss of detail. For example, organic chemists often use



Figure 6.1 Picture of commercial molecular model kits.

small molecular model kits to study their conformation and stereochemistry (Figure 6.1). However, because of the high price of the model kits, it is not economical to build models containing large number of atoms. Furthermore, without the knowledge of correct atom sizes, bond lengths and bond angles, building a model of a large molecule is difficult if those parameters differ significantly from the standardized values based on which the molecular models are created. For these reasons, production of 3D-printed models directly from digital information should provide much more accurate structural representation (Figure 6.2). Crystallography is even more dependent on 3D representations, and most chemists immersed in this field have likely spent numerous hours turning crystal structure models on their computer screens to produce a view that sacrifices the least information. The situation becomes even more problematic for large networks—such as MOFs—which have large unit cells and would require too much material; so far, only plastic Wobbly[™] bond models have been used successfully for building such structures, but they are very much lacking in atomic detail (Figure 6.3). An ability to easily build color 3D models of crystal structures is thus clearly needed.

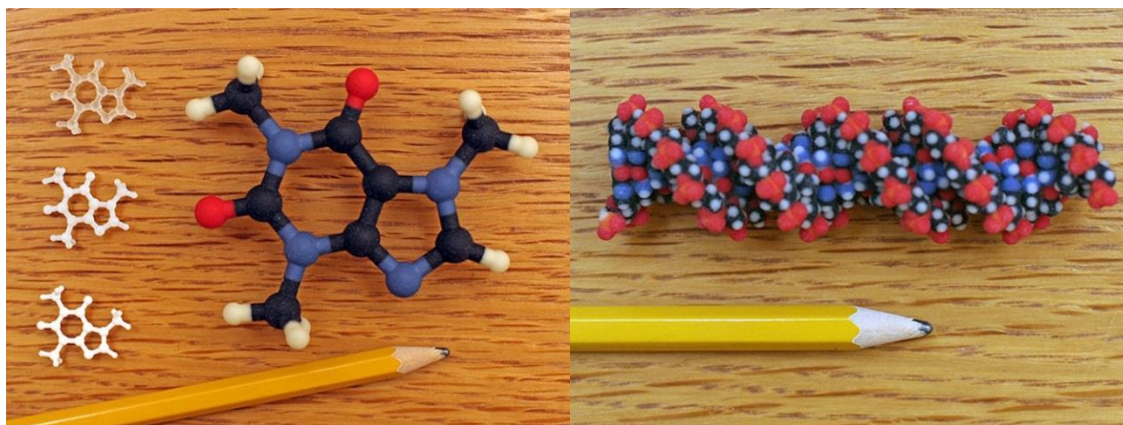


Figure 6.2 3D printed models of caffeine molecules (left) and DNA (right).⁵

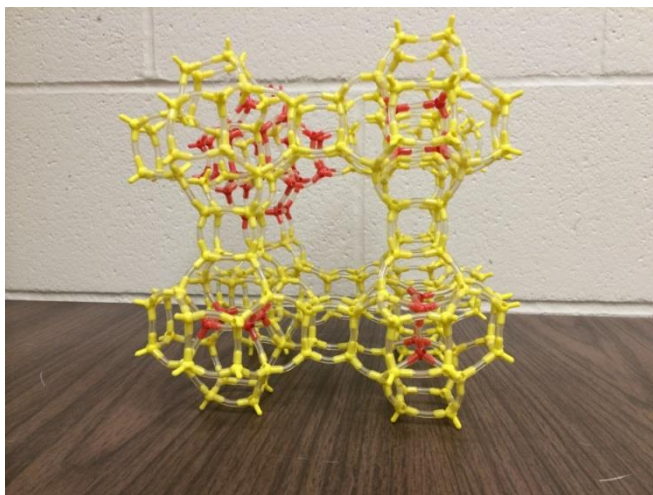


Figure 6.3 A model of segment of zeolite's infinite network.⁶

We have developed a convenient step-by-step procedure on how to convert a .cif file—which is a typical end product of crystal structure refinement—into a 3D-printed physical model of a crystal structure. We use **MOFF-3** (Figure 3.5)—one of our published extended MOF structures—as an illustration for this method. This procedure is broadly applicable to many other structures and we have printed 3D models of more than thirty different small molecules and MOFs.

Our procedure is neither the only nor the first method for achieving the conversion of crystallographic information files into 3D printed models.^{7,8} Its advantages are: (a) the ability to produce models of both discrete molecules and segments of extended “infinite” structures such as MOFs; (b) the use of freely available and highly intuitive software packages with ample helpful documentation available online, and (c) its reliance on a commercial 3D printing service provided by *Shapeways*, which obviates the need for an in-house 3D printer.

The main disconnect between the crystal structure manipulation programs and the 3D printing software lies in the mutual incompatibility of file formats. Out of the commonly used crystal structure processing programs, only PyMOL⁹ is able to directly export crystal structure data contained in .cif files into the VRML (.wrl) format most commonly used for color 3D printing.¹⁰ This feature enables the printing of small molecule models via PyMOL. However, many crystal structure processing operations—e.g. connectivity expansion, addition of multiple unit cells, etc.—are rather difficult to do in PyMOL. Our protocol thus resorts to using two programs which together offer greater flexibility in manipulating both the crystal structure and the 3D model. Mercury¹¹ is used to produce a .pdb file of the crystal structure, which is then imported into Blender—a semiprofessional 3D printing program—for additional processing and conversion into a .wrl file. This combination is necessary since Blender appears to be unable to import .pdb files produced by programs other than Mercury.

6.2 Procedure

Four separate pieces of software are required for this conversion: Mercury 3.3,¹¹ Blender 2.62 and 2.69,¹² and the open-source embedded Python Molecular Viewer (ePMV) plugin, which runs molecular-modelling software directly in Blender.¹³ In our work, we used the Windows versions of these programs; since all of the requisite programs are also available for the Linux and MacOSX operating systems, it is

reasonable to assume that a very analogous procedure should function on this platform as well.

Instructions are as follows:

1. Set user preferences in Blender 2.62. Open Blender 2.62 then click on *File > User Preferences > Addons*. Make sure that under the *Import–export* tab, option *Web3D X3D/VRML* format is checked. Under the *System* tab, options *autoPack*, *ePMV* and *ePMV synchro* should all be checked. Click on *Save as Default*. As a result, *ePMV* and *autoPACK* buttons will show in the upper right corner of the Blender 2.62 window (Figure 6.4).

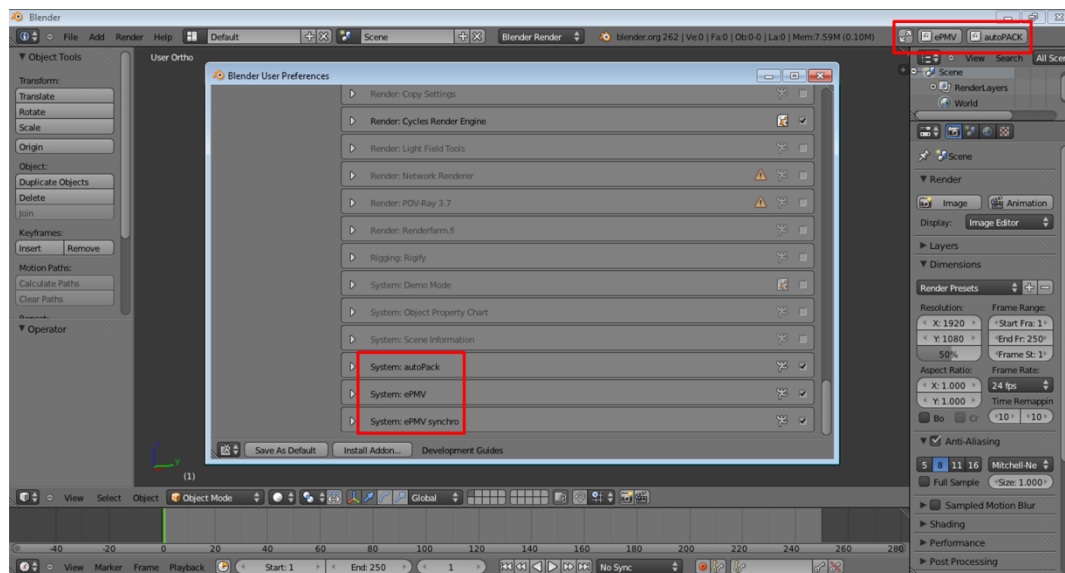


Figure 6.4 Exemplary screenshot during the setup steps in Blender. Specific buttons required are highlighted in red; refer to the text for details.

2. Set user preferences in Blender 2.69. Open Blender 2.69 then click on *File > User Preferences > Addons*. Make sure that under the *Import–export* tab, options *Web3D X3D/VRML* format and *VRML2 (Virtual Reality Modelling Language)* are both checked. Under the *Mesh* tab, option *3D Print Toolbox* should be checked. Click on *Save User Settings*.

3. Open the crystal structure's CIF file in Mercury and produce the desired packing (one or more molecules/unit cell). At this stage, it may be also useful if disordered atoms or side chains are deleted so that only one orientation remains—unless the objective is to highlight the disorder. To delete undesired features of the structure, click on *Edit > Edit Structure... > Remove*, and then click on the atoms or molecules that need to be removed (Figure 6.5).

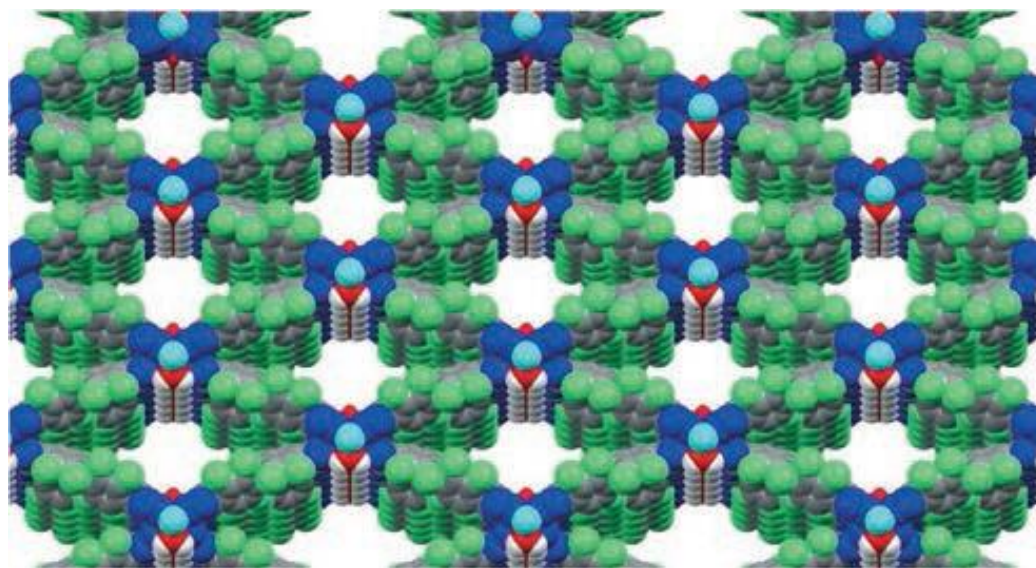


Figure 6.5 2D representation of the MOFF-3 structure produced directly from its .cif file using *Mercury 3.3*.

4. The resulting data should be saved as a PDB file (*File > Save As...*). In our case, only PDB files produced by Mercury could be successfully used in the subsequent steps.

5. Open Blender 2.62 and click on the *ePMV* button on the top right. As a result, the *ePMV* interface will appear on the left-side panel. Delete the cube, camera, and light objects in the main Blender window (Figure 6.6, this is done by simply right-clicking on those objects followed by pressing the *Delete* button).

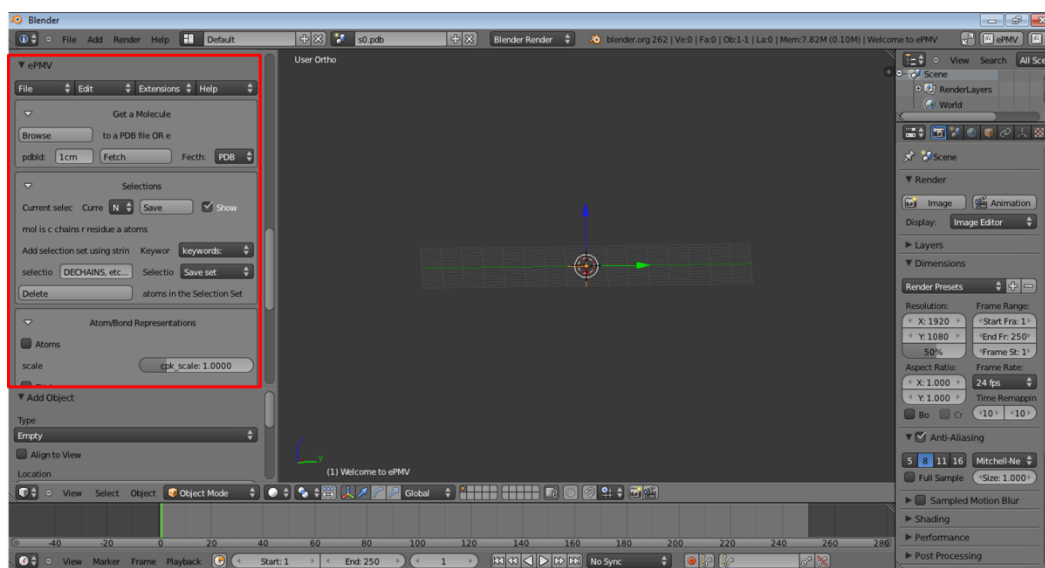


Figure 6.6 Exemplary screenshot of *ePMV* interface highlighted in red; refer to the text for details.

6. In the *ePMV* panel, choose *Browse* and navigate to the PDB file produced in step 4. Upon loading, a series of dots will appear in the main Blender window; these represent individual atoms.

7. In the *Atom/Bond Representation* subpanel on the left, choose the desired structural representation; for most organic and inorganic structures, *Atoms* or *Sticks*

representations are the most appropriate. The ensuing calculation will take between several seconds and several hours depending on the complexity of the structure. Values for the *cpk_scale*, *bs_scale*, and *bs_ratio*, as well as element colors should be adjusted at this point (if desired), since further changes are not permitted after the file is saved. Changing these parameters will affect all atoms (or bonds) of a given kind; individual atoms can also be modified using the description given in step 10 below.

8. Save the file and export it as an .x3d file: click on *File > Export > X3D Extensible 3D (.x3d)*.

9. Close Blender 2.62 and open Blender 2.69. Import the .x3d file created in the previous step: click on *File > Import > X3D Extensible 3D (.x3d)*.

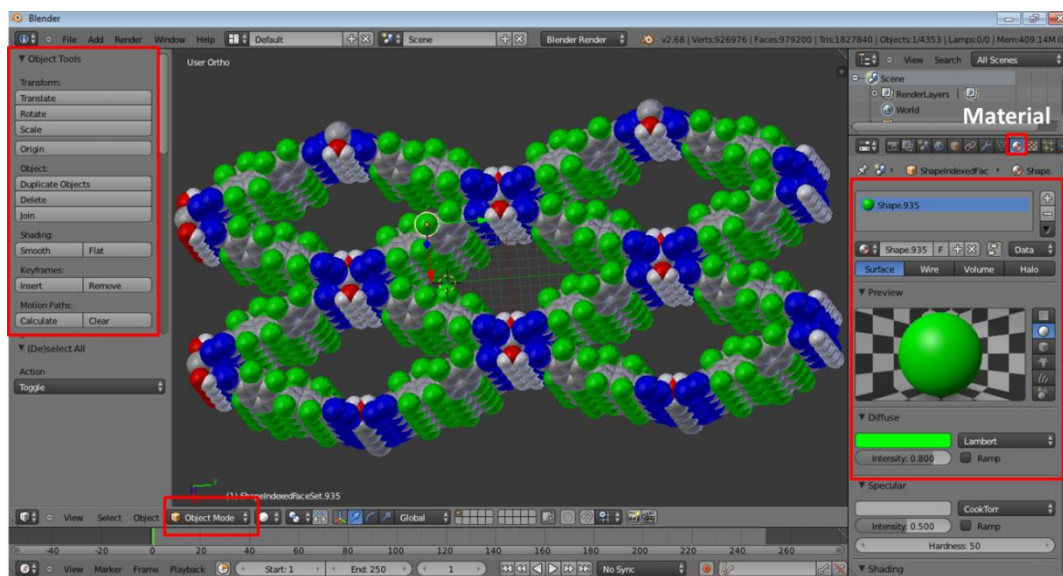




Figure 6.7 Exemplary screenshot during the processing of procedure 10. Specific buttons required are highlighted in red; refer to the text for details.

10. In *Object Mode*, you can select and delete individual atoms and bonds and adjust the size of any item (Figure 6.7). For example, to adjust the size of an atom, right-click on the desired atom and choose *Scale* in the *Object Tools* on the interface on the right. To change the color of atoms and bonds, click on the *Material* icon . Click (–) to remove the original material and (+) to add a new one. The color can be adjusted using the *Diffuse* option. You can rename the material and click  to save it then apply it to any item that you want to have the same color. This feature is particularly useful if certain parts of the structure need to be emphasized.

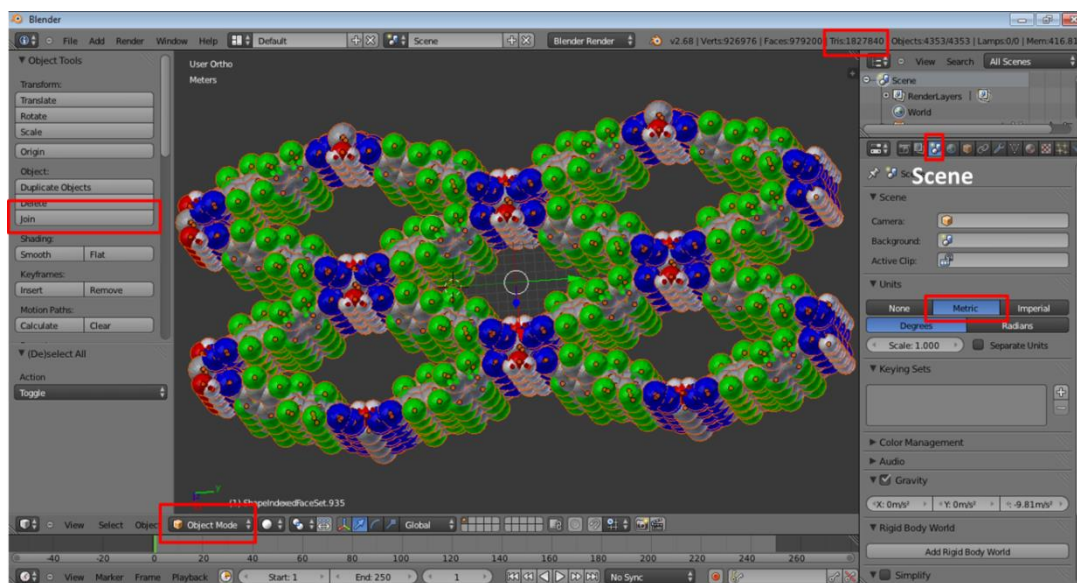


Figure 6.8 Exemplary screenshot during the processing of procedure 11. Specific buttons required are highlighted in red; refer to the text for details.

11. The produced model will most likely need to be resized to be of dimensions that are practical for printing. To do so, click on the *Scene* button on the right-side panel (third button from the left; highlighted in red in Figure 6.8). Change *Units* to *Metric*. Then, select all atoms by pressing A (with the cursor located in the view window), which

should result in the entire structure being highlighted in the main Blender window. Click on *Join* on the left-side panel to connect all of the separate parts, and then use the *Scale* button in the left-side panel to adjust the size of the structure. We have typically found the originally imported structures to be too large, and most of them needed to be scaled down. It should be noted that the dimensions provided by Blender do not correlate well with the size of the printed model (*vide infra*), so adjustment of dimensions for 3D printing requires some trial and error.

12. Once satisfied with the model size, click on the *Object Mode* button on the bottom left and switch the selection to *Edit Mode*. Then, press *W* (with the cursor located in the view window) and click on *Remove Doubles*, which should remove artefact vertices in the structure.

13. Export the resultant data to a VRML2 (.wrl) file: click on *File > Export > VRML2 (.wrl)*.

14. The created .wrl file can now be handled by many commercial and academic 3D-printing facilities. Models presented in this work have been printed by the popular website *Shapeways*.¹⁴ After brief user registration, the source file can be uploaded onto the Shapeways website by clicking on *Make + Sell > Upload > Select 3D File* and then choosing the produced .wrl file (Figure 6.9). Units should be set to inches, and the *Upload Now* button should be clicked. The *Shapeways* website will then perform the upload, estimate the model size, and confirm whether the model is indeed printable. The two most commonly encountered problems during the upload are the large file sizes

(*Shapeways* imposes a limit of 64 megabytes, which can be somewhat expanded by uploading compressed ZIP files) and a large number of polygons. The latter are created during conversion of the structure in Blender and their number can be checked by consulting the *Tris* number on the top-right bar in the Blender window (Figure 6.8). *Shapeways* limits the complexity of the uploaded models to 1,000,000 polygons.

The screenshot shows the Shapeways website interface for a model named 'MOFF-3 Supercell'. The model is a complex, multi-colored 3D structure. The page displays the file name 'MOFF-3 supercell[test].wrl' and provides both original and oriented bounding box dimensions in inches and centimeters. The volume is 216.3942 cm³ and the density is 17.00%. Below the model information, there is a table of materials available for purchase, including various plastics and Aluride, with their respective prices and 'Add to Cart' buttons.

Material	Initial Printability Check	Automated Wall Thickness Check	Price	Action
White	✓	✓	\$166.98	ADD TO CART
Black	✓	✓	\$208.59	ADD TO CART
White Polished	✗ Too Big	✓		ADD TO CART
Violet Purple Polished	✗ Too Big	✓		ADD TO CART
Coral Red Polished	✗ Too Big	✓		ADD TO CART
Hot Pink Polished	✗ Too Big	✓		ADD TO CART
Royal Blue Polished	✗ Too Big	✓		ADD TO CART
Aluride	✓	✓	\$380.19	ADD TO CART
Polished Aluride	✗ Too Big	✓		ADD TO CART

Figure 6.9 The screenshot of *Shapeways* webpage after the .wrl file of **MOFF-3** was uploaded.

15. If the model size is not satisfactory, the model should be scaled again (step 11 and onward) and the process repeated until a desired size is obtained as the estimate. Once the model size is finalized, the *Shapeways* team will check the printability of the proposed model and inform the user if there are potential issues. If no error is reported, the model can be printed. All that remains is to choose a material for the 3D model. At the time of this writing, *Shapeways* offered a wide variety of plastic, ceramic and metallic substrates (steel, silver, brass, bronze), but the only material offering full-color functionality was *Full Color Sandstone*, a proprietary mixture of plaster, vinyl polymers, and carbohydrates.¹⁵ Incidentally, this is one of the least expensive 3D printing materials offered. If a monochromatic model is desired, we anticipate that most other materials would function well (although we have not tested them).

16. If printability errors are reported, they are most commonly related to the physical limitations of the sandstone material used in printing. Thus, structures with many bonds may make those bonds too thin (< 2 mm) to support themselves; in such cases, either a smaller fragment of the structure should be chosen for printing or the representation should be switched to Space-filling, with larger *cpk_scale* values used in step 7. Some examples of screenshots of 3D modified crystal structures and the corresponding 3D printed models are shown in Chapter 6.3 (Figure 6.10–41). At current (July 2014) prices, a model similar to those shown in Chapter 6.3 will cost between \$20 and \$150 depending on the size.¹⁶ Because sandstone is essentially plaster, models produced from it are rather fragile (they will easily shatter if dropped), thermostable only up to 60 °C, not resistant to water and have grainy surfaces. There are two solutions to

the last two problems. First, the printed model can be dipped in glue (e.g. ZPrinter Z-Bond 90 Infiltrant) to form a coating that gives a strengthened material with a glossy finish when dried. The usage and safety instructions for this product should be followed. For example, when the models are dipped into a plastic container full of the glue, there is a large temperature increase (exothermic) and outgassing is significant enough to warrant the use of personal protective equipment and a ventilated area (fume hood). The model is then patted dry to remove excess glue. The glue penetrates ~2 mm into the model; excess glue will pool and deteriorate the finish. A simpler method that gives similar results makes use of a glossy acrylic spray that can be applied with repetitive spray–dry cycles (4–5 times).

6.3 3D Modified Crystal Structures and 3D Printed Models

6.3.1 Triply Ferrocene-bridged Boroxine Cyclophane

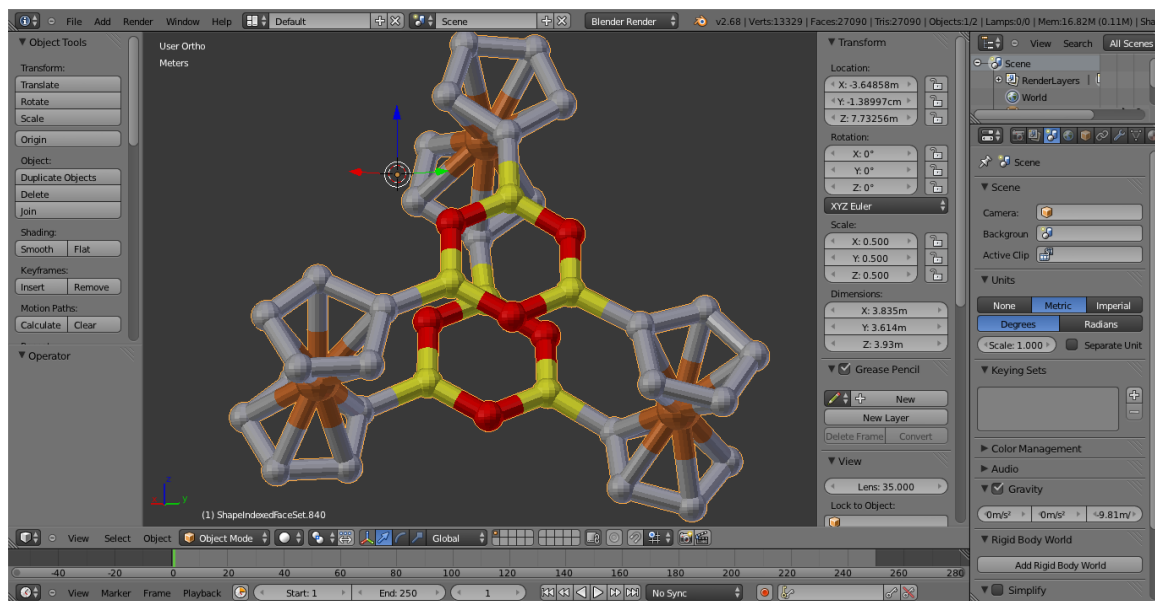


Figure 6.10 3D modified crystal structure of triply ferrocene-bridged boroxine cyclophane.

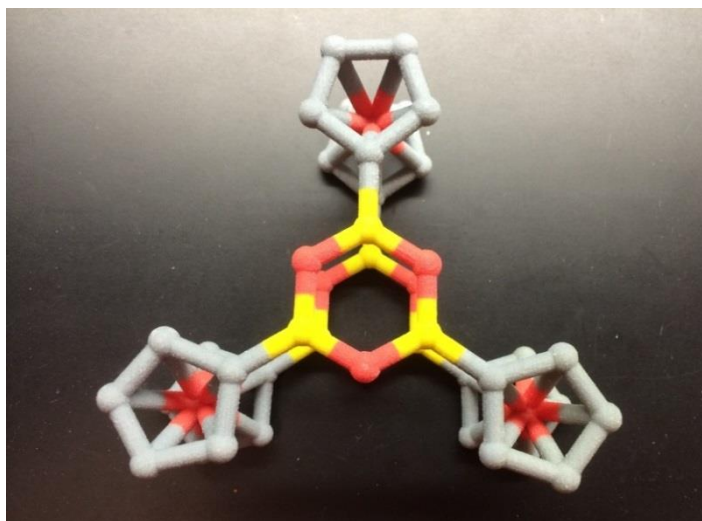


Figure 6.11 3D printed model of triply ferrocene-bridged boroxine cyclophane.

6.3.2 MOFF-2

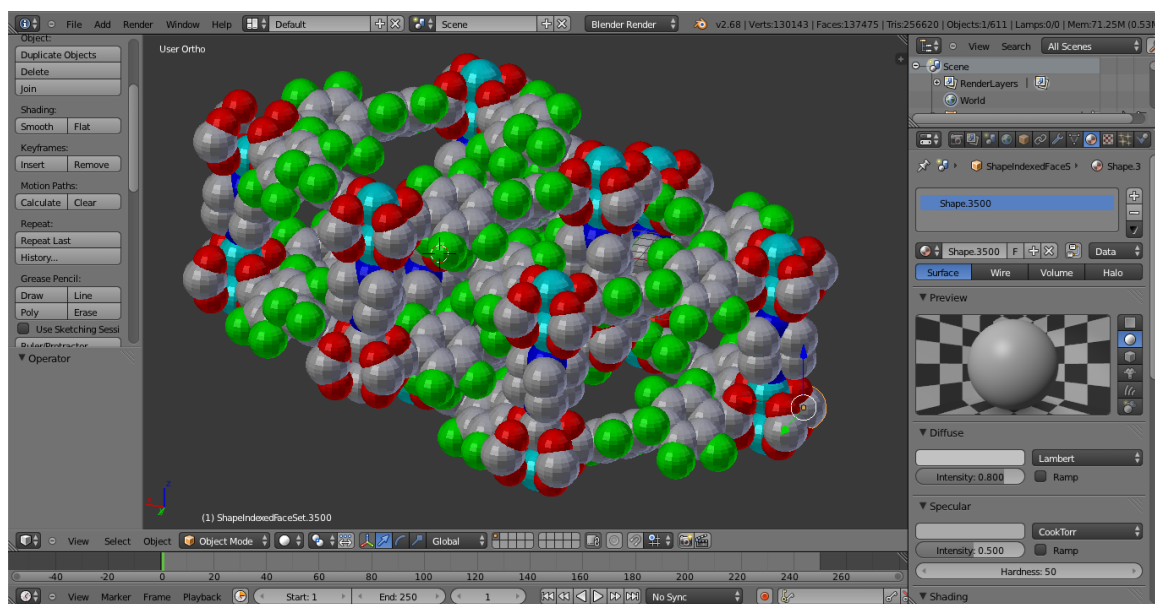


Figure 6.12 3D modified crystal structure of MOFF-2.

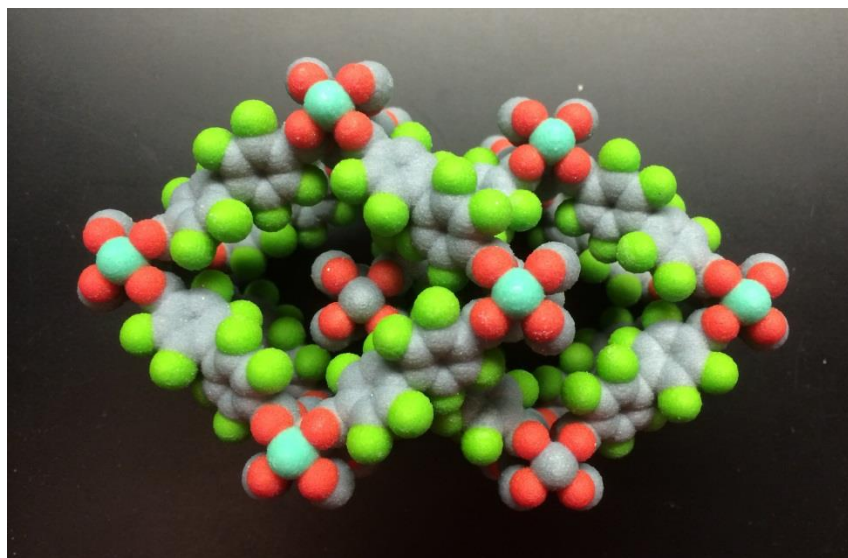


Figure 6.13 3D printed model of MOFF-2.

6.3.3 Unit Cell of MOFF-3

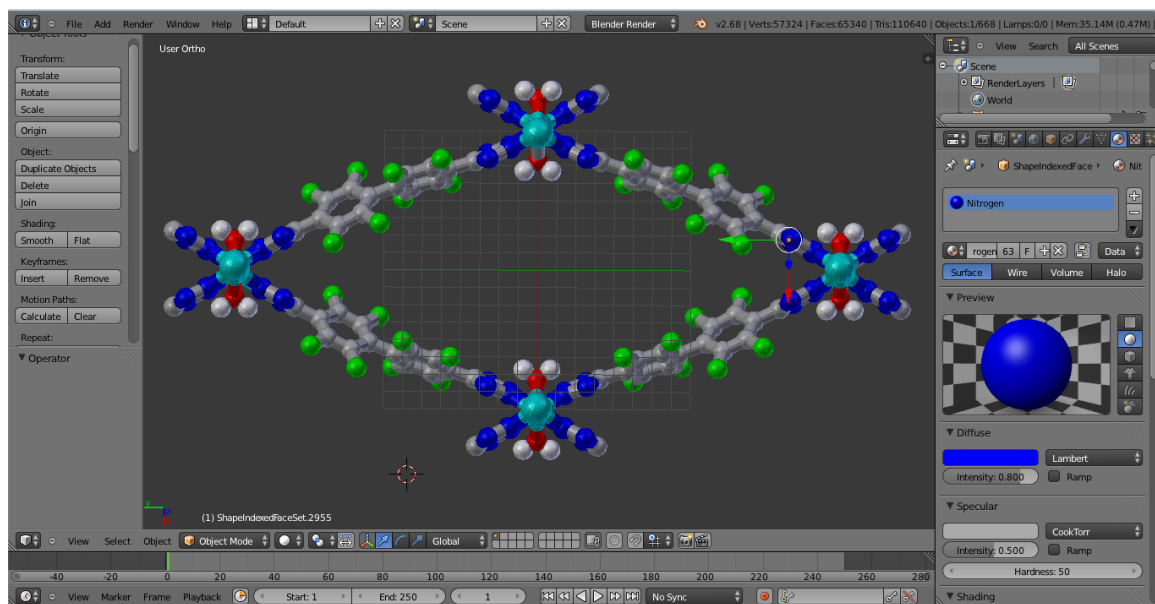


Figure 6.14 3D modified crystal structure of the unit cell of **MOFF-3**.

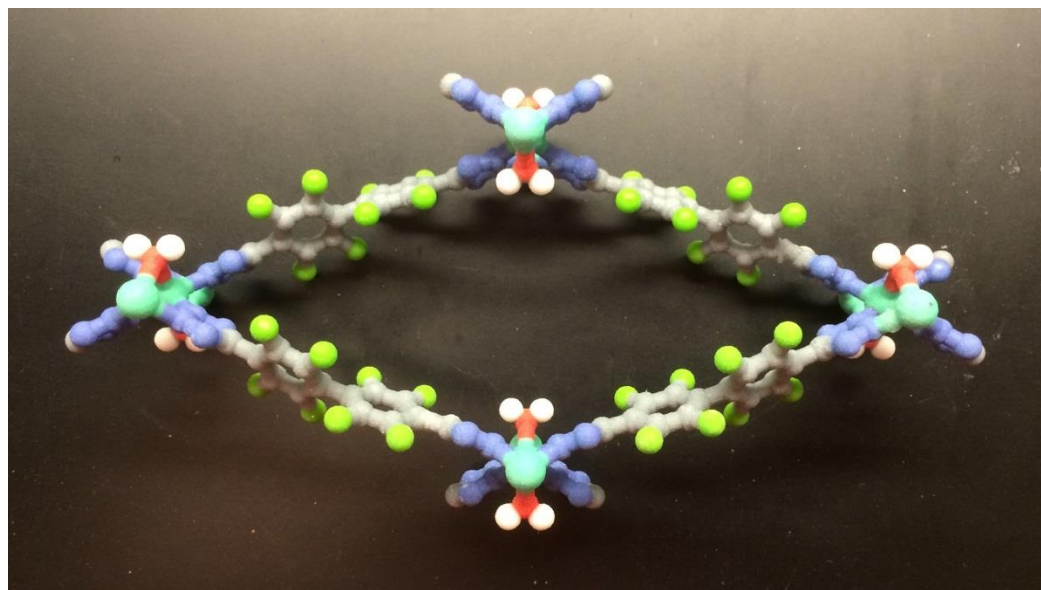


Figure 6.15 3D printed model of the unit cell of **MOFF-3**.

6.3.4 Supercell of MOFF-3

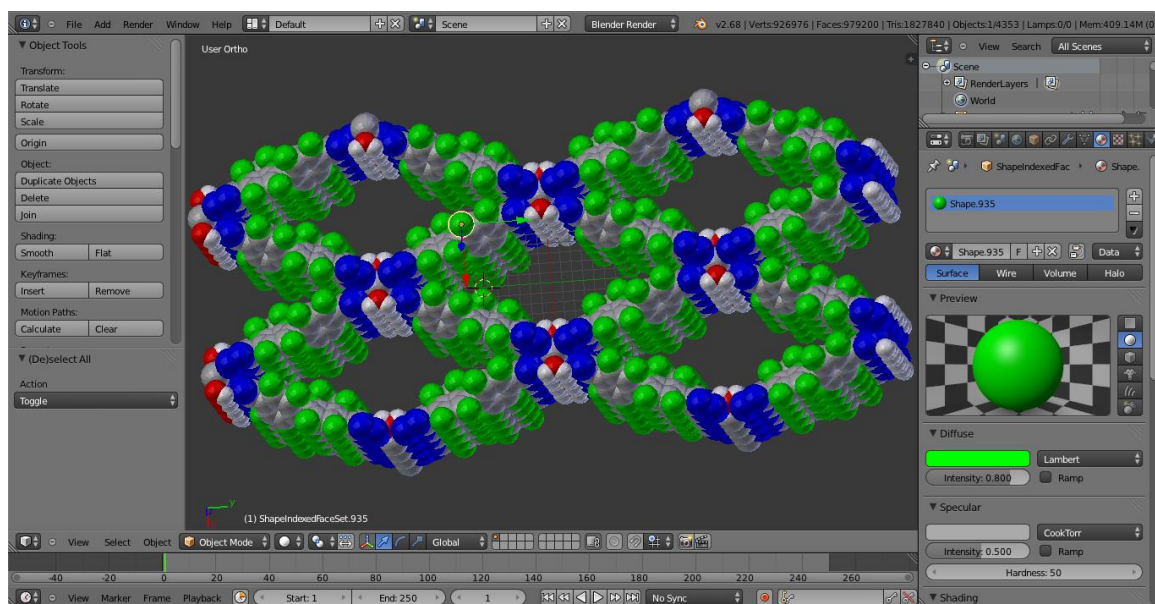


Figure 6.16 3D modified crystal structure of the supercell of **MOFF-3**.

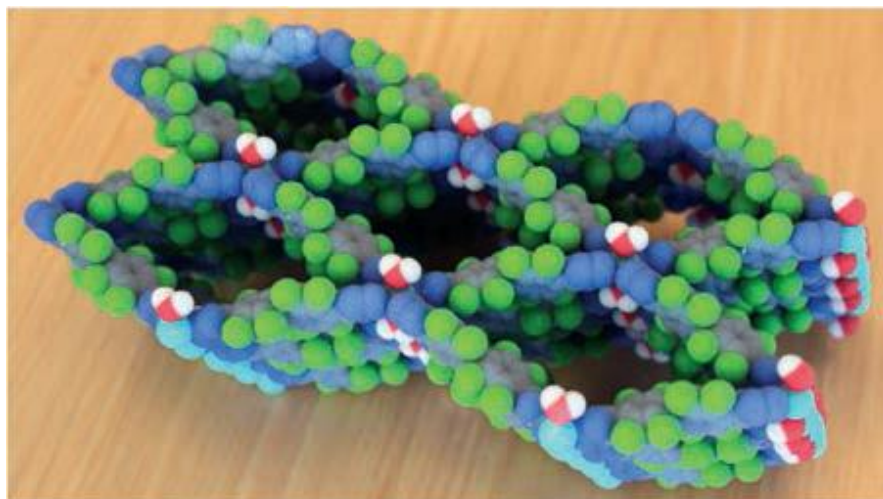


Figure 6.17 3D printed model of the supercell of **MOFF-3**.

6.3.5 MOFF-5

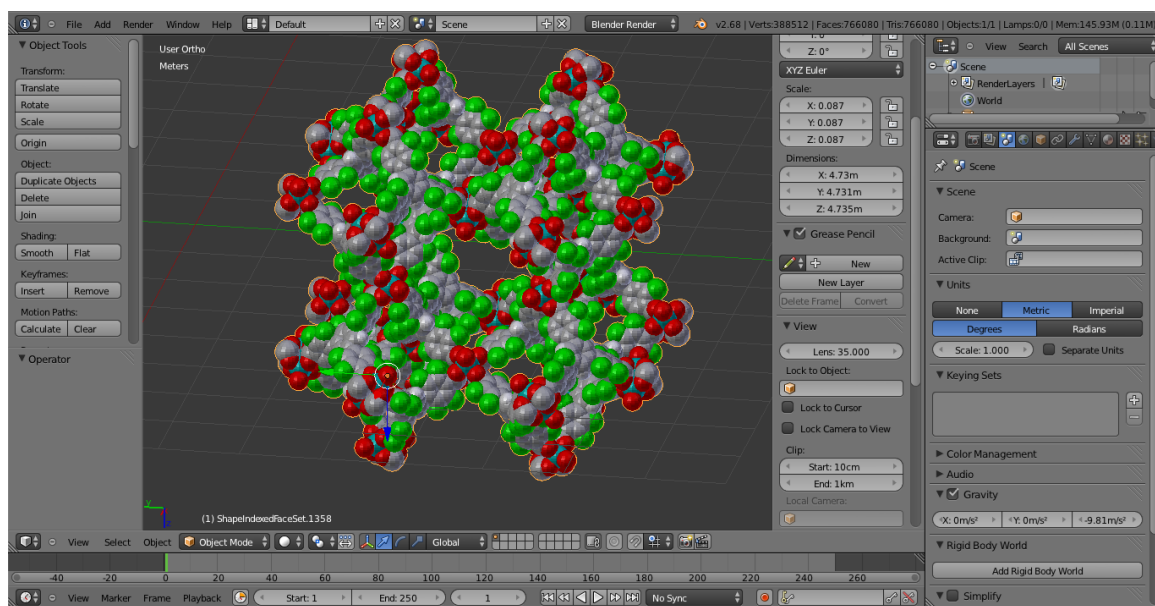


Figure 6.18 3D modified crystal structure of MOFF-5.

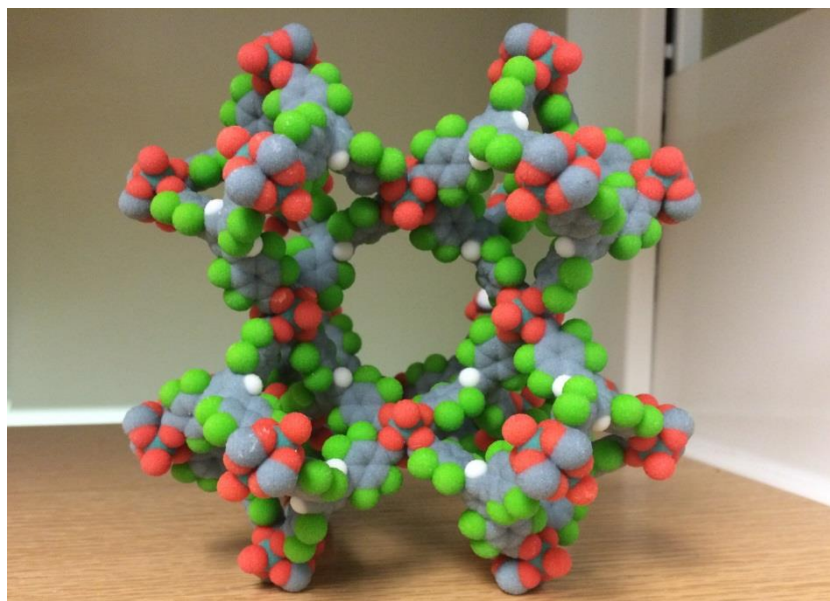


Figure 6.19 3D printed model of MOFF-5.

6.3.6 MOFF-6

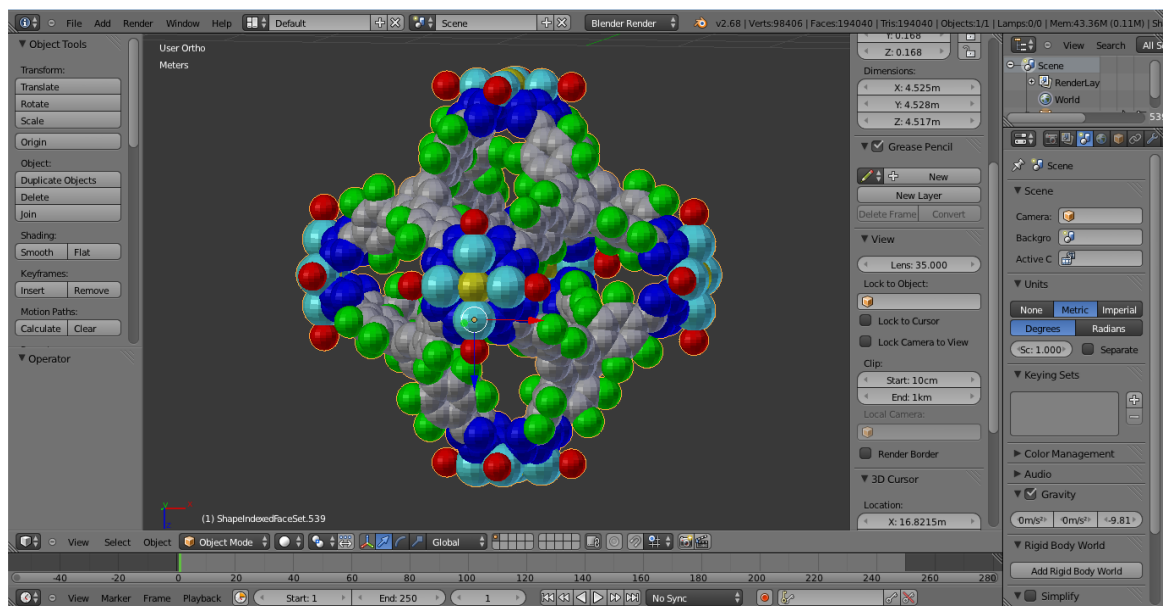


Figure 6.20 3D modified crystal structure of MOFF-6.

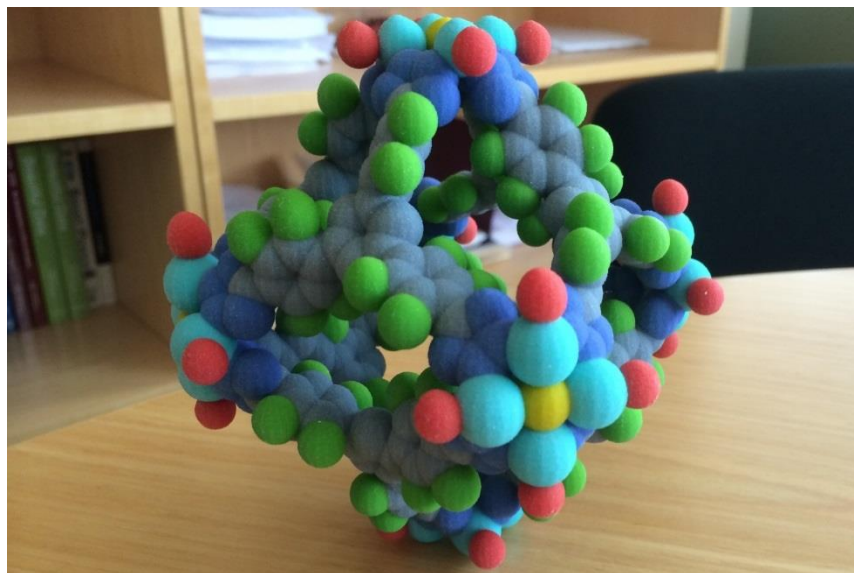


Figure 6.21 3D printed model of MOFF-5.

6.3.7 nCOF

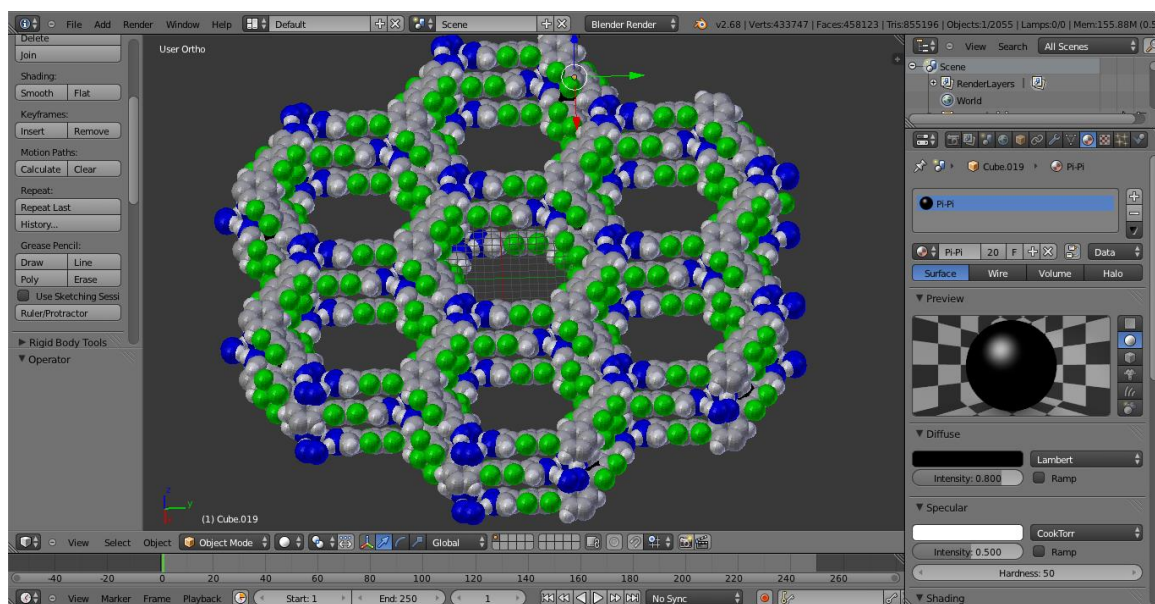


Figure 6.22 3D modified crystal structure of nCOF.

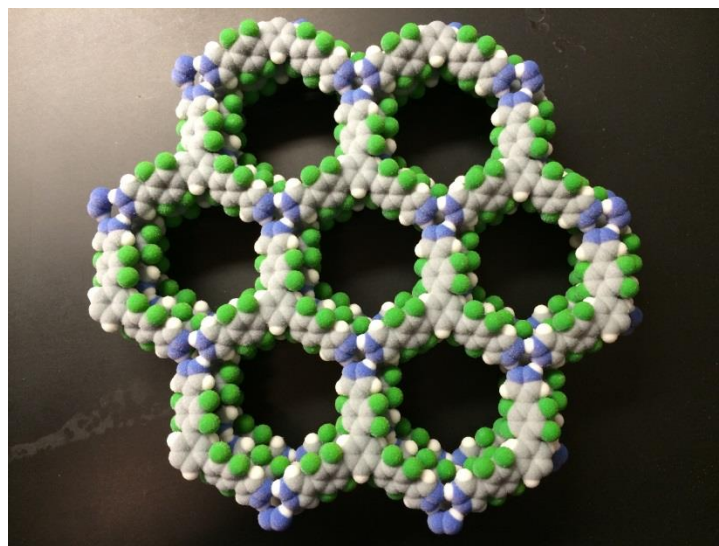


Figure 6.23 3D printed model of nCOF.

6.3.8 $[\pi\cdots\pi]$ Stacking of Macrocycle 1 in Zn-MCMOF

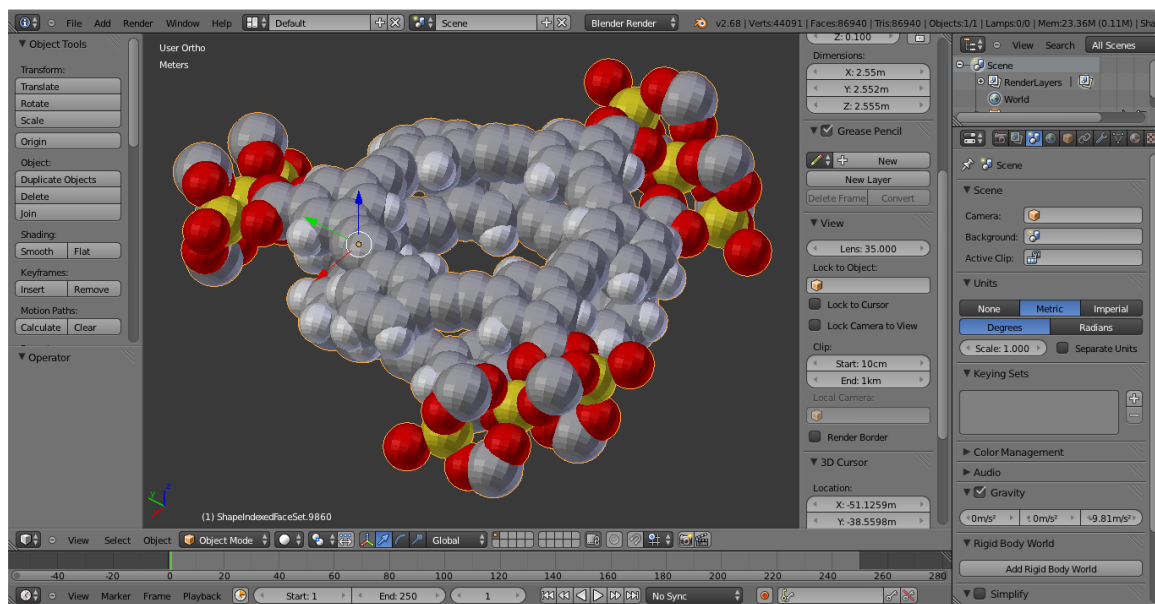


Figure 6.24 3D modified crystal structure of $[\pi\cdots\pi]$ stacking of macrocycle **1** in **Zn-MCMOF**.

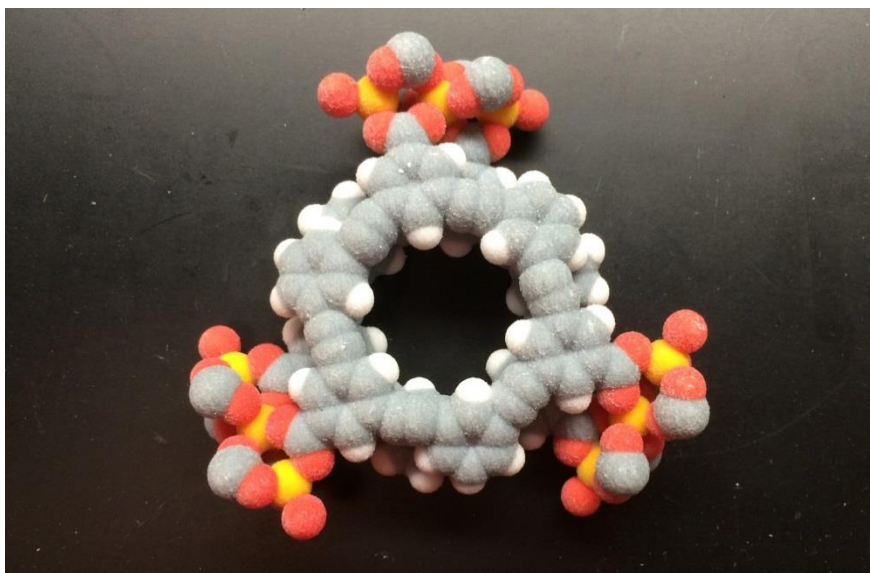


Figure 6.25 3D printed model of $[\pi\cdots\pi]$ stacking of macrocycle **1** in **Zn-MCMOF**.

6.3.9 Zn-MCMOF

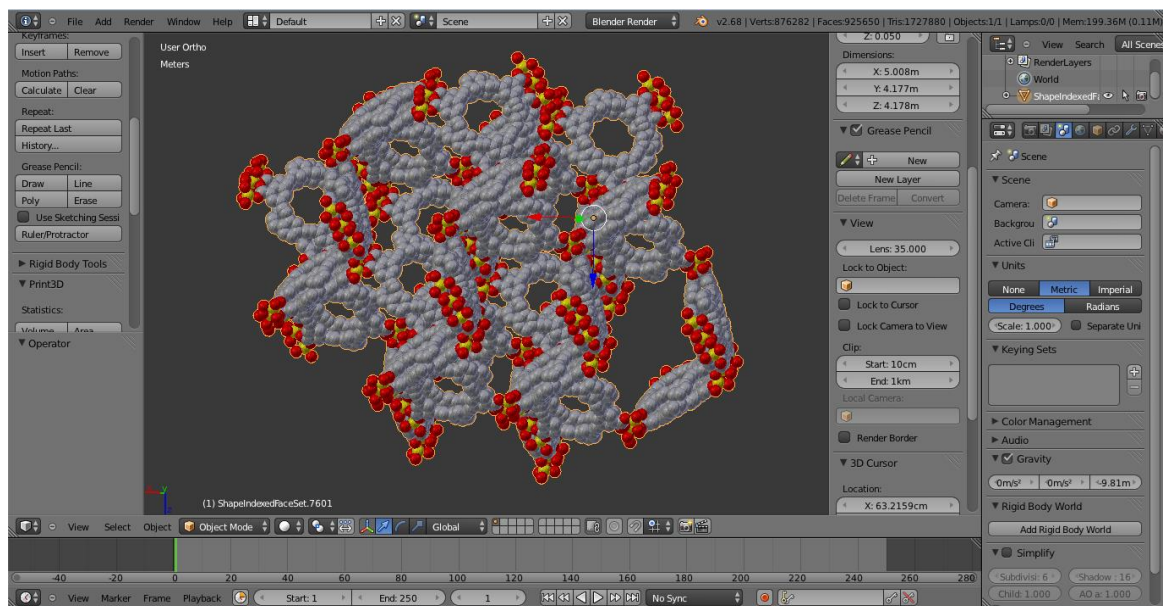


Figure 6.26 3D modified crystal structure of Zn-MCMOF.

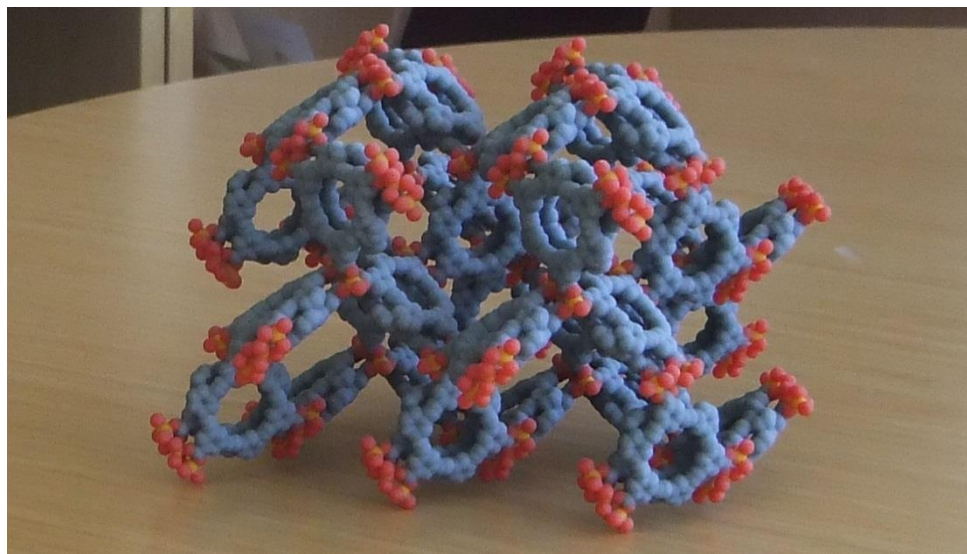


Figure 6.27 3D printed model of Zn-MCMOF.

6.3.10 Zr-MCMOF

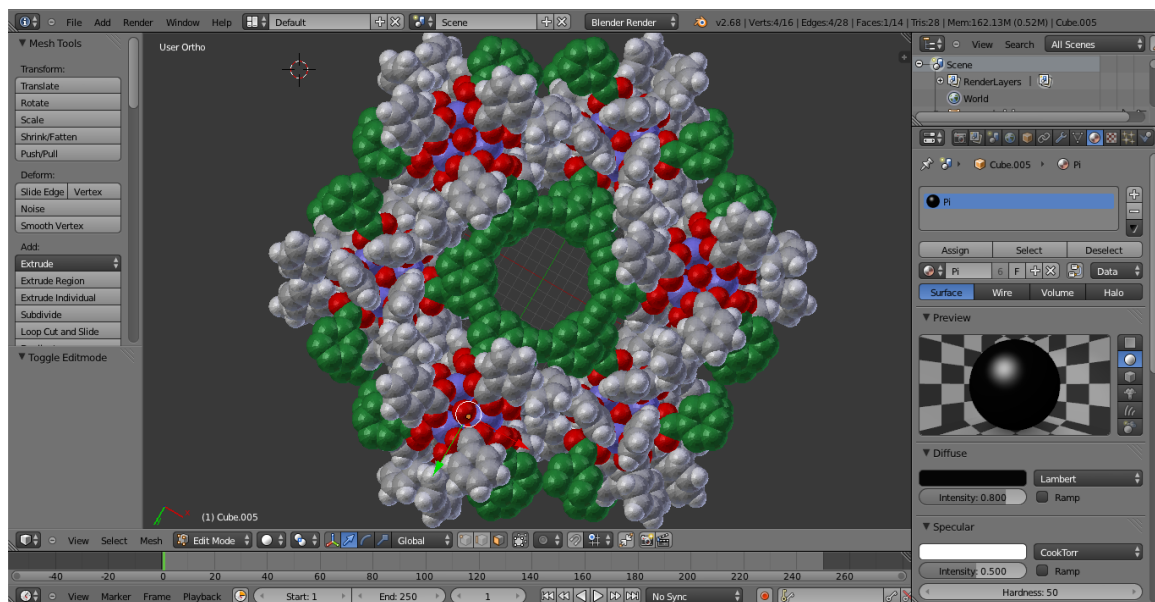


Figure 6.28 3D modified crystal structure of **Zr-MCMOF**.

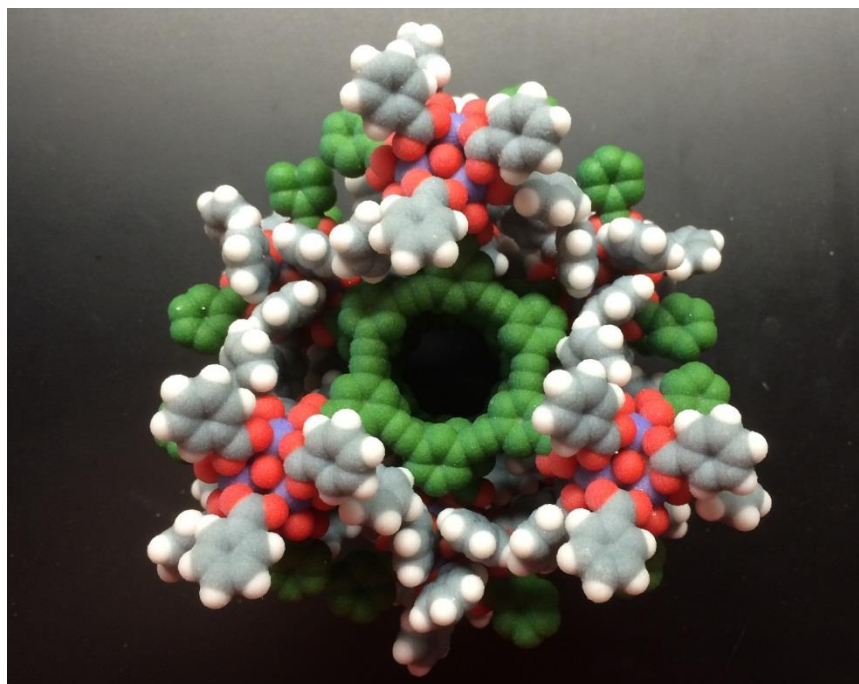


Figure 6.29 3D printed model of **Zr-MCMOF**.

6.3.11 1,3,5-Trifluorobenzene@macrocycle 2

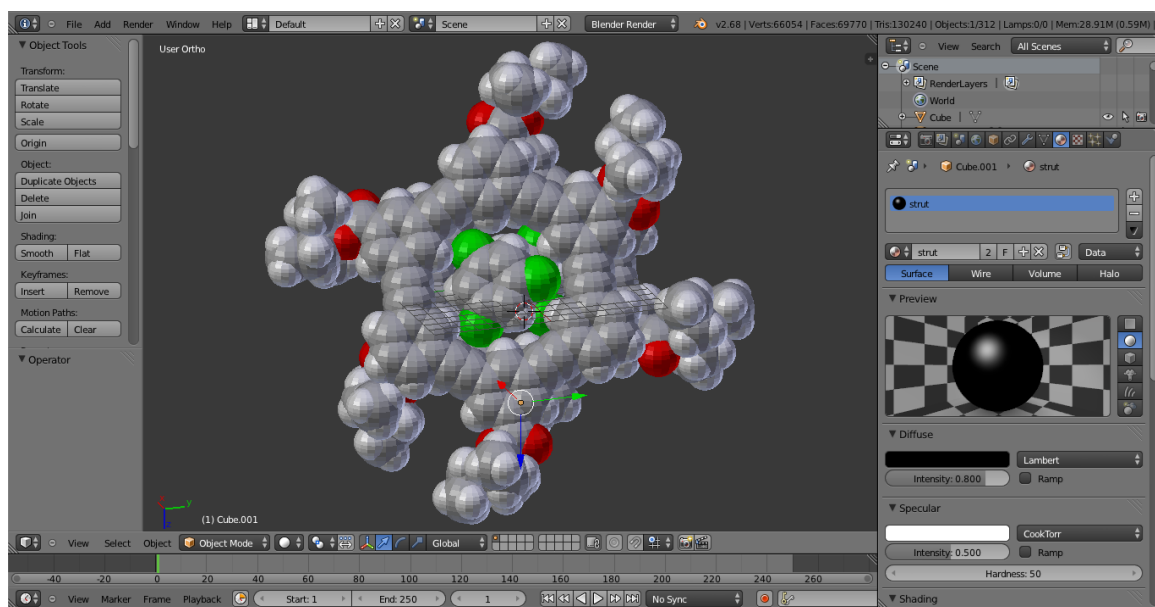


Figure 6.30 3D modified crystal structure of 1,3,5-trifluorobenzene@macrocycle 2.

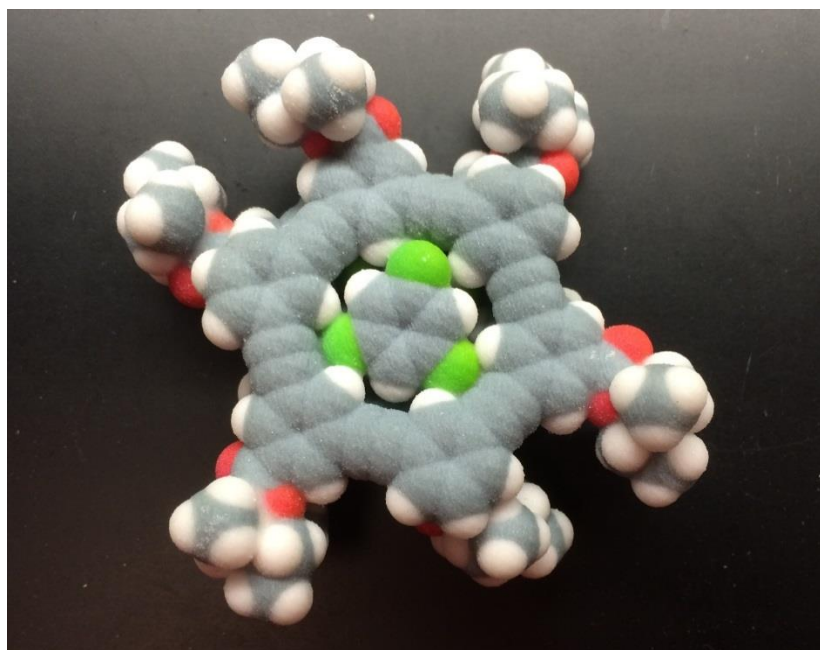


Figure 6.31 3D printed model of 1,3,5-trifluorobenzene@macrocycle 2.

6.3.12 1,4-Trifluorobenzene@macrocycle 2

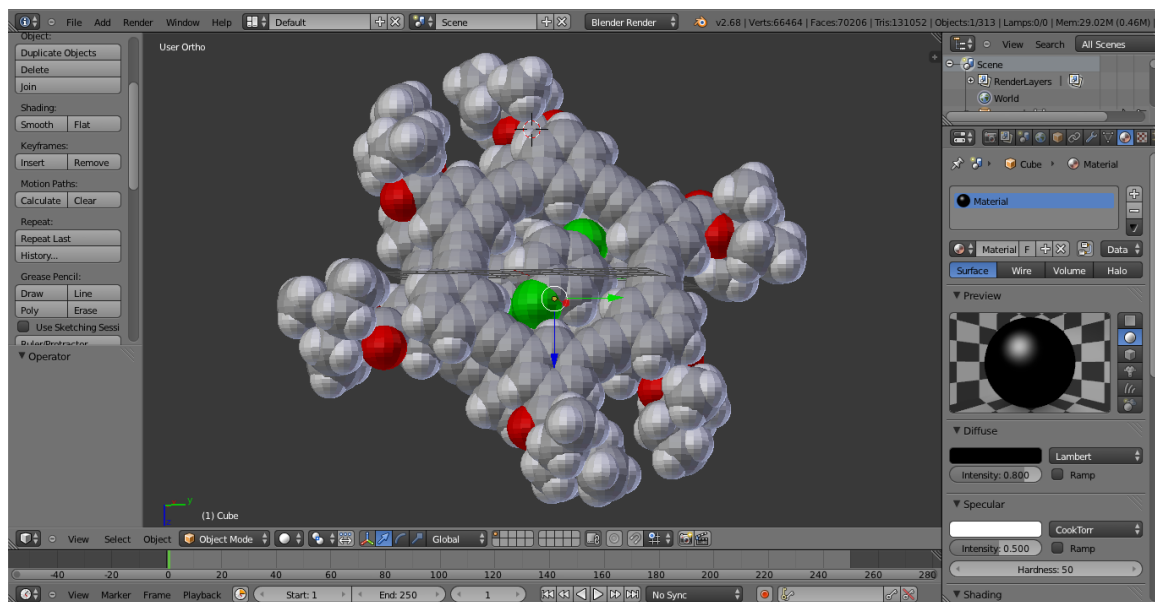


Figure 6.32 3D modified crystal structure of 1,4-trifluorobenzene@macrocycle2.

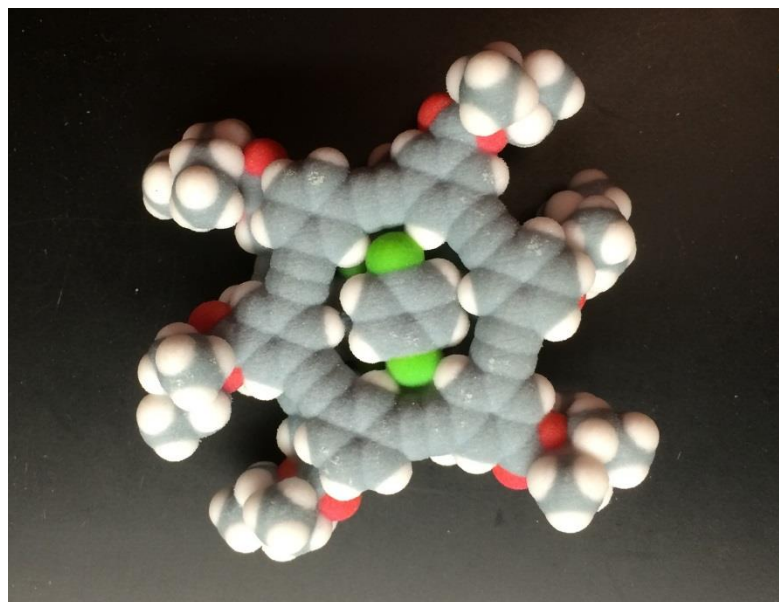


Figure 6.33 3D printed model of 1,4-trifluorobenzene@macrocycle 2.

6.3.13 Unit Cell of $V^{4+}(O)BDC$ ¹⁷

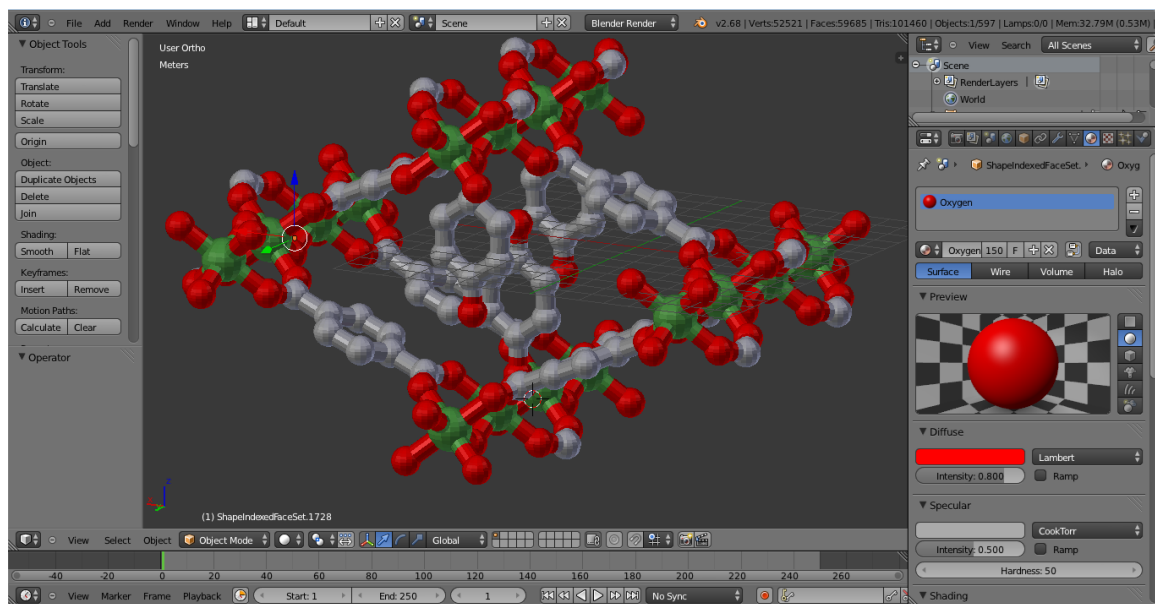


Figure 6.34 3D modified crystal structure of the unit cell of $V^{4+}(O)BDC$.

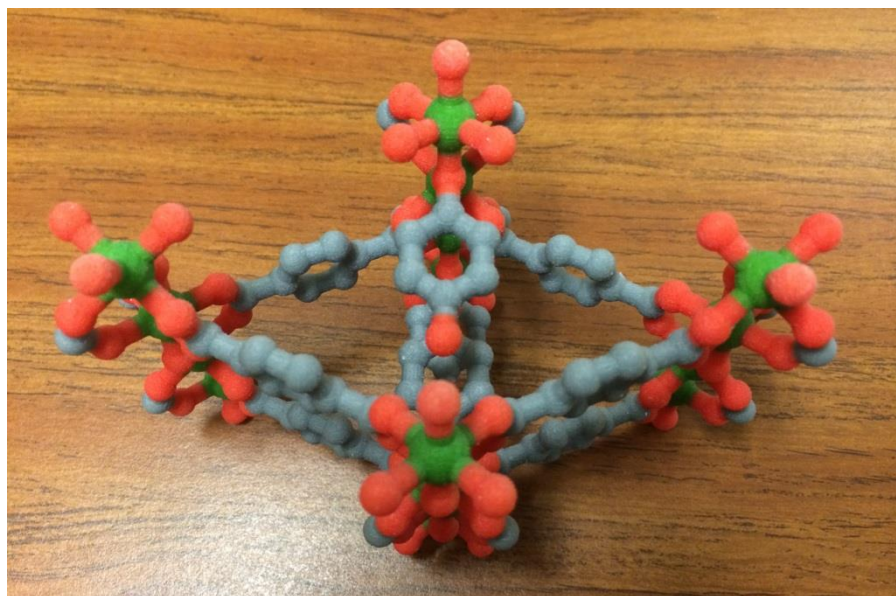


Figure 6.35 3D printed model of the unit cell of $V^{4+}(O)BDC$.

6.3.14 Unit cell of MOF-5¹⁸

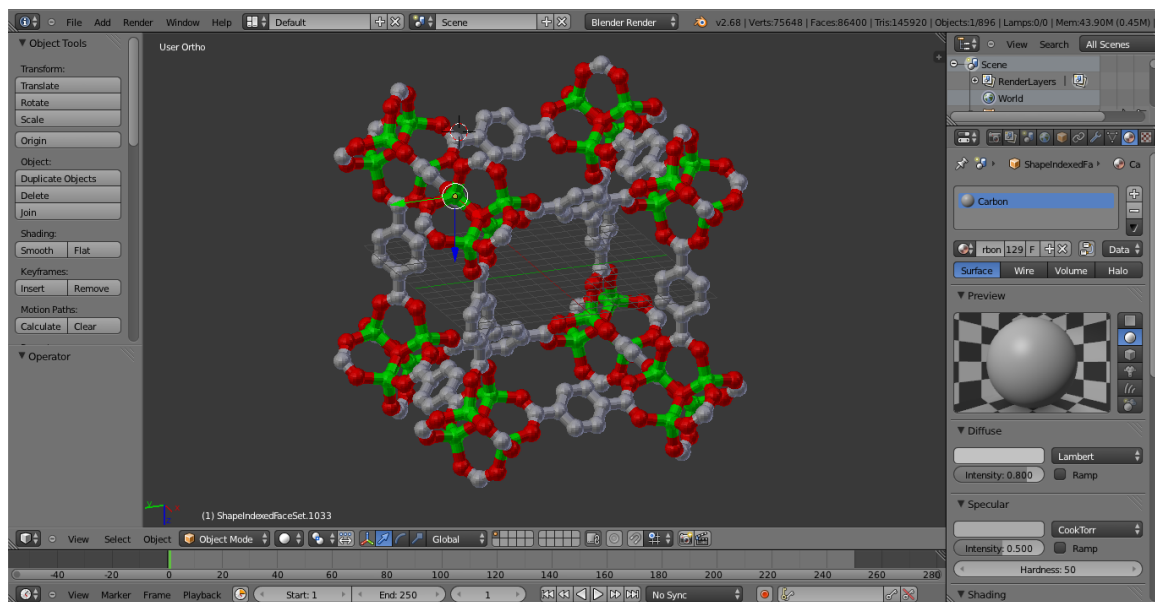


Figure 6.36 3D modified crystal structure of the unit cell of MOF-5.

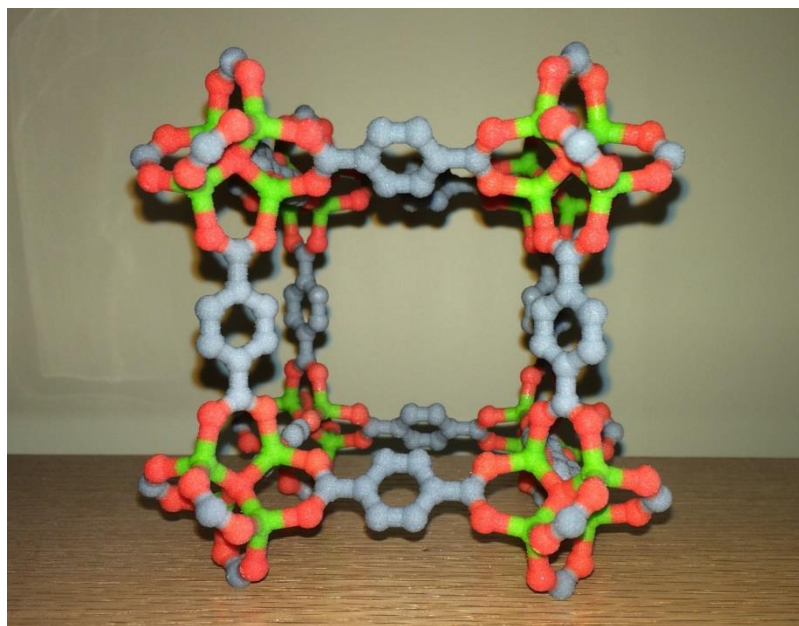


Figure 6.37 3D printed model of the unit cell of MOF-5.

6.4 Conclusions and Outlook

In conclusion, we presented here a set of guidelines on how to convert any small-molecule or extended material crystal structure into a 3D printed model. The value of these models should be in facilitating communication of crystal structure details both in the classroom and between experienced practitioners in the field. The users do not need to overly worry about the apparently complicated interface of Blender, as only a handful of its numerous features are being used in our procedure. Our set of instructions uses freely available software, requires no programming knowledge and no knowledge of 3D printing techniques, and produces models using a commercial easy-to-use website.

As with many rapidly developing technologies, we expect these instructions to be outdated within several years, as 3D printers enter the mainstream and crystal structure processing software becomes better integrated with this obviously very relevant technology. Until then, we hope that our colleagues will find this protocol—and its 3D printed products—useful and educational.

6.5 References

- [1] Chen, T.-H.; Lee, S.; Flood, A. H.; Miljanić, O. Š. *CrystEngComm* **2014**, *16*, 5488–5493. Highlighted by *C&EN News* and *Chemistry World*. Featured on the cover page of *CrystEngComm*.
- [2] Freedman, D. H. *Technology Review* **2012**, *115*, 50–53.

- [3] Additive Manufacturing: Solid Print, in the Economist Special Report on Manufacturing and Innovation, April 21 **2012**, p 14–15.
- [4] (a) Mathieson, J. S.; Rosnes, M. H.; Sans, V.; Kitson, P. J.; Cronin, L.; *Beilstein J. Nanotechnol.* **2013**, *4*, 285–291. (b) Kitson, P. J.; Symes, M. D.; Dragone, V.; Cronin, L. *Chem. Sci.* **2013**, *4*, 3099–3103. (c) Kitson, P.; Rosnes, M.; Sans, V.; Dragone, V.; Cronin, L. *Lab Chip* **2012**, *12*, 3267–3271. (d) Symes, M. D.; Kitson, P. J.; Yan, J.; Richmond, C. J.; Cooper, G. J. T.; Bowman, R. W.; Vilbrandt T.; Cronin, L.; *Nat. Chem.* **2012**, *4*, 349–354.
- [5] https://www.shapeways.com/blog/archives/2141-designer-spotlight-ivo-laros.html?%2Farchives%2F2141-designer-spotlight-ivo-laros_html=
- [6] Picture was taken from Prof. Allan J. Jacobson's lab in University of Houston.
- [7] For examples of printing structures of distinct proteins, see: <http://cbe.wisc.edu/assets/docs/pdf/srp-bio/stongrevised.pdf>. For small molecules and proteins, see: <http://barneybioproductslab.cfans.umn.edu/3d-printing-and-molecular-models/>. For a commercial service offering 3D printed molecular models, see: <http://models.scripps.edu/>. See also: Jones, N. *Nature* **2012**, *487*, 22–23.
- [8] (a) Kitson, P.; Macdonell, A.; Tsuda, S.; Zang, H.; Long, D.-L.; Cronin, L. *Cryst. Growth Des.* **2014**, *14*, 2720–2724. (b) Scalfani, V. F.; Vaid, T. P. *J. Chem. Educ.* **2014**, doi: 10.1021/ed400887t.

[9] The *PyMOL Molecular Graphics System, Version 1.5.0.4*, Schrödinger, LLC. Freely available from: www.pymol.org.

[10] It should be noted that other 3D printing file formats (*e.g.* .STL) can be used if color models are not required. There is much instructional value in monochromatic models as well, since they can be printed quickly and inexpensively on many of the hobbyist 3D printers that use ABS plastics as substrates. Full color 3D printers are still prohibitively expensive (and large) for individual use, and are thus typically housed in commercial and academic facilities.

[11] Freely available for Linux, MacOSX and Windows operating systems, from: <http://www.ccdc.cam.ac.uk/Solutions/CSDSystem/Pages/Mercury.aspx>. Last accessed on February 11, 2014.

[12] Blender is free software, available for Linux, MacOSX and Windows operating systems at: <http://www.blender.org/download/>. Last accessed on February 11, 2014. Blender is convenient to use because of the wealth of use available online, which is further complemented by numerous YouTube videos illustrating individual features. This body of helpful information should make troubleshooting easier for the users of this procedure.

[13] Freely available at: <http://epmv.scripps.edu/download-installfree/installers/>. ePMV is available for Linux, MacOSX and Windows operating systems. Last accessed on February 11, 2014. Note that—at the time of this writing—ePMV operates on Blender 2.62, which is not the same as the latest version of the program (Blender 2.69 for

Windows and Blender 2.70 for MacOSX). Therefore, both versions of Blender should be downloaded and used, which is fortunately possible. It is reasonable to assume that these functionalities will eventually be combined in a single version of the program, which would simplify our procedure. See also: Johnson, G. T.; Autin, L.; Goodsell, D. S.; Sanner, M. F.; Olson, A. J.; *Structure* **2011**, *19*, 293–303.

[14] <http://www.shapeways.com>.

[15] Material Safety Data Sheet (MSDS) for Full Color Sandstone can be found at: http://www.shapeways.com/rrstatic/material_docs/m-sds-sandstone.pdf.

[16] For comparison, building a model of a supercell of **MOFF-3** (Figure 6.17) using modular **commercial** molecular model kits would cost ~\$300. In addition, these sizes of atoms in these kits are too large to make them practical for MOF structures with numerous atoms; thus, a single unit cell model for **MOFF-3** would be $30 \times 30 \times 30$ cm large. 3D-Printed model permit much smaller feature size of approximate dimensions: $16 \times 8 \times 7$ cm.

[17] Wang, X.; Liu, L.; Jacobson, A. J. *Angew. Chem., Int. Ed.* **2006**, *45*, 6499–6503.

[18] Li, H.; Eddaoudi, M.; O'Keeffe, M.; Yaghi, O. M. *Nature* **1999**, *402*, 276–279.